Understanding the Structural and Electrochemical Behavior of High Energy Density Layered Oxide Cathodes for Sodium and Lithium Ion Batteries

James William Somerville

Linacre College

University of Oxford

A thesis submitted for the degree of

Doctor of Philosophy

Hilary 2019

This thesis is dedicated to the memory of my grandfathers,
William Nimmo and Jack Somerville.
Two great men who inspired me with their passion for solving problems.
I will always cherish the time I had with them.

Acknowledgements

Professional

Professor Peter Bruce, thank you for giving me the opportunity, guidance, and financial support to tackle some of the truly interesting problems within battery technology under your supervision.

Dr. Matthew Roberts, thank you for being an incredible mentor throughout my DPhil as well as an endless source of experience and wisdom. Dr. Urmimala Maitra, thank you for always being there to bounce ideas off of and demonstrating to me the importance of thinking critically even when it is inconvenient. Dr. Nuria Tapia-Ruiz, thank you for tolerating all of my "Why do you do it this way?" questions and teaching me that productive investigation comes from the right balance of experimentation and analysis. Dr. Liyu Jin, Dr. Christian Kuss, Dr. Miguel Perez Osorio, Dr. Jitti Kasemchainan, and Dr. Adam Sobkowiak, thank you for showing me the high bar one must set for their work to produce meaningful results which don't get lost among the noise of this research field.

Robert House, it has been a pleasure working alongside you. Our *many* discussions (often turned debates) and mutual competitiveness constantly challenged me to work harder and dig deeper into questions. Dominic Förrstermann, Dr. Rong Hao, Dr. Xiangwen Gao, and Dr. Niccolo Guerrini, I couldn't have asked for better colleagues and friends to learn from these past few years. When experiments were not working and research was mentally taxing, you made showing up to lab everyday a lot more enjoyable.

And finally, thank you to everyone in the PGB group, past and present. It wouldn't have been possible to complete this DPhil without your support.

Personal

To my extraordinary girlfriend, Emily, words cannot convey the gratitude I feel to have you in my life. Thank you for pushing me to attend Oxford even though it meant years of living thousands of miles apart. Thank you for being there for me through everything from failed experiments to adjusting to the "less than ideal" UK climate. Thank you for your hours and hours of meticulous proofreading. Thank you for dedicating your amazing mind to learning all you could about battery

materials just to help me and making fantastic suggestions for improving this thesis. Your love and support have been tremendous and unwavering.

To my parents, Joyce and David, I am so grateful for the childhood you gave me and opportunities that resulted from it. This DPhil is as much a credit to you as it is to me. Thank you for always being at the end of a phone to advise me on any problem I encountered, thank you for visiting often, and thank you for creating an incredible network of friends and family throughout the UK which has made living abroad a lot less scary.

To my little sisters, Katie and Fiona, over these last few years, you both have grown into incredible women whose advice I value greatly. Thank you for being much better than me at keeping in contact with phone calls and text messages. Our conversations, although too infrequent, were always a pleasant break away.

To my grandmas, Susan and Rena, having you both so close has been incredible. I'm very happy I was able to visit more often (although still not enough) and thankful that I could be there at the important times. Knowing you were both just a train ride away always gave me comfort.

And thank you to all the other family and friends who have made these past 4.5 years so very enjoyable. I would like to thank especially Karyn and Bill Spear, Lorna and Paddy Stewart, Eddie and Mags Somerville, Alex, Lisa, and Leslie Pautonnier, Liz and Bob Fleming, Robert and Ellen Fleming, Liz and Mike Edwards, and the many amazing people in Linacre College and the Oxford Football club.

Abstract

The world's crucial need for energy storage has provoked intense interest in cheaper, more sustainable battery chemistries, such as Na-ion. One of the main bottlenecks toward the utilization of Na-ion batteries, however, is the lack of an optimal cathode material. In this thesis, the class of cathode compounds known as layered transition metal oxides are investigated because of their ability to reversibly intercalate (insert/extract) a relatively large quantity of Na and Li-ions (i.e. high capacity).

P2-$Na_{2/3}[Ni_{1/3}Mn_{2/3}]O_2$ is first investigated to probe its utility as a cathode but is demonstrated to possess certain drawbacks including Na deficiency in the as-synthesized state, unsatisfactory cyclability, and a strong driving force for Na-ion ordering. These obstacles are shown to be sufficiently overcome by means of partial metal substitution of Fe as well as a new pre-treatment process using Na-naphthalide to intercalate extra Na-ions into the pristine structure.

Attention is then turned to the mechanism by which partial Fe substitution improves cyclability. It is found that this enhancement largely stems from an altered structural transition at high voltages (i.e. "Z"-phase) resulting in less overall volume changes. The true structural identity of the "Z"-phase is then resolved for the first time as an evolving P2:O2 intergrowth.

Finally, the possibility of using oxygen (instead of heavier transition metals) as a redox center is examined for a collection of layered transition metal oxide materials. It is discovered that oxygen-redox can be activated in the presence of Mg in P2-$Na_{2/3}[Mg_{0.28}Mn_{0.72}]O_2$ and is reversible over hundreds of cycles in O3-$Li[Li_{1/5}Ni_{1/5}Mn_{3/5}]O_2$. Moreover, through investigation of P2-$Na_{3y}[Li_yMn_{1-y}]O_2$ (y = 1/5, 1/4), it is determined that the discharge voltage of oxygen-redox compounds strongly depends on cation ordering within the transition metal layer.

In total, the aim of this thesis is to communicate new fundamental insight into the nature of layered transition metal oxide cathodes in order to provide a platform for their further development.

Contents

Publication List

(1) Somerville, J. W.; House, R. A.; Tapia-Ruiz, N.; Sobkowiak, A.; Ramos, S.; Chadwick, A. V.; Roberts, M. R.; Maitra, U.; Bruce, P. G. *Journal of Materials Chemistry A* **2018**, *6*, 5271–5275.

(2) Somerville, J. W.; Sobkowiak, A.; Tapia-Ruiz, N.; Billaud, J.; Lozano, J. G.; House, R. A.; Gallington, L. C.; Ericsson, T.; Häggström, L.; Roberts, M. R.; Maitra, U.; Bruce, P. G. *Energy & Environmental Science* **2019**, *12*, 2223–2232.

(3) Maitra, U.; House, R. A.; Somerville, J. W.; Tapia-Ruiz, N.; Lozano, J. G.; Guerrini, N.; Hao, R.; Luo, K.; Jin, L.; Pérez-Osorio, M. A.; Massel, F.; Pickup, D. M.; Ramos, S.; Lu, X.; McNally, D. E.; Chadwick, A. V.; Giustino, F.; Schmitt, T.; Duda, L. C.; Roberts, M. R.; Bruce, P. G. *Nature Chemistry* **2018**, *10*, 288–295.

(4) House, R. A.; Jin, L.; Maitra, U.; Tsuruta, K.; Somerville, J. W.; Förstermann, D. P.; Massel, F.; Duda, L.; Roberts, M. R.; Bruce, P. G. *Energy and Environmental Science* **2018**, *11*, 926–932.

(5) Tapia-Ruiz, N.; Dose, W. M.; Sharma, N.; Chen, H.; Heath, J.; Somerville, J. W.; Maitra, U.; Islam, M. S.; Bruce, P. G. *Energy & Environmental Science* **2018**, *11*, 1470–1479.

(6) House, R. A.; Maitra, U.; Jin, L.; Lozano, J. G.; Somerville, J. W.; Rees, N. H.; Naylor, A. J.; Duda, L. C.; Massel, F.; Chadwick, A. V.; Ramos, S.; Pickup, D. M.; McNally, D. E.; Lu, X.; Schmitt, T.; Roberts, M. R.; Bruce, P. G. *Chemistry of Materials* **2019**, *31*, 3293–3300.

(7) House, R. A.; Maitra, U.; Pérez-Osorio, M.; Lozano, J. G.; Jin, L.; Somerville, J. W.; Duda, L. C.; Nag, A.; Walters, A.; Zhou, K.; Roberts, M. R.; Bruce, P. G. *Nature* **2019**, In Press.

(8) Overcoming alkali-ion deficiency in battery cathode materials with naphthalene based pre-treatment. In Preparation.

List of Abbreviations

ALD . . . . . Atomic Layer Deposition

ALS . . . . . Advanced Light Source

APS . . . . . Advanced Photon Source

CEI . . . . . Cathode Electrolyte Interface

CS . . . . . Center Shift

D-W . . . . . Debye-Waller

DEC . . . . . Diethyl Carbonate

DFT . . . . . Density Functional Theory

DLS . . . . . Diamond Light Source

DMC . . . . . Dimethyl Carbonate

EC . . . . . Ethylene Carbonate

EOC . . . . . End of Charge

EV . . . . . Electric Vehicle

EXAFS . . . . Extended X-ray Absorption Fine Structure

^{57}**Fe-MS** . . . . ^{57}Fe Mössbauer Spectroscopy

GGA . . . . . Generalized Gradient Approximation

GITT . . . . . Galvanostatic Intermittent Titration Technique

HT-XRD . . . High Temperature-X-ray Diffraction

ICP . . . . . Inductively Coupled Plasma

ICP-MS . . . . Inductively Coupled Plasma-Mass Spectrometry

ICP-OES . . . Inductively Coupled Plasma-Optical Emission Spectrometry

LDA . . . . . Localized-Density Approximation

LZZ . . . . . Large Zig Zag

MAS-NMR . Magic Angle Spinning-Nuclear Magnetic Resonance

MS . . . . . Mass Spectrometry

$NaMO_2$ . . . . Layered Sodium Transition Metal Oxide

NCA . . . . . $Li[Ni_{0.8}Co_{0.15}Al_{0.05}]O_2$

ND . . . . . Neutron Diffraction

NMC811 . . . $Li[Ni_{0.8}Mn_{0.1}Co_{0.1}]O_2$

NMP N-Methyl-2-Pyrrolidone

OEMS . . . . . Online Electrochemical Mass Spectrometry

PC . . . . . Propylene Carbonate

PDF . . . . . Pair Distribution Function

PDOS . . . . . Projected Density of States

PTFE . . . . . Polytetrafluoroethylene

PVDF . . . . . Polyvinylidene Fluoride

QS . . . . . Quadrupolar Splitting

RF-gel . . . . . Resorcinol Formaldehyde Gel

RIXS . . . . . Resonant Inelastic X-ray Scattering

SEI . . . . . Solid Electrolyte Interface

SEM . . . . . Scanning Electron Microscopy

SHE . . . . . Standard Hydrogen Electrode

SG . . . . . Space Group

SOF . . . . . Site Occupancy Factor

TFY . . . . . Total Fluorescence Yield

THF . . . . . Tetrahydrofuran

TM . . . . . Transition Metal

TMO_2 . . . . . Transition Metal Oxide

TOF . . . . . Time of Flight

XAFS . . . . . X-ray Absorption Fine Structure

XANES . . . . X-ray Absorption Near Edge Structure

XAS . . . . . X-ray Absorption Spectroscopy

XRD . . . . . X-ray Diffraction

1 Introduction

Contents

The invention of the lithium-ion (Li-ion) rechargeable battery changed the world. It facilitated a revolution of the portable electronics industry, allowing smart phones, laptops, and tablets to be capable of running all day on a single charge and become an integral part of our daily lives.[1, 2] More recently, the cost of the Li-ion battery has decreased to the point where a similar revolution has

begun in the automobile industry with mass production of electric vehicles (EVs).[3] Rechargeable Li-ion batteries are also being used to support renewable energy sources, such as solar and wind, acting as modulators on the grid to compensate for differences in energy supply and demand.[4, 5]

As with all classes of technology, the world is racing to improve rechargeable batteries year after year. Primary considerations include cost, energy density, cycle life, power capability, and safety.[6] Unfortunately, optimizing one of these parameters usually comes at the detriment of another.[7] In the past decade, there has been a renewed interest in the development of sodium-ion (Na-ion) rechargeable batteries as a lower cost alternative to Li-ion.[8] Although a large amount of research has been dedicated to Na-ion batteries to date, much more is still needed for this technology to truly compete with Li-ion, particularly with regards to energy density. Successful implementation can only be achieved if there is first a solid foundation in understanding of the underlying chemistry.

Currently, one of the main bottlenecks to Na-ion technology is the lack of a suitable positive electrode material. While many classes of material, including polyanion and prussian blue analogues, have been identified as candidates to fill this void, layered sodium transition metal oxides ($NaMO_2$) are the most promising in terms of energy density.

The intent of this chapter is to provide a survey of the current knowledge base on layered $NaMO_2$ positive electrodes for Na-ion batteries which will be built on in subsequent chapters. Analogous Li-ion materials are also considered when appropriate parallels can be drawn. The chapter will begin with a brief introduction to basic battery principles before moving on to an in-depth review of layered transition metal oxide systems. A discussion follows regarding the detrimental phase transitions which occur in these cathode systems when most of the Na (or Li) is removed. Finally, the intriguing prospect of storing charge on oxygen, instead of heavy transition metals, will be examined in detail.

1.1 History and Key Concepts

1.1.1 A Brief History of the Battery

The original concept of a battery arose from experiments undertaken by Luigi Galvani where it was observed that touching a frog's leg with two different metals simultaneously (in a closed loop) induced a muscle spasm. Galvani initially thought that the animal itself was a source of electricity but a prominent physicist of the time, Alessandro Volta, argued that the electricity must be produced by the metals themselves.[9] In 1800, Volta proved his hypothesis by inventing what is considered the world's first battery, known as the "Voltaic pile". This battery contained stacks of silver and zinc disks which were separated by a cloth soaked in brine.[10, 11]

Over the next century and a half, a diverse array of battery types followed this advancement. In 1866, the ubiquitous (non-rechargeable) alkaline battery was invented by Georges-Lionel Leclanchè.[10, 12] The first rechargeable battery, the lead-acid battery, was invented by Gaston Plantè in 1860.[13] This was later followed by Waldmar Jungner's nickel-cadmium battery in 1899 and Thomas Edison's nickel-iron battery in 1901.[2, 14] These landmark chemistries eventually matured into today's nickel-metal hydride batteries.[14]

In the early 1970s, Whittingham and colleagues at Stanford University started experimenting on a new class of materials that could store ions by a mechanism known as "intercalation".[2] This process involves the storage of a guest species (e.g. Li^+) within a crystalline host matrix (e.g. TiS_2) with minimal volume change.[15] They went on to commercialize a battery at Exxon composed of the intercalation compound, TiS_2, on the positive side of the battery and a Li-Al alloy on the negative side of the battery.[16–18] Lazzari and Scrosati in Italy later demonstrated the benefit of pairing Whittingham's TiS_2 with another intercalation compound, WO_2 (instead of the Li-Al alloy), to develop the first true Li-*ion* battery (where Li exists purely in ionic form). By creating a cell with two intercalation electrodes, labeled a "rocking chair battery", the authors were able to boast improved cyclability.[19]

By 1980, a substantial amount of research had been dedicated to discovery and advancement of intercalation compounds. Of note, fundamental research on transition metal oxide (TMO_2) hosts that could store Na-ions was carried out by Fouassier, Delmas, Hagenmuller, and others in France.[20–23] Building from this platform, John Goodenough at the University of Oxford made the pivotal discovery that Li^+ could be reversibly de-intercalated from $LiCoO_2$ at high voltages ($\approx$ 4 V vs. Li^+/Li), a revelation that would significantly increase the amount of energy a battery could store.[1, 24]

Similarly paramount discoveries followed for the negative side of the battery. Samar Basu and others at Bell Labs demonstrated that Li^+ could be reversibly intercalated into graphite at a very low voltage (this material would eventially become the negative electrode of choice for Li-ion batteries).[25–27] At nearly the same time, a petrolium coke negative electrode was developed by Akira Yoshino of Asahi Kasei Corp in Japan.[28] This allowed Sony in 1991 to commercialize a new battery chemistry to power their camcorders, using Goodenough's $LiCoO_2$ on the positive side and Yoshino's petrolium coke on the negative side.[2, 29] This new generation of Li-ion batteries boasted a step change in energy density and ushered in the age of portable electronics.

1.1.2 How Batteries Store Energy

Active and Inactive Components

As was first discovered by Volta over two centuries ago, the energy which a battery possesses is derived from its two "electrode" materials; one that is positive and one that is negative. A convention has arisen among the battery research community of referring to the positive and negative electrodes as the cathode and anode respectively.[30] Despite the electrodes only acting as such during discharge (from an electrochemical perspective), this is the convention that will be followed for the remainder of this thesis.

A schematic of a conventional Li-ion battery is shown in Figure 1.1. The anode material in this case is graphite and the cathode material is $LiCoO_2$. An electrolyte

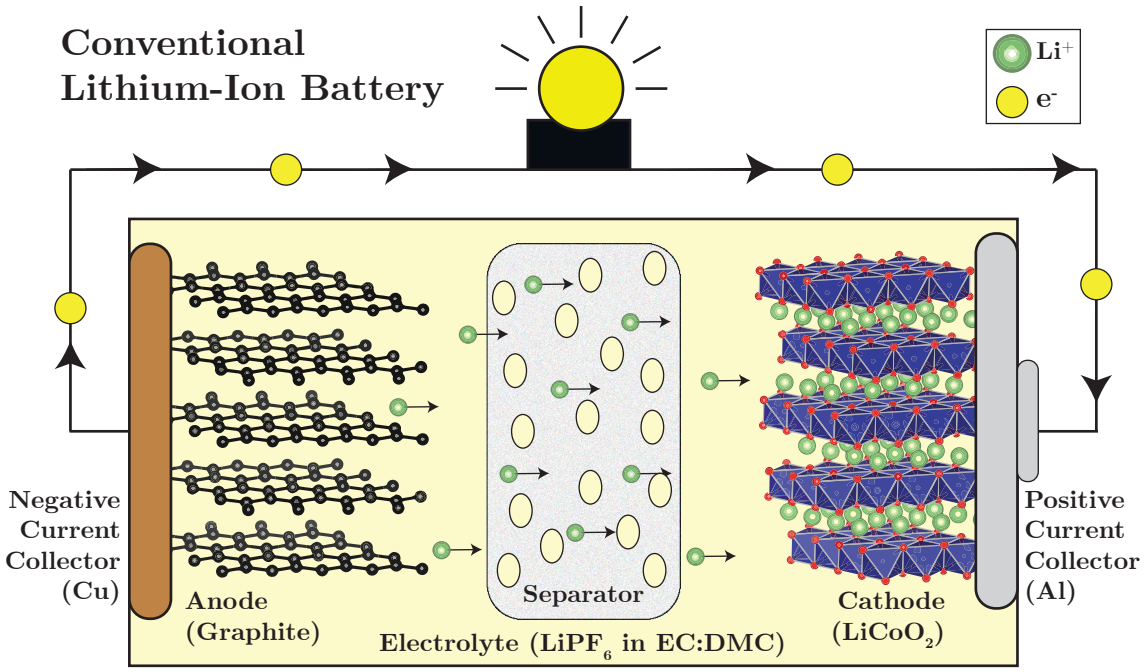

Figure 1.1: A schematic of the conventional Li-ion battery is shown during discharge with Li-ions and electrons moving from anode to cathode in order to power the light bulb.

is found in between the two (shaded as yellow) which acts to electronically isolate chemical reactions occurring at the two electrodes while providing a conducting pathway for Li-ions to be transported between these reactions. This is typically a Li salt, such as $LiPF_6$, dissolved in a carbonate-based solvent such as dimethyl carbonate (DMC) and ethylene carbonate (EC).

There are several other components which should not actively participate in the electrochemical reactions but are equally important to the proper function of the battery. The positive current collector (typically Al metal) and negative current collector (typically Cu metal) facilitate the flow of electrons between their respective electrodes and the outer circuit. The separator provides a physical barrier between the electrodes to prevent electrical short circuiting yet is porous to allow electrolyte infiltration.

The maximum amount of energy that a battery can store is a direct function of the properties and quantity of the anode and cathode materials. The mass and volume of all other components within the system should therefore be minimized

to optimize the energy density.

Redox Reactions: Chemical to Electrical Energy

The battery is an incredibly efficient transducer of energy from chemical to electrical form and vice versa. It operates by separating the two half reactions of a reduction-oxidation (redox) reaction, a type of chemical reaction that involves the transfer of electrons. When the battery is discharged, the anode is oxidized (donates electrons) and the cathode is reduced (receives electrons). To maintain charge neutrality, ions also proportionally flow from anode to cathode. This process is reversed during charge. Because the electrolyte only conducts ions between the two half reactions, the redox reaction can only proceed if the electrons journey out of the battery and around an outer circuit. The *internal* chemical reaction of the battery can therefore be governed by controlling the flow of electrons on the *external* circuit. This can be achieved using something as complicated as a battery management system or as simple as a light switch.

For intercalation electrodes such as $LiCoO_2$, it is important to note that the Li-ions are neither oxidized nor reduced during charge and discharge. It is the CoO_2 host rather which acts as the supplier/recipient of electrons for the redox reaction.[31] This can be conceptualized as the oxidation/reduction of Co-ion between the 3+ and 4+ oxidation states.

All chemical reactions involve a change in the free energy of the system. The more negative this change is (energy supplied *by* the system), the greater the driving force is for the reaction to proceed. In an electrochemical cell such as a battery, this driving force (i.e. the electromotive force) to discharge can be quantified in terms of voltage (units of volts [V]) by the Nernst equation:[30]

$$E = -\frac{\Delta G}{zF} \tag{1.1}$$

where E is the voltage of the battery, ΔG is the change in the Gibb's free energy of the system, z is the number of electrons transferred (i.e. charge of the ion), and F is the Faraday constant. The electromotive force of the battery can be utilized

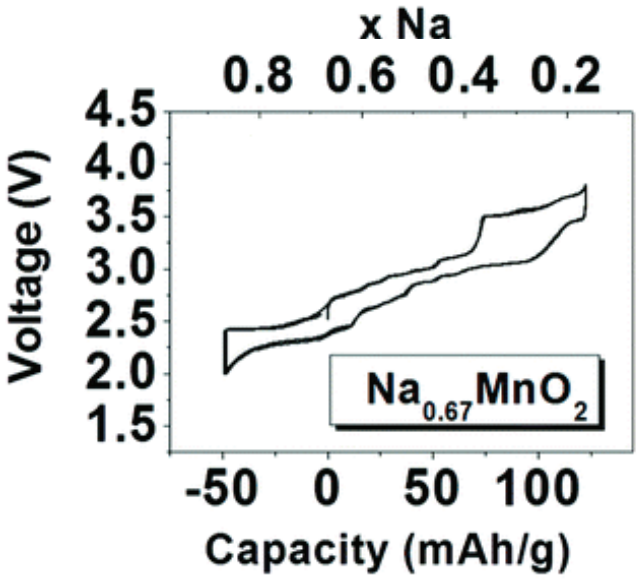

Figure 1.2: A typical Na_xMO_2 electrochemical load curve is shown, using $Na_{2/3}MnO_2$ as an example. This measures the battery's voltage response to an applied current. The specific capacity can be logged either in terms of mAh g^{-1} (bottom x-axis) or in terms of the (de-)intercalated Na-ions, x (top x-axis). Adapted from Ref. [32] with permission from The Royal Society of Chemistry.

by inserting electronics such as a light bulb on the external circuit. Conversely, by applying an opposing voltage greater than E to the battery, the redox reaction will proceed in reverse "storing" the energy given to it by the circuit, or charging.

Important Battery Parameters and Units

The voltage, E, is an intensive property of the battery which means it is independent of the quantity of reactants/products involved in the reaction. On the other hand, the capacity of a battery is an extensive property (scales with the quantity of reactants/products) and is determined by how many ions and electrons that can be provided/stored by each electrode.[30] The capacity is typically quantified in terms of the number of hours a 1 A current could be supplied (units of Ah). This value can be multiplied by the average voltage to determine the energy stored by the battery (units of Wh).

When investigating the fundamental properties of electrode materials, it is beneficial to calculate the intensive form of capacity and energy characteristic to a material. This can be done by dividing the capacity and energy by the mass of

the electrode material to obtain specific capacity (mAh g^{-1}) and specific energy (mWh g^{-1}) respectively. Alternatively, one can divide by the volume of the electrode material to obtain capacity density (mAh L^{-1}) and energy density (mWh L^{-1}).

For intercalation electrodes such as $LiCoO_2$, the specific capacity can be easily translated to the moles of Li-ions which are inserted or extracted from the host (Δx) by the equation:

$$\Delta x = q\left(\frac{M}{zF}\right) \tag{1.2}$$

where q is the specific capacity, M is the molar mass of the electrode material, z is the number of electrons transferred and F is the Faraday constant. Figure 1.2 shows a typical $NaMO_2$ electrochemical load curve which tracks a battery's voltage response to an applied current. The top and bottom x-axis labels read x in Na_xMnO_2 and mAh g^{-1} respectively, demonstrating the linear relationship between the two sets of units. Electrochemical load curves are incredibly useful in monitoring changes of an electrode material as a function of their composition.

Another metric used to analyze rechargeable batteries is cyclability. This is usually quantified in terms of capacity retention (% of first cycle capacity retained) as a function of cycle number. The cyclability of a material gives insight into the reversibility of the electrochemical and structural processes occurring.

1.1.3 Comparison of the Li and Na-Ion Battery

Na-ion batteries function in a manner very similar to Li-ion batteries with the obvious distinction of utilizing Na-ions instead of Li-ions to transport/store charge between/in the electrodes. However, such a seemingly simple substitution can dramatically impact the battery performance.

A few of the most basic properties of Li and Na are summarized in Table 1.1. The reduction potential of Na metal is approximately 0.3 V greater than that of Li metal which corresponds to a slightly decreased operating voltage for the battery. Moreover, the mass of Na is significantly greater than Li which reduces the specific capacity of the battery for the same amount of charge delivered.

Table 1.1: A comparison of Li and Na. Adapted from Ref. [33] with permission from The Royal Society of Chemistry and [34], 2013 WILEY-VCH Verlag GmbH & Co. KGaA, Weinheim.

Category	**Lithium**	**Sodium**
E^o vs. SHE (V)	-3.04	-2.7
Cost Carbonates (\$ ton^{-1})	5000	150
Molar Mass (g)	6.9	23.0
Cation Radius (Å)	0.76	1.06
Coordination Preference	Octahedral and Tetrahedral	Octahedral and Trigonal Prismatic

Despite these disadvantages, the cost difference between the two alkali metal precursors immediately reveals the motivation for developing Na-ion batteries. At \$150 per ton, the Na raw materials amount to just 3% the cost of the analogous Li compounds. When comparing these parameters, however, it must be considered that Li or Na-ions usually make up a relatively small percentage of an intercalation electrode (e.g. 7% mass of $LiCoO_2$, 20% mass of $NaCoO_2$). At the cell level, this percentage is diluted even further by the current collectors, cell casing, and other inactive components. While this has the positive effect of mitigating the mass difference between Na and Li, it also greatly diminishes the cost savings. In fact, a recent analysis by Vaalma et al. concluded that there is no direct economic benefit in terms of dollars per watt hour for the Na-ion electrodes available today (cathode: $NaMnO_2$, anode: hard carbon).[35] However, in applications where cycle life is more crucial (e.g. grid storage), some Na-ion cathodes such as prussian blue analogues may already be competitive in terms of dollars per watt hour *per cycle*.[36] Moreover, the tremendous abundance and widespread geographical distribution of Na compared with Li should theoretically make it more resistant to any pricing fluctuations caused by political or economic disruptions.

Probably the most substantial benefit of the Na-ion chemistry is that it enables the use of Al metal as a negative current collector instead of Cu.[37] While Li alloys with Al, Na does not. A negative current collector composed of Al metal is not only cheaper and lighter than Cu but also functions to make the battery safer. If Li-ion batteries are overdischarged and the Cu current collector potential

rises above approximately 3.5 V vs. Li^+/Li, Cu will oxidize and begin to dissolve into the electrolyte. On subsequent charging of the battery, the dissolved Cu is reduced onto the anode forming dendrites which can short circuit the battery and cause dangerous fires or explosions.[38, 39] On the other hand, Al is passivated by the electrolyte and does not dissolve even when charged to voltages greater than 4 V vs. Li^+/Li. The superior stability of the Al negative current collector can even allow the Na-ion battery to be discharged to an operating voltage of 0 V ($E_{\text{cathode}} = E_{\text{anode}} \approx 2.8$ V vs. Na^+/Na) for dramatically safer transportation, as recently demonstrated by the start-up company Faradion.[40]

Another benefit of the Na-ion chemistry is the option to utilize a greater variety of elements (including cheap, abundant Fe) in layered $NaMO_2$ intercalation cathodes. The compositional diversity stems from the fact that a layered structure forms in this class of compound as a result of large differences in the ionic radii between small transition metal ions and larger alkali metal ions.[41] High-spin Fe^{3+} has a relatively large ionic radius for a TM (0.645 Å), approaching that of Li^+ (r = 0.76 Å).[42] Therefore, conventional high temperature synthesis of $LiFeO_2$ results in a disordered rock salt phase that is electrochemically inactive. Conversely, the larger ionic radius of Na^+ (1.06 Å) enables the formation of an ideal layered structure for $NaFeO_2$.[43] A similar effect is seen for $NaMO_2$ compounds containing Cr and, to a lesser extent, Ni.[44, 45]

While beneficial in some respects, the greater size of Na^+ also poses some challenges. For example, there is generally a greater volume change of the host structure during (de-)intercalation of $NaMO_2$ intercalation cathodes. Moreover, the larger size also allows Na^+ to be stable in a trigonal prismatic coordination often resulting in multiple phase transformations, as will be discussed in the next section.[46]

Overall, Na-ion batteries possess certain advantages from a safety and structural perspective. Although the economic benefit of Na-ion batteries may have been slightly exaggerated in the past, the low cost advantage could still be realized if electrode materials with higher energy density and longer cycle life are developed.[47]

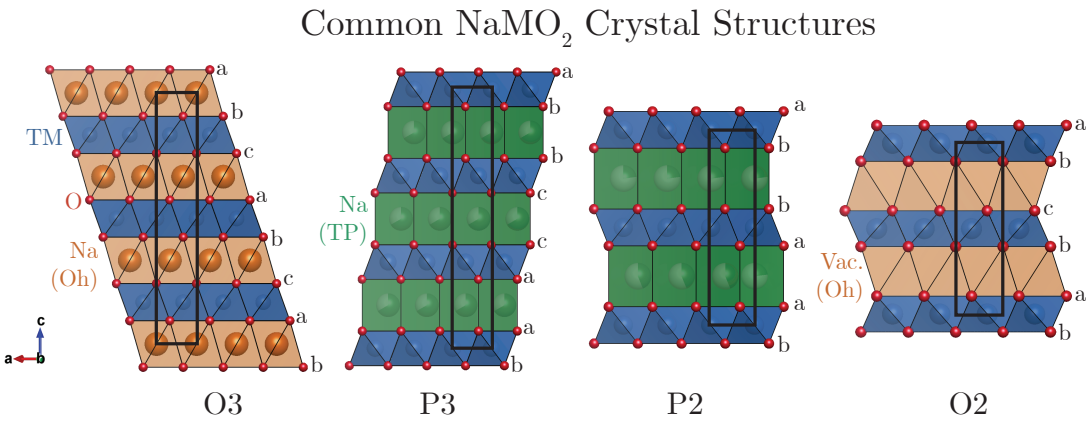

Figure 1.3: The figure illustrates the four most common $NaMO_2$ crystal structures: O3, P3, P2, and O2 (from left to right). All TMs (blue) are in octahedral sites whereas Na can be located in either trigonal prismatic sites (green) or octahedral sites (orange). The black rectangle overlaid on each structure represents the unit cell.

1.2 Layered $NaMO_2$ Cathodes

The three most promising classes of cathode material for Na-ion batteries are the layered $NaMO_2$ (e.g. $Na[Ni_{1/3}Mn_{1/3}Fe_{1/3}]O_2$)[48], prussian blue analogue (e.g. $Na_{1.92}Fe[Fe(CN)_6]$)[49], and polyanion chemistries (e.g. $Na_3V_3(PO_4)_3$)[50]. Each have shown sufficient promise to warrant efforts toward their commercial development by Faradion, Natron Energy, and RS2E researchers respectively.

The layered $NaMO_2$ compounds are the most promising in terms of specific capacity and energy.[51, 52] In application, however, many of these compounds are encumbered by low operating voltages with various steps in the voltage curve, Na deficiency in the as-synthesized compound, and inadequate cyclability.[53–55] Thus, a fundamental understanding of $NaMO_2$ cathodes' electronic and atomic structure evolution is vital in order to make the needed improvements.

1.2.1 Structural Information and Classification

In 1980, a method for describing layered TMO_2 compound was proposed by Delmas and coworkers.[23] This system organizes the various types of layered oxide structures by their alkali metal ion coordination and oxygen stacking sequence. Four of the most common $NaMO_2$ structures are illustrated in Figure 1.3. A letter and a number

are assigned to describe each structure. The letter indicates the coordination of the alkali metal ion: P - trigonal prismatic and O - octahedral (also T - tetrahedral less commonly). The number indicates the minimum number of TMO_2 slabs needed in the unit cell to reproduce the oxygen stacking sequence: O3 - ab ca bc, P3 - ab bc ca, P2 - ab ba, and O2 - ab cb. An apostrophe symbol can also be added to indicate a distortion of the ideal unit cell (e.g. P'2 $Na_{2/3}MnO_2$).

The preferred coordination of an alkali metal ion is primarily dependent on its size.[56] Li^+ prefers smaller sites such as tetrahedra and octahedra while larger ions such as K^+ have a strong tendency toward large trigonal prisms. Due to the intermediate size of Na^+, however, it can occupy both octahedra and trigonal prisms.[57] In fact, the energy difference between these two sites is so minimal that the stable Na^+ coordination varies dependent on the Na occupancy in the compound (x in Na_xMO_2).[58] During synthesis, the O3 structure tends to form for compounds with higher Na contents ($x \geq 0.8$) while P2 and P3 structures are more stable at intermediate Na contents ($0.5 \leq x \leq 0.8$).[55] The O2 phase is only formed at $x \approx 0$, which generally can only be accomplished by electrochemical preparation.[59]

Interestingly, room temperature Na^+ (de-)intercalation can also alter the Na^+ coordination of $NaMO_2$ compounds through a "gliding" of the TMO_2 slabs. The layer gliding enables structural transitions between O3 $\leftrightarrow$ P3 and P2 $\leftrightarrow$ O2.[43] However, other transitions such as O3 $\leftrightarrow$ P2 cannot occur at room temperature because these would require breaking the strong TM-O bonds.[60] Although facile, the layer gliding structural transitions often have a negative effect on the cyclability of the cathode material and should therefore be avoided if possible.[61]

P-type structures are generally thought to have faster diffusion than O-type structures as the activation energy to move from trigonal prism to trigonal prism is smaller than that required to move from octahedron to octahedron (via an intermediate tetrahedron).[53, 57, 62]

1.2.2 $NaMO_2$ Trade Offs: Voltage, Capacity, and Cyclability

As explained in section 1.1.2, energy is the product of capacity and voltage. Therefore, raising either of these two metrics will improve the energy storage capability of the compound. However, enhancing battery materials is often a process of optimizing between various trade offs. For example, increasing voltage can come at the expense of the capacity if the potential exceeds the stability limit of the electrolyte. Likewise, boosting the capacity can compromise cyclability as $NaMO_2$ compounds often become less stable as more Na is de-intercalated. Thus, understanding the fundamental mechanisms of these trade offs is key to improving electrode chemistries.

Voltage Controlled by TM Layer Composition

The energy change (i.e. voltage) during the (de-)intercalation of layered oxide cathode materials is primarily determined by the compounds' electronic structure, which is chiefly influenced by the composition of the TM layer.[63] There are three key properties of each TM which effect the voltage:

1. Nuclear charge (atomic number)
2. Electron configuration (i.e. oxidation state)
3. Covalency of the TM-O bond

As a general rule, the voltage of a $NaMO_2$ compound tends to increase with the atomic number of M across the period [64] because the 3d states drop in energy due to a greater charge of the nucleus. This approximation, however, often breaks down due to electronic interactions with the coordinating oxygens.[65, 66]

When a TM is octahedrally coordinated by oxygen, the five 3d orbitals of the TM are split in energy by the crystal field into the lower energy t_{2g} ($3d_{xy}$, $3d_{yz}$, and $3d_{xz}$) and higher energy e_g states ($3d_{x^2-y^2}$ and $3d_{z^2}$).[68] Depending on how many d electrons the TM cation has (i.e. its oxidation state), the highest energy electrons will either be located in the e_g states (higher in energy and available at

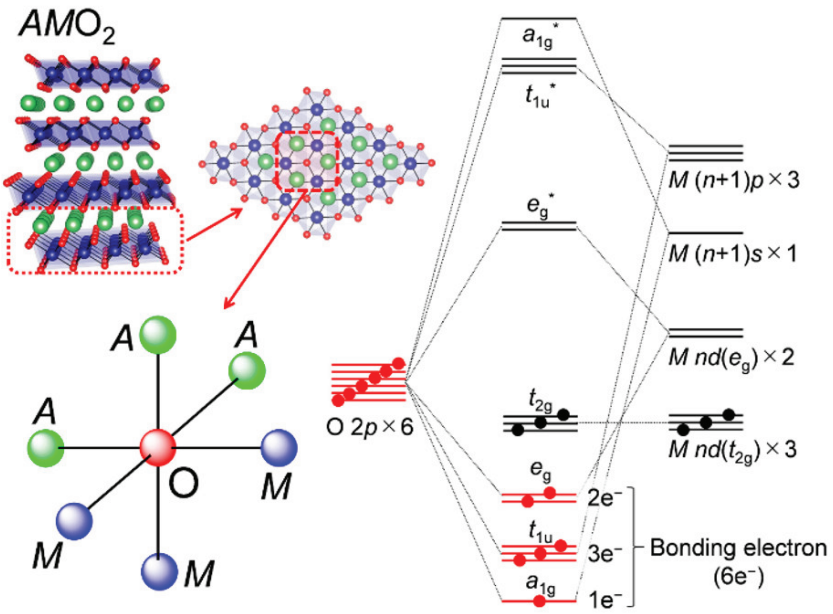

Figure 1.4: An illustration of the crystal structure of a layered oxide compound is shown on the left with the oxygen coordination environment highlighted. A molecular orbital diagram of the TM-O interaction is shown on the right, using a nd^3 electron configuration for the TM as an example. Adapted with permission from Ref. [67]. Copyright 2017 American Chemical Society.

a lower voltage) or in the t_{2g} states (lower in energy and only accessible at higher voltages). Moreover, energy states are more stable when they are unoccupied, half occupied, or fully occupied.[69] This makes the configurations of $[Ar]3d^0$, $[Ar]3d^3$, high-spin $[Ar]3d^5$, low-spin $[Ar]3d^6$, $[Ar]3d^8$, and $[Ar]3d^{10}$ particularly stable.

The higher energy e_g states are then further impacted by covalent interactions with oxygen anions. This was presented elegantly in a paper by Okubo and Yamada and is shown in Figure 1.4.[67] The covalency of the TM-O bond drives the antibonding e_g^* states higher in energy thus making electrons accessible at even lower voltages. One of the best examples of this is the "redox potential paradox" given by Nanba et al. who demonstrated that over the same Na composition range for two similar $NaMO_2$ compounds, the $Ni^{3+/2+}$ redox couple occurred at higher voltage than $Ni^{4+/3+}$ due to the higher covalency of the Ni^{3+} - O 2p interaction.[64] The t_{2g} states are less effected by covalency due to the geometry of an octahedron.

A summary of the common oxidation states and electron configurations for all 3d TMs is shown in Table 1.2. By experimental investigation, it has been

Table 1.2: Summary of the common oxidation states and electron configurations of 3d TMs in layered oxide compounds. Adapted from Ref. [55], 2018 WILEY-VCH Verlag GmbH & Co. KGaA, Weinheim.

Element	**Common Oxidation States in Layered Oxides (Spin State)**	**Electron Configuration**
Sc	3+	[Ar] $3d^0$ ($t_{2g}{}^0$ $e_g{}^0$)
Ti	4+	[Ar] $3d^0$ ($t_{2g}{}^0$ $e_g{}^0$)
V	3+	[Ar] $3d^2$ ($t_{2g}{}^2$ $e_g{}^0$)
	4+	[Ar] $3d^1$ ($t_{2g}{}^1$ $e_g{}^0$)
Cr	3+	[Ar] $3d^3$ ($t_{2g}{}^3$ $e_g{}^0$)
	4+	[Ar] $3d^2$ ($t_{2g}{}^2$ $e_g{}^0$)
Mn	3+ (High Spin)	[Ar] $3d^4$ ($t_{2g}{}^3$ $e_g{}^1$)
	4+	[Ar] $3d^3$ ($t_{2g}{}^3$ $e_g{}^0$)
Fe	3+ (High Spin)	[Ar] $3d^5$ ($t_{2g}{}^3$ $e_g{}^2$)
	4+ (High Spin)	[Ar] $3d^4$ ($t_{2g}{}^3$ $e_g{}^1$)
Co	3+ (Low Spin)	[Ar] $3d^6$ ($t_{2g}{}^6$ $e_g{}^0$)
	4+ (Low Spin)	[Ar] $3d^5$ ($t_{2g}{}^5$ $e_g{}^0$)
Ni	2+	[Ar] $3d^8$ ($t_{2g}{}^6$ $e_g{}^2$)
	3+ (Low Spin)	[Ar] $3d^7$ ($t_{2g}{}^6$ $e_g{}^1$))
Cu	2+	[Ar] $3d^9$ ($t_{2g}{}^6$ $e_g{}^3$)
Zn	2+	[Ar] $3d^{10}$ ($t_{2g}{}^6$ $e_g{}^4$)

determined that the TM redox couples of $Cr^{4+/3+}$, $Fe^{4+/3+}$, $Co^{4+/3+}$, and $Ni^{4+/3+/2+}$ have suitable operating voltages (>3 V vs. Na^+/Na) for use in $NaMO_2$ cathodes,[55, 70–74] which matches well with the trends discussed above. The $Mn^{4+/3+}$ and $Ti^{4+/3+}$ redox couples typically show lower voltages yet are often still incorporated into $NaMO_2$ materials to add structural stability and because of their high abundance. 4d and 5d redox couples have also been examined, such as $Ru^{5+/4+}$.[75] However, the heavier mass and lower abundance of these elements seemingly limits their utility to fundamental studies rather than practical applications.

How Voltage Impacts Capacity

The capacity of a $NaMO_2$ cathode is equivalent to the quantity of Na-ions (Δx) that can be reversibly (de-)intercalated. In order to keep x within a structurally stable range as well as preserve an electrochemically stable interface, a lower and upper voltage limit is imposed. Tuning of the TM layer composition, as described above, alters the voltage limits needed to cycle the same Δx. However, a proportional

upward shift in the operating range can be detrimental as voltages that are too high compromise the interface stability and lead to oxidation of the electrolyte in place of the cathode. Consequently, higher voltage cathodes may have lower capacities as the upper voltage limit is constrained by the electrolyte stability (related to voltage) and not structural stability (related to x).

A good example is provided by comparing two prevalent Li-ion cathodes: $LiCoO_2$ and $Li[Ni_{0.8}Mn_{0.1}Co_{0.1}]O_2$ (NMC811). While both cathodes have virtually the same theoretical capacity (274 vs. 276 mAh g^{-1} respectively), NMC811 shows a much higher capacity (160 vs. 190 mAh g^{-1}) when cycled to the same 4.3 V cutoff.[76, 77] To obtain the same capacity as NMC811, $LiCoO_2$ must be charged to 4.5 V but this initiates interface reactions that quickly degrade the reversible capacity of the compound.[78]

$NaMO_2$ compounds display similar phenomena. Two studies on partial Ti substitution (for Mn) found this raised the average voltage of the cathode material.[74, 79] In both cases, however, the capacity of the compound decreased as less Na had been extracted from the compound when the 4.5 V upper voltage limit was reached. On the other hand, the cyclability of both compounds increased as a result which highlights another important relationship.

How Capacity Impacts Cyclability

Improving the capacity of a cathode often leads to worsened cyclability. Strategies to increase the capacity of cathode materials are therefore better described as efforts to combat the degradation reactions which limit the amount of Δx that can be utilized.

A graphic illustrating the common degradation mechanisms is shown in Figure 1.5.[80] These processes can be divided into three main categories: 1) interface reactions (electrolyte decomposition, surface layer formation, TM dissolution, gas evolution), 2) first order structural changes (structural disordering, irreversible phase transitions), and second order structural changes (micro-cracking, loss of contact to conductive particles).

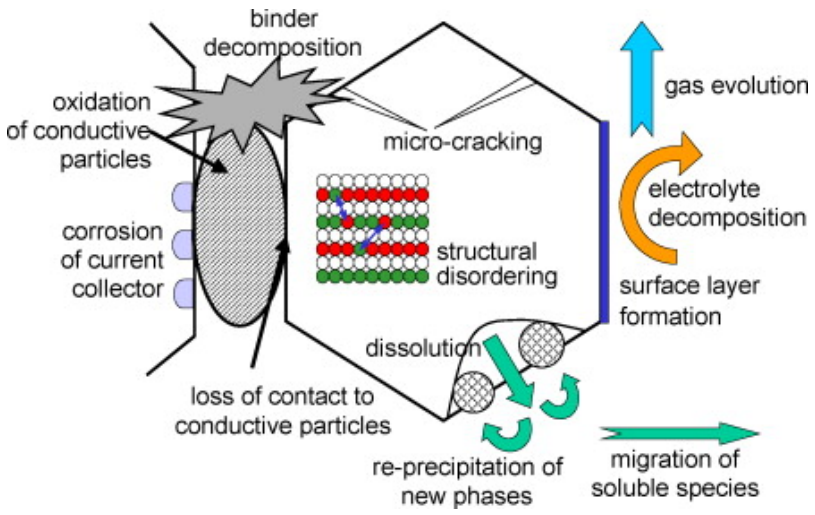

Figure 1.5: The above schematic elegantly illustrates the many mechanisms that can degrade a cathode material. Reprinted from Ref. [80], with permission from Elsevier.

It is often quite difficult to pinpoint which of these mechanisms is the root cause of limiting cyclability. Yabuuchi et al. showed the negative effect of increasing the upper voltage cut off (and the quantity of Na extracted) on the cycling of O3-$NaFeO_2$ reproduced in Figure 1.6.[81] Although increasing the voltage window just 0.1 V higher (from 3.4 to 3.5 V) improves the capacity by 25%, charging to higher voltages, dramatically decreases the discharge capacity (even as charge capacity continues to rise). The authors attributed this decline in cyclability to first order structural changes (structural phase transitions/disorder).[81] However, a follow-up study by Lee et al. later found evidence of oxidized Fe (Fe^{4+}) catalyzing a reaction with the electrolyte that created a resistive surface layer.[82] It is both degradation reactions that cause the battery performance to deteriorate.

Strategies to Increase Capacity (Without Sacrificing Cyclability)

In order to suppress degradation reactions and increase reversible capacity, the compound's structure must be stabilized over a greater Δx and the cathode electrolyte interface must be able to endure the voltage range needed.

To preserve the integrity of the interface, one effective strategy has been applying a protective surface coating. For example, a carbon coating has been shown to

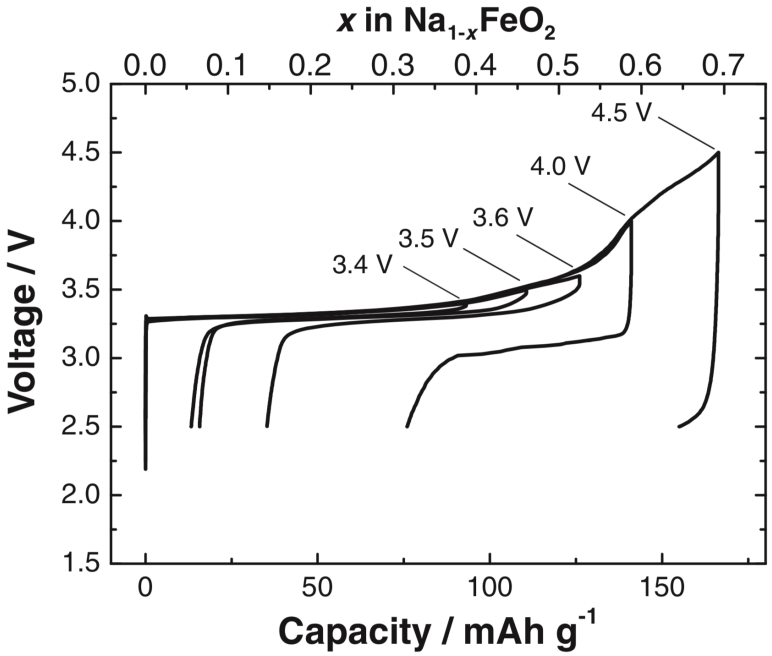

Figure 1.6: The voltage load curve is shown for 5 cells of $NaFeO_2$ charged to different cutoff voltages. No further reversible capacity is gained on charging beyond 3.5 V vs. Na^+/Na. Reproduced with permission from Ref. [81]

improve the cyclability of O3-$NaCrO_2$ when charged to 3.6 V vs. Na^+/Na.[83] However, the procedure for applying the carbon coating is limiting as it necessitates a high temperature heating step under Ar gas that would not be feasible for easily reduceable metals such as Mn and Co.[55] Another successful surface coating is Al_2O_3 which can be applied via atomic layer deposition (ALD). This process has been shown to stabilize the CEI of P2-$Na_{2/3}[Ni_{1/3}Mn_{2/3}]O_2$ to boost cyclability when charged to 4.5 V vs. Na^+/Na.[84] More recently, $Na_2Ti_3O_7$, a material extensively investigated as an anode material,[85] has been trialled as a coating on $Na_{2/3}[Ni_{1/3}Mn_{2/3}]O_2$, also showing improved cyclability with an upper voltage cutoff of 4.5 V.[86]

In terms of structural integrity, $NaMO_2$ compounds can be effectively stabilized by bulk substituents.[54] For example, the structural transitions which plague $NaFeO_2$ during cycling are dramatically reduced when 50% of the Fe is substituted for Co (O3-$Na[Fe_{1/2}Co_{1/2}]O_2$).[72] This modification enables more than 2/3 of the Na (compared to only 0.4) to be reversibly de-intercalated from the compound, substantially boosting the specific capacity from 100 to 160 mAh g^{-1}. A deeper

discussion of the structural degradation mechanisms occurring in $NaMO_2$ materials will follow in Section 1.3.

Overall, it has been substantiated that $NaMO_2$ performance is often a trade off between voltage, capacity, and cyclability. Another key specification of battery materials, which has not yet been discussed, is rate capability (i.e. ability to deliver capacity at high currents). This metric is heavily influenced by Na-ion ordering which features more prominently in $NaMO_2$ materials than Li analogues. This phenomenon will now be discussed.

1.2.3 Na-ion Ordering in $NaMO_2$ Compounds

A long-range repetitive arrangement of Na-ions (or Li-ions), which occurs to lower electrostatic repulsion, is known as ordering. Although Li-ion ordering does occur at times in $LiMO_2$ compounds,[87] there is generally a larger driving force for Na-ions to order in $NaMO_2$ compounds. This is because Na is more electropositive than Li, meaning Na^+-Na^+ repulsion is stronger than Li^+-Li^+ repulsion.[63] Moreover, the P2 and P3 type structures (which form with Na but not Li) have two times the available Na sites compared to O-type structures. Therefore, the number of possible ordering arrangements increases dramatically for intermediate Na contents where these structures are stable.

Ordering of Na-ions is generally considered disadvantageous in terms of kinetics (rate capability).[88] Mo et al. demonstrated that Na^+-Na^+ repulsion was actually the primary rate limiting factor in P2 type compounds.[89] Fortunately, experimental evidence demonstrates that Na-ion ordering can be effectively controlled by tuning the TM composition.[90, 91]

Na-ion ordering can only occur if there is a concurrent charge ordering of the TM layer.[90] In most single TM $NaMO_2$ compounds, dynamic TM charge ordering (e.g. between Mn^{3+} and Mn^{4+}) readily occurs to facilitate Na-ion ordering as all metals in the TM layer have the same redox potential and can easily exchange electrons. This is largely reduced in systems with two or three transition metals but

can still occur if the redox potentials of metals are very similar.[91] This section will review the literature on Na-ion ordering as well as examine strategies to disrupt it.

Na-ion Ordering in Single TM $NaMO_2$ Compounds

Na-ion ordering is commonly identified by electrochemical and/or diffraction methods. Each ordering scheme typically occurs over a very narrow range of Δx, but changes the system's energy rather suddenly in that region. Consequently, Na-ion ordering often appears as a noticeable "step" in the electrochemical load curve.[92, 93]

$NaCoO_2$ is an excellent example of a single TM compound that shows a high degree of Na-ion ordering. Berthelot, Carlier, and Delmas investigated P2-Na_xCoO_2 (where $x \geq 0.5$) using *in situ* X-ray diffraction (XRD) of a galvanostatic intermittent titration technique (GITT) experiment.[95] By employing these techniques collectively, they were able to demonstrate that the steps in the voltage curve coincided with discontinuities in the lattice parameter evolution of the structure. The most pronounced voltage steps occurred at $x = 2/3$ and $x = 1/2$. At these compositions, extra peaks were also evident in the diffraction pattern, corroborating prior computational and experimental studies concluding the presence of an ordered superstructure of Na-ions.[96–98]

Na-ion ordering is also seen in a variety of other $NaMO_2$ compounds including P2-Na_xVO_2.[94] The *in situ* XRD of P2-Na_xVO_2 shown in Figure 1.7 elegantly displays the shifting of the superstructure peaks (induced by Na-ion ordering) over solid solution regions as narrow as $\Delta x = 0.04$ mol Na. In addition, $NaNiO_2$, $NaMnO_2$, and $NaCrO_2$ all demonstrate pronouced voltage steps on cycling suggesting Na-ion ordering is also occurring in these compounds. [93, 99, 100].

Recently, Toumar et al. predicted 18 distinguishable ground state Na-ion ordering configurations in the O3 structure using high throughput density functional theory (DFT).[88] The calculations modeled structures over a full range of Na contents $0 \leq x \leq 1$ and contrasted the ordering phenomena in $NaMO_2$ compounds containing each 3d TM independently. It is noteworthy that the two phase behavior of $NaFeO_2$ in the range of $1/2 \leq x \leq 1$ was well represented by the predictions; although

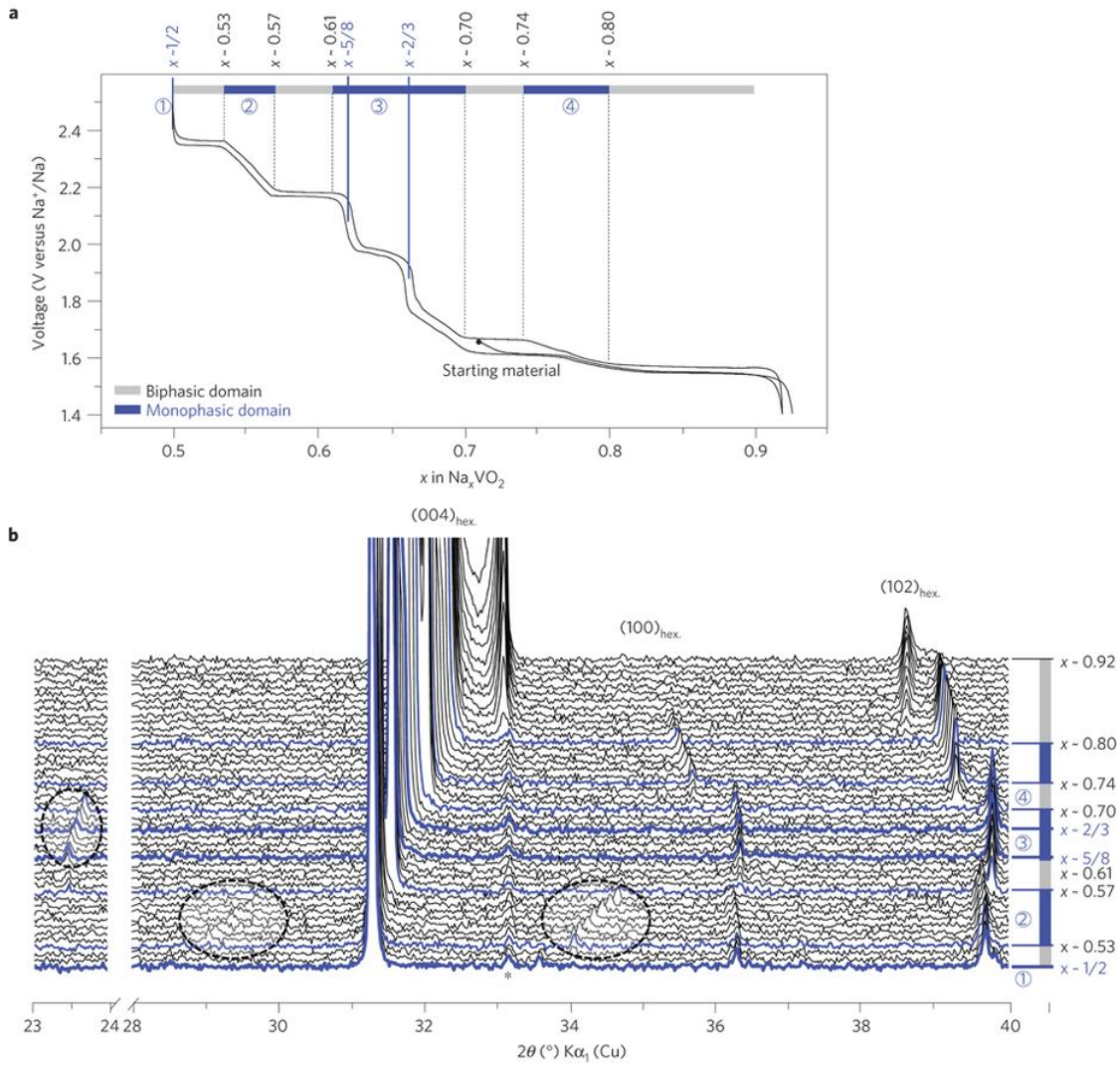

Figure 1.7: The electrochemical voltage curve of P2-$Na_{2/3}VO_2$ is shown at the top (a) with biphasic and monophasic domains labeled appropriately. *In situ* XRD of P2-$Na_{2/3}VO_2$ recorded during a GITT experiment is shown at the bottom (b) with select Na-ion ordering superstructure peaks circled. Reprinted by permission from Springer Nature: Nature Materials Ref. [94].

there has been no evidence by diffraction of Na-ion ordering in $Na_{1/2}FeO_2$ as of yet. [81, 82, 101] However, the deficiency in the study lies in that most O3 $NaMO_2$ compounds transition to a P3 structure after de-intercalating a small quantity of Na ($\Delta x \approx 0.1 - 0.3$ mol Na).[82] As such, direct experimental comparison is not possible for most of the compounds modeled. A comparable in-depth study of Na-ion ordering in the P2 or P3 structures would be helpful to further conceptualize the behavior of Na-ions throughout (de-)intercalation.

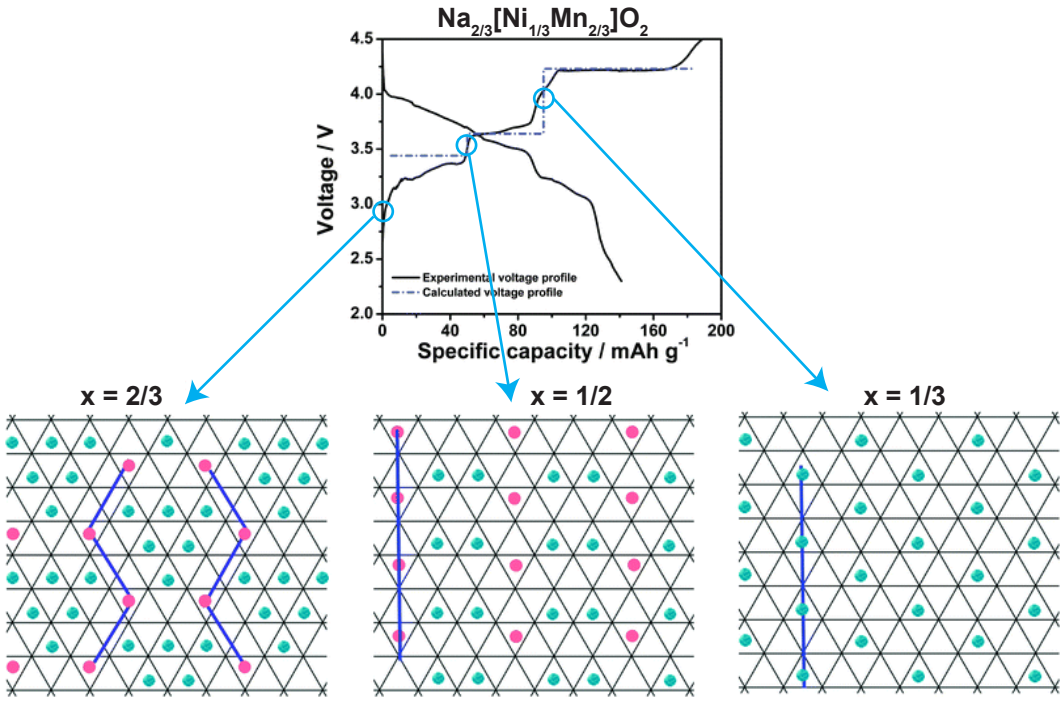

Figure 1.8: The electrochemical voltage curve of $Na_{2/3}[Ni_{1/3}Mn_{2/3}]O_2$ is shown at the top along with the equilibrium voltage calculated by DFT. The three ground state Na-ion ordering configurations at $x = 2/3$, $1/2$, and $1/3$ calculated by DFT are shown at the bottom. The green and pink circles differentiate the two unique Na sites (green - edge sharing with TM, pink - face sharing with TM). Adapted from Ref. [102] with permission from the PCCP Owner Societies.

Na-ion Ordering in Multi-TM $NaMO_2$ Compounds

Although a multi-metal TM layer generally coincides with weakening Na-ion ordering behavior (e.g. P2-$Na_{2/3}[Mn_{1/2}Fe_{1/2}]O_2$ [103]), P2-$Na_{2/3}[Ni_{1/3}Mn_{2/3}]O_2$ is a marked exception to this trend. In 2013, Lee et. al evidenced Na-ion ordering in $Na_{2/3}[Ni_{1/3}Mn_{2/3}]O_2$ (pristine and after 1 cycle) by synchrotron XRD.[102] The authors also predicted three ground state ordering configurations for this compound at $x = 2/3, 1/2$, and $1/3$ using DFT, which corresponded well to voltage steps seen in the experimental electrochemistry (Figure 1.8). A recent work on P3-$NaTiS_2$ proposed that Na^+ diffusion in highly ordered P-type structures may be restricted to "anti-phase" boundaries between large ordered domains.[104] Presumably, the limited diffusion pathways caused by the ordering has a detrimental effect on the rate capability of P2-$Na_{2/3}[Ni_{1/3}Mn_{2/3}]O_2$ as well.

Gutierrez et al. recently exhibited that the Na-ion ordering in this compound could be completely suppressed by merely changing the ratio of Ni to Mn from 1:2 to 1:3 ($Na_{0.61}[Ni_{1/4}Mn_{3/4}]O_2$).[105] They theorized the introduction of a third metal center (Mn^{3+} into the TM layer disrupted the charge ordering. It is surprising that such a minor alteration in the composition would be sufficient to evoke this change, especially since the $Mn^{4+/3+}$ redox couple could still facilitate charge ordering within the TM layer. The authors do cite partial substitution of Ti and Mg in $Na_{2/3}[Ni_{1/3}Mn_{2/3}]O_2$ as examples of third metal centers introduced in other studies to disrupt Na-ion ordering, but these experiments were conducted with significantly higher levels of substitution ($\geq 1/6$).[74, 106] Moreover, a study on Co^{3+} substitution in $Na_{2/3}[Ni_{1/3}Mn_{2/3}]O_2$ to the same extent showed the voltage step at $x = 1/2$ (caused by Na-ion ordering) was clearly maintained, despite the introduction of a third metal center.[107] An alternative explanation of the suppressed Na-ion ordering in $Na_{0.61}[Ni_{1/4}Mn_{3/4}]O_2$ could be the presence of additional non-stoichiometric oxygen in the material (i.e. introduction of TM vacancies). Indeed, the very similar composition of $Na_{0.78}[\square_{0.08}Ni_{0.23}Mn_{0.69}]O_2$ ($\square$: TM vacancy) also exhibits a smooth voltage profile without Na-ion ordering.[108]

In general, the most successful substituents reported in the literature have been those that are not redox active including TM vacancies $\square$, Li^+, Mg^{2+}, Zn^{2+}, Al^{3+}, and Ti^{4+}.[71, 74, 106, 108–110] However, the substitution of Fe^{3+} has also been shown to suppress Na-ion ordering in some cases,[91, 103, 111] which could make Fe^{3+} preferred to inactive substituents as it does not reduce the theoretical capacity of the compound.

1.2.4 The Issue with Na-Deficient $NaMO_2$ Compounds

Prior discussion illuminated the ways in which the TM layer composition of $NaMO_2$ cathodes can be adapted to produce higher voltage and capacity as well as improved cyclability and kinetics. One of the problems that remains somewhat elusive is the deficiency of Na-ions in as-synthesized Na_xMO_2 materials ($x < 1$). P2 and P3-type Na_xMO_2 compounds can only be synthesized with a Na content in the

range of $0.5 \leq x \leq 0.8$. When tested in a half cell against a Na metal counter electrode, the deficit is not an issue. Extra Na-ions provided by the counter electrode can be inserted on discharge to compensate for the deficiency, allowing for the cathode's Na content at the end of discharge to be higher than the pristine. However, in a full cell when paired with an anode that does not initially contain Na itself (e.g. hard carbon), the capacity of the battery is limited by the insufficient quantity of Na-ions in the cathode.

Presently, two possible approaches for overcoming Na deficiency in Na_xMO_2 compounds have been identified: sacrificial salts and high energy ball milling with Na metal. The sacrificial salt, NaN_3, was first investigated in 2013 by Singh et al. The authors showed that the first cycle coulombic efficiency (i.e. ratio of discharge to charge capacity) of P2-$Na_{2/3}[Mn_{1/2}Fe_{1/2}]O_2$ could be improved by incorporating the salt into the cathode mixture (active material + conductive additive + binder + NaN_3).[112] The same group later ran tests in full cells (vs. a hard carbon anode instead of Na metal) which further validated the concept.[113] There are, however, a few drawbacks to using NaN_3. The first is the evolution of N_2 gas when NaN_3 decomposes during the initial charge. The gas could easily diffuse to the anode side of the cell and disrupt the formation of the necessary solid electrolyte interphase (SEI). The second drawback is that the salt adds extra volume and mass to the electrode which lowers the energy density of the battery.[114] In 2017, Sathiya et al. proposed the use of Na_2CO_3 as a sacrificial salt, however it has many of the same problems as NaN_3.[115] Na_2CO_3 will also evolve gas (CO_2) during the first charge and clearly also adds additional mass to the electrode material. Moreover, the presence of surface carbonate species has been shown to be detrimental to electrode kinetics and cause the de-fluorination of the typically used binder polyvinylidene fluoride (PVDF) during electrode slurry preparation.[55, 116]

An alternative approach to overcome Na-deficiency proposed by Zhang et al. is a high energy ball milling of the cathode active material (P2-$Na_{2/3}[Mn_{1/2}Fe_{1/2}]O_2$) with Na metal.[114] When fresh interfaces are created by the ball milling process, the Na metal effectively reduces $Na_{2/3}[Mn_{1/2}Fe_{1/2}]O_2$ while inserting additional

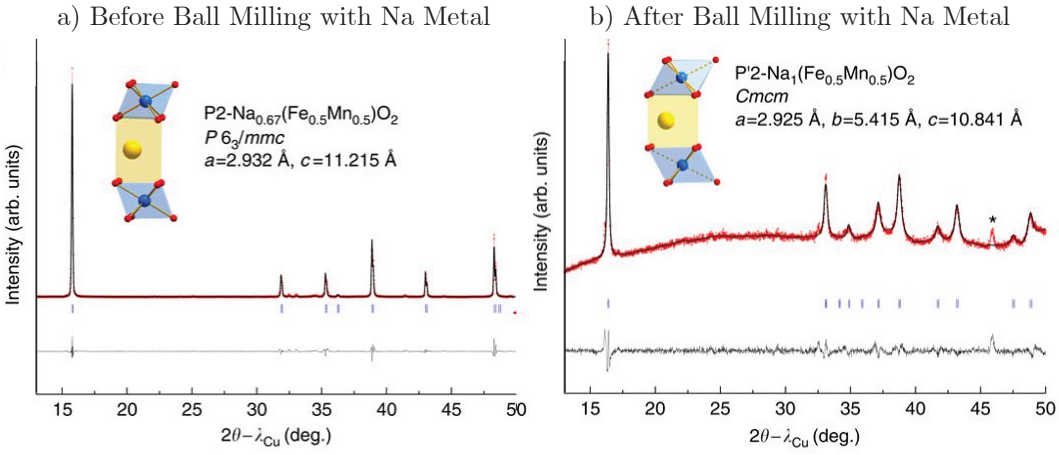

Figure 1.9: $Na_{2/3}[Mn_{1/2}Fe_{1/2}]O_2$ was ball milled with Na metal in order to reduce the Na-deficiency intrinsic to Na_xMO_2 compounds. XRD was performed a) before and b) after the ball milling process showing a change of the structure from P2 to P'2. The lattice parameters and an illustration of the structures are shown as an inset. Adapted with permission under the Creative Commons Attribution 4.0 International License from Ref. [114].

Na-ions into the layered structure. This results in a distortion of the P2 structure to P'2 (shown in Figure 1.9) caused by the increased fraction of Jahn-Teller active Mn^{3+} ($t_{2g}{}^3$ $e_g{}^1$).[117] This approach may be better than sacrificial salts as there is neither evolution of potentially detrimental gases during battery operation nor any volume added to the battery electrode. It remains to be seen, however, whether high energy ball milling could be utilized at the commercial scale.

The issue of Na deficiency in P2 and P3-$NaMO_2$ compounds is one that will need to be addressed if these types of compounds are to achieve the capacities necessary to compete at a commercial level.

1.3 High Voltage Structural Transitions in Layered Oxide Cathodes

Na_xMO_2 compounds often undergo one or more structural transitions during (de-)intercalation. These structural transitions can be categorized as follow:

- Distortions (indicated by a ' symbol, e.g. P'2)
- Na layer re-coordination as a result of gliding TMO_2 slabs (e.g. O3 $\leftrightarrow$ P3)

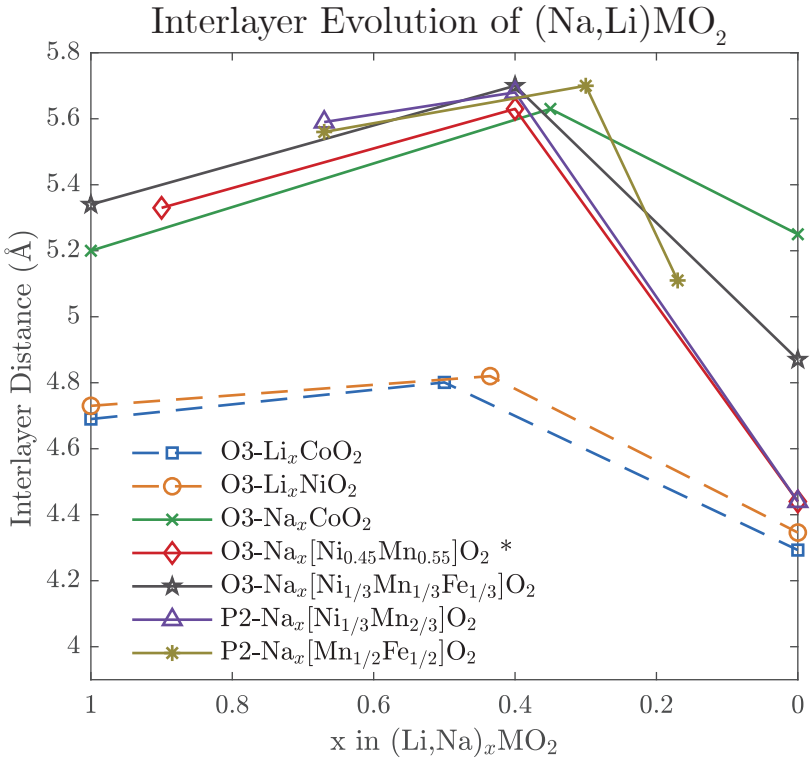

Figure 1.10: The approximate interlayer distances are plotted as a function of Na or Li content in the compound for O3-$LiCoO_2$ (data from Ref. [24, 118, 119], O3-$LiNiO_2$ (data from Ref. [120–122]), O3-$NaCoO_2$ (data from Ref. [51]), O3-$Na_{0.9}[Ni_{0.45}Mn_{0.55}]O_2$ (data from Ref. [79, 123]), O3-$Na[Ni_{1/3}Mn_{1/3}Fe_{1/3}]O_2$ (data from Ref. [51]), P2-$Na_{2/3}[Ni_{1/3}Mn_{2/3}]O_2$ (data from Ref. [59, 74]), and P2-$Na_{2/3}[Mn_{1/2}Fe_{1/2}]O_2$ (data from Ref. [124]). This graph clearly demonstrates the generally greater interlayer contraction of $NaMO_2$ compounds compared with $LiMO_2$ compounds. * The intermediate interlayer spacing for $Na_{0.9}[Ni_{0.45}Mn_{0.55}]O_2$ has not been reported thus the value used here is that of $Na_{0.4}[Ni_{1/2}Mn_{1/2}]O_2$.

- Migration of TMs to the Na layer

Analogous to Li compounds, the structural transitions that occur at low Na contents (and generally high voltage) tend to be the most detrimental to the cycling stability of the compound. In particular, materials significantly depleted of Na undergo a sharp contraction of the interlayer space (distance [d] between adjacent TMO_2 slabs) which has been shown to cause particle fracture and electronic isolation.[3, 80, 125] These volume changes are generally greater for Na compounds than Li compounds because of the larger ionic radius of Na^+, as shown in Figure 1.10.

The detrimental high voltage structural changes often necessitate employing a lower voltage cutoff on charging to sustain cycling.[77] Therefore, understanding

and engineering solutions to prevent the structural transitions occurring at low Na contents provides a significant opportunity for meaningful gains in capacity and voltage. This section will review the current understanding of the structural transitions in as-synthesized O3 and P2 structured compounds.

1.3.1 O3 Phase Transformations

$LiMO_2$ Compounds

O3-$LiMO_2$ compounds have been studied to a much greater extent than their $NaMO_2$ counterparts. As such, there are key learning points gleaned from investigating Li materials (especially at low Li-contents) that can be applied to Na compounds. Thus, O3-$LiMO_2$ materials' structure and phase transformations are first reviewed here.

One of the Li-ion cathode materials most utilized for commercial applications is O3-$LiCoO_2$.[127] The structural evolution of this compound is summarized in Figure 1.11. Structural characterization of Li_xCoO_2 using *in situ* XRD was first carried out in 1992 by Riemers and Dahn and soon after by Ammatucci et al. (charging to 4.35 V and 5.1 V vs. Li^+/Li respectively).[118, 128] Both reports demonstrated the maintenance of the O3 structure at lower voltages (higher x) with the exception of a monoclinic distortion (O'3) caused by Li-ion ordering at $x = 0.5$. Upon further Li extraction beyond $x \approx 0.31$, however, Ammatucci et al. discovered the formation of two new phases (XRD data in Figure 1.11b). One new phase at 5.1 V ($x \approx 0$) had a very small interlayer spacing of $d \approx 4.29$ Å and was classified by the authors as an O1 structure. This layered-type structure contains octahedral vacancies in the Li layer that face share with TM octahedra (Co in this case) in each adjacent TM layer (Figure 1.11d).[118] The other new phase, occurring at 4.6 V ($x \approx 0.12$), was later identified as a hybrid structure by Van der Ven et al. and Lu et al. containing alternating layers of O1 and O3-type; this hybrid structure was labeled as the H1-3 phase (also Figure 1.11d).[126, 129] The presence of hybrid phases with varied stacking sequences may also be relevant to Na-ion compounds.

O3-$LiNiO_2$, the parent compound of commercially relevant Ni-rich cathodes, has also been studied in great detail. Ammatucci et al. initially indicated that

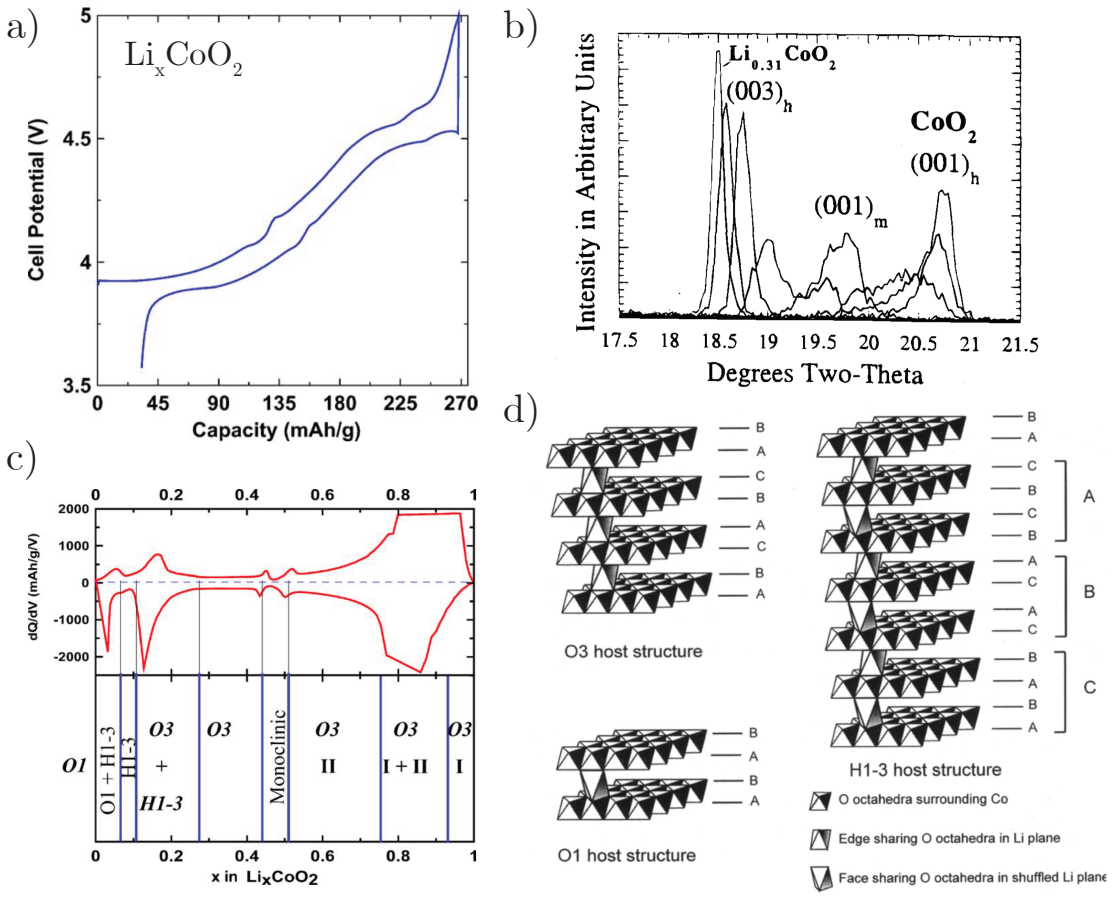

Figure 1.11: The structural evolution of $LiCoO_2$ is shown. The electrochemical load curve is shown in a) for reference (Reprinted from Ref. [78] with permission from Elsevier). The *in situ* XRD data in b) focuses on the (003) reflection at $x \leq 0.31$ (Reproduced with permission from Ref. [118]. Copyright 1996, The Electrochemical Society.). The phase diagram of the compound is shown in c) along with the corresponding differential capacity curve (Reprinted from Ref. [78] with permission from Elsevier). The H1-3 structure appearing at low x is illustrated in d) along with its structural components, O3 and O1 (Reproduced with permission from Ref. [126]. Copyright 1998, The Electrochemical Society.).

the O3 phase was maintained upon full de-intercalation (5.1 V) of Li_xNiO_2 albeit with a significant volume contraction ($d \approx 4.53$ Å).[118] However, later work by Crogguenec et al. determined that the phase of this compound at the end of charge was not necessarily fixed at O3 but rather largely dependent on the Ni-Li anti-site disorder (i.e. Ni in Li layer and vice versa) in the as-synthesized compound.[120, 130] In compounds with low anti-site disorder, the O1 phase was evident upon full de-intercalation with an interlayer spacing of $d \approx 4.35$ Å.[130] Although Na-ion compounds do not experience anti-site disorder, TMs can migrate to the Na layer

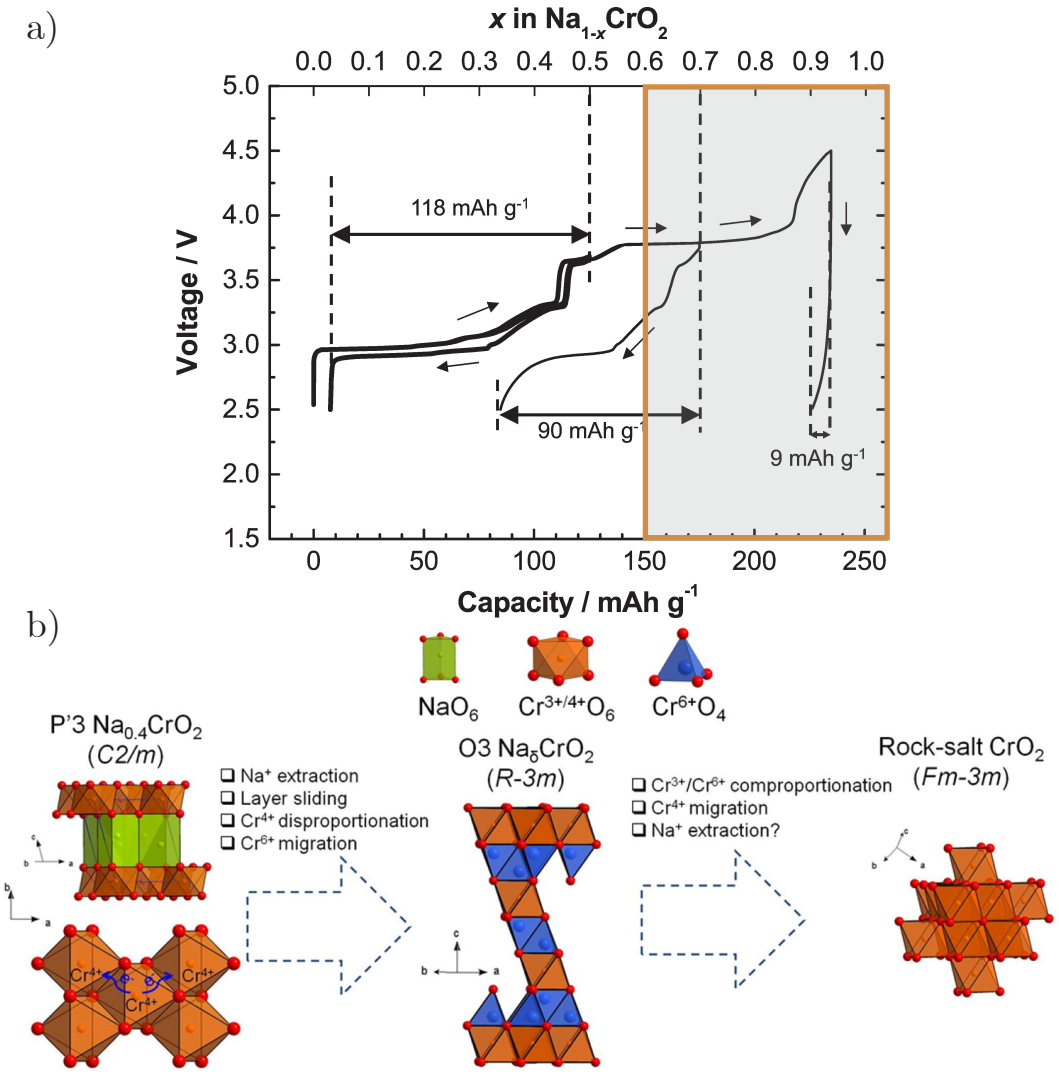

Figure 1.12: The electrochemical load curve of O3-Na_xCrO_2 is shown in a) cycled to different voltage cutoffs (Adapted with permission from Ref. [131]. Copyright 2014 American Chemical Society.). b) shows the Cr migration mechanism proposed by Bo et al. (Adapted with permission under the ACS AuthorChoice License from Ref. [132] `https://pubs.acs.org/doi/abs/10.1021/acs.chemmater.5b04626`. Further permissions related to the material excerpted should be directed to the ACS.)

during de-intercalation. Thus, $LiNiO_2$ represents an informative model on how this may change the mechanism of structural evolution.

TM Migration in O3-$NaMO_2$ Compounds

As was previously discussed, the most promising 3d TMs to incorporate in $NaMO_2$ materials to optimize voltage are Cr, Fe, Co, and Ni. There have been in-depth structural studies on single TM O3-$NaMO_2$ compounds containing each of these

TMs. While there is a general lack of consensus regarding the terminology and structural classifications, many $NaMO_2$ materials containing these TMs have been studied in detail.

Both O3-$NaCrO_2$ and O3-$NaFeO_2$ undergo significant TM migration upon (de-)intercalation that distorts and evolves the O3 structure to limit cyclability. Bo et al. recently proposed a mechanism for the degradation of $NaCrO_2$, shown in Figure 1.12, involving the O3 structure initially transforming to a monoclincally distorted P'3 (from $x = 1$ to $x \approx 0.7$) which remains stable until $x \approx 0.4$ at which point a transition back to O3 occurs.[132] The authors argue that during this transition, Cr migrates into the Na-layer and this eventually transforms the structure further into a CrO_2 disordered rock salt. By contrast, $NaFeO_2$ does not transition to a P3-type structure on charging, but still undergoes a similar process when charged beyond $x \approx 0.5$ with Fe^{3+} ([Ar] d^5: no crystal field preference between tetrahedral and octahedral) migrating to tetrahedral sites in the Na layer.[81, 101] The TM migration in $NaCrO_2$ and $NaFeO_2$ unfortunately makes both compounds inappropriate as a cathode material despite their adequate voltage and high elemental abundance. In multi-TM systems, however, it has been proposed that reducing the Cr or Fe fraction is effective for suppressing migration and improving cyclability.[55]

The "X"-Phase, "Y"-Phase, and Suppression of TM Migration

Kubota et al. demonstrated that O3-$Na[Co_{1/2}Fe_{1/2}]O_2$ outperforms either of the two single TM parent compounds in terms of reversible capacity.[133] Unlike $NaFeO_2$, $Na[Co_{1/2}Fe_{1/2}]O_2$ transitions to a P3 structure on charging, which presumably helps to combat Fe migration at intermediate Na contents as there are no tetrahedral sites in the Na layer for the Fe to migrate to. On continued charging of the compound past $x \approx 0.4$ (x in $Na_x[Co_{1/2}Fe_{1/2}]O_2$), there is another phase transition that manifests itself as a rapid contraction of the interlayer spacing, which the authors assign as a "P'3-O'3 solid solution transition".[133] The sharp decrease of the interlayer spacing seen for O3-$Na[Co_{1/2}Fe_{1/2}]O_2$ ($x \leq 0.4$) has also been observed for other charged O3 $NaMO_2$ compounds, albeit with varying conclusions

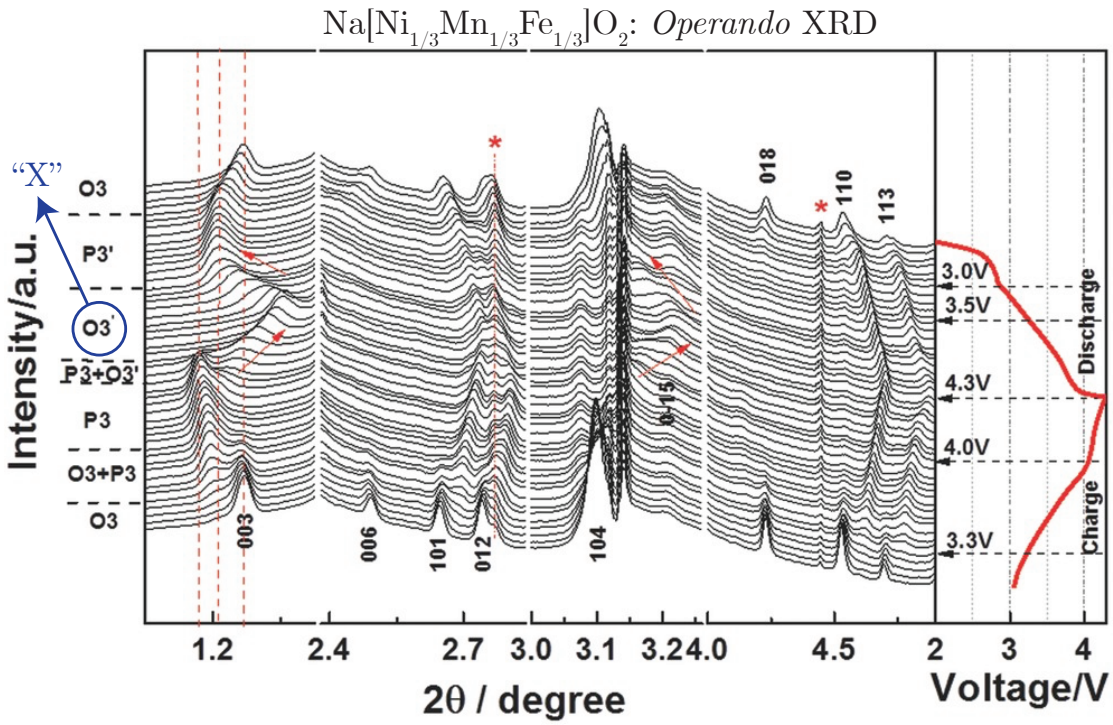

Figure 1.13: *Operando* synchrotron XRD ($\lambda = 0.1174$ Å) of O3-Na$[Ni_{1/3}Mn_{1/3}Fe_{1/3}]O_2$ is shown with the various phase transitions labeled on the left and the electrochemical load curve on the right. The O3' phase indicated by the authors is consistent with the "X"-phase as is evident by the progressive positive shift of the (003) peak indicating interlayer contraction. Adapted with permission from Ref. [135], 2016 WILEY-VCH Verlag GmbH & Co. KGaA, Weinheim.

on the structure's identity.[51] For consistency, the high voltage (low x) structural transition of O3 compounds which occurs through progressive interlayer contraction will be labeled hereon as the "X"-phase (as it has been done by some authors [134]) to better communicate its ambiguity.

O3-type $NaMO_2$ compounds containing only Co and/or Ni (without Cr or Fe) also undergo structural transition with interlayer contractions corresponding to the aforementioned "X"-phase yet display greatly improved reversibly capacity relative to $NaFeO_2$ and $NaCrO_2$.[51, 136] Improved cyclability seems to be related to suppressed TM migration as predicted by DFT and experimentally verified with transmission electron microscopy (TEM).[51, 137]

Zheng et al. presented *ex situ* XRD of O3-$Na_{0.9}[Ni_{0.45}Mn_{0.55}]O_2$ after the compound was charged to 4.5 V ($x \leq 0.1$) which showed the formation of a new phase (hereon labeled the "Y"-phase) with a very small interlayer spacing ($d \approx 4.44$

Table 1.3: A summary of the interlayer spacing of O3 compounds charged to low Na contents (x).

Compound	**Voltage (V)**	**≈ x**	**d** (Å)	**Phase Assigned**	**Ref.**
Li_xCoO_2	5.1	0	4.29	O1	[118]
Li_xNiO_2	4.45	0	4.35	O1	[130]
$Na_x[Ni_{0.45}Mn_{0.55}]O_2$	4.5	0	4.44	O3	[79]
$Li_x[Ni_{0.8}Mn_{0.1}Co_{0.1}]O_2$	4.6	0.25	4.58	None	[138]
Na_xCrO_2	4.0	0.1	4.71	Rock-salt	[132]
$Na_x[Ni_{1/3}Mn_{1/3}Fe_{1/3}]O_2$	4.5	0	4.87	O3	[51]
Na_xFeO_2	4.5	Unk.	4.9	Spinel	[51]
$Na_x[Mn_{1/3}Fe_{2/3}]O_2$	4.3	0.08	5.02	"X"	[139]
$Na_x[Fe_{1/2}Co_{1/2}]O_2$	4.5	0.18	5.06	O3	[51]
Na_xCoO_2	4.5	0	5.25	O3	[51]
Na_xNiO_2	4.5	0.06	5.55	O3	[51]

Å).[79] This new phase appeared to stem from a biphasic reaction and therefore should be distinct from the "X"-phase which shows a progressive collapse of the interlayer space. This interlayer spacing of charged $Na_x[Ni_{0.45}Mn_{0.45}]O_2$ is much smaller than has been seen for any other charged O3-$NaMO_2$ compounds, to the best of my knowledge, but does, however, approach that of the fully de-intercalated O1-Li_xNiO_2 and O1-Li_xCoO_2 ($x \approx 0$).[118, 130]

Yuan et al. demonstrated that partial substitution of Fe for Mn and Ni, resulting in the composition $Na[Ni_{0.4}Mn_{0.4}Fe_{0.2}]O_2$, altered the compound's behavior to match that of the "X"-phase (authors assigned as OP2).[111] They cited the possibility of Fe migration as the cause for this difference. *In situ* synchrotron XRD was later collected on the closely related composition $Na[Ni_{1/3}Mn_{1/3}Fe_{1/3}]O_2$, by Xie et al., which clearly showed the evolution of the "X"-phase (labeled as O3' by the authors) (Figure 1.13). An additional study demonstrated that the interlayer spacing of this compound decreased to $d \approx 4.87$ Å at 4.5 V, which is still significantly larger than that of the previously discussed "Y"-phase.[51]

Table 1.3 summarizes the end of charge structures of several relevant O3-type layered oxide compounds. A thorough understanding of the "X" and "Y"-phases is important to be able to utilize the capacity at high voltage/low Na-contents ($x \leq 0.4$). As of now, the literature clearly lacks consensus as to the nature of these

two phases, how they might relate to one another, and whether TM migration to the Na layer plays a role. In the papers reviewed above alone the conservatively labeled "X"-phase was designated as O3, O'3, OP2, and O'3-P'3 intergrowth, despite displaying largely the same characteristics. A unifying theory on the topic would be extremely helpful and warrants significant effort moving forward.

1.3.2 P2 Phase Transformations

As discussed previously, the O3 structure is stabilized by high Na contents during synthesis ($x \geq 0.8$). Upon de-intercalation, most O3-type $NaMO_2$ compounds transition to a P3 structure when approaching intermediate Na contents ($0.4 \leq x \leq 0.7$) and then transition again to the "X"-phase at low Na contents ($x < 0.4$). By contrast, P2-structured $NaMO_2$ compounds are synthesized with intermediate Na contents ($0.5 \leq x \leq 0.8$) and undergo a different structural evolution upon cycling. For instance, it may be expected that if Na^+ is intercalated into the P2 compound so as to increase the Na content beyond 0.8, the TMO_2 slabs would glide to form the O2 structure, analogous to the O3 $\leftrightarrow$ P3 transition; however, this does not occur in practice.[95, 140] Presumably this is due to the fact Na occupancy is unfavorable in the O2 structure as all Na sites face share with TM octahedra. The P2 stability range is therefore extended to $x \geq 0.9$ electrochemically.[95, 140, 141] The suppressed layer-gliding at high Na contents is theoretically beneficial to the cyclability of P2-type compounds.[61]

At low Na-contents ($x < 0.4$), layer gliding can occur as there is no longer enough Na present to destabilize the O2 structure. In 2001, Lu and Dahn used *operando* XRD to show that P2-$Na_x[Ni_{1/3}Mn_{2/3}]O_2$ transitioned to the O2 structure via a biphasic reaction at $x \approx 1/3$.[59] The O2 structure observed had a very small interlayer spacing of $d \approx 4.44$ Å, which coincidentally matches almost exactly with the interlayer spacing of the charged O3-$Na_x[Ni_{0.45}Mn_{0.55}]O_2$ compound discussed previously. It seems despite the different structure and TM layer composition of these two compounds, the interlayer spacing of approximately 4.44 Å represents that of a fully de-intercalated Na-ion compound.

No other P2-type Na_xMO_2 material, to the best of my knowledge, has been reported to undergo such a dramatic interlayer contraction as $Na_{2/3}[Ni_{1/3}Mn_{2/3}]O_2$. In fact, most P2-type compounds by contrast undergo a distinctly different (and more controversial) structural evolution when charged to high voltages (low Na contents). $Na_{2/3}[Mn_{1/2}Fe_{1/2}]O_2$ is one such compound. In 2012, Yabuuchi et al. showed by *ex situ* synchrotron XRD that charging the compound to 4.2 V caused a conversion to a new structure which they identified as the OP4 phase (alternating P2-type and O2-type layers).[142]

A later *operando* XRD experiment by Mortemorde de Boisse et al. demonstrated for the first time that the interlayer spacing of $Na_x[Mn_{1/2}Fe_{1/2}]O_2$ phase progressively decreases during the high voltage phase.[124] In the *operando* set up, however, the authors could not identify enough diffraction peaks to determine the stacking type so they labeled this ambiguous structure the "Z"-phase. It will be referred to as such hereon.

A follow-up study by Pang et al. using *operando* synchrotron XRD reported the "Z"-phase of $Na_x[Mn_{1/2}Fe_{1/2}]O_2$ to be OP4 but asserted a different stacking sequence than Yabuuchi et al.'s (alternating layers of P2 and O3 rather than P2 and O2).[140] The transition of the P2 structure to this P2-O3 stacking sequence of OP4, however, would require a breaking strong TM-O bonds to rearrange the TMO_2 slab itself rather than a more facile gliding of the slabs. This impracticality is something the authors did not address.

Talaie et al. later used pair distribution function (PDF) analysis of the total X-ray scattering from chemically de-intercalated $Na_x[Mn_{1/2}Fe_{1/2}]O_2$ to propose a new model for the high voltage "Z"-phase. The authors argued that over 10% of the Fe migrates to the Na layer, a process that instigates a layer glide to O2 stacking in order to create stable tetrahedral sites for Fe^{3+} to occupy.[70] They provided further evidence of the Fe migration with ^{57}Fe Mössbauer spectroscopy (^{57}Fe-MS) by fitting an extra doublet with large quadrupolar splitting (QS). A model of the Fe migrated O2 structure is shown in Figure 1.14 along with the PDF and ^{57}Fe-MS fittings. The same group later identified that partial substitution of Mn with Ni or

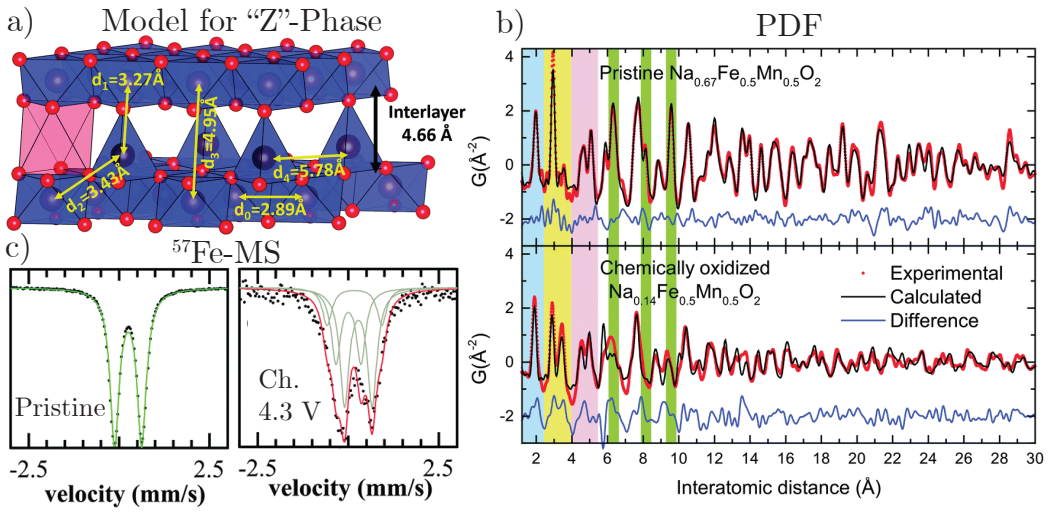

Figure 1.14: A model for the high voltage "Z"-phase of $Na_x[Mn_{1/2}Fe_{1/2}]O_2$, as reported by Talaie et al., is shown with supporting evidence. An illustration of the model is shown in a), a fitting of the PDF data is shown b), and a fitting of the ^{57}Fe-MS data is shown in c). Adapted with permission under the Creative Commons Attribution 3.0 License from Ref. [70] Published by The Royal Society of Chemistry.

Cu served to alleviate most of the TM migration and improve cyclability; however the change did not suppress the phase transformation to O2 stacking.[70, 143]

Very recently, Kubota et al. revisited the subject of the high voltage "Z"-phase when investigating the compound $Na_{2/3}[Ni_{1/4}Mn_{2/3}Cu_{1/12}]O_2$.[144] The authors proposed that the "Z"-phase of this compound was a disordered OP4 structure (i.e. P2 and O2-type layers not alternating) termed P2-O2 50:50 intergrowth using a combination of *operando* and *ex situ* XRD with stacking fault simulations to argue their case. A schematic comparing the OP4 and P2-O2 50:50 intergrowth is shown in Figure 1.15.

In summary, P2-type compounds are structurally stable (i.e. no layer gliding) over a larger range of x than O3-type compounds, making them a promising class of cathode materials. Like O3 compounds, however, P2 compounds undergo a structural evolution at high voltages (low Na content, $x < 0.4$) that is detrimental to cyclability. The P2 to O2 biphasic transition of $Na_{2/3}[Ni_{1/3}Mn_{2/3}]O_2$ has been shown in particular to be associated with a rather severe volume contraction ($> 20\%$). Some improvement to the cyclability is seen, however, in P2 compounds that transition to the high voltage structure termed the "Z"-phase. The exact nature of this "Z"-phase

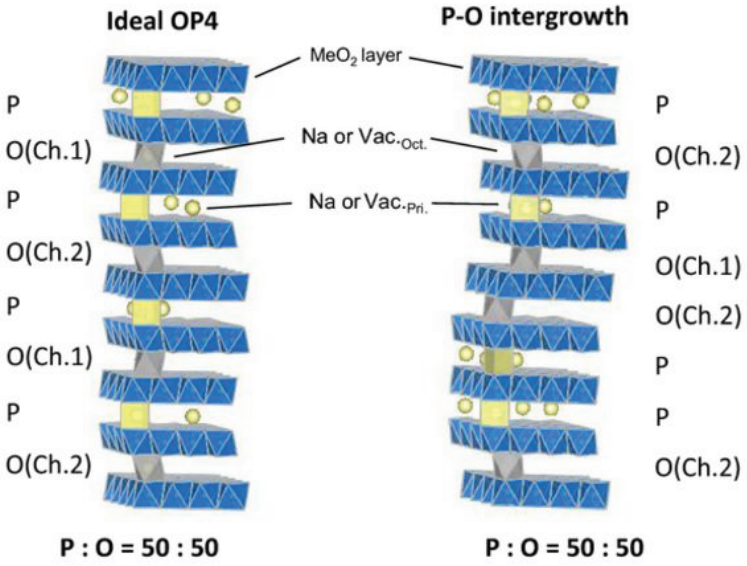

Figure 1.15: This schematic compares the ordered OP4 structure (alternating P2 and O2-type layers) with the disordered P2-O2 50:50 intergrowth assigned to $Na_{2/3}[Ni_{1/4}Mn_{2/3}Cu_{1/12}]O_2$ ($x < 0.3$) by Kubota et al. "Ch. 1" and "Ch. 2" indicate the two different *choices* of glide vector to achieve O2 stacking from P2 stacking. Reproduced with permission from Ref. [144] Copyright 2017, The Electrochemical Society.

currently lacks consensus in the literature. It is important to reiterate that the utilization of the cathode at low Na contents not only delivers additional capacity but also does so at a high voltage, offering a substantial payoff in energy density. As such, understanding the structural evolution of P2 (and O3) compounds at low Na contents is an important component of developing better cathode materials.

1.4 Oxygen Redox in Layered Oxide Cathodes

The large variety of cathode materials discussed so far compensate the (de-)intercalation of Na or Li-ions through the (oxidation) reduction of a TM redox center (e.g. $Co^{4+/3+}$). The past decade has garnered significant interest in a new class of cathode materials where the oxide anion can participate in the redox reaction to provide *extra* capacity beyond what is theoretically possible through TM-redox alone. This class of cathode materials, often labeled O-redox compounds, offers huge promise to potentially increase the quantity of Li or Na-ions that are stored while simultaneously reducing the cathode weight and cost by lessening the need for TMs (i.e. large increase in specific capacity).

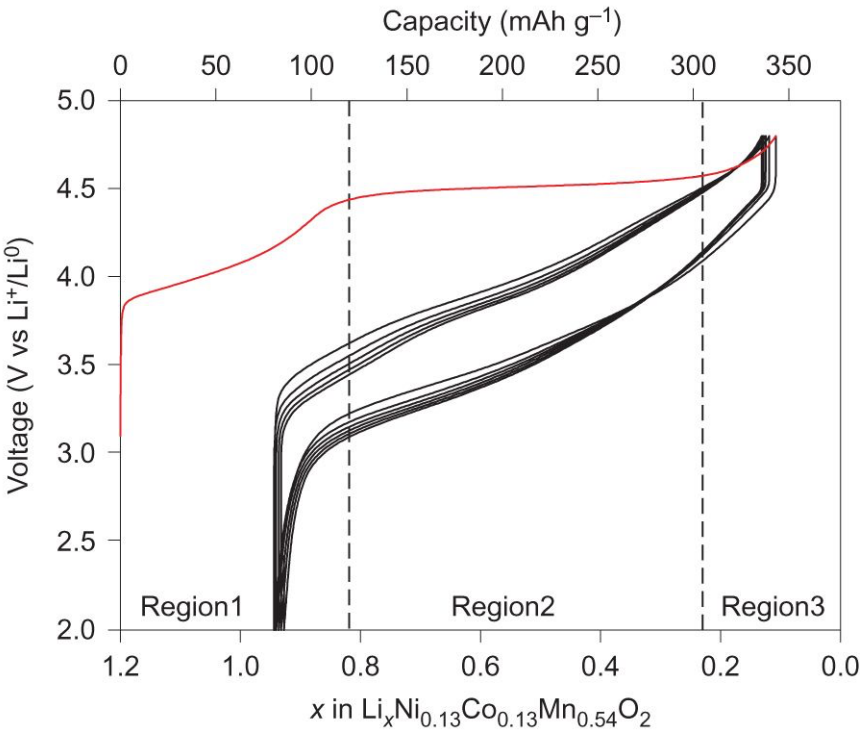

Figure 1.16: The electrochemical load curve for $Li_xNi_{0.13}Co_{0.13}Mn_{0.54}O_2$. This compound displays the characteristic long plateau on the first charge (red) followed by a dramatic change to the load curve's shape on subsequent cycles. Reprinted by permission from Springer Nature: Nature Chemistry Ref. [145].

Most of the research on O-redox compounds has focused on "Li-rich" materials (Li:TM ratio > 1) which are generally derivatives of the compound Li_2MnO_3 (i.e. $Li[Li_{1/3}Mn_{2/3}]O_2$ with Li occupying the Li layer *and* TM layer). More recently, O-redox has been identified in Na-ion compounds as well. In this penultimate section of the Introduction, the literature on O-redox compounds will be reviewed with an emphasis on advances in the fundamental understanding of how O participates.

1.4.1 Li-ion O-Redox Compounds

Interest in Li-rich cathodes began as early as 1997 with the identification of a solid solution existing between $LiCoO_2$ and Li_2MnO_3.[146] This was soon followed by the investigation of $Li[Li_{1/5}Cr_{2/5}Mn_{2/5}]O_2$ in 2001.[147] Most notably, the solid solution between $Li[Ni_{1/2}Mn_{1/2}]O_2$ and Li_2MnO_3 was explored by Lu and Dahn in 2001 who observed "anomalous capacity" (not attributable to Mn or Ni redox) when the cathode was charged beyond 4.5 V.[148] This extra capacity manifested

itself as a long voltage plateau on the electrochemical load curve. A typical Li-rich voltage curve is shown in Figure 1.16 for reference illustrating this behavior. On first charge, the voltage profile displays an initial sloped region (region 1), followed by a long plateau (region 2), and finally an uptick which takes the voltage to the upper limit (region 3). On subsequent discharge and cycling, the region 2 plateau is lost, resulting in a severe hysteresis (energy inefficiency).

Initial Investigations of "Anomalous" Capacity

For the $Li[Li_{(1-2y)/3}Mn_{(2-y)/3}Ni_y]O_2$ ($y < 0.5$) materials, Lu and Dahn initially reconciled the source of "anomalous" capacity to be irreversible extraction of O from the structure on charge followed by Mn reduction on discharge.[149] This theory was later corroborated by work from Armstrong et al. who used online electrochemical mass spectrometry (OEMS) to confirm that O_2 gas was evolved from the structure (O-loss).[150] During this period, the O-loss theory was called into question by findings from electrochemical cycling carried out at 55 °C which pointed to electrolyte degradation along with H^+-Li^+ ion-exchange as the primary electrochemical mechanism.[151, 152] However, Tran et al. demonstrated that this process did not occur to any appreciable extent at room temperature using ^1H magic angle spinning-nuclear magnetic resonance (MAS-NMR).[153] Instead, the authors argued for O-loss and subsequent "densification" of the structure; this involved TMs at the surface, destabilized by O-loss, migrating toward the bulk of particles.[153] Substantiating this speculation, it had been shown previously that Li^+ could be extracted from both the TM and Li layers on charge, which would leave a high quantity of vacancies in the structure for TMs to diffuse through.[154]

Competition between O-Loss and O-Redox

Work by Hong et al. contradicted this model however, showing that the weight loss of the electrode during the plateau (from O-loss) was not enough to account for the extra capacity seen.[155] Thus reversible O-redox was first suggested. Ito et al. then performed *operando* X-ray absorption spectroscopy (XAS) and evidenced limited Mn reduction on discharge, also indirectly evidencing O-redox.[156] In

2011, Yabuuchi et al. suggested the reversible O-redox reaction on cycling may occur through re-reduction of the O_2 gas evolved from the structure on charge back onto the surface of the cathode as Li_2CO_3.[157] This proposed process was endorsed by findings in other reports.[158, 159]

By 2013, it was becoming clear that the bulk and surface processes of Li-rich compounds may be different. This led Koga et al. to propose a new hybrid model in which reversible O-redox occurred in the bulk of particles while O-loss on charge produced densificiation near the surface.[160, 161] Soon after, the first direct evidence of O-redox in the bulk was obtained via soft XAS of the O K-edge. This technique revealed an increased intensity in the pre-edge region of the spectra during the plateau.[162] Reports by Luo et al. in 2016 reinforced these findings with further evidence of O-redox using resonant inelastic X-ray spectroscopy (RIXS).[145, 163] Moreover, the same authors also demonstrated that O-loss (vs. O-redox) is only predominate when charging beyond the end of the plateau (region 3 of Figure 1.16), a finding also corroborated by others.[145, 164] Around the same time, Seo et al. showed through DFT that O could in fact be oxidized when charging Li-rich compounds because of the very ionic nature of the Li-O bond.[165] Thus, computational and experimental results seemed to be converging on the theory of O-redox and attention turned to understanding the processes that limited its reversibility.

Reversibility of O-Redox and Voltage Fading

A significant amount of resources had been dedicated to developing Li-rich materials for EV batteries as part of a USA Department of Energy (DOE) project.[166] Commercialization has so far been thwarted mainly due to the issue of "voltage fading": the decline of the average discharge voltage with cycling.[167] Important work by Croy, Thackeray, and others elucidated irreversible TM migration into the Li layer as the primary cause for this decline.[168–171]

Sathiya et al. reported that TM migration and voltage fading were an "inseparable part" of the charge/discharge of Li-rich materials and was correlated directly with

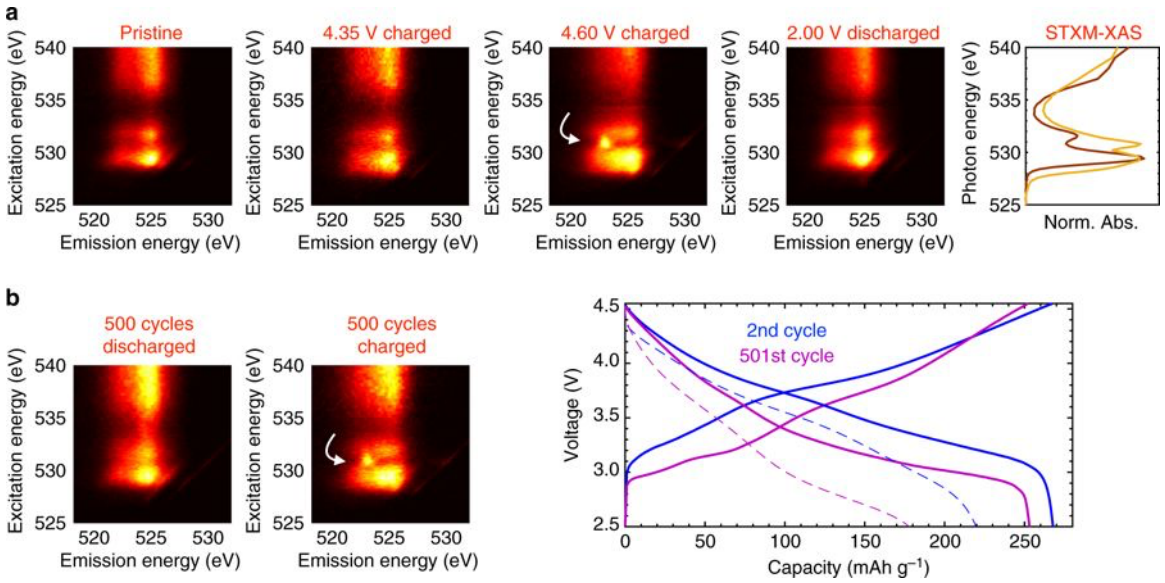

Figure 1.17: Resonant inelastic X-ray scattering (RIXS) maps are shown for the compound $Li[Li_{0.17}Ni_{0.21}Co_{0.08}Mn_{0.54}]O_2$ at different states of charge during the first cycle a) and on the 500th cycle b). The electrochemical load curve (solid: C/68 current rate, dashed: 2C current rate) and XAS is also shown for comparison. Reproduced with permission under the Creative Commons Attribution 4.0 International License from Ref. [175].

O-loss.[172] The authors, however, argued that this effect could be curtailed by 1) utilizing large cations (e.g. Sn) in the TM layer, which they claimed are less likely to migrate and 2) using 4d and 5d redox active TMs, which could "reductively couple" to the O-redox reaction.[159, 172] The proposed reductive coupling mechanism was elaborated on by Saubanère et al. who declared reversible O-redox could only occur through the creation of "peroxo-like" species (i.e. O-O bonding) with the subsequent covalent stabilization of those species by 4d or 5d TMs (i.e. $TM(O_2)^{n-}$ where n< 4).[173] In accordance with this concept, DFT calculations indicated that the interaction of 3d TMs and O was not sufficiently covalent to facilitate reversibility.[174]

Invalidating these conclusions, Gent et al. exhibited sustained reversibility of the O-redox couple for $Li[Li_{1.17}Ni_{0.21}Co_{0.08}Mn_{0.54}]O_2$ even on the 500th cycle.[175] Their results, obtained using RIXS mapping of the O K-edge, are shown in Figure 1.17. Moreover, the authors claimed their spectroscopy results indicated that reversible migration of TM cations between the TM and Li layer octahedral sites was in fact

coupled to the O-redox reaction. However, this concept of reversible TM migration into octhedral sites in the Li layer is inconsistent with others' data. For example, a recent report by Kleiner et al. of a long duration synchrotron XRD study evidenced reversible migration of TMs into Li layer tetrahedral sites ($\approx 8\%$ each cycle) but indicated that TM migration into Li layer octahedral sites was irreversible.[171] It is evident that the nature and role of TM migration in O-redox is still ambiguous.

Presently, RIXS mapping is being heavily promoted as the go-to method for identifying O-redox by Yang and others at the Advanced Light Source synchrotron.[176] They claim the "signature of O-redox" is a low energy emission indicated by an arrow in Figure 1.17.[175–177] Interestingly, the feature seen in the RIXS maps of charged Li-rich cathodes was shown to match well with that of Li_2O_2 giving possible credence to the idea of "peroxo-like" bond formation.[178] However, the authors were quick to advise that further theoretical investigation was needed before conclusions could be drawn regarding the true origin of this signature beyond merely evidencing oxidized O.[177]

Overall, the battery research field seems to be coming to a consensus on the certain O-redox mechanisms characteristic of Li-rich cathodes. These can be summarized as follows: 1) O-redox is reversible upon cycling,[175, 179, 180] 2) O-O interactions of some sort may serve to stabilize the oxidized O,[67, 174, 181] 3) TM migration to the Li layer appears to happen to some extent during the charging process either reversibly or irreversibly,[169–172, 182] and 4) although heavily reliant on composition, O-loss seems to be largely a surface process.[160, 164, 183–185]

However, many questions still remain unanswered particularly surrounding the nature of oxidized O and how it relates to hysteresis and O-loss. Recently, there have been reports of O-redox in Na-ion cathode materials. Most of these compounds cannot be classified as Na-rich as their Na:TM ratio is generally not greater than 1 with the exception of 4d TM systems. Nonetheless, the Na-ion chemistry may serve as a convenient test bed to better understand the fundamental mechanisms of the O-redox chemistry and possibly engineer solutions to overcome the present limitations.

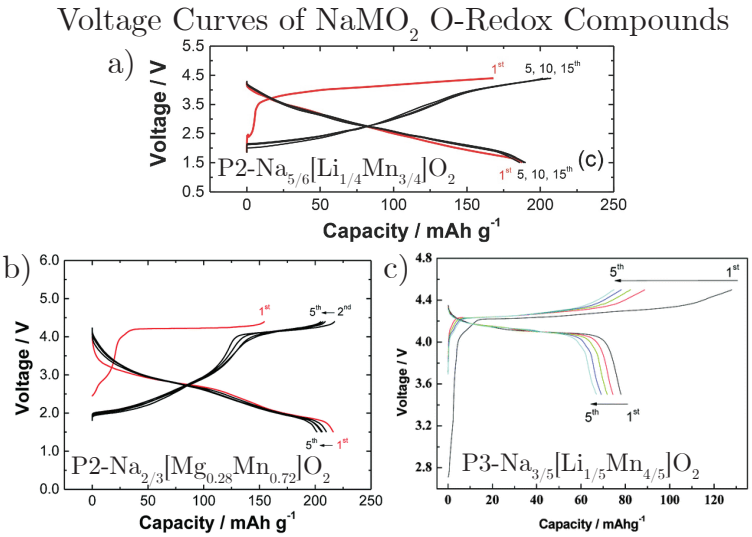

Figure 1.18: The electrochemical load curves for Na-ion compounds displaying anomalous capacity on charge are shown including a) P2-$Na_{5/6}[Li_{1/4}Mn_{3/4}]O_2$ (Reproduced from Ref. [186] with permission from WILEY), b) P2-$Na_{2/3}[Mg_{0.28}Mn_{0.72}]O_2$ (Reproduced from Ref. [187] with permission from The Royal Society of Chemistry), and c) P2-$Na_{3/5}[Li_{1/5}Mn_{4/5}]O_2$ (Reproduced from Ref. [188] with permission from The Royal Society of Chemistry).

1.4.2 Na-ion O-Redox Compounds

O-redox in Na-ion batteries is a fairly recent subject within the battery research field. Yabuuchi et al. initiated inquiry in 2014 with investigations of two compounds that documented "anomalous capacity" in $NaMO_2$ cathodes for the first time (P2-$Na_{5/6}[Li_{1/4}Mn_{3/4}]O_2$ and P2-$Na_{2/3}[Mg_{0.28}Mn_{0.72}]O_2$).[186, 187]. Both compounds showed a long plateau on charge (Figures 1.18a and b) and significant hysteresis, reminiscent of the Li-rich voltage curve.

In 2016, De la Llave et al. reported a new compound (P2-$Na_{0.6}[Li_{0.2}Mn_{0.8}]O_2$) with slightly less Na and Li but similar performance to the one reported by Yabucchi et al.[189] The authors established via DFT and experiments that O was oxidized in this compound, but presumed O-loss rather than O-redox. Interestingly, a P3-structured compound with the same composition was reported the same year and remarkably displayed a >4 V plateau on discharge with minimal hysteresis (Figure 1.18 c).[188] The authors ascribed this phenomenon to reversible O-redox, but with minimal supporting evidence.

It is very interesting, indeed, that the stacking sequence (P3 vs. P2) at this composition seemed to affect the voltage hysteresis and reversibility to such a great extent. By contrast, P3-$Na_{2/3}[Mg_{1/3}Mn_{2/3}]O_2$, reported in 2019, did not overcome the voltage hysteresis seen for P2-$Na_{2/3}[Mg_{0.28}Mn_{0.72}]O_2$.[190]

Rong et al. further characterized low hysteresis P3-$Na_{0.6}[Li_{0.2}Mn_{0.8}]O_2$ showing neutron PDF evidence of O-O "dimerization" with a bond distance of approximately 2.5 Å.[191] The authors attributed the structural stability of the compound to the P-type structure but did not venture to comment on why the P2-structured compound did not show the same low hysteresis. Very recently, a similarly minimal hysteresis was seen for the compound $Na_{4/7}[\square_{1/7}Mn_{6/7}]O_2$ ($\square$: TM vacancy).[192] The authors proposed that TM layer vacancies were an essential component to the low hysteresis.

The above reports on Na-ion O-redox compounds display several inconsistencies that warrant further investigation. Like the analogous Li-rich compounds, questions remain regarding the mechanism of hysteresis. Nonetheless, the present literature suggests that Na-ion compounds could provide vital insight toward achieving truly reversible O-redox (with low hysteresis) and pave a path to higher energy battery cathodes.

1.5 Thesis Objectives

The cost of batteries must be lowered and their performance improved if these devices are to satisfy the world's growing need for energy storage. Na-ion batteries represent a promising avenue for achieving these goals. Therefore, the investigation and analysis of this battery chemistry warrants significant effort. In particular, selecting a suitable cathode material remains a critical yet elusive task due to the strict requirements posed by today's applications (i.e. cheap, safe, high energy, high power, etc.).

The objectives of this thesis center on advancing the fundamental understanding of $NaMO_2$ cathode materials in order to provide a valid platform for their further development. However, it is worth noting the similarity between $NaMO_2$ and $LiMO_2$ compounds and consequently, the key learning points ascertained herein

may well find applications in Li-ion cathodes as well. The new inquiries presented in pursuit of the aforementioned goal will be divided among three results chapters (Chapters 3, 4, and 5) On a principal level, each of these chapters can be considered to include strategies to improve the energy density of $NaMO_2$ cathode materials while utilizing low-cost and abundant elements.

A more detailed outline of this thesis's objectives are as follows:

1. Investigating new P2-type $NaMO_2$ cathodes (Chapter 3)
    - Develop insight into the high voltage P2-$Na_{2/3}[Ni_{1/3}Mn_{2/3}]O_2$ cathode material, especially concerning its electrochemical performance, cation ordering phenomena, and structural changes.
    - Explore the ternary composition space of $Na_x[Ni_{(x-y)/2}Mn_{1-(x+y)/2}Fe_y]O_2$ ($x \geq 2/3$, $0 \leq y \leq 1$) to identify structural trends, phase stability boundaries, and specific candidate materials to achieve a high-performing Na-ion cathode.
    - Validate Fe as a redox-active component of P2-$Na_{2/3}[Ni_{1/6}Mn_{1/2}Fe_{1/3}]O_2$.
    - Overcome the issue of Na-deficiency in P2 compounds by a Na-naphthalide pre-treatment procedure.
2. High voltage structural evolution of P2-type compounds (Chapter 4)
    - Perform *operando* measurements to elucidate the structural evolution of P2-$NaMO_2$ compounds.
    - Develop a comprehensive model to better explain the structural changes seen for the so-called "Z"-phase when P2-$NaMO_2$ compounds are charged to high voltages (low Na contents).
3. Oxygen redox in layered oxides (Chapter 5)
    - Further the understanding of which specific structural and electronic properties of a compound facilitate the oxidation of oxygen within the stability limit of the electrolyte.

- Identify new ways to suppress oxygen gas loss in favor of solid state oxygen redox.
- Address the first-cycle hysteresis of oxygen redox compounds and develop novel methods for controlling this phenomenon.

1.6 References

(1) Whittingham, M. S. *Chemical Reviews* **2004**, *104*, 4271–4301.

(2) Whittingham, M. S. *Proceedings of the IEEE* **2012**, *100*, 1518–1534.

(3) Myung, S.-T.; Maglia, F.; Park, K.-J.; Yoon, C. S.; Lamp, P.; Kim, S.-J.; Sun, Y.-K. *ACS Energy Letters* **2017**, *2*, 196–223.

(4) Yang, Z.; Zhang, J.; Kintner-Meyer, M. C. W.; Lu, X.; Choi, D.; Lemmon, J. P.; Liu, J. *Chemical Reviews* **2011**, *111*, 3577–3613.

(5) Díaz-González, F.; Sumper, A.; Gomis-Bellmunt, O.; Villafáfila-Robles, R. *Renewable and Sustainable Energy Reviews* **2012**, *16*, 2154–2171.

(6) Armand, M.; Tarascon, J.-M. *Nature* **2008**, *451*, 652–657.

(7) Massé, R. C.; Liu, C.; Li, Y.; Mai, L.; Cao, G. *National Science Review* **2017**, *4*, 26–53.

(8) Delmas, C. *Advanced Energy Materials* **2018**, *8*, 1703137.

(9) Mauro, A. *Journal of the History of Medicine and Allied Sciences* **1969**, *24*, 140–150.

(10) Scrosati, B. *Journal of Solid State Electrochemistry* **2011**, *15*, 1623–1630.

(11) Wikipedia Voltaic Pile., 2018.

(12) Dell, R. M. *Solid State Ionics* **2000**, *134*, 139–158.

(13) Kurzweil, P. *Journal of Power Sources* **2010**, *195*, 4424–4434.

(14) Thackeray, M. M.; Wolverton, C.; Isaacs, E. D. *Energy and Environmental Science* **2012**, *5*, 7854–7863.

(15) Nitta, N.; Wu, F.; Lee, J. T.; Yushin, G. *Materials Today* **2015**, *18*, 252–264.

(16) Whittingham, M. S. *Science* **1976**, *192*, 1126–1127.

(17) Pereira, N.; Amatucci, G. G.; Whittingham, M. S.; Hamlen, R. *Journal of Power Sources* **2015**, *280*, 18–22.

(18) Winter, M.; Barnett, B.; Xu, K. *Chemical Reviews* **2018**, *118*, 11433–11456.

(19) Lazzari, M.; Scrosati, B. *Journal of The Electrochemical Society* **1980**, *127*, 773.

(20) Fouassier, C.; Delmas, C.; Hagenmuller, P. *Mat. Res. Bull.* **1975**, *10*, 443–450.

(21) Parant, J.-P.; Olazcuaga, R.; Devalette, M.; Fouassier, C.; Hagenmuller, P. *Journal of Solid State Chemistry* **1971**, *3*, 1–11.

(22) Delmas, C.; Fouassier, C.; Hagenmuller, P. *Materials Science and Engineering* **1977**, *31*, 297–301.

(23) Delmas, C.; Fouassier, C.; Hagenmuller, P. *Physica B+C* **1980**, *99*, 81–85.

(24) Mizushima, K.; Jones, P.; Wiseman, P.; Goodenough, J. *Solid State Ionics* **1981**, *3-4*, 171–174.

(25) Basu, S. Ambient temperature rechargeable battery., US Patent 4,423,125, 1983.

(26) Levy, S. C.; Cieslak, W. R. In *Conference: 9. annual battery conference on applications and advances*, United States, 1993.

(27) Goodenough, J. B. *ACS Catalysis* **2017**, *7*, 1132–1135.

(28) Yoshino, A.; Sanechika, K.; Nakajima, T. Secondary battery., US Patent 4,668,595, 1987.

(29) OZAWA, K. *Solid State Ionics* **1994**, *69*, 212–221.

(30) Huggins, R. A., *Advanced Batteries*; 5685; Springer US: Boston, MA, 2009; Vol. 276, pp 1–474.

(31) Yoon, W.-S.; Kim, K.-B.; Kim, M.-G.; Lee, M.-K.; Shin, H.-J.; Lee, J.-M.; Lee, J.-S.; Yo, C.-H. *The Journal of Physical Chemistry B* **2002**, *106*, 2526–2532.

(32) Billaud, J.; Singh, G.; Armstrong, A. R.; Gonzalo, E.; Roddatis, V.; Armand, M.; Rojo, T.; Bruce, P. G. *Energy Environ. Sci.* **2014**, *7*, 1387–1391.

(33) Sawicki, M.; Shaw, L. L. *RSC Adv.* **2015**, *5*, 53129–53154.

(34) Slater, M. D.; Kim, D.; Lee, E.; Johnson, C. S. *Advanced Functional Materials* **2013**, *23*, 947–958.

(35) Vaalma, C.; Buchholz, D.; Weil, M.; Passerini, S. *Nature Reviews Materials* **2018**, *3*, 18013.

(36) Hurlbutt, K.; Wheeler, S.; Capone, I.; Pasta, M. *Joule* **2018**, *2*, 1950–1960.

(37) Eftekhari, A.; Kim, D. W. *Journal of Power Sources* **2018**, *395*, 336–348.

(38) Bandhauer, T. M.; Garimella, S.; Fuller, T. F. *Journal of The Electrochemical Society* **2011**, *158*, R1–R25.

(39) Lu, L.; Han, X.; Li, J.; Hua, J.; Ouyang, M. *Journal of Power Sources* **2013**, *226*, 272–288.

(40) Barker, J. In *Fifth International Conference for Na-ion Batteries*, St. Malo, 2018.

(41) Yamada, A. *Electrochemistry* **2016**, *84*, 654–661.

(42) Shannon, R. D.; Prewitt, C. T. *Acta Crystallographica Section B Structural Crystallography and Crystal Chemistry* **1969**, *25*, 925–946.

(43) Kubota, K.; Yabuuchi, N.; Yoshida, H.; Dahbi, M.; Komaba, S. *MRS Bulletin* **2014**, *39*, 416–422.

(44) Komaba, S.; Takei, C.; Nakayama, T.; Ogata, A.; Yabuuchi, N. *Electrochemistry Communications* **2010**, *12*, 355–358.

(45) Han, M. H.; Gonzalo, E.; Casas-Cabanas, M.; Rojo, T. *Journal of Power Sources* **2014**, *258*, 266–271.

(46) Li, Y.; Lu, Y.; Zhao, C.; Hu, Y. S.; Titirici, M. M.; Li, H.; Huang, X.; Chen, L. *Energy Storage Materials* **2017**, *7*, 130–151.

(47) Kim, Y.; Ha, K. H.; Oh, S. M.; Lee, K. T. *Chemistry - A European Journal* **2014**, *20*, 11980–11992.

(48) Kim, D.; Lee, E.; Slater, M.; Lu, W.; Rood, S.; Johnson, C. S. *Electrochemistry Communications* **2012**, *18*, 66–69.

(49) Wang, L.; Song, J.; Qiao, R.; Wray, L. A.; Hossain, M. a.; Chuang, Y.-D.; Yang, W.; Lu, Y.; Evans, D.; Lee, J.-J.; Vail, S.; Zhao, X.; Nishijima, M.; Kakimoto, S.; Goodenough, J. B. *Journal of the American Chemical Society* **2015**, *137*, 2548–2554.

(50) Plashnitsa, L. S.; Kobayashi, E.; Noguchi, Y.; Okada, S.; Yamaki, J.-i. *Journal of The Electrochemical Society* **2010**, *157*, A536–A543.

(51) Li, X.; Wang, Y.; Wu, D.; Liu, L.; Bo, S. H.; Ceder, G. *Chemistry of Materials* **2016**, *28*, 6575–6583.

(52) Wang, P.-F.; You, Y.; Yin, Y.-X.; Guo, Y.-G. *Advanced Energy Materials* **2018**, *8*, 1701912.

(53) Han, M. H.; Gonzalo, E.; Singh, G.; Rojo, T. *Energy & Environmental Science* **2015**, *8*, 81–102.

(54) Kubota, K.; Komaba, S. *Journal of The Electrochemical Society* **2015**, *162*, A2538–A2550.

(55) Kubota, K.; Kumakura, S.; Yoda, Y.; Kuroki, K.; Komaba, S. *Advanced Energy Materials* **2018**, *8*, 1703415.

(56) Pauling, L. *Journal of the American Chemical Society* **1929**, *51*, 1010–1026.

(57) Katcho, N. A.; Carrasco, J.; Saurel, D.; Gonzalo, E.; Han, M.; Aguesse, F.; Rojo, T. *Advanced Energy Materials* **2016**, 1601477.

(58) Radin, M. D.; Van der Ven, A. *Chemistry of Materials* **2016**, *28*, 7898–7904.

(59) Lu, Z.; Dahn, J. R. *Journal of The Electrochemical Society* **2001**, *148*, A1225–A1229.

(60) Paulsen, J. M.; Dahn, J. R. *Solid State Ionics* **1999**, *126*, 3–24.

(61) Radin, M. D.; Alvarado, J.; Meng, Y. S.; Van Der Ven, A. *Nano Letters* **2017**, *17*, 7789–7795.

(62) Clément, R. J.; Bruce, P. G.; Grey, C. P. *Journal of The Electrochemical Society* **2015**, *162*, A2589–A2604.

(63) Radin, M. D.; Hy, S.; Sina, M.; Fang, C.; Liu, H.; Vinckeviciute, J.; Zhang, M.; Whittingham, M. S.; Meng, Y. S.; Van der Ven, A. *Advanced Energy Materials* **2017**, *7*, 1602888.

(64) Nanba, Y.; Iwao, T.; de Boisse, B. M.; Zhao, W.; Hosono, E.; Asakura, D.; Niwa, H.; Kiuchi, H.; Miyawaki, J.; Harada, Y.; Okubo, M.; Yamada, A. *Chemistry of Materials* **2016**, *28*, 1058–1065.

(65) Liu, C.; Neale, Z. G.; Cao, G. *Materials Today* **2016**, *19*, 109–123.

(66) Assadi, M. H. N.; Shigeta, Y. *Journal of Power Sources* **2018**, *388*, 1–4.

(67) Okubo, M.; Yamada, A. *ACS Applied Materials and Interfaces* **2017**, *9*, 36463–36472.

(68) Goodenough, J. B. *Chemistry of Materials* **2014**, *26*, 820–829.

(69) Samsonov, G. V. *Soviet Powder Metallurgy and Metal Ceramics* **1966**, *5*, 955–963.

(70) Talaie, E.; Duffort, V.; Smith, H. L.; Fultz, B.; Nazar, L. F. *Energy & Environmental Science* **2015**, *8*, 2512–2523.

(71) Wu, D.; Li, X.; Xu, B.; Twu, N.; Liu, L.; Ceder, G. *Energy & Environmental Science* **2015**, *8*, 195–202.

(72) Yoshida, H.; Yabuuchi, N.; Komaba, S. *Electrochemistry Communications* **2013**, *34*, 60–63.

(73) Guo, S.; Liu, P.; Sun, Y.; Zhu, K.; Yi, J.; Chen, M.; Ishida, M.; Zhou, H. *Angewandte Chemie International Edition* **2015**, *54*, 11701–11705.

(74) Yoshida, H.; Yabuuchi, N.; Kubota, K.; Ikeuchi, I.; Garsuch, A.; Schulz-Dobrick, M.; Komaba, S. *Chem. Commun.* **2014**, *50*, 3677–3680.

(75) Mortemard de Boisse, B.; Liu, G.; Ma, J.; Nishimura, S.-i.; Chung, S.-C.; Kiuchi, H.; Harada, Y.; Kikkawa, J.; Kobayashi, Y.; Okubo, M.; Yamada, A. *Nature Communications* **2016**, *7*, 11397.

(76) Wang, Z.; Wang, Z.; Peng, W.; Guo, H.; Li, X.; Wang, J.; Qi, A. *Ionics* **2014**, *20*, 1525–1534.

(77) Kondrakov, A. O.; Schmidt, A.; Xu, J.; Geßwein, H.; Mönig, R.; Hartmann, P.; Sommer, H.; Brezesinski, T.; Janek, J. *Journal of Physical Chemistry C* **2017**, *121*, 3286–3294.

(78) Chen, Z.; Dahn, J. *Electrochimica Acta* **2004**, *49*, 1079–1090.

(79) Zheng, L.; Obrovac, M. *Electrochimica Acta* **2017**, *233*, 284–291.

(80) Vetter, J.; Novák, P.; Wagner, M.; Veit, C.; Möller, K.-C.; Besenhard, J.; Winter, M.; Wohlfahrt-Mehrens, M.; Vogler, C.; Hammouche, A. *Journal of Power Sources* **2005**, *147*, 269–281.

(81) Yabuuchi, N.; Yoshida, H.; Komaba, S. *Electrochemistry* **2012**, *80*, 716–719.

(82) Lee, E.; Brown, D. E.; Alp, E. E.; Ren, Y.; Lu, J.; Woo, J.-J.; Johnson, C. S. *Chemistry of Materials* **2015**, *27*, 6755–6764.

(83) Yu, C.-Y.; Park, J.-S.; Jung, H.-G.; Chung, K.-Y.; Aurbach, D.; Sun, Y.-K.; Myung, S.-T. *Energy & Environmental Science* **2015**, *8*, 2019–2026.

(84) Alvarado, J.; Ma, C.; Wang, S.; Nguyen, K.; Kodur, M.; Meng, Y. S. *ACS Applied Materials and Interfaces* **2017**, *9*, 26518–26530.

(85) Xu, J.; Ma, C.; Balasubramanian, M.; Meng, Y. S. *Chemical communications* **2014**, *50*, 12564–7.

(86) Dang, R.; Chen, M.; Li, Q.; Wu, K.; Lee, Y. L.; Hu, Z.; Xiao, X. *ACS Applied Materials & Interfaces* **2019**, *11*, 856–864.

(87) Shao-Horn, Y.; Levasseur, S.; Weill, F.; Delmas, C. *Journal of The Electrochemical Society* **2003**, *150*, A366–A373.

(88) Toumar, A. J.; Ong, S. P.; Richards, W. D.; Dacek, S.; Ceder, G. *Physical Review Applied* **2015**, *4*, 1–9.

(89) Mo, Y.; Ong, S. P.; Ceder, G. *Chemistry of Materials* **2014**, *26*, 5208–5214.

(90) Wang, Y.; Xiao, R.; Hu, Y.-S.; Avdeev, M.; Chen, L. *Nature communications* **2015**, *6*, 6954.

(91) Vassilaras, P.; Kwon, D.-H.; Dacek, S. T.; Shi, T.; Seo, D.-H.; Ceder, G.; Kim, J. C. *Journal of Materials Chemistry A* **2017**, *5*, 4596–4606.

(92) Ceder, G.; Van der Ven, A. *Electrochimica Acta* **1999**, *45*, 131–150.

(93) Vassilaras, P.; Ma, X.; Li, X.; Ceder, G. *Journal of The Electrochemical Society* **2013**, *160*, A207–A211.

(94) Guignard, M.; Didier, C.; Darriet, J.; Bordet, P.; Elkaïm, E.; Delmas, C. *Nature materials* **2013**, *12*, 74–80.

(95) Berthelot, R.; Carlier, D.; Delmas, C. *Nature Materials* **2011**, *10*, 74–80.

(96) Huang, Q.; Foo, M. L.; Lynn, J. W.; Zandbergen, H. W.; Lawes, G.; Wang, Y.; Toby, B. H.; Ramirez, A. P.; Ong, N. P.; Cava, R. J. *Journal of Physics: Condensed Matter* **2004**, *16*, 5803–5814.

(97) Meng, Y. S.; Hinuma, Y.; Ceder, G. *The Journal of chemical physics* **2008**, *128*, 104708.

(98) Platova, T. A.; Mukhamedshin, I. R.; Alloul, H.; Dooglav, A. V.; Collin, G. *Physical Review B* **2009**, *80*, 224106.

(99) Li, X.; Ma, X.; Su, D.; Liu, L.; Chisnell, R.; Ong, S. P.; Chen, H.; Toumar, A.; Idrobo, J.-c.; Lei, Y.; Bai, J.; Wang, F.; Lynn, J. W.; Lee, Y. S.; Ceder, G. *Nature materials* **2014**, *13*, 586–92.

(100) Yabuuchi, N.; Ikeuchi, I.; Kubota, K.; Komaba, S. *ACS Applied Materials and Interfaces* **2016**, *8*, 32292–32299.

(101) Li, Y.; Gao, Y.; Wang, X.; Shen, X.; Kong, Q.; Yu, R.; Lu, G.; Wang, Z.; Chen, L. *Nano Energy* **2018**, *47*, 519–526.

(102) Lee, D. H.; Xu, J.; Meng, Y. S. *Physical chemistry chemical physics : PCCP* **2013**, *15*, 3304–12.

(103) Yabuuchi, N.; Komaba, S. *Science and Technology of Advanced Materials* **2014**, *15*, 043501.

(104) Vinckevičiûte, J.; Radin, M. D.; Van Der Ven, A. *Chemistry of Materials* **2016**, *28*, 8640–8650.

(105) Gutierrez, A.; Dose, W. M.; Borkiewicz, O.; Guo, F.; Avdeev, M.; Kim, S.; Fister, T. T.; Ren, Y.; Bareño, J.; Johnson, C. S. *Journal of Physical Chemistry C* **2018**, *122*, 23251–23260.

(106) Tapia-Ruiz, N.; Dose, W. M.; Sharma, N.; Chen, H.; Heath, J.; Somerville, J. W.; Maitra, U.; Islam, M. S.; Bruce, P. G. *Energy & Environmental Science* **2018**, *11*, 1470–1479.

(107) Yoshida, J.; Guerin, E.; Arnault, M.; Constantin, C.; Mortemard de Boisse, B.; Carlier, D.; Guignard, M.; Delmas, C. *Journal of the Electrochemical Society* **2014**, *161*, A1987–A1991.

(108) Ma, C.; Alvarado, J.; Xu, J.; Clément, R. J.; Kodur, M.; Tong, W.; Grey, C. P.; Meng, Y. S. *Journal of the American Chemical Society* **2017**, *139*, 4835–4845.

(109) Xu, J.; Lee, D. H.; Clément, R. J.; Yu, X.; Leskes, M.; Pell, A. J.; Pintacuda, G.; Yang, X.-Q.; Grey, C. P.; Meng, Y. S. *Chemistry of Materials* **2014**, *26*, 1260–1269.

(110) Zhao, W.; Kirie, H.; Tanaka, A.; Unno, M.; Yamamoto, S.; Noguchi, H. *Materials Letters* **2014**, *135*, 131–134.

(111) Yuan, D. D.; Wang, Y. X.; Cao, Y. L.; Ai, X. P.; Yang, H. X. *ACS Applied Materials & Interfaces* **2015**, *7*, 8585–8591.

(112) Singh, G.; Acebedo, B.; Cabanas, M. C.; Shanmukaraj, D.; Armand, M.; Rojo, T. *Electrochemistry Communications* **2013**, *37*, 61–63.

(113) Martinez De Ilarduya, J.; Otaegui, L.; López del Amo, J. M.; Armand, M.; Singh, G. *Journal of Power Sources* **2017**, *337*, 197–203.

(114) Zhang, B.; Dugas, R.; Rousse, G.; Rozier, P.; Abakumov, A. M.; Tarascon, J.-M. *Nature Communications* **2016**, *7*, 10308.

(115) Sathiya, M.; Thomas, J.; Batuk, D.; Pimenta, V.; Gopalan, R.; Tarascon, J.-M. *Chemistry of Materials* **2017**, *29*, 5948–5956.

(116) Grenier, A.; Liu, H.; Wiaderek, K. M.; Lebens-Higgins, Z. W.; Borkiewicz, O. J.; Piper, L. F. J.; Chupas, P. J.; Chapman, K. W. *Chemistry of Materials* **2017**, *29*, 7345–7352.

(117) Kumakura, S.; Tahara, Y.; Sato, S.; Kubota, K.; Komaba, S. *Chemistry of Materials* **2017**, *29*, 8958–8962.

(118) Amatucci, G. G.; Tarascon, J. M.; Klein, L. C. *Journal of The Electrochemical Society* **1996**, *143*, 1114–1123.

(119) Reimers, J. N.; Dahn, J. R. *Journal of the Electrochemical Society* **1992**, *139*, 2091–2097.

(120) Croguennec, L.; Pouillerie, C.; Delmas, C. *Journal of The Electrochemical Society* **2000**, *147*, 1314.

(121) Li, H.; Zhang, N.; Li, J.; Dahn, J. R. *Journal of The Electrochemical Society* **2018**, *165*, A2985–A2993.

(122) Ohzuku, T. *Journal of The Electrochemical Society* **1993**, *140*, 1862.

(123) Komaba, S.; Yabuuchi, N.; Nakayama, T.; Ogata, A.; Ishikawa, T.; Nakai, I. *Inorganic chemistry* **2012**, *51*, 6211–20.

(124) Mortemard de Boisse, B.; Carlier, D.; Guignard, M.; Bourgeois, L.; Delmas, C. *Inorganic chemistry* **2014**, *53*, 11197–205.

(125) Wang, K.; Yan, P.; Sui, M. *Nano Energy* **2018**, *54*, 148–155.

(126) Van der Ven, A.; Aydinol, M. K.; Ceder, G. *Journal of The Electrochemical Society* **1998**, *145*, 2149–2155.

(127) Blomgren, G. E. *Journal of The Electrochemical Society* **2017**, *164*, A5019–A5025.

(128) Reimers, J. N.; Dahn, J. R. *Journal of The Electrochemical Society* **1992**, *139*, 2091.

(129) Chen, Z.; Lu, Z.; Dahn, J. R. *Journal of The Electrochemical Society* **2002**, *149*, A1604–A1609.

(130) Croguennec, L.; Pouillerie, C.; Delmas, C. *Solid State Ionics* **2000**, *135*, 259–266.

(131) Kubota, K.; Ikeuchi, I.; Nakayama, T.; Takei, C.; Yabuuchi, N.; Shiiba, H.; Nakayama, M.; Komaba, S. *The Journal of Physical Chemistry C* **2015**, *119*, 166–175.

(132) Bo, S.-H.; Li, X.; Toumar, A. J.; Ceder, G. *Chemistry of Materials* **2016**, *28*, 1419–1429.

(133) Kubota, K.; Asari, T.; Yoshida, H.; Yaabuuchi, N.; Shiiba, H.; Nakayama, M.; Komaba, S. *Advanced Functional Materials* **2016**, *26*, 6047–6059.

(134) Mortemard De Boisse, B.; Cheng, J. H.; Carlier, D.; Guignard, M.; Pan, C. J.; Bordère, S.; Filimonov, D.; Drathen, C.; Suard, E.; Hwang, B. J.; Wattiaux, A.; Delmas, C. *Journal of Materials Chemistry A* **2015**, *3*, 10976–10989.

(135) Xie, Y.; Wang, H.; Xu, G.; Wang, J.; Sheng, H.; Chen, Z.; Ren, Y.; Sun, C.-J.; Wen, J.; Wang, J.; Miller, D. J.; Lu, J.; Amine, K.; Ma, Z.-F. *Advanced Energy Materials* **2016**, 1601306.

(136) Wang, L.; Wang, J.; Zhang, X.; Ren, Y.; Zuo, P.; Yin, G.; Wang, J. *Nano Energy* **2017**, *34*, 215–223.

(137) Kim, S.; Ma, X.; Ong, S. P.; Ceder, G. *Physical Chemistry Chemical Physics* **2012**, *14*, 15571–15578.

(138) Kondrakov, A. O.; Geßwein, H.; Galdina, K.; De Biasi, L.; Meded, V.; Filatova, E. O.; Schumacher, G.; Wenzel, W.; Hartmann, P.; Brezesinski, T.; Janek, J. *Journal of Physical Chemistry C* **2017**, *121*, 24381–24388.

(139) Mortemard de Boisse, B.; Cheng, J.-H.; Carlier, D.; Guignard, M.; Pan, C.-J.; Bordère, S.; Filimonov, D.; Drathen, C.; Suard, E.; Hwang, B.-J.; Wattiaux, a.; Delmas, C. *J. Mater. Chem. A* **2015**, 10976–10989.

(140) Pang, W. K.; Kalluri, S.; Peterson, V. K.; Sharma, N.; Kimpton, J.; Johannessen, B.; Liu, H. K.; Dou, S. X.; Guo, Z. *Chemistry of Materials* **2015**, *27*, 3150–3158.

(141) Mortemard de Boisse, B.; Carlier, D.; Guignard, M.; Delmas, C. *Journal of the Electrochemical Society* **2013**, *160*, A569–A574.

(142) Yabuuchi, N.; Kajiyama, M.; Iwatate, J.; Nishikawa, H.; Hitomi, S.; Okuyama, R.; Usui, R.; Yamada, Y.; Komaba, S. *Nature Materials* **2012**, *11*, 512–517.

(143) Talaie, E.; Kim, S. Y.; Chen, N.; Nazar, L. F. *Chemistry of Materials* **2017**, *29*, 6684–6697.

(144) Kubota, K.; Yoda, Y.; Komaba, S. *Journal of The Electrochemical Society* **2017**, *164*, A2368–A2373.

(145) Luo, K.; Roberts, M. R.; Hao, R.; Guerrini, N.; Pickup, D. M.; Liu, Y.-S.; Edström, K.; Guo, J.; Chadwick, A. V.; Duda, L. C.; Bruce, P. G. *Nature Chemistry* **2016**, *8*, 684–691.

(146) Numata, K.; Sakaki, C.; Yamanaka, S. *Chemistry Letters* **1997**, *26*, 725–726.

(147) Ammundsen, B.; Paulsen, J.; Davidson, I.; Liu, R.-S.; Shen, C.-H.; Chen, J.-M.; Jang, L.-Y.; Lee, J.-F. *Journal of The Electrochemical Society* **2002**, *149*, A431.

(148) Lu, Z.; MacNeil, D. D.; Dahn, J. R. *Electrochemical and Solid-State Letters* **2001**, *4*, A191–A194.

(149) Lu, Z.; Dahn, J. R. *Journal of The Electrochemical Society* **2002**, *149*, A815–A822.

(150) Armstrong, R.; Holzapfel, M.; Novák, P.; Johnson, C. S.; Kang, S. H.; Thackeray, M. M.; Bruce, P. G. *Journal of the American Chemical Society* **2006**, *128*, 8694–8698.

(151) Robertson, A. D.; Bruce, P. G. *Chemistry of Materials* **2003**, *15*, 1984–1992.

(152) Robertson, A. D.; Bruce, P. G. *Electrochemical and Solid-State Letters* **2004**, *7*, A294–A298.

(153) Tran, N.; Croguennec, L.; Me, M.; Weill, F.; Jordy, C.; Delmas, C. *Chem. Mater.* **2008**, *20*, 4815–4825.

(154) Grey, C. P.; Yoon, W.-S.; Reed, J.; Ceder, G. *Electrochemical and Solid-State Letters* **2004**, *7*, A290–A293.

(155) Hong, Y.-S.; Park, Y. J.; Wu, X.; Ryu, K. S.; Chang, S. H. *Electrochemical and Solid-State Letters* **2003**, *6*, A166.

(156) Ito, A.; Sato, Y.; Sanada, T.; Hatano, M.; Horie, H.; Ohsawa, Y. *Journal of Power Sources* **2011**, *196*, 6828–6834.

(157) Yabuuchi, N.; Yoshii, K.; Myung, S.-T.; Nakai, I.; Komaba, S. *Journal of the American Chemical Society* **2011**, *133*, 4404–4419.

(158) Hong, J.; Lim, H. D.; Lee, M.; Kim, S. W.; Kim, H.; Oh, S. T.; Chung, G. C.; Kang, K. *Chemistry of Materials* **2012**, *24*, 2692–2697.

(159) McCalla, E.; Sougrati, M. T.; Rousse, G.; Berg, E. J.; Abakumov, A.; Recham, N.; Ramesha, K.; Sathiya, M.; Dominko, R.; Van Tendeloo, G.; Novák, P.; Tarascon, J.-M. *Journal of the American Chemical Society* **2015**, *137*, 4804–4814.

(160) Koga, H.; Croguennec, L.; Ménétrier, M.; Mannessiez, P.; Weill, F.; Delmas, C. *Journal of Power Sources* **2013**, *236*, 250–258.

(161) Koga, H.; Croguennec, L.; Ménétrier, M.; Douhil, K.; Belin, S.; Bourgeois, L.; Suard, E.; Weill, F.; Delmas, C. *Journal of The Electrochemical Society* **2013**, *160*, A786–A792.

(162) Oishi, M.; Yogi, C.; Watanabe, I.; Ohta, T.; Orikasa, Y.; Uchimoto, Y.; Ogumi, Z. *Journal of Power Sources* **2015**, *276*, 89–94.

(163) Luo, K.; Roberts, M. R.; Guerrini, N.; Tapia-Ruiz, N.; Hao, R.; Massel, F.; Pickup, D. M.; Ramos, S.; Liu, Y. S.; Guo, J.; Chadwick, A. V.; Duda, L. C.; Bruce, P. G. *Journal of the American Chemical Society* **2016**, *138*, 11211–11218.

(164) Strehle, B.; Kleiner, K.; Jung, R.; Chesneau, F.; Mendez, M.; Gasteiger, H. A.; Piana, M. *Journal of The Electrochemical Society* **2017**, *164*, A400–A406.

(165) Seo, D.-H.; Lee, J.; Urban, A.; Malik, R.; Kang, S.; Ceder, G. *Nature Chemistry* **2016**, *8*, 692–697.

(166) Croy, J. R.; Balasubramanian, M.; Gallagher, K. G.; Burrell, A. K. *Accounts of Chemical Research* **2015**, *48*, 2813–2821.

(167) Bettge, M.; Li, Y.; Gallagher, K.; Zhu, Y.; Wu, Q.; Lu, W.; Bloom, I.; Abraham, D. P. *Journal of the Electrochemical Society* **2013**, *160*, A2046–A2055.

(168) Croy, J. R.; Gallagher, K. G.; Balasubramanian, M.; Long, B. R.; Thackeray, M. M. *Journal of the Electrochemical Society* **2013**, *161*, A318–A325.

(169) Gallagher, K. G.; Croy, J. R.; Balasubramanian, M.; Bettge, M.; Abraham, D. P.; Burrell, A. K.; Thackeray, M. M. *Electrochemistry Communications* **2013**, *33*, 96–98.

(170) Mohanty, D.; Li, J.; Abraham, D. P.; Huq, A.; Payzant, E. A.; Wood, D. L.; Daniel, C. *Chemistry of Materials* **2014**, *26*, 6272–6280.

(171) Kleiner, K.; Strehle, B.; Baker, A. R.; Day, S. J.; Tang, C. C.; Buchberger, I.; Chesneau, F. F.; Gasteiger, H. A.; Piana, M. *Chemistry of Materials* **2018**, *30*, 3656–3667.

(172) Sathiya, M.; Abakumov, A. M.; Foix, D.; Rousse, G.; Ramesha, K.; Saubanère, M.; Doublet, M. L.; Vezin, H.; Laisa, C. P.; Prakash, a. S.; Gonbeau, D.; VanTendeloo, G.; Tarascon, J.-M. *Nature materials* **2015**, *14*, 230–8.

(173) Saubanere, M.; McCalla, E.; Tarascon, J.-M.; Doublet, M.-L. *Energy & Environmental Science* **2016**, 984–991.

(174) Xie, Y.; Saubanère, M.; Doublet, M.-L. *Energy & Environmental Science* **2017**, *10*, 266–274.

(175) Gent, W. E.; Lim, K.; Liang, Y.; Li, Q.; Barnes, T.; Ahn, S.-J.; Stone, K. H.; McIntire, M.; Hong, J.; Song, J. H.; Li, Y.; Mehta, A.; Ermon, S.; Tyliszczak, T.; Kilcoyne, D.; Vine, D.; Park, J.-H.; Doo, S.-K.; Toney, M. F.; Yang, W.; Prendergast, D.; Chueh, W. C. *Nature Communications* **2017**, *8*, 2091.

(176) Xu, J.; Sun, M.; Qiao, R.; Renfrew, S. E.; Ma, L.; Wu, T.; Hwang, S.; Nordlund, D.; Su, D.; Amine, K.; Lu, J.; McCloskey, B. D.; Yang, W.; Tong, W. *Nature Communications* **2018**, *9*, 947.

(177) Wu, J.; Li, Q.; Sallis, S.; Zhuo, Z.; Gent, W.; Chueh, W.; Yan, S.; Chuang, Y.-d.; Yang, W. *Condensed Matter* **2019**, *4*, 5.

(178) Zhuo, Z.; Pemmaraju, C. D.; Vinson, J.; Jia, C.; Moritz, B.; Lee, I.; Sallies, S.; Li, Q.; Wu, J.; Dai, K.; Chuang, Y. D.; Hussain, Z.; Pan, F.; Devereaux, T. P.; Yang, W. *Journal of Physical Chemistry Letters* **2018**, *9*, 6378–6384.

(179) Dai, K.; Wu, J.; Zhuo, Z.; Li, Q.; Sallis, S.; Mao, J.; Ai, G.; Sun, C.; Li, Z.; Gent, W. E.; Chueh, W. C.; Chuang, Y.-d.; Zeng, R.; Shen, Z.-x.; Pan, F.; Yan, S.; Piper, L. F.; Hussain, Z.; Liu, G.; Yang, W. *Joule*, (in press).

(180) Assat, G.; Iadecola, A.; Foix, D.; Dedryvere, R.; Tarascon, J. M. *ACS Energy Letters* **2018**, *3*, 2721–2728.

(181) Li, X.; Qiao, Y.; Guo, S.; Xu, Z.; Zhu, H.; Zhang, X.; Yuan, Y.; He, P.; Ishida, M.; Zhou, H. *Advanced Materials* **2018**, *30*, 2–7.

(182) Takahashi, I.; Fukuda, K.; Kawaguchi, T.; Komatsu, H.; Oishi, M.; Murayama, H.; Hatano, M.; Terai, T.; Arai, H.; Uchimoto, Y.; Matsubara, E. *Journal of Physical Chemistry C* **2016**, *120*, 27109–27116.

(183) Teufl, T.; Strehle, B.; Müller, P.; Gasteiger, H. A.; Mendez, M. A. *Journal of The Electrochemical Society* **2018**, *165*, A2718–A2731.

(184) Yan, P.; Xiao, L.; Zheng, J.; Zhou, Y.; He, Y.; Zu, X.; Mao, S. X.; Xiao, J.; Gao, F.; Zhang, J. G.; Wang, C. M. *Chemistry of Materials* **2015**, *27*, 975–982.

(185) Qiu, B.; Zhang, M.; Wu, L.; Wang, J.; Xia, Y.; Qian, D.; Liu, H.; Hy, S.; Chen, Y.; An, K.; Zhu, Y.; Liu, Z.; Meng, Y. S. *Nature Communications* **2016**, *7*, 12108.

(186) Yabuuchi, N.; Hara, R.; Kajiyama, M.; Kubota, K.; Ishigaki, T.; Hoshikawa, A.; Komaba, S. *Advanced Energy Materials* **2014**, *4*, 1301453.

(187) Yabuuchi, N.; Hara, R.; Kubota, K.; Paulsen, J.; Kumakura, S.; Komaba, S. *J. Mater. Chem. A* **2014**, *2*, 16851–16855.

(188) Du, K.; Zhu, J.; Hu, G.; Gao, H.; Li, Y.; Goodenough, J. B. *Energy and Environmental Science* **2016**, *9*, 2575–2577.

(189) De la Llave, E.; Talaie, E.; Levi, E.; Nayak, P. K.; Dixit, M.; Rao, P. T.; Hartmann, P.; Chesneau, F.; Major, D. T.; Greenstein, M.; Aurbach, D.; Nazar, L. F. *Chemistry of Materials* **2016**, *28*, 9064–9076.

(190) Song, B.; Hu, E.; Liu, J.; Zhang, Y.; Yang, X.-Q.; Nanda, J.; Huq, A.; Page, K. *Journal of Materials Chemistry A* **2019**, *7*, 1491–1498.

(191) Rong, X.; Liu, J.; Hu, E.; Liu, Y.; Wang, Y.; Wu, J.; Yu, X.; Page, K.; Hu, Y. S.; Yang, W.; Li, H.; Yang, X. Q.; Chen, L.; Huang, X. *Joule* **2018**, *2*, 125–140.

(192) Mortemard de Boisse, B.; Nishimura, S.-i.; Watanabe, E.; Lander, L.; Tsuchimoto, A.; Kikkawa, J.; Kobayashi, E.; Asakura, D.; Okubo, M.; Yamada, A. *Advanced Energy Materials* **2018**, *8*, 1800409.

2 Methods

Contents

2.1 Materials Synthesis and Initial Characterization

2.1.1 Solid State Synthesis

Solid state synthesis represents a relatively uncomplicated method for making mixed metal oxide systems. It involves obtaining the pertinent precursor materials, mixing those precursors to an acceptable level, and then heating the mixture to high temperatures to induce thermal decomposition and diffusion. This method is commonly used for making Li-ion and Na-ion cathode materials.

Precursors

To synthesize the compounds analyzed in this thesis, Na_2CO_3 and/or Li_2CO_3 was mixed with the appropriate transition metal oxides (e.g. MnO_2, Mn_2O_3, Fe_2O_3, NiO, MgO). Other sodium and lithium sources (e.g. NaOH) are better options for use as precursors when lower temperature structures are targeted.

Mixing and Heating

Mixing the precursors is either carried out by hand with a mortar and pestle or by using a ball mill. Subsequently, the powder is typically pressed into pellets using a die set and hydraulic press under several metric tons of pressure. These steps serve to increase surface area and shorten the diffusion lengths between the precursor particles, which increases the speed of the chemical reaction.[1] The pellets are then placed in a furnace and temperatures high enough to ensure the reactions are no longer diffusion limited.[1] The exact temperature selected is optimized in order to obtain a desired structure with a high degree of crystallinity and no impurity phases.

Choice of Atmosphere

Like temperature, the atmosphere in which the solid-state reaction takes place can have a significant impact on the synthesis outcome, particularly for tuning the TM oxidation states. In terms of metal oxides, this is due to the oxygen partial pressure and can be rationalized by the following equation:

$$\mathrm{TM}_x\mathrm{O}_y(s) \leftrightarrow \mathrm{TM}_x\mathrm{O}_{y-z}(s) + \frac{z}{2}\mathrm{O}_2(g) \tag{2.1}$$

As such, high oxygen partial pressures will maintain higher oxidation states for the TMs because it shifts the equilibrium of Equation 2.1 to the left.[1] By contrast, an Ar atmosphere during heating, despite being inert, can reduce the TM oxides at high temperatures due to the entropy gain of evolving O_2 gas, thus shifting the equilibrium of Equation 2.1 to the right.

2.1.2 Resorcinal Formaldehyde-Gel Synthesis

Another synthetic process for producing Na or Li TMO_2 compounds is the resorcinal formaldehyde-gel (RF-gel) synthesis. This method has proven to be successful in generating high performing cathode materials.[2] Precursors of the desired metals (typically metal acetates: $M[CH_3COO]_y$ $y \geq 1$) are first dissolved in an aqueous media before being combined with a solution of equal parts resorcinol ($C_6H_{12}O_2$) and formaldehyde (CH_2O). When subsequently heated to approximately 80 °C, the resorcinol formaldehyde solution polymerizes, trapping the metal ions in an atomically dispersed solution throughout the polymer.[2, 3] The gel is dried and then heated to 500 °C to decompose the organic component of the gel and isolate an intimately mixed powder containing the metal ions. A final heating step is then performed to produce a compound of the desired crystal structure (typically at approximately 900 °C although the exact value is variable for different compounds to best optimize the structure).

2.1.3 Inductively Coupled Plasma

An inductively coupled plasma (ICP) is a specific type of plasma that is maintained via induction from a high-frequency magnetic field.[4] This type of plasma can be incorporated with a spectrometer to create an instrument that is able to identify the composition of an unknown compound to a very high degree of accuracy.

The compound of interest is first dissolved, or *digested*, into a liquid matrix (usually 2% HNO_3). It is then diluted so the concentrations of each constituent

can be interpolated from available standard solutions with known molarity.[5] The diluted solution is then fed into an ICP instrument that uses plasma to convert the liquid solution into free ions.

There are two main types of ICP instruments that use different methods of detection for differentiating and quantifying the free ions. The first, optical emission spectrometry (OES), utilizes the characteristic light (in the visible spectrum) that is emitted from an atom as its electrons decay from an excited state to a ground state.[5] The second method, mass spectrometry (MS), uses a quadrupole to separate the ions based on their mass to charge ratio (m/z).[6] ICP-MS therefore has the advantage of isotope differentiation.[6] ICP-OES was used in the analysis of compounds in this thesis.

2.1.4 Scanning Electron Microscopy

Scanning electron microscopy (SEM) is a powerful tool for characterizing the morphology of a material. This technique makes use of the low wavelength of high energy electrons ($\lambda \approx 0.1$ Å for energies of ~10 keV) to perform high resolution imaging superior to that of optical microscopy.

In SEM, free electrons originating from a source material, emitted either by heating the material to high temperatures (i.e. thermionic emission) or by the use of an electric field (i.e. field emission), act as an "electron gun".[7] The electrons are then accelerated through a sequence of condenser lenses forming a beam which can be rastered over an area of interest in the sample.[7] When the electron beam interacts with the sample, secondary electrons, auger electrons, back-scattered electrons, and X-rays are produced which can all be captured for analysis.[7] The most common detection mode for imaging utilizes the secondary electrons because these allow for the highest spacial resolution.[7]

SEM is often used in battery research to characterize the particle size and distribution as well as the shape of the electrode materials.

2.2 Electrochemical Methods

Electrochemical testing is key to developing a good understanding of an electrode material and how it performs in a battery as this is predominantly the intended utility. However, it also provides an important method of synthesizing metastable compounds through the controlled (de-)intercalation Na^+ or Li^+, which cannot be created via other methods.[8] This section provides an overview of the electrochemical methods used in this thesis.

2.2.1 Electrode Preparation

On their own, electrode materials rarely perform well in an electrochemical cell. This is because most electrode materials (especially layered oxides) are semi-conductors meaning they do not conduct electrons well. In order to avoid a large internal resistance caused by this lack of conductivity, composite electrodes are usually prepared by creating a mixture of active, conductive, and binder materials.[9] The most common conductive additive is carbon black and common binder materials include the polymers: polyvinylidene difluoride (PVDF) and polytetrafluoroethylene (PTFE). Any added materials should be electrochemically inert within the voltage range required. The ratios of each component vary depending on the material (active: conductive: binder ratio of 75:15:10 or 80:10:10 were used in the experiments presented in this thesis).

Preparing Casted Electrode Laminates

The electrode composites utilized in the experiments presented in Chapters 3 and 4 were prepared via the casting method. This involves the initial creation of a PVDF solution in the solvent N-methyl-2-pyrrolidone (NMP) (~ 6% by mass).[10] This binder solution is then added to the active material and conductive additive and mixed thoroughly — usually by ball milling. Once a homogeneous ink is created, it is then coated directly onto the current collector (e.g. Al metal) using a specialized doctor blade or rolling pin. The coated foil is then dried at approximately 80 °C to evaporate the NMP solvent while leaving the composite electrode adhered

to the current collector. Once completed, discs are punched from this electrode laminate for use in electrochemical testing. Casting is the preferred method for commercial electrode production as it can be executed in a highly automated roll-to-roll processing line.

Preparing Free-Standing Electrodes Films

Free-standing electrode films were prepared for the experiments presented in Chapter 5. These are created by mixing the active material, conductive additive, and PTFE binder with a mortar and pestle until agglomeration occurs. The agglomerated mixture is then folded over on itself several times and further mixed to improve homogeneity. Finally, a manual rolling press is used to reduce the thickness of the electrode composite to $\approx$100 μm. The free-standing composites are then cut to an appropriate size and used for electrochemical testing.

2.2.2 Electrolyte Preparation

While the Li-ion research field is now quite established and high-quality electrolytes can be purchased directly from suppliers (e.g. BASF), the Na-ion electrolytes used in the experiments presented in this thesis were largely prepared in-house. $NaPF_6$ was used as an electrolyte salt (to make the electrolyte solution ionically conducting) and a blend of ethylene carbonate (EC), propylene carbonate (PC), and/or diethyl carbonate (DEC) was used as a solvent. A non-aqueous, carbonate-based solvent was chosen over a water-based solvent to stabilize the electrolyte over a greater voltage range. The electrolytes were prepared by adding approximately 10 mL of solvent to the salt to create a 1 M solution. This process was carried out entirely within an Ar-glovebox so as to avoid even trace levels of H_2O in the electrolyte. The solution was then stirred for several hours and subsequently filtered to remove any undissolved particulates (e.g. NaF impurity). Dried molecular sieves were then added to the electrolyte solution to maintain a high degree of dryness and avoid undesired de-fluorination of the $NaPF_6$ salt.

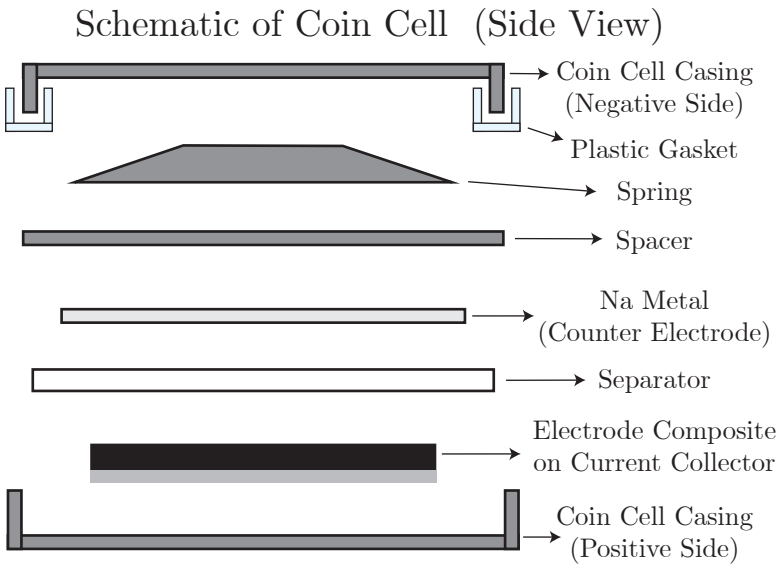

Figure 2.1: A schematic representation of a typical Na-ion coin cell is shown with the parts labeled to the right.

2.2.3 Coin Cell Assembly

Coin cells are the most conventional architecture for testing battery materials in a laboratory setting. They come in various sizes which are normally documented by four numbers to indicate the diameter and thickness (e.g. 2032: 20 mm diameter, 3.2 mm thickness). A schematic of the various components is shown in Figure 2.1. Coin cells are usually assembled by placing the positive (larger) coin cell casing on the work surface and then carefully stacking the parts in order. For the counter/reference electrode, a thin Na metal foil is typically prepared by compressing a small Na metal chunk with a hydraulic press and then punching a small disk for use. During the cell assembly process, the electrolyte is directly added to the separator drop wise until saturation. Once all parts are stacked, the cell is hermetically sealed by a coin cell crimping machine and is ready for testing.

2.2.4 Galvanostatic Cycling

Galvanostatic cycling or constant-current cycling is one of the most common electrochemical measurements performed on battery materials and was used often in this thesis to assess a material's performance. Testing is carried out in a battery

cycling machine (MACCOR or Bio-Logic) with the current rate normalized to the mass of active material and the voltage under constant monitoring. When the voltage of the battery reaches a pre-defined upper voltage cutoff on charge (typically 4.5 V), the current is reversed and the cell is discharged until a pre-defined lower voltage cutoff is reached (typically 1.5 V). This process is typically repeated over many cycles. The two main parameters recorded for a cell during cycling are 1) experiment time and 2) voltage (monitored as a function of time). The specific capacity (q) is determined by taking the product of the time (t) and current (i) and normalizing by the active mass (m) as follows:

$$q = \frac{i\Delta t}{m} \tag{2.2}$$

The specific energy (W) can then be calculated as the integral of the voltage (E) with respect to the specific capacity:

$$W = \int E \; dq \tag{2.3}$$

As discussed in section 1.1.2 of the introduction, galvanostatic cycling is typically plotted as an electrochemical load curve with capacity on the x-axis and voltage on the y-axis. Alternatively, taking the derivative of capacity with respect to voltage ($dq \; dE^{-1}$) is often useful for identifying subtle changes in the slope of the load curve. These features can be related to the phase transformations of an electrode material by Gibb's phase rule:

$$F = C - P + 2 \tag{2.4}$$

where F is the number of thermodynamic intensive variables that are needed to define the system (i.e. degrees of freedom, e.g. pressure, temperature, voltage), C is the number of components present, and P is the number of phases present.[11] An intercalation electrode is generally defined as a two component system ($C = 2$, TMO_2 host + guest species). Thus when the electrode enters a biphasic (two-phase, $P = 2$) domain, then $F = 2 - 2 + 2 = 2$. In this case, assuming temperature and pressure are held constant, the system is adequately defined and no other

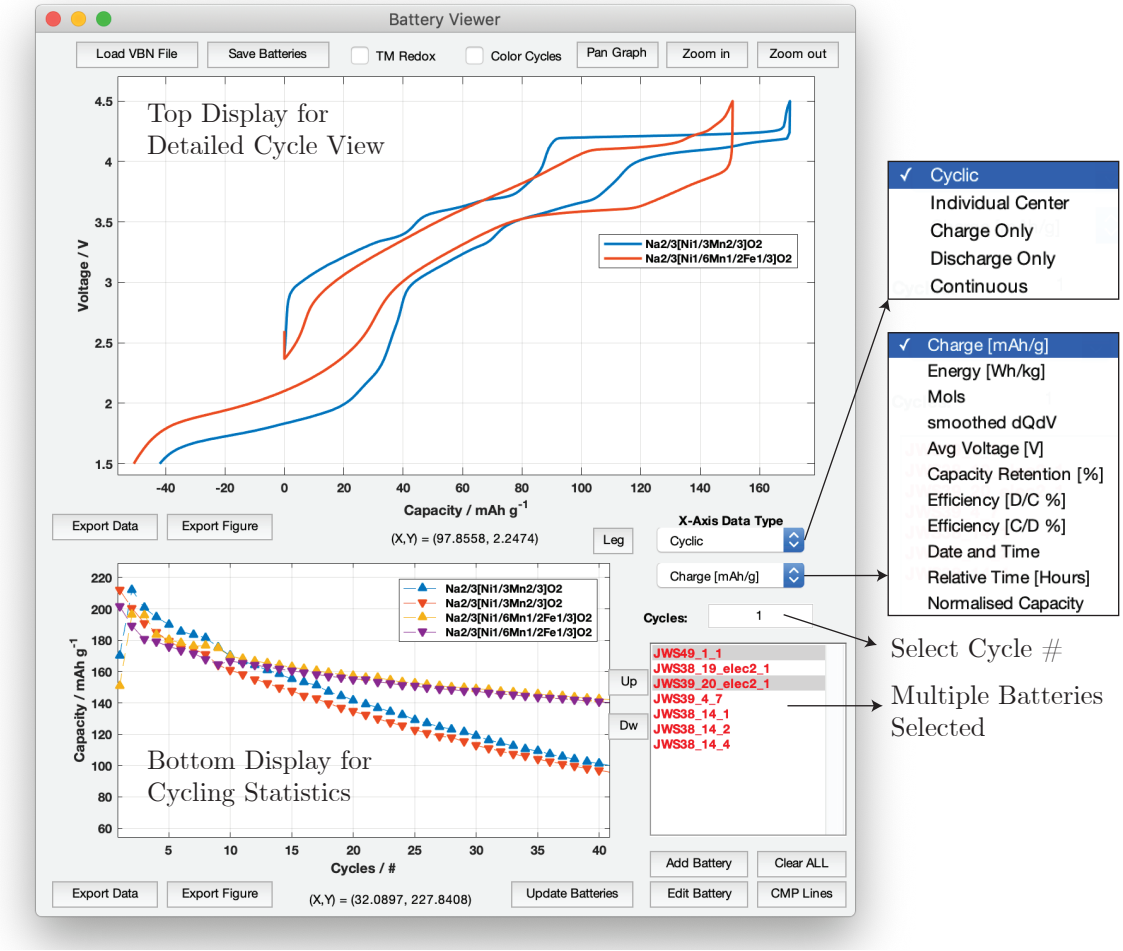

Figure 2.2: The graphical user interface of the Battery Viewer program is shown. This application allows for detailed data inspection of each cycle (top display) or relevant statistics plotted as a function of cycle number (bottom display).

intensive variable (e.g. voltage) can vary. As such, the phenomenon of a biphasic reaction will manifest itself as a voltage plateau in the electrochemical load curve. On the other hand, if the electrode is in a single phase regime, then $F = 3$ and with temperature and pressure remaining constant, the voltage can vary, producing a sloped electrochemical load curve.

2.2.5 Data Analysis with MATLAB

To provide fast, comprehensive data analysis for galvanostatic cycling, a software application was created in MATLAB named Battery Viewer. Figure 2.2 illustrates the graphical user interface of the software as well as some of its capabilities. The

program was designed to process data output from both MACCOR and EC-LAB battery cyclers as well as enable direct comparison of multiple batteries at once.

2.2.6 Online Electrochemical Mass Spectrometry

Online electrochemical mass spectrometry (OEMS) is a useful method for identifying and quantifying the gaseous products of an electrochemical reaction. It was used in this thesis to probe specifically for the evolution of O_2 gas in an O-redox $NaMO_2$ cathode, which is presented in Chapter 5. The technique works by coupling a custom-made electrochemical cell (with a gas inlet and outlet port) to a mass spectrometer via sealed tubing. Inert gas (e.g. Ar) is then flowed through the cell at a controlled rate. This in turn flows any evolved gases out of the cell and toward the MS where the molecules are ionized. The ionized molecules are differentiated by the MS based on their mass to charge ratio (m/z) and can be accurately quantified as a function of experimental time. Thus, the technique is able to directly correlate gas evolution with particular stages of the electrochemical cycle.

2.2.7 *Ex Situ* Sample Preparation

Ex situ sample preparation refers to the process of removing a battery electrode of interest after it has undergone an electrochemical testing protocol. This method was most often used in this thesis to probe the electrode material at various states of charge over the first electrochemical cycle. In general, coin cells were used to charge/discharge the material to the desired state. As soon as the testing protocol was finished, the coin cells were quickly transported into an inert Ar glovebox. Once there, the cells were carefully disassembled, making sure to avoid short circuits, and the electrode material was removed. Subsequently, the electrode material was washed vigorously with dimethyl carbonate (DMC) to remove any salt adhered to the surface. Finally, the washed electrode material was dried under vacuum to remove the DMC and carefully packaged for further characterization.

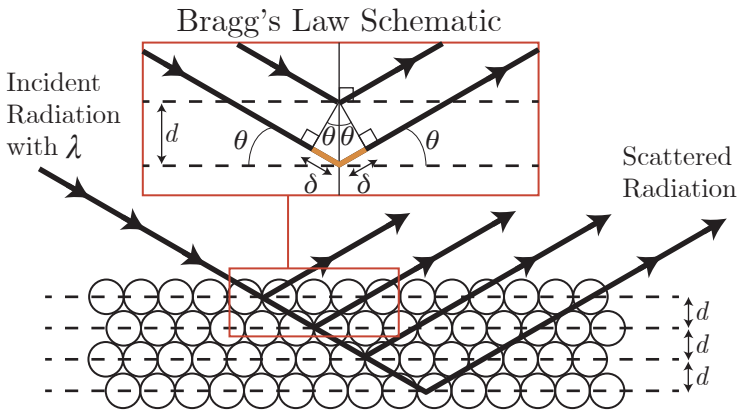

Figure 2.3: A schematic depicting the variables involved in Bragg's Law (Equation 2.7) is shown. The difference in path length between subsequent atomic planes is highlighted in orange.

2.3 X-ray and Neutron Scattering

2.3.1 A Brief Introduction to Diffraction

Diffraction is one of the most frequently used and arguably best technique for characterizing a compound's crystal structure. The technique itself harnesses the physical principle that waves of the correct wavelength impinging on an ordered collection of atoms (i.e. a crystal structure) will constructively and destructively interfere to create an interference pattern. A simple relationship for this interference pattern was discovered by Bragg in 1912. He recognized that constructive interference can only occur if the difference in the path length (2δ) between two waves interacting with successive planes of atoms is equal to an integer multiple (n) of the wavelength (λ).[12] A schematic of this principle is shown in Figure 2.3. As is evident in the schematic, the difference in path length (2δ, highlighted in orange) is related to the spacing (d) of the atomic layers by an angle (θ). As such, Bragg's Law[13] can be derived as follows:

$$n\lambda = 2\delta \tag{2.5}$$

$$\delta = d\sin(\theta) \tag{2.6}$$

$$n\lambda = 2d\sin(\theta) \quad \text{(Bragg's Law)} \tag{2.7}$$

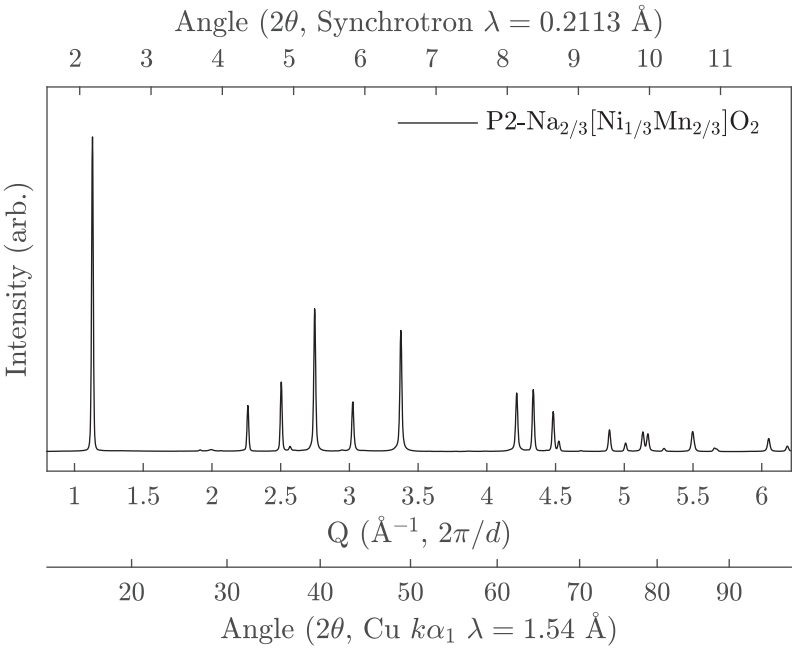

Figure 2.4: A synchrotron XRD pattern for P2-$Na_{2/3}[Ni_{1/3}Mn_{2/3}]O_2$ is plotted as a function of Q ($Å^{-1}$) and Angle (2θ, for two different wavelengths λ) for comparison. It can be noticed from the graph that these units are not linearly related to one another.

Bragg's Law applies to X-rays, neutrons, and electrons as each can behave as both a particle and a wave. In a typical diffraction experiment, the intensity of the diffracted beam is recorded as a function of angle 2θ (for reasons related to the experimental geometry). In this thesis, the magnitude of the scattering vector Q is used instead of 2θ. Q is defined by Equation 2.8 [14] and represents a wavelength independent unit of measurement (i.e. better for comparing data originating from different sources, e.g. synchrotron XRD, laboratory XRD, and neutron diffraction).

$$Q = \frac{4\pi \sin(\theta)}{\lambda} = \frac{2\pi}{d} \tag{2.8}$$

Figure 2.4 compares a synchrotron XRD pattern plotted in terms of Q with the corresponding 2θ values of Cu $k\alpha_1$ ($\lambda = 1.54$ Å) and synchrotron radiation ($\lambda = 0.2113$ Å).

It is important to note that Bragg's Law can sometimes predict reflections at an angle θ which do not occur in practice, leading to a so-called "forbidden" reflection. This is because the intensity of the diffracted radiation relates to the

type of crystal structure present as well as the identity of the atoms that compose it. A specific atomic plane can be defined by its normal vector (using the unit cell basis) with a magnitude that is inversely proportional to the spacing of the planes in that direction (i.e. $h\ k\ l$).[12] Each distinct atom type that composes the crystal structure will scatter radiation to a different extent which is characteristic to that atom. This is quantified by the atom's scattering factor/length (f) and depends strongly on the type of radiation used. Bringing these two points together, the intensity of the diffracted radiation from a plane of atoms (defined by the ($h\ k\ l$) vector) is equivalent to the square of the structure factor (F), defined as follows:[12]

$$F = \sum_i f_i e^{2\pi i(hu_i + kv_i + lw_i)} \tag{2.9}$$

where u_i, v_i, and w_i are the unit cell coordinates of the atom i.

There are two additional terms which, along with the structure factor, affect the diffraction intensity for a particular Q value. The first is the multiplicity (p), which quantifies the number of non-unique reflections for a given d-spacing;[12] for example, $d_{100} = d_{010} = d_{001} = d_{\bar{1}00} = d_{0\bar{1}0} = d_{00\bar{1}}$ (d_{hkl}) in a cubic structure leads to a 6x increase in intensity at that d. The second is the Debye-Waller (D-W) factor (sometimes called the temperature factor). This represents the average displacement of an atom from its average site in the unit cell.[15] The D-W factor reduces the intensity of a reflection as any displacement of an atom from its average position leads to diffuse scattering instead of Bragg scattering.

2.3.2 X-ray Diffraction

X-ray diffraction (XRD) is the most commonly utilized diffraction method and is intrinsically well suited for analyzing crystal structures as the wavelength (λ) of X-rays is of the same order of magnitude as the spacing of the atomic planes (~0.1–10 Å). X-rays interact with the electrons of the atoms; thus the X-ray scattering factor (f) of an atom scales with the number of electrons the atom has, and accordingly, with the atomic number z. However, f also decreases significantly as a function of increasing Q because of the atomic form factor. This relationship

is related to the nature of the interaction between the X-ray and electron cloud.[16] This means that a typical XRD pattern will show higher intensity peaks at low Q values and lower intensity peaks at high Q values.

The Lorentz-polarization factor (LP) must also be considered when calculating the intensity of an XRD reflection. This factor takes into account the polarization of the X-ray beam and the geometry of the atomic planes (Equation 2.10).

$$LP = \frac{1 + \cos^2(2\theta)}{\sin^2(\theta)\cos(\theta)} \tag{2.10}$$

XRD can either be performed on a laboratory diffractometer or at a synchrotron. A laboratory diffractometer takes an elemental source (e.g. Fe, Co, Cu, Mo, Ag) and harnesses its characteristic X-ray emission, usually Kα (discussed further in subsection 2.3.6).[12] By contrast, a synchrotron produces X-rays through the rapid deceleration of electrons in a magnetic field,[14] which are subsequently monochromatized (a single wavelength selected) and directed toward the sample. XRD can be conducted in a few different geometries that are classified as either reflection mode (e.g. Bragg-Brentano) or transmission mode (e.g. Debye-Scherrer).[17]

All diffraction experiments analyzed in this thesis are powder XRD. This method involves grinding a material into a fine powder. The sample powder can then be measured under the assumption that a large number of crystallites exist and are randomly oriented in reference to the X-ray beam.[14] In reality, some degree of preferential orientation is difficult to avoid, particularly in the reflection mode.[18]

Operando or *in situ* X-ray diffraction methods are especially useful for capturing a material's crystal structure as it is changing during an experiment. One example is high temperature-XRD (HT-XRD), which uses a customized furnace that is built as an attachment into the diffractometer. Utilizing this attachment, XRD can be carried out during the synthesis of a material (as a function of time and temperature) in order to capture key phase transitions. Likewise, *operando* electrochemical XRD is an extremely powerful method for capturing an electrode material's structure as a function of its state of charge. This technique is typically conducted using a customized electrochemical cell that has one or two X-ray transparent windows.

Both of these *operando* methods require modified set-ups to those traditionally used (e.g. custom HT-XRD attachment vs. normal furnace) and as such, extra caution must be taken to avoid spurious features originating from these modifications and impacting the results.[19]

2.3.3 Rietveld Refinement

The Rietveld method for powder diffraction refinement was named after Hugo Rietveld for his approach.[20] The method uses a least-squares minimization to refine a simulated diffraction pattern to match closely with an experimental diffraction pattern. The refinement procedure can be summarized by four key steps: 1) calculate the position and intensity for each reflection using the unit cell and structure factor of a hypothesized model structure, while also taking into account Debye-Waller and Lorentz-polarization factors, 2) convolve these intensities with appropriate peak profile functions stemming from instrumental broadening and material-dependent broadening (e.g. strain, particle size), 3) add the newly convolved intensities to a background function, and 4) compare this simulated pattern to the experimental data (calculate "goodness of fit") and allow certain parameters of the model to be methodically adjusted using a least-squares minimization algorithm (e.g. Levenberg–Marquardt least-squares minimizer [21]).

The "goodness of fit" between simulated and experimental data can be calculated in a variety of ways but the most common method is to use R factors, particularly the weighted profile R factor (R_{wp}) and the expected R factor (R_{exp}). R_{wp} is a discrepancy index that quantifies the weighted sum of the squared differences between the observed and computed intensity values.[22] R_{exp} represents the best possible R_{wp} that is possible to achieve with that data.[18] The ratio between these two R factors has been termed the goodness of fit or χ (often reported as χ^2).[22]

The R factors and χ^2 are calculated as follows:[18, 22]

$$R_{\text{wp}} = \left\{ \Big(\sum_i w_i [y_i(\text{obs}) - y_i(\text{calc})]^2 \Big) / \Big(\sum_i w_i [y_i(obs)]^2 \Big) \right\}^{1/2} \tag{2.11}$$

$$R_{\text{exp}} = \left\{ (N - P) / \sum_i^N w_i y_i(obs)^2 \right\}^{1/2} \tag{2.12}$$

$$\chi^2 = R_{\text{wp}}^2 / R_{\text{exp}}^2 \tag{2.13}$$

where y_i is the intensity (observed and calculated), w_i is the weighting of each intensity difference, N is the number of observations, and P is the number of refined parameters.

2.3.4 Neutron Diffraction

Neutron diffraction (ND) can be used as a complimentary technique to XRD. While X-rays are scattered by the electron clouds of atoms, neutrons are primarily scattered by the nuclei.[23] This affects the scattering factor f (called scattering length for neutrons) dramatically, which in turn affects the structure factor F. For example, there is no atomic form factor for neutron radiation (i.e. F has much less Q-dependence),[16] meaning the signal to noise ratio of higher Q reflections is generally much better for ND than XRD. Moreover, while the X-ray scattering factor rises slowly with the atomic number, the neutron scattering length changes sporadically from element to element (and even isotope to isotope).[24] This provides an advantage of being able to differentiate two atom types that are very close in atomic number (e.g. Mn-25 and Ni-28).[25] ND does, however, have the drawbacks of being much more difficult to access (only available at special facilities) and requiring a longer measurement acquisition time.[26]

2.3.5 Total Scattering and Pair Distribution Function

When analyzing diffraction data, a background is typically fit which encompasses scattering from the air and sample holder as well as diffuse scattering from the sample itself. In a total scattering experiment, the scattering from the sample (Bragg and diffuse) is carefully isolated from the background signal and then Fourier

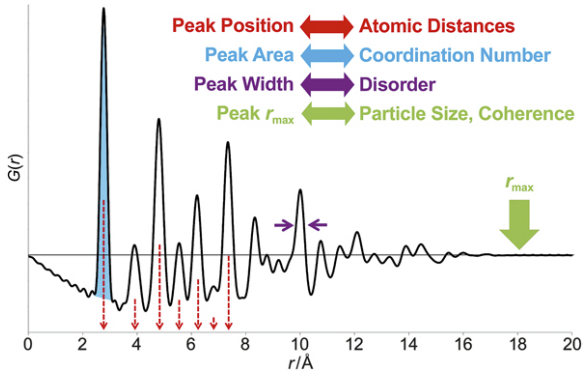

Figure 2.5: A pair distribution function (PDF) of a material is shown. This real space visualization of atom pair distances can be qualitatively and quantitatively interpreted through the peak positions, areas, widths, and $r_{\max}$. Reproduced with permission from Ref. [27].

transformed into real space (from reciprocal space).[28] This gives a distribution function (G) of atom pairs (as a function of their distance r) within the crystal structure, which is weighted by the atoms' scattering factors/lengths (i.e. pair distribution function or PDF). The equation to calculate the PDF is as follows:[29]

$$G(r) = \frac{2}{\pi} \int_0^\infty Q[S(Q) - 1] \sin(Qr)\, dQ \tag{2.14}$$

where $G(r)$ is the PDF and $S(Q)$ is the total scattering function of the material. In reality, it is impossible to collect Q values to ∞ but a sufficiently broad range of Q (≥ 20 Å^{-1}) must be used in order to obtain a high resolution PDF.[27] As this is not attainable on most laboratory instruments (e.g. using Cu kα), synchrotron X-ray or neutron radiation is often used.

PDF is particularly useful for materials with little or no long range order (i.e. amorphous materials).[27] Powder diffraction depends on long range order in the crystal structure to obtain Bragg reflections. By contrast, a PDF can detect and expose the short range ordering of a compound. PDF can be qualitatively and quantitatively analyzed through the peak characteristics, each representing one or more atomic pairs, as shown in Figure 2.5.

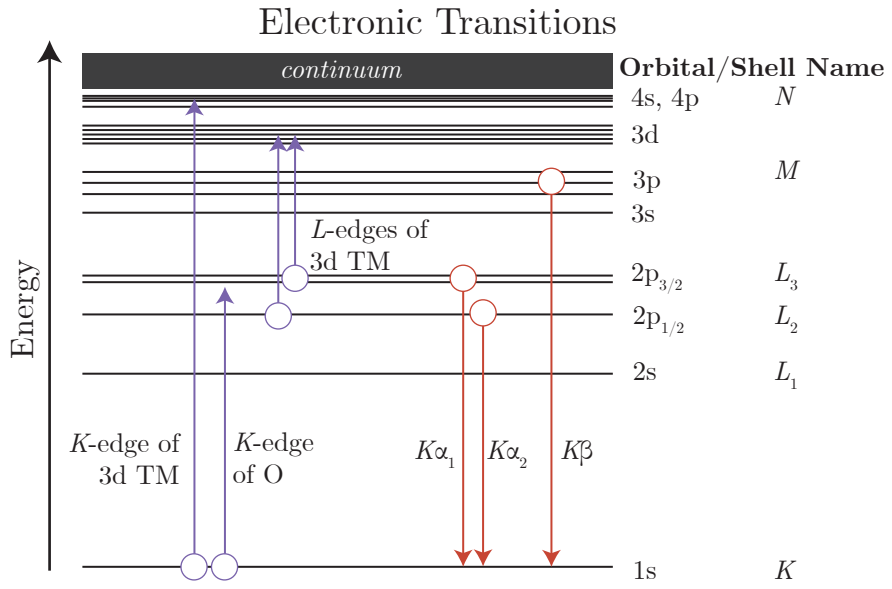

Figure 2.6: The labeled electronic structure of an atom is shown with selected dipole-allowed electronic transitions. Electron excitation transitions (occurring through the absorption of an X-ray photon) are shown in purple whereas electron decay transitions (occurring through the emission of an X-ray photon) are shown in red.

2.3.6 X-ray Absorption Spectroscopy

Diffraction and total scattering experiments focus on the elastic interactions of radiation with a sample. In addition to these, there are also significant inelastic scattering processes that occur, especially during an X-ray experiment. Inelastic scattering occurs through the excitation of a compound to a higher vibrational, rotational, or electronic state.[30] As a result of this excitation, the X-ray photon will donate some of its energy to the material and is thus inelastically scattered. An example of this phenomenon when an incident photon is absorbed by a atom with subsequent emission of another photon with lower energy (i.e. fluorescence).[31] The characterization technique known as X-ray absorption spectroscopy (XAS), or sometimes X-ray absorption fine structure (XAFS), focuses on the absorption of X-rays corresponding to the electronic transitions of a material. This is a powerful technique for collecting element-specific information on oxidation state, coordination environment, and electronic structure of a material.[26]

A monochromator is used to isolate X-rays of a certain energy (E) from a

synchrotron X-ray beam. This monochromatized X-ray beam can be used to determine the absorption coefficient of the material (μ) as a function of E, by measuring the intensity of the X-ray beam before (I_0) and after transmission through a sample (I_t) with the Beer-Lambert law:[26]

$$I_t = I_0 e^{-\mu x} \tag{2.15}$$

$$\mu \propto \log\left(\frac{I_0}{I_t}\right) \tag{2.16}$$

where x is the sample thickness. This is how most XAS measurements are conducted.

The absorption coefficient of a material $\mu(E)$ will show sharp increases at certain energies which depend on the elements present in the sample and their electronic states. This is because a material can only absorb an incident X-ray photon when the photon energy is exactly equal to the energy needed to make an electronic transition.[32] In XAS, the X-ray energy is scanned over a range that encompasses the specific energy needed to excite a core electron (e.g. 1s state) to the unoccupied states above the Fermi energy. The sharp increase in absorption of the sample when the correct threshold energy (to allow an electronic transition) is reached is referred to as an absorption "edge".

The lowest unoccupied energy states are often relatively bound to an atom and thus behave much like atomic orbitals. Due to the symmetry of atomic orbitals, electrons are only "allowed" to transition between orbitals according to certain criteria known as selection rules:[32]

- Dipole: $\Delta l = \pm 1$
- Quadropole: $\Delta l = \pm 2, 0$

where l is the orbital angular momentum (i.e. s orbital: $l = 0$, p: $l = 1$, d: $l = 2$, f: $l = 3$). Dipole transitions tend to dominate an X-ray absorption spectra as their transition probability is approximately 100 times greater than quadrupolar transitions.[32]

An atomic orbital can be labeled according to its principal quantum number (K: $n = 1$, L: $n = 2$, M: $n = 3$, N: $n = 4$).[33] The excitation process from

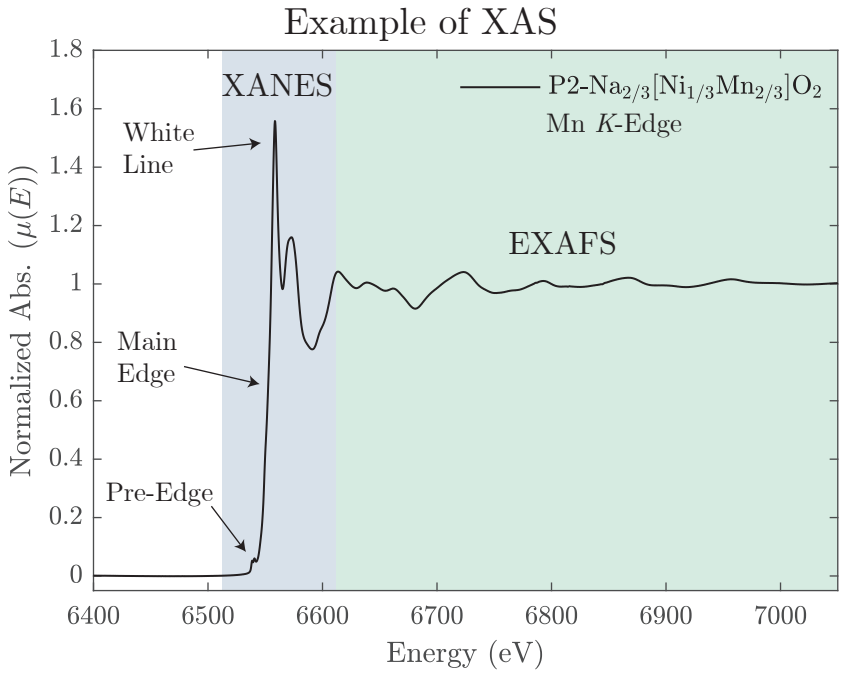

Figure 2.7: A normalized XAS spectrum is shown for the Mn K-edge of P2-$Na_{2/3}[Ni_{1/3}Mn_{2/3}]O_2$ with various aspects of the spectrum labeled. X-ray absorption near edge structure (XANES) is highlighted in blue and the extended X-ray absorption fine structure (EXAFS) is highlighted in green.

the absorption of an X-ray photon is generally labeled by the initial state of the electron (e.g. 1s $\rightarrow$ 4p: *K*-edge of a 3d TM). This is further illustrated in Figure 2.6. As mentioned previously, an X-ray photon emission can also follow an absorption event.[33] This is also illustrated in Figure 2.6 and must follow the same selection rules. This behavior is relevant for resonant inelastic X-ray scattering (RIXS) discussed later in this section.

X-ray Absorption Near Edge Structure

The XAS spectra can be divided into two main parts: the X-ray absorption near edge structure (XANES) and the extended X-ray absorption fine structure (EXAFS). These are both illustrated in Figure 2.7 for the Mn K-edge of P2-$Na_{2/3}[Ni_{1/3}Mn_{2/3}]O_2$. This thesis only incorporates XANES analyses. The most common use of XANES for battery materials is to investigate the TM oxidation state by measuring the TM K-edges. The energies of the main-edge, pre-edge, and white line (defined in Figure 2.7) have each been shown to correlate to the oxidation state of the element.[34,

35] Thus by comparing the measured spectrum to a set of standards, oxidation state can be determined. Moreover, by probing the edges of a battery material at different states of charge (by preparing *ex situ* samples), the charge compensation mechanism of a battery can be investigated.[36]

Soft X-ray Absorption Spectroscopy

Soft X-ray absorption spectroscopy (soft XAS) simply specifies the energy range of the X-ray beam used for the XAS experiment: typically less than 1000 eV. The oxygen K-edge and 3d TM L-edges can be found within this energy regime. Using this energy range therefore has the advantage of directly probing the electronic states of a battery material that are most often involved in charge compensation (i.e. TM 3d and O 2p). Unfortunately, X-rays of this energy range are easily absorbed in air so the measurement must be carried out under ultra-high vacuum.[37] Related to this, soft XAS is not usually measured in a transmission-mode but rather by utilizing the compound's fluorescence.[26] The fluorescence-mode of detection assumes that for every photon absorbed by the sample, there will be a photon that is emitted.[38] The emitted photons can be quantified by a detector and compared with the incident intensity to obtain the absorption coefficient (μ). Typically only the XANES region of a soft XAS spectrum is analyzed.

Resonant Inelastic X-ray Scattering

Resonant inelastic X-ray scattering (RIXS) has proven to be an incredibly useful method for identifying changes in the oxygen oxidation state.[39] As was stated in the soft XAS section above, the absorption of X-ray photons (by the excitation of an electron) will subsequently generate the emission (fluorescence) of another X-ray photon as electrons relax to fill the core hole. The fluorescence emitted from the sample also contains significant information on the electronic structure of the material. In a RIXS experiment, the fluorescence signal is differentiated by its energy using an high resolution, energy discriminatory detector.[40] The recorded fluorescence data can then be plotted as a function of both excitation energy and

emission energy.[39] This is usually done as a color map. In this thesis, the RIXS spectra shown are obtained by exciting the O K-edge and analyzing the K_α emission.

2.4 Other Techniques

2.4.1 Density Functional Theory

Density functional theory (DFT) is one of the best computational methods for calculating materials' properties. It is a first principles method, which means its theory is derived from the fundamental laws of physics and not based on empirical information. A material's electrons are determinant of its properties which can be modeled by the time-independent Schrödinger equation:[41]

$$\hat{H}\Psi = E\Psi \tag{2.17}$$

where $\hat{H}$ is the Hamiltonian operator, Ψ is the electron wave function, and E is the energy of the system.

In 1964, Hohenberg and Kohn developed a theorem that proves a system's total energy (E) is a functional (i.e. a function of a function) of the electron density $\rho(r)$ (where r is position).[42] The system energy (E) can be calculated as follows:[43]

$$E[\rho] = T[\rho] + \int V_{\text{ext}}(r)\rho(r)dr + \int \rho(r)dr \int \frac{\rho(r')}{|r-r'|}dr' + E_{xc}[\rho] \tag{2.18}$$

where $T[\rho]$ is the kinetic energy, $V_{\text{ext}}(r)$ is the attractive nuclear potential and $E_{xc}[\rho]$ is the exchange-correlation energy. The third term of the equation represents the coulombic electron-electron repulsion.

While all the other terms can be solved exactly, the $E_{xc}[\rho]$ involves certain approximations. This term is essentially a correction that decreases the coulombic interaction between electrons (in the model) because of the Pauli exclusion principle and the correlation between electron movements.[43]

Using such approximations (e.g. LDA, GGA, etc.) for the exchange-correlation energy, the electron density can be solved though a self-consistent field method using the Kohn-Sham equation:[43]

$$\left[-\nabla^2 - \sum_I \frac{2Z_I}{|r-R_I|} + 2\int \frac{\rho(r')}{|r-r'|}dr' + V_{xc}(r) \right] \phi_i(r) = \epsilon_i \phi i \tag{2.19}$$

where $\phi_i(r)$ belongs to a series of one electron wave functions such that:

$$\rho(r) = \sum_{i=1}^{N} |\phi_i(r)|^2 \tag{2.20}$$

In Equation 2.19, R_I is the position vector for the nucleus and Z_I is its charge while $V_{xc}(r)$ is the functional derivitive of the exchange-correlation energy, ∇ is the Laplacian, and ϵ_i is the eigenvalue solution to the equation. In Equation 2.20, N is the number of electrons in the system.[43]

If a system's total energy is minimized (according to Equation 2.18), the ground state properties of that system can be determined. In the case of strongly correlated systems (e.g. TMO_2 compounds), however, most approximations lead to an inaccurate exchange-correlation energy. Therefore, these compounds require an additional Hubbard U term to be added to Equation 2.18, which more effectively addresses the electron self-interaction error and better models the ground state properties.[44]

In this thesis, DFT was used to calculate the ground state energy and electronic states of various structural models. All DFT calculations were carried out using the software package Quantum Espresso, which utilizes a plane wave basis set to represent the one electron wave functions. As is standard for DFT calculations, the number of electrons (N) was reduced by using pseudopotentials to model the core electrons. The Broyden–Fletcher–Goldfarb–Shanno (BFGS) algorithm was used for geometrical optimization. In addition, the software calculated the magnetization for each atom by integrating over a sphere around the atom.

2.4.2 ^{57}Fe-Mössbauer Spectroscopy

^{57}Fe-Mössbauer spectroscopy (^{57}Fe-MS) is a specialized technique for the study of Fe in compounds. It takes advantage of what is known as the Mössbauer effect: the emission or absorption of a γ-ray by the nucleus of an atom without loss of energy due to recoil or thermal broadening.[45] In ^{57}Fe-MS, a ^{57}Co source is used. This source has an unstable nucleus which decays to produce a γ-ray. This γ-ray can then be absorbed by the Fe nuclei in the measured sample if its energy matches

exactly with the energy required to excite the nucleus to a higher energy state. This is similar conceptually to the excitation of electrons discussed previously, however, Mössbauer spectroscopy utilizes the Doppler effect (instead of a monochromator) to scan the γ-ray energy. The intensity of absorption can then be quantified as a function of the energy probed in units of mm s^{-1}. With this technique, it is possible to detect minute changes in the interaction energy of the Fe nuclei and surrounding electrons, which were previously thought to be negligible.[45]

The interaction of ^{57}Fe nucleus with the surrounding electrons produces a shifting or a splitting of the nuclear energy levels that is captured with ^{57}Fe-MS.[46] The "isomer shift" or center shift (CS) is impacted predominantly by the s orbital electron clouds surrounding the Fe nucleus and is dependent on the valence state of the ion (lower CS = higher oxidation state).[46] Another important parameter is the quadrupolar splitting (QS) of the Mössbauer signal. This is caused by interactions with the surrounding electric field that result in the nucleus deviating from spherical symmetry (higher QS = less isotropic).[46]

^{57}Fe-MS has been used in a variety of studies to investigate the Fe oxidation state and coordination environment in battery materials.[47–50] It is used in this thesis to probe the oxidation state of Fe in $Na_{2/3}[Ni_{1/6}Mn_{1/2}Fe_{1/3}]O_2$ and investigate the possibility that Fe changes coordination environments during charge (from octahedral to tetrahedral coordination).

2.5 References

(1) Husing, N.; Schubert, U., *Synthesis of Inorganic Materials*, 3rd ed.; Wiley-VCH: Weinheim, 2012, pp 1–370.

(2) Luo, K.; Roberts, M. R.; Hao, R.; Guerrini, N.; Liberti, E.; Allen, C. S.; Kirkland, A. I.; Bruce, P. G. *Nano Letters* **2016**, *16*, 7503–7508.

(3) Al-Muhtaseb, S. A.; Ritter, J. A. *Advanced Materials* **2003**, *15*, 101–114.

(4) Fassel, V. A.; Kniseley, R. N. *Analytical Chemistry* **1974**, *46*, 1110A–1120A.

(5) Boss, C. B.; Fredeen, K. J. Concepts, Instrumentation and Techniques in Inductively Coupled Plasma Optical Emission Spectrometry., Sheldon, CT, 2004.

(6) Linge, K. L.; Jarvis, K. E. *Geostandards and Geoanalytical Research* **2009**, *33*, 445–467.

(7) Vernon-Parry, K. *III-Vs Review* **2000**, *13*, 40–44.

(8) Delmas, C.; Ménétrier, M.; Croguennec, L.; Levasseur, S.; Pérès, J. P.; Pouillerie, C.; Prado, G.; Fournès, L.; Weill, F. *International Journal of Inorganic Materials* **1999**, *1*, 11–19.

(9) Marks, T.; Trussler, S.; Smith, A. J.; Xiong, D.; Dahn, J. R. *Journal of The Electrochemical Society* **2011**, *158*, A51.

(10) Kayyar, A.; Huang, J.; Samiee, M.; Luo, J. *Journal of Visualized Experiments* **2012**, 1–5.

(11) Huggins, R. A., *Advanced Batteries*; 5685; Springer US: Boston, MA, 2009; Vol. 276, pp 1–474.

(12) Suryanarayana, C.; Grant Norton, M., *X-Ray Diffraction A Practical Approach*; Plenum Press: New York, 1998.

(13) Bragg, W. H.; Bragg, W. L. *Proceedings of the Royal Society A: Mathematical, Physical and Engineering Sciences* **1913**, *88*, 428–438.

(14) Zolotoyabko, E., *Basic Concepts of X-Ray Diffraction*; Wiley-VCH: Weinheim, 2014.

(15) Wikipedia contributors Debye–Waller factor., 2018.

(16) Wikipedia Atomic form factor., 2018.

(17) Cockroft, J. K.; Fitch, A. N. In *Powder Diffraction Theory and Practice*, Dinnebier, R. E., Billinge, S. J. L., Eds., Cambridge, 2008.

(18) Mccusker, L. B.; Von Dreele, R. B.; Cox, D. E.; Louër, D.; Scardi, P. *Journal of Applied Crystallography* **1999**, *32*, 36–50.

(19) Borkiewicz, O. J.; Wiaderek, K. M.; Chupas, P. J.; Chapman, K. W. *The Journal of Physical Chemistry Letters* **2015**, *6*, 2081–2085.

(20) Rietveld, H. M. *Journal of Applied Crystallography* **1969**, *2*, 65–71.

(21) Toby, B. H.; Von Dreele, R. B. *Journal of Applied Crystallography* **2013**, *46*, 544–549.

(22) Toby, B. H. *Powder Diffraction* **2006**, *21*, 67–70.

(23) Fischer, W. E.; Morf, R.; Storni, M., *X-Rays, Neutrons and Muons*; Wiley-VCH: Weinheim, 2012.

(24) Sears, V. F. *Neutron News* **1992**, *3*, 26–37.

(25) Lu, Z.; Donaberger, R. a.; Dahn, J. R. *Chemistry of Materials* **2000**, *12*, 3583–3590.

(26) Lin, F.; Liu, Y.; Yu, X.; Cheng, L.; Singer, A.; Shpyrko, O. G.; Xin, H. L.; Tamura, N.; Tian, C.; Weng, T. C.; Yang, X. Q.; Meng, Y. S.; Nordlund, D.; Yang, W.; Doeff, M. M. *Chemical Reviews* **2017**, *117*, 13123–13186.

(27) Chapman, K. W. *MRS Bulletin* **2016**, *41*, 231–238.

(28) Chupas, P. J.; Qiu, X.; Hanson, J. C.; Lee, P. L.; Grey, C. P.; Billinge, S. J. *Journal of Applied Crystallography* **2003**, *36*, 1342–1347.

(29) Masadeh, A. S. *Journal of Experimental Nanoscience* **2016**, *11*, 951–974.

(30) Hollas, J. M., *Modern Spectroscopy*, 4th ed.; John Wiley & Sons, Ltd.: West Sussex, 1987, pp 1–452.

(31) Liu, X.; Yang, W.; Liu, Z. *Advanced Materials* **2014**, *26*, 7710–7729.

(32) Bunker, G., *Introduction to XAFS: A Practical Guide to X-ray Absorption Fine Structure Spectroscopy*; Cambridge University Press: Cambridge, 2010, pp 1–260.

(33) Als-Nielsen, J.; McMorrow, D., *Elements of Modern X-ray Physics*, 2nd ed.; John Wiley & Sons, Ltd.: West Sussex, 2011, pp 1–419.

(34) Farges, F. *Physical Review B* **2005**, *71*, 155109.

(35) Yoon, W.-S.; Grey, C. P.; Balasubramanian, M.; Yang, X.-Q.; McBreen, J. *Chemistry of Materials* **2003**, *15*, 3161–3169.

(36) Yoon, W.-S.; Balasubramanian, M.; Chung, K. Y.; Yang, X.-Q.; McBreen, J.; Grey, C. P.; Fischer, D. A. *Journal of the American Chemical Society* **2005**, *127*, 17479–17487.

(37) Ye, Y.; Kapilashrami, M.; Chuang, C.-H.; Liu, Y.-S.; Glans, P.-A.; Guo, J. *MRS Communications* **2017**, *7*, 53–66.

(38) Glatzel, P.; Weng, T. C.; Kvashnina, K.; Swarbrick, J.; Sikora, M.; Gallo, E.; Smolentsev, N.; Mori, R. A. *Journal of Electron Spectroscopy and Related Phenomena* **2013**, *188*, 17–25.

(39) Wu, J.; Li, Q.; Sallis, S.; Zhuo, Z.; Gent, W.; Chueh, W.; Yan, S.; Chuang, Y.-d.; Yang, W. *Condensed Matter* **2019**, *4*, 5.

(40) Qiao, R.; Li, Q.; Zhuo, Z.; Sallis, S.; Fuchs, O.; Blum, M.; Weinhardt, L.; Heske, C.; Pepper, J.; Jones, M.; Brown, A.; Spucces, A.; Chow, K.; Smith, B.; Glans, P.-A.; Chen, Y.; Yan, S.; Pan, F.; Piper, L. F. J.; Denlinger, J.; Guo, J.; Hussain, Z.; Chuang, Y.-D.; Yang, W. *Review of Scientific Instruments* **2017**, *88*, 033106.

(41) Wikipedia Schrödinger equation., 2019.

(42) Hohenberg, P.; Kohn, W. *Physical Review* **1964**, *136*, B864–B871.

(43) Anisimov, V.; Izyumov, Y., *Electronic Structure of Strongly Correlated Materials*; Cardona, M., Fulde, P., von Klitzing, K., Queisser, H.-J., Merlin, R., Stormer, H., Eds.; Springer: Berlin, 2010, pp 1–288.

(44) Zhou, F.; Cococcioni, M.; Marianetti, C. A.; Morgan, D.; Ceder, G. *Physical Review B - Condensed Matter and Materials Physics* **2004**, *70*, 1–8.

(45) Greenwod, N. N.; Gibb, T. C., *Mössbauer Spectroscopy*; Chapman and Hall Ltd: London, 1971, pp 1–659.

(46) Nasu, S. In *Mössbauer Spectroscopy*, Yoshida, Y., Langouche, G., Eds.; Springer: Berlin, 2013; Chapter 1, pp 1–22.

(47) Takeda, Y.; Nakahara, K.; Nishijima, M.; Imanishi, N.; Yamamoto, O.; Takano, M.; Kanno, R. *Materials Research Bulletin* **1994**, *29*, 659–666.

(48) Zhao, J.; Zhao, L.; Dimov, N.; Okada, S.; Nishida, T. *Journal of the Electrochemical Society* **2013**, *160*, A3077–A3081.

(49) Wang, X.; Liu, G.; Iwao, T.; Okubo, M.; Yamada, A. *The Journal of Physical Chemistry C* **2014**, *118*, 2970–2976.

(50) Mortemard De Boisse, B.; Cheng, J. H.; Carlier, D.; Guignard, M.; Pan, C. J.; Bordère, S.; Filimonov, D.; Drathen, C.; Suard, E.; Hwang, B. J.; Wattiaux, A.; Delmas, C. *Journal of Materials Chemistry A* **2015**, *3*, 10976–10989.

3

Pursuing High Voltage, Earth Abundant P2-Type Cathodes

Contents

3.1 Abstract

Layered sodium transition metal oxide compounds with a P2 structure represent a promising class of compound as cathodes for Na-ion batteries due to their high energy density. In this chapter, $Na_{2/3}[Ni_{1/3}Mn_{2/3}]O_2$, a model P2 compound displaying high voltage (de-)intercalation, is investigated in detail to probe its utility as a cathode. The drawbacks of this compound are outlined which include Na deficiency in the as-synthesized state, unsatisfactory cycle life, and a strong driving force toward

Na ordering which is thought to be detrimental to the rate performance. After gaining a fundamental understanding of these challenges, practical solutions are offered by way of tuning the electrochemical properties with partial Fe-substitution as well as a new pre-treatment process (Na naphthalide solution) to overcome the Na deficiency of P2 compounds.

3.2 Introduction

In order to expand the applicability of the Na-ion battery, there is a strong need for better cathode materials. The ideal cathode would have high voltage, high capacity, high power, and a long cycle life as well as be safe from thermal runaway and composed of sustainable, low cost elements. As of now, no such perfect cathode exists. Some of the most promising candidates under investigation are from the class of materials known as layered sodium transition metal oxides ($NaMO_2$).

As was set out in the Introduction Section 1.2.1, there are four different $NaMO_2$ structural types. P2 and O3-type compounds are by far the most widely explored. P2 cathodes may benefit from generally faster diffusion as compared to O3 because of lower migration barriers as well as better structural stability (fewer phase transitions).[1] One of the first P2-type $NaMO_2$ cathodes studied was $Na_{2/3}[Ni_{1/3}Mn_{2/3}]O_2$.[2] This compound has a high average voltage of approximately 3.5 V vs. Na^+/Na (when cycled between 2.3 V and 4.5 V), which is compensated by the $Ni^{4+/2+}$ redox couple.[3] It also has a relatively good capacity for this voltage range of 130 mAh g^{-1}, however that capacity fades quickly on cycling.[3] Another limitation is the ordering of the Na-ions that occurs during the charge/discharge cycle hampering rate capability.[4]

There have been many active and inactive element substituents tested in order to improve the properties of $Na_{2/3}[Ni_{1/3}Mn_{2/3}]O_2$. Zhao et al. discovered that substitution of Al, Mg, Co, or Fe for Ni smooths the voltage steps in the electrochemical load curve corresponding to Na ordering arrangements.[5] Moreover, Li et al. later showed that Mg substitution might also improve Na mobility.[6]

In parallel to the exploration of $Na_{2/3}[Ni_{1/3}Mn_{2/3}]O_2$, perhaps an even more promising compound was discovered, composed entirely of inexpensive and abundant elements: $Na_{2/3}[Mn_{1/2}Fe_{1/2}]O_2$.[7] This compound retains its capacity (190 mAh g^{-1}) much better on cycling, but has a significantly lower average voltage of 2.7 V when cycled between 1.5 and 4.3 V. Talaie et al. later showed that by partially substituting Ni for Fe and Mn in the transition metal (TM) layer of this compound, the capacities and cycling retention could be further improved.[8]

In this chapter, $Na_{2/3}[Ni_{1/3}Mn_{2/3}]O_2$ is first explored in detail to understand its advantages and main drawbacks in its use as a cathode. The identified drawbacks include Na-ion ordering at various states of charge, poor capacity retention, and that the compound can only be synthesized in Na deficient form ($x = 2/3$ in Na_xMO_2). So far, Na deficiency has been intrinsic to all P2 type Na cathodes. Subsequently, possible approaches to overcome these drawbacks will be presented along with evidentiary support. The composition space between MnO_2, $NaFeO_2$, and $Na[Ni_{1/2}Mn_{1/2}]O_2$ is explored with the goal of determining the composition that optimizes both sustainability *and* performance. This led to the discovery of $Na_{2/3}[Ni_{1/6}Mn_{1/2}Fe_{1/3}]O_2$ which boasts among the highest specific energies of P2-type Na cathodes. Finally, the problem of Na deficiency is addressed using a pre-treatment process of the reducing agent, Na-naphthalide, to intercalate extra Na-ions into the compound prior to cycling.

3.3 Experimental

All compounds were synthesized via solid state methods described in Section 2.1, i.e. mixing Na_2CO_3 (5% excess) and the relevant metal oxides (NiO, Mn_2O_3 or MnO_2, Fe_2O_3 and MgO) and heating the mixture to temperatures between 900 °C and 1030 °C. For all Fe containing compounds, this process was done in a tube furnace under flowing oxygen gas while all other compounds were heated in a box furnace in air.

These compounds were prepared into electrodes by mixing them with carbon Super P to improve conductivity and PVDF as a binder using NMP as a solvent. The resulting ink was coated onto Al foil and dried at 80 °C for 12 or more

hours before being punched into discs. The electrode disks were assembled into coin cells using Na metal as a counter electrode, glass fiber separators, and 1M $NaPF_6$ in EC:PC or EC:DEC as an electrolyte. These coin cells are described in more detail within Section 2.2.

For galvanostatic cycling tests, the materials were charged and discharged at a constant specific current of 10 mA g^{-1} using a MACCOR battery testing system. *Ex situ* samples were recovered from the coin cell, washed with DMC to remove residual salt, and dried under vacuum.

Chemical analyses were performed on a Perkin Elmer Optima 8000 ICP-OES. The compositions reported were normalized so the cations existing in the TM layer of the compound sum to 1. SEM was conducted on a Zeiss Merlin Analytical SEM. Lab powder X-ray diffraction (XRD) was carried out on a Rigaku Smart Lab instrument with a Cu kα source and in parallel beam geometry. Synchrotron XRD was collected at the Advanced Photon Source (APS) in Chicago, IL on 11-ID-B or 11-BM. Data reduction as well as refinements were carried out using the GSAS-II software package.[9] Neutron diffraction was carried out on the GEM instrument at ISIS Neutron Source (Harwell, UK). X-ray absorption spectroscopy was measured at Diamond Light Source (DLS) B-18 and data was normalized with the Athena software package.[10] ^{57}Fe Mössbauer spectroscopy was collected in transmission mode using a ^{57}CoRh source under flowing nitrogen gas and fitted with the method outlined by Lagarec and Rancourt using the software package, Recoil.[11] High temperature XRD was performed on the Rigaku instrument described above utilizing an Anton Paar HTK 2000N high temperature attachment. *Operando* XRD data was collected for $Na_{2/3}[Ni_{1/3}Mn_{2/3}]O_2$ at APS on the 11-ID-B beamline using the AMPIX cell described by Borkiewicz et al.[12].

Table 3.1: ICP-OES Composition Confirmation

Element	Na	Ni	Mn
Concentration (ppm)	0.85(1)	0.99(1)	1.95(2)
Normalized Composition	0.70	0.32	0.68
Expected Composition	0.67	0.33	0.67

3.4 Results and Discussion

3.4.1 $Na_{2/3}[Ni_{1/3}Mn_{2/3}]O_2$: A High Voltage Cathode

Pristine Characterization

$Na_{2/3}[Ni_{1/3}Mn_{2/3}]O_2$ was synthesized with solid state methods and the composition was confirmed with ICP-OES, shown in Table 3.1. Synchrotron XRD was used to identify the crystal structure of the compound as the P2 structure, which has hexagonal symmetry (space group: $P6_3/mmc$). The Rietveld refinement fitting is plotted in Figure 3.1 and the corresponding structural parameters are documented in Table 3.2. The a parameter (i.e. TM to TM distance) is 2.896 Å and the c parameter (i.e. 2x interlayer spacing) is 11.110 Å. The refined fraction of Na in trigonal prismatic sites that share edges with TMs is approximately double that of Na in trigonal prismatic sites that share faces with TMs.

There are also three extra peaks in the data, highlighted in the inset of Figure 3.1, which are not modeled in the refinement. Lee et al. established that these peaks were a result of a particular Na-ion ordering arrangement occurring at $x = 2/3$ in Na_xMO_2, which they classified as "Large Zig Zag" (LZZ) ordering.[3]

Neutron diffraction (ND) was also carried out to differentiate the scattering contribution of Ni and Mn. These elements have very similar X-ray scattering factors (based on atomic number: Mn: 25, Ni: 28) but have very different neutron scattering lengths (Mn: -3.73 fm vs. Ni: 10.3 fm).[13, 14] The ND pattern (Figure 3.2) provides evidence for the ordering of these TMs. There are extra peaks, highlighted in the grey regions, which do not correspond to the standard (disordered) P2 model. These peaks have been previously shown to be due to "honeycomb" ordering of the Ni and Mn, which is illustrated in the inset.[15]

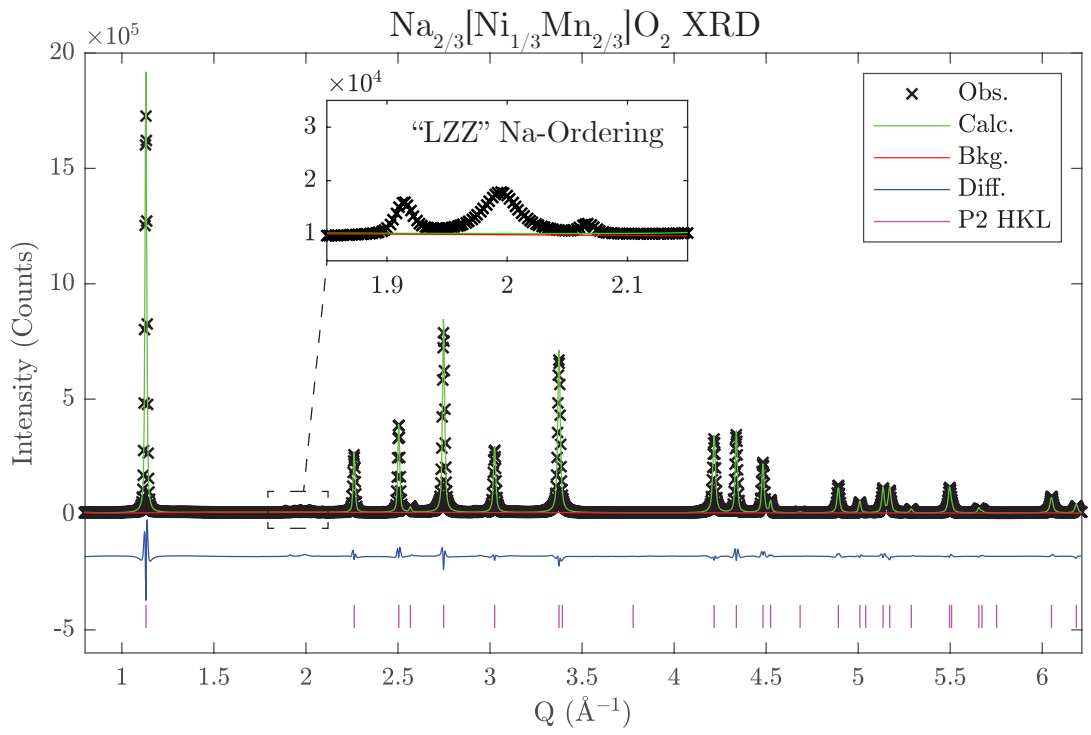

Figure 3.1: XRD data is shown with the corresponding fitting from the Rietveld refinement. Refined parameters are listed in Table 3.2. This data set was collected at APS 11-ID-B with the aid of Dr. Olaf Borkiewicz (APS beamline scientist).

High Temperature - XRD

Given that P2 compounds are generally thought to have a very high Na diffusion coefficient, it is interesting that the Na-ions in $Na_{2/3}[Ni_{1/3}Mn_{2/3}]O_2$ are static enough at room temperature to present the long range order evidenced in the diffraction techniques. High temperature XRD (HT-XRD) was performed to see at what stage of the synthesis procedure the Na ordering peaks become visible.

Table 3.2: Rietveld refinement results for $Na_{2/3}[Ni_{1/3}Mn_{2/3}]O_2$ from data collected at APS 11-ID-B.

S.G. *P6₃/mmc*, *a*: 2.8968(1) Å, *c*: 11.1099(4) Å, Rwp: 11.48%, Rexp: 0.58%					
Atom	**x**	**y**	**z**	**SOF**	**Uiso (Å²)**
Na (2b)	0	0	1/4	0.218(4)	0.032(2)
Na (2d)	2/3	1/3	1/4	0.449(4)	0.032(2)
Ni (2a)	0	0	0	1/3	0.0035(4)
Mn (2a)	0	0	0	2/3	0.0035(4)
O (4f)	2/3	1/3	-0.0929(3)	1	0.014(1)

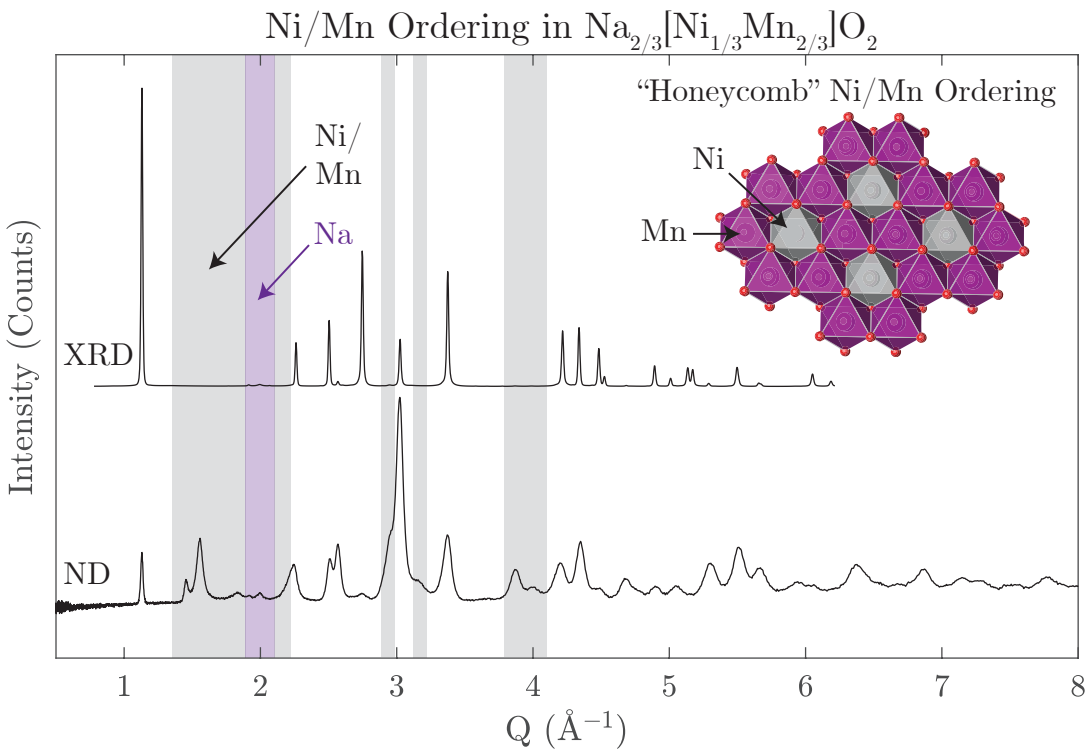

Figure 3.2: The same XRD data as Figure 3.1 is replotted in order to compare to the ND data (bottom). Ni/Mn ordering is evident in the ND due to the difference in scattering lengths of two nuclei. A model of the "honeycomb" Ni/Mn ordering is shown in the top right of the figure. The ND data set was collected at ISIS Neutron Source by Dr. Matthew Roberts.

An *in situ* synthesis was conducted utilizing the HT-XRD attachment, as described in the Experimental Section 3.3 and is presented in Figure 3.3. The precursors were placed into a heated chamber and a pattern was taken every 30 minutes over the heating procedure. The heating steps are shown in Figure 3.3b. At approximately 400 °C, peaks corresponding to the P3 layered structure started to become visible, particularly the strong (003) peak at $Q = 1.1$ Å^{-1}. Upon further heating to 700 °C, the P3 crystallized more at the expense of the precursor peaks. After holding for 7 hours at 700 °C, the furnace temperature was heated to 900 °C. On ramping past approximately 850 °C, the P3 peaks disappeared and new peaks corresponding to the P2 structure were evident. Interestingly, this is at almost the exact temperature which Na_2CO_3 decomposes. This is in line with findings by Sathiya et al. which showed that using excess Na_2CO_3 during synthesis promoted

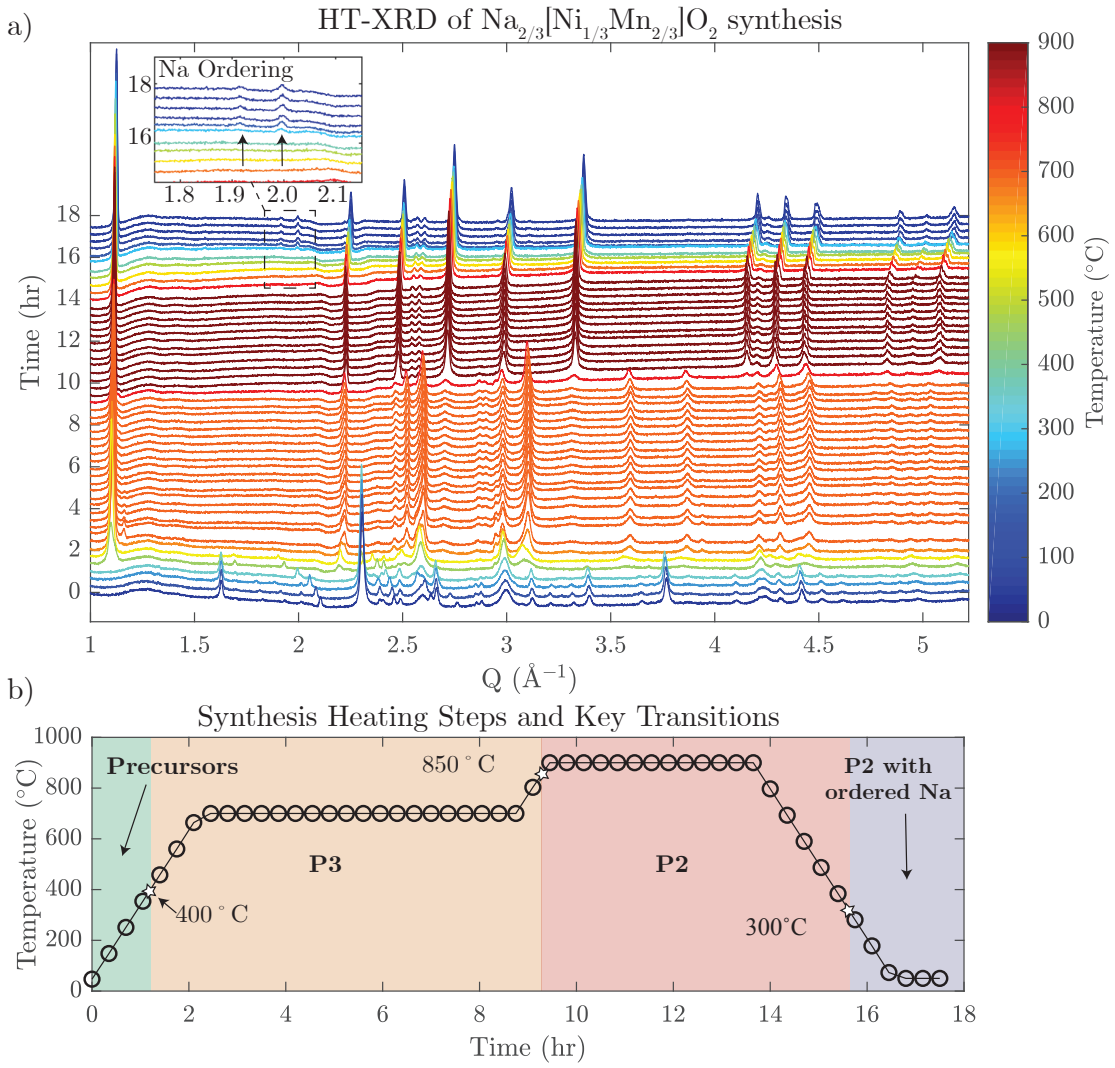

Figure 3.3: High temperature XRD (HT-XRD) was used to track the synthesis process of $Na_{2/3}[Ni_{1/3}Mn_{2/3}]O_2$. The XRD patterns shown in a) are colored based on the temperature shown in the color bar as well as stacked corresponding to the time (hrs). b) shows the various heating steps more clearly over time as well as the key structural events of the synthesis process extracted from the diffraction patterns.

the P2 structure over the P3.[16] As will be shown in subsequent sections, the stability of different stacking sequences is heavily dependent on Na content.

On cooling to room temperature, the "LZZ" Na ordering peaks appeared, shown in the inset of Figure 3.3a. What is surprising, however, is that they become visible at 300 °C. The stabilization of the Na ordering at such a high temperature shows just how thermodynamically favorable taking on such an arrangement is for the structure. As will be shown in the next section, this has a detrimental effect on Na mobility.

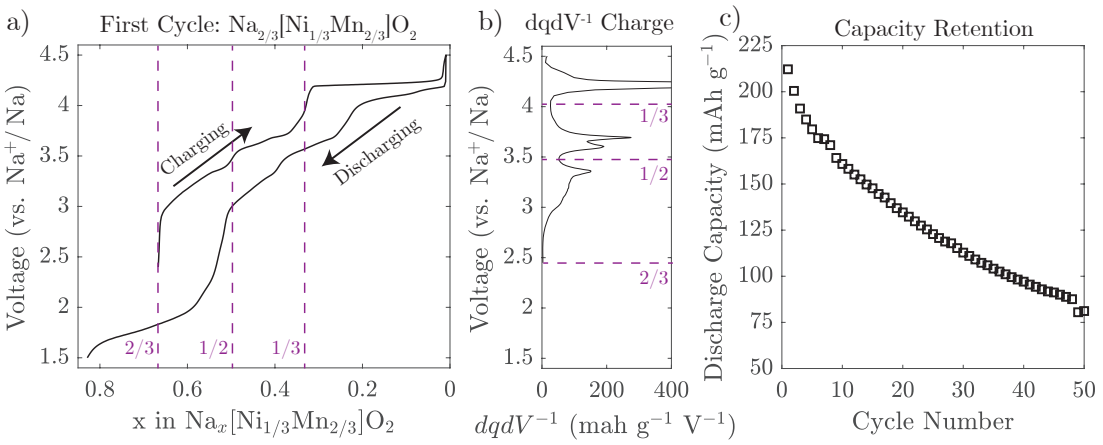

Figure 3.4: The electrochemical performance of $Na_{2/3}[Ni_{1/3}Mn_{2/3}]O_2$ was probed with galvanostatic cycling at 10 mA g^{-1} between 1.5 and 4.5 V vs. Na^+/Na. The first cycle is shown in a), the differential capacity plot in b) and the capacity retention in c).

Electrochemistry

Presently, experimental studies have only examined the ordering of the pristine $Na_{2/3}[Ni_{1/3}Mn_{2/3}]O_2$ compound. However, Lee et al. predicted through density functional theory (DFT) calculations that several ordering schemes occur corresponding to different voltage "steps" in the load curve, particularly those at Na contents of $Na_x[Ni_{1/3}Mn_{2/3}]O_2$, $x = 2/3, 1/2$ and $1/3$.[3] The electrochemical performance of this material was therefore reinvestigated.

$Na_{2/3}[Ni_{1/3}Mn_{2/3}]O_2$ was cycled galvanostatically (constant current) at a low rate of 10 mA g^{-1} in order to see equilibrium processes occurring. The resulting voltage response is shown in Figure 3.4 with the load curve of the first cycle shown in a). It is immediately clear that there are many steps in the load curve which are even more evident in the $dq\ dV^{-1}$ plot in Figure 3.4b. As was computed by Lee et al., voltage steps are associated with Na-ion ordering and seen in a variety of similar compounds.[17, 18] Interestingly, no diffraction-based evidence has been provided for the existence of Na-ion ordering in $Na_x[Ni_{1/3}Mn_{2/3}]O_2$ other than the pristine $x = 2/3$, already discussed. The discharge capacities, shown in Figure 3.4c, fade quickly with cycling, the cause of which, will be discussed in detail in Chapter 4.

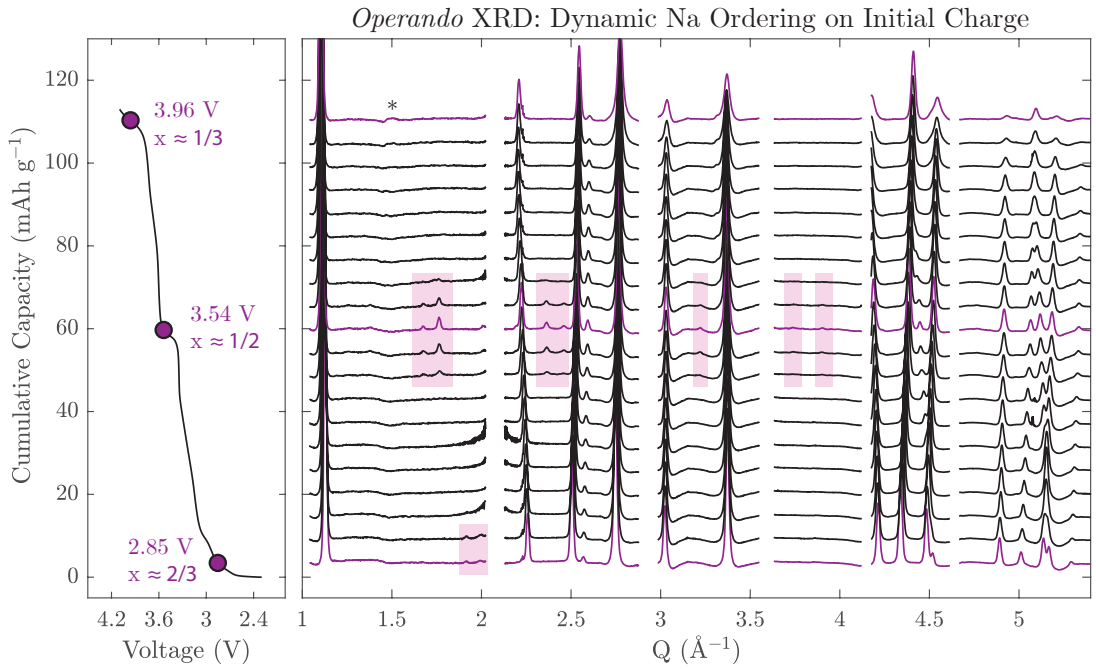

Figure 3.5: *Operando* XRD was carried out at APS 11-ID-B on initial charge of $Na_{2/3}[Ni_{1/3}Mn_{2/3}]O_2$ to 4.1 V vs. Na^+/Na. Superstructure peaks stemming from Na-ion ordering are highlighted with purple shading. The bump marked with an asterisk at 3.96 V is a spurious feature of the background subtraction and is not a peak. Intense peaks from the counter electrode (metallic Na) are omitted from the pattern.

Dynamic Na Ordering Evidenced by *Operando* XRD

Synchrotron *operando* XRD was undertaken to identify if there were any extra peaks stemming from long range Na ordering at either the $x = 1/2$ or $1/3$ compositions. *Ex situ* work has been carried out previously by Lee et al. but the samples were not adequately protected from moisture exposure.[3] For the *operando* data reported here, the patterns corresponding to the first charge up to 4.1 V vs. Na^+/Na are shown in Figure 3.5. At $x = 1/2$, there are indeed several extra peaks that appear in the pattern. This is the first diffraction-based experimental evidence of Na-ion ordering at this composition. Attempts to fit this data to the computationally predicted model by Lee et al. were unsuccessful. Instead, the ordering arrangement of $Na_{1/2}[Ni_{1/3}Mn_{2/3}]O_2$ matches that of $Na_{1/2}CoO_2$ reported by Bertelot et al. and Huang et al.[17, 19]: an orthorhombic $\sqrt{3}a \times 2a \times c$ superstructure (space group: *Pnmn*) of the original small hexagonal unit cell (space group: $P6_3/mmc$). A Rietveld refinement was carried out with this larger unit cell with the results

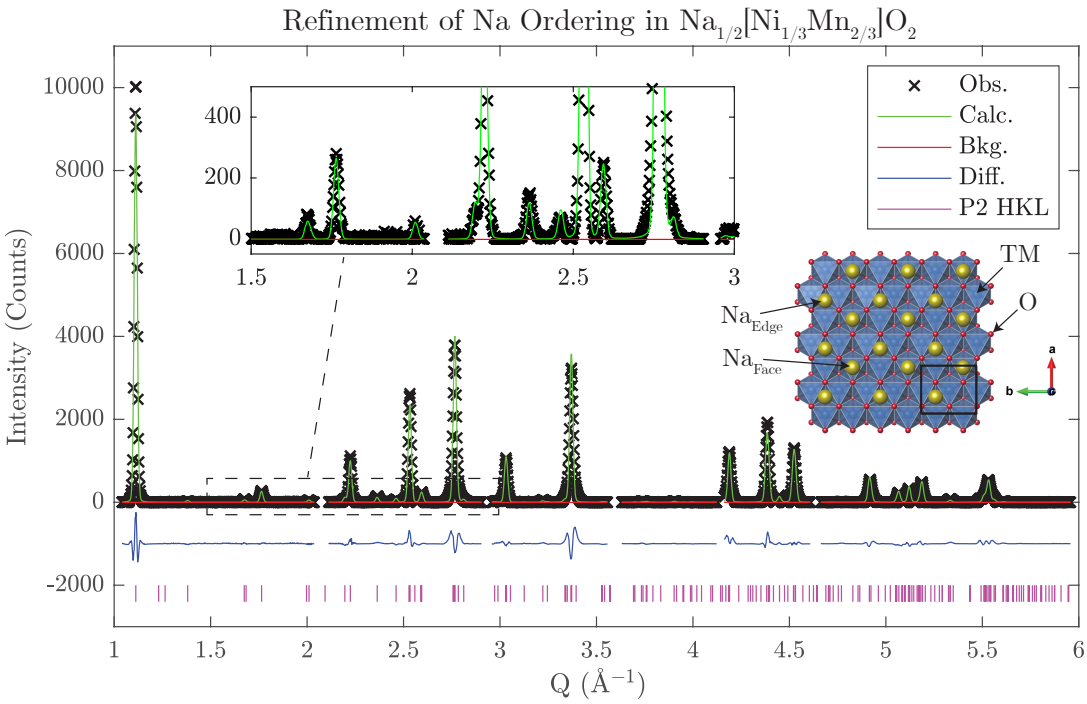

Figure 3.6: A Rietveld refinement of the 3.54 V ($Na_{1/2}[Ni_{1/3}Mn_{2/3}]O_2$) pattern from the background subtracted *operando* XRD data set. The highlighted inset shows the good fit of the small Na ordering peaks by the model. The Na-ion ordering arrangement proposed by Huang et al. is shown at the bottom right.[19] Refined parameters are shown in Table 3.3.

shown in Figure 3.6 and Table 3.3. The inset of Figure 3.6 highlights the good fit of all the additional peaks stemming from the Na-ion ordering superstructure. The Na-ion ordering arrangement proposed by Huang et al. is illustrated on the crystal structure in the figure and is made up of alternating rows of Na-ions face sharing with a TM and Na-ions that edge share with a TM.

No extra peaks are seen at the composition $x = 1/3$. This is not surprising as it was previously shown that this composition is plagued with stacking faults (interlayer disorder).[20] Therefore, while Na ordering could very well be occurring at this Na content, the domain size may be too small to probe with long-range diffraction techniques.

All of these results clearly support the fact that $Na_{2/3}[Ni_{1/3}Mn_{2/3}]O_2$ is a highly ordered material. While this compound has the strong appeal of a very high average voltage and capacity, its capacity retention on cycling is far from satisfactory.

Table 3.3: Results from the Rietveld refinement of the 3.54 V ($Na_{1/2}[Ni_{1/3}Mn_{2/3}]O_2$) pattern. Fit is shown in Figure 3.6

S.G. *Pnmn*, *a*: 4.9706(5) Å, *b*: 5.7229(4) Å, *c*: 11.298(1) Å, Rwp: 23.71%, Rexp: 7.65%					
Atom	**x**	**y**	**z**	**SOF**	**Uiso (Å²)**
Na (2b)	-0.035(5)	1/4	3/4	1	0.065(5)
Na (2a)	0.331(5)	3/4	3/4	1	0.065(5)
Ni (4e)	0	1/4	0	1/3	0.013(1)
Mn (4e)	0	1/4	0	2/3	0.013(1)
Ni (4d)	1/2	0	0	1/3	0.013(1)
Mn (4d)	1/2	0	0	2/3	0.013(1)
O (4e)	0.322(2)	1/4	0.103(2)	1	0.035(3)
O (4e)	0.347(4)	3/4	0.067(2)	1	0.035(3)
O (8g)	-0.172(2)	-0.012(2)	0.083(1)	1	0.035(3)

Moreover, the various voltage steps caused by Na-ion ordering are not favorable for a real battery cell as this could cause sudden changes in the delivered power to a device (unless an advanced battery management system is used). Significant research has therefore been dedicated to tuning the composition of this compound with substituents to improve the capacity retention and suppress the Na-ion ordering while retaining a high voltage.

3.4.2 Exploration of Na[Ni, Fe, Mn]O_2 Compounds

While Ni and Mn are commonly found in commercial Li-ion battery cathodes materials, Li-ion layered oxide compounds containing Fe have shown relatively poor performance to date. It has been postulated that this is due to the large ionic radius of Fe^{3+} (comparable to that of Li^+), which induces anti-site disorder.[21] Na-ion layered oxide cathodes have an inherent benefit by comparison as Na^+ is larger than Li^+ and therefore, layered structures are more easily stabilized even for large TMs such as Fe^{3+}.[22]

As such, the composition space between MnO_2, $Na[Ni_{1/2}Mn_{1/2}]O_2$ and $NaFeO_2$ was explored with the goal of identifying a P2 compound that contains mostly Fe and Mn due to the low cost of these elements but also has a high voltage. The capacity compensated by the $Mn^{4+/3+}$ redox couple should therefore be kept to a minimum as this generally operates at a much lower voltage than the $Ni^{4+/2+}$

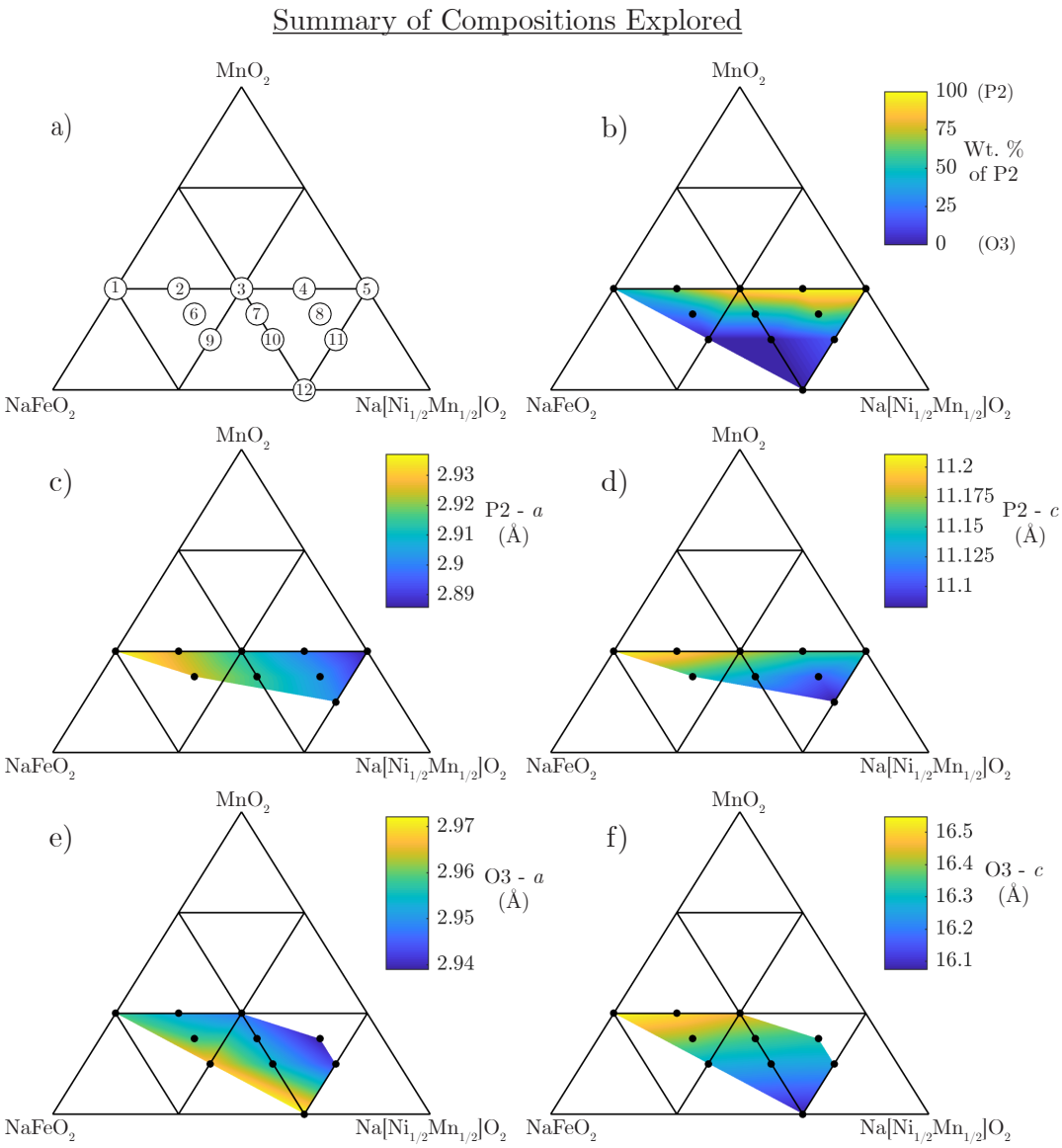

Figure 3.7: Twelve compositions were synthesized at 900 °C under flowing oxygen and the resulting compounds were evaluated with XRD. a) shows the compositions on the ternary composition diagram with the numbers referencing Table 3.4. b) shows the refined weight percentages of the P2 and O3 phases. c) and d) show the P2 a and c parameters, respectively. e) and f) show the O3 a and c parameters, respectively.

and $Fe^{4+/3+}$ redox.[23] Figure 3.7 displays a ternary composition diagram between the previously mentioned end member compositions. In total, twelve compositions (listed in Table 3.4) were investigated by XRD. Full refinement results are available in the Appendix (Figures A.1 - A.12 and Tables A.1 - A.12). A summary of the results is plotted on the ternary diagram as a linearly interpolated color map. The P2 and O3 lattice parameters, shown in Figure 3.7c - f, change steadily with

Table 3.4: Numbered Compositions from Figure 3.7

#	1	2	3	4	5	6	7	8	9	10	11	12
Na	2/3	2/3	2/3	2/3	2/3	3/4	3/4	3/4	5/6	5/6	5/6	1
Ni	0	1/12	1/6	1/4	1/3	1/8	5/24	7/24	1/6	1/4	1/3	1/3
Mn	1/3	5/12	1/2	7/12	2/3	3/8	11/24	13/24	1/3	5/12	1/2	1/3
Fe	2/3	1/2	1/3	1/6	0	1/2	1/3	1/6	1/2	1/3	1/6	1/3
O	2	2	2	2	2	2	2	2	2	2	2	2

composition as expected by Vegard's Law.[24]

Moving from top to bottom in this ternary diagram, the Na content increases from 0 to 1. No compositions were synthesized above the $Na_{2/3}MO_2$ (M = Ni, Fe, and/or Mn) line because 1) this would decrease the amount of capacity compensated by the high voltage $Ni^{4+/2+}$ and $Fe^{4+/3+}$ redox couples and 2) the ideal cathode candidate would not be Na deficient as this limits its capacity in a full cell (i.e. not a half cell vs. Na metal). As can be seen in Figure 3.7b, P2 compounds could only be synthesized very close to this upper limit. Shifting down in the ternary diagram of Figure 3.7b, the color changes from yellow to blue indicating the weight percentage of the P2 phase decreases at the expense of the O3 phase. It is well known that the stability of the P2 vs. O3 phases depends heavily on the Na content.[25, 26]

Interestingly, the percentage of P2 phase also seems to decrease as a function of Fe content (with Na remaining constant), moving from right to left in the diagram. The relationship of the structural stability (P2 vs. O3) based on the TM composition is much less understood than the relationship with Na content. For example, some groups have been able to extend the P2 solid solution as high as $x = 0.83$ Na per formula unit by substituting Li into the TM layer of the compound.[27–29] One hypothesis is that the P2 vs. O3 stabilities depend heavily on the interlayer spacing (P2 stabilized by greater spacing, O3 stabilized by lesser spacing).[30] The Li-O bond is very ionic, which means more charge will be localized on the oxygen rather than shared between the cation and anion (covalent). This excess negative charge on oxygen may increase the interlayer repulsion, and consequently the interlayer spacing, causing the stabilization of P2 with higher Na contents. This is also in line with findings by Delmas et al. that there is a correlation between the covalency of

the TM-O bond and the synthesized structure (higher covalency stabilizes O3).[31] Along that line of thinking, it is proposed here that the higher covalency of the Fe-O bond as compared to the Ni-O and Mn-O bonds, reduces interlayer repulsion and causes the preference for the O3 structure seen in these results.

Now returning to the original objective of identifying a low cost, high voltage P2 compound, it is clear that there are three options which fall in the P2 region of the diagram: that is $Na_{2/3}[Ni_{1/3-y/2}Mn_{2/3-y/2}Fe_y]O_2$ where $y = 0$, 1/6 and 1/3. Although the $y = 1/3$ composition is optimal in terms of cost (lowest amount of Ni), it was decided to characterize both the $y = 1/6$ and 1/3 to try to better understand the influence of Fe on the electrochemical and structural properties of the material. The $y = 0$ composition, which has already been detailed in this chapter, will be used as appropriate for comparison.

3.4.3 $\mathbf{Na_{2/3}[Ni_{1/3-y/2}Mn_{2/3-y/2}Fe_y]O_2}$ $\mathbf{(y = 1/6, 1/3)}$

The composition of two Fe containing compounds, $Na_{2/3}[Ni_{1/4}Mn_{7/12}Fe_{1/6}]O_2$ and $Na_{2/3}[Ni_{1/6}Mn_{1/2}Fe_{1/3}]O_2$ were confirmed with ICP-OES (Table 3.5) and further evaluated with synchrotron XRD (Appendix Figures A.13 and A.14, Tables A.13 and A.14), ND, and SEM shown in Figure 3.8. The SEM images in Figure 3.8a show that all three compounds crystallized into faceted particles ranging in size from 1 to 5 μm and were made up of stacked layers, which likely stem from the layered crystal structure. ND (Figure 3.8b) revealed that the honeycomb (TM ordering) superstructure peaks are lower in intensity in $Na_{2/3}[Ni_{1/4}Mn_{7/12}Fe_{1/6}]O_2$ than $Na_{2/3}[Ni_{1/3}Mn_{2/3}]O_2$, and completely disappear for $Na_{2/3}[Ni_{1/6}Mn_{1/2}Fe_{1/3}]O_2$.

Table 3.5: ICP-OES Composition Confirmation

Element	Na	Ni	Mn	Fe
Concentration (ppm)	0.748(7)	1.569(38)	0.633(4)	0.471(7)
Normalized Composition	0.68	0.59	0.23	0.18
Expected Composition	0.67	0.58	0.25	0.17
Concentration (ppm)	0.829(15)	1.553(23)	0.481(4)	0.959(31)
Normalized Composition	0.67	0.53	0.32	0.15
Expected Composition	0.67	0.5	0.33	0.17

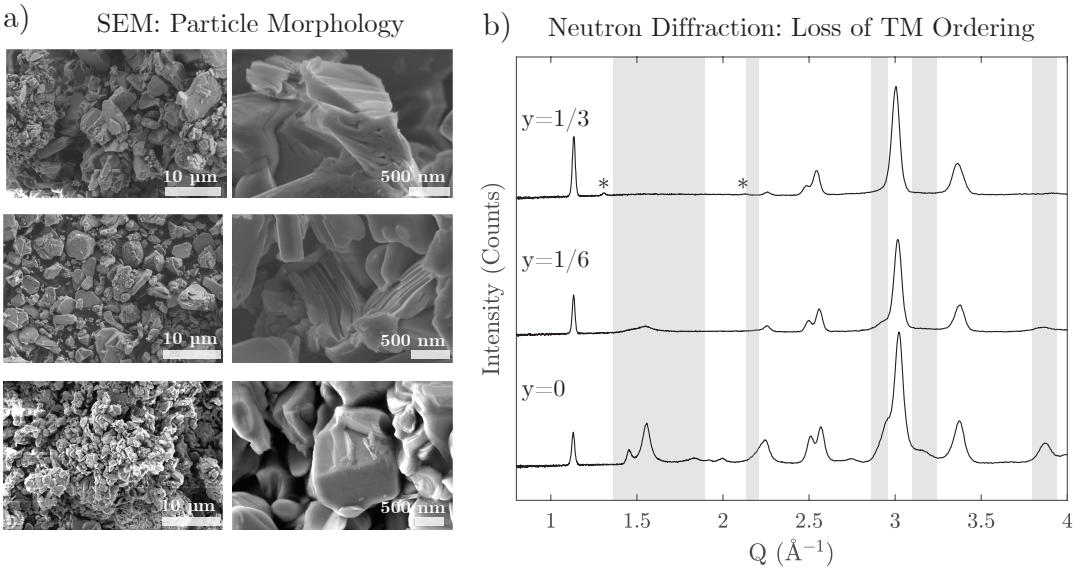

Figure 3.8: Scanning electron microscopy (SEM) images (taken by Dr. Urmimala Maitra) are shown in a) for $Na_{2/3}[Ni_{1/3-y/2}Mn_{2/3-y/2}Fe_y]O_2$; $y = 0$ (bottom), $y = 1/6$ (middle), and $y = 1/3$ (top). The neutron diffraction patterns (samples measured by Dr. Matthew Roberts) for each of these compounds are shown in b) with the grey regions highlighting the superstructure peaks stemming from honeycomb ordering of the TMs. The asterisks identify a very small quantity of Fe_3O_4.

This indicates that the substitution of Fe successfully disrupts the ordering between the Ni and Mn. This is in contrast to Mg substitution which retains the honeycomb superstructure.[32]

The substitution of Fe also has a rather profound effect on the electrochemistry. As can be seen in Figure 3.9a, the galvanostatic load curve was substantially smoothed by the addition of Fe. This is even more evident in the differential capacity plot in Figure 3.9b. The substitution of Fe not only breaks down the ordering in the TM layer in the pristine material but also seems to suppress the dynamic ordering of the Na-ions during charge and discharge. This comes at only a slight cost to the initial specific energy delivered ($y = 0$: 640, $y = 1/6$: 599, and $y = 1/3$: 587 Wh kg^{-1}). The first cycle discharge capacity is decreased for the Fe substituted samples and there is greater hysteresis of the load curve (ΔV of charge and discharge) at low Na contents. The structural evolution at low Na contents will be addressed in the next chapter. On the other hand, capacity retention improves with increasing Fe content as can be seen in Figure 3.9c.

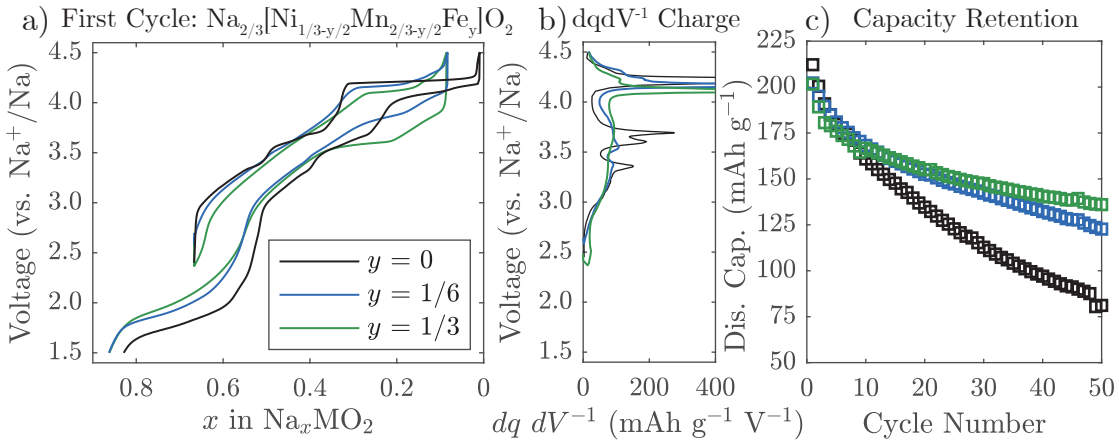

Figure 3.9: The electrochemical performance of $Na_{2/3}[Ni_{1/3}Mn_{2/3}]O_2$ ($y = 0$), $Na_{2/3}[Ni_{1/4}Mn_{7/12}Fe_{1/6}]O_2$ ($y = 1/6$), and $Na_{2/3}[Ni_{1/6}Mn_{1/2}Fe_{1/3}]O_2$ ($y = 1/3$) were probed with galvanostatic cycling at 10 mA g^{-1} between 1.5 and 4.5 V vs. Na^+/Na. The first cycle is shown in a), the differential capacity plot in b) and the capacity retention in c).

While the voltage range used here (1.5 - 4.5 V vs. Na^+/Na) is probably too large for real world applications, these compounds do show significant capacity above 3 V and have among the highest specific energies for any Na cathodes reported.[33] To better understand the mechanism of charge compensation in these Fe substituted compounds, the X-ray absorption near edge structure (XANES) was examined, *ex situ*, at several states of charge.

XANES is an excellent method for tracking oxidation states of a specific element of interest. In Figure 3.10, the XANES of $Na_{2/3}[Ni_{1/4}Mn_{7/12}Fe_{1/6}]O_2$ is shown in a) and that of $Na_{2/3}[Ni_{1/6}Mn_{1/2}Fe_{1/3}]O_2$ is shown in b). The various stopping points are shown in Figure 3.12. The Ni K-edge (excitation of the Ni 1s core electrons) shows the most change of the three TM edges on charge and discharge. On initial charge to 4.5 V, the Ni K-edge shows a positive shift for both compounds indicating a change to a higher oxidation state. Unfortunately, there is no good Ni^{4+} oxide standard, but the edge energy of both compounds does reach a very similar energy to that of $K_2Ni^{4+}F_6$, suggesting tetravalent Ni at the top of charge. Interestingly, the rate of change of the Ni K-edge energies is different for the two compounds. For $Na_{2/3}[Ni_{1/4}Mn_{7/12}Fe_{1/6}]O_2$, the edge shifts progressively until the upper voltage cutoff of 4.5 V is reached. On the other hand, for $Na_{2/3}[Ni_{1/6}Mn_{1/2}Fe_{1/3}]O_2$, the

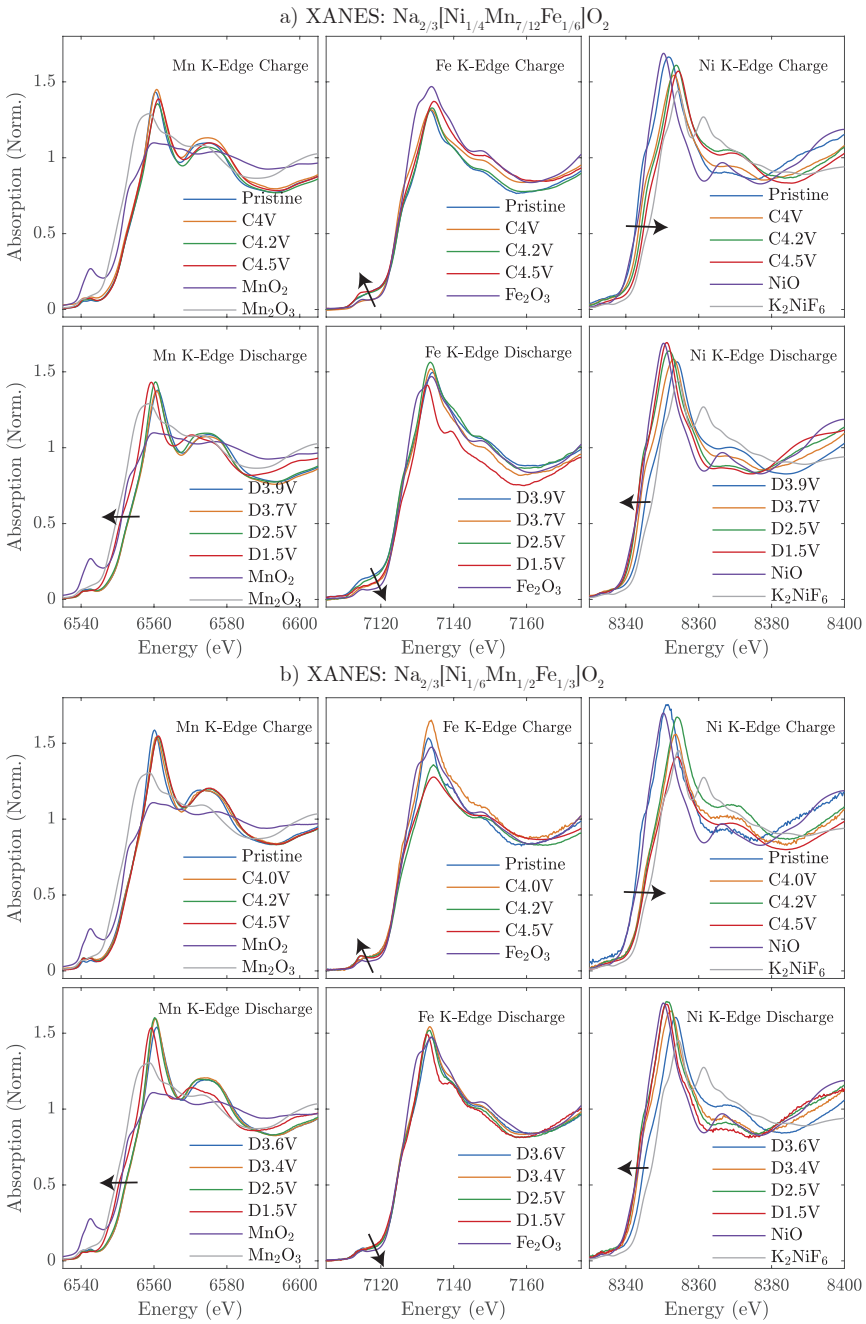

Figure 3.10: The XANES spectra of a) $Na_{2/3}[Ni_{1/4}Mn_{7/12}Fe_{1/6}]O_2$ and b) $Na_{2/3}[Ni_{1/6}Mn_{1/2}Fe_{1/3}]O_2$ are shown at various states of charges. Data was collected with the help of Dr. Nuria Tapia-Ruiz at DLS B-18 (Harwell, UK).

Ni K-edge shifts dramatically up until 4.0 V and then shows minimal change at higher charging voltages. It is generally understood that Ni^{2+} is oxidized before Fe^{3+} in $NaMO_2$ compounds, so this difference between the two compounds is likely an effect of the different concentrations of Ni.

The Mn K-edge does not show any rigid movement for either compound on charge. This is expected as Mn^{4+} is already the maximum oxidation state in layered compounds.[34] Upon discharge below 2.5 V, however, the edge shifts negatively towards that of the Mn_2O_3 (Mn^{3+}) standard indicating a reduction of Mn to account for this lower voltage capacity. At these low voltages, more Na is inserted into the compound than was present in the pristine state. This is only possible because P2 compounds are synthesized in a Na deficient state, as was discussed in the Introduction chapter (Section 1.2.4). It is therefore natural that another redox couple has to be activated to compensate for this extra insertion.

The Fe K-edge shows the least change of the three TM edges probed. This has been the case for a number of similar compounds, even when Fe is active in the charge compensation of Na extraction.[7] The two most noticeable modifications of the edge during charging are a) a decrease in the intensity of the "white line" - the most intense peak of the edge corresponding to electronic transitions from the 1s to 4p states and b) a slight increase in the intensity of the "pre-edge" - the small peak before the edge corresponding to transitions from the 1s to 3d states. Normal dipole selection rules indicate the pre-edge transition should be forbidden. Nevertheless, it is always seen in layered compounds due to a) slight anisotropy of the octahedra leading to mixing of the 3d and 4p orbitals and b) quadrupolar transitions which should appear an order of magnitude or so lower in intensity than allowed dipole transitions. The changes to the white line are consistent with the oxidation of Fe reported for $Na_{2/3}[Mn_{1/2}Fe_{1/2}]O_2$.[7] The pre-edge is more complicated. On one hand, an increase in intensity could merely indicate an increased anisotropy of the octahedra. On the other hand, it could also suggest that a small percentage of Fe is moving to tetrahedral sites, thus increasing anisotropy.

A technique that is more sensitive to the local environment of Fe, ^{57}Fe-Mössbauer Spectroscopy (^{57}Fe-MS), was therefore employed to better understand the behavior of Fe. Stopping points for the *ex situ* samples are again shown in Figure 3.12. ^{57}Fe-MS was carried out on the compound with higher Fe content, $Na_{2/3}[Ni_{1/6}Mn_{1/2}Fe_{1/3}]O_2$, at various states of charge and the results are shown in Figure 3.11. The pristine

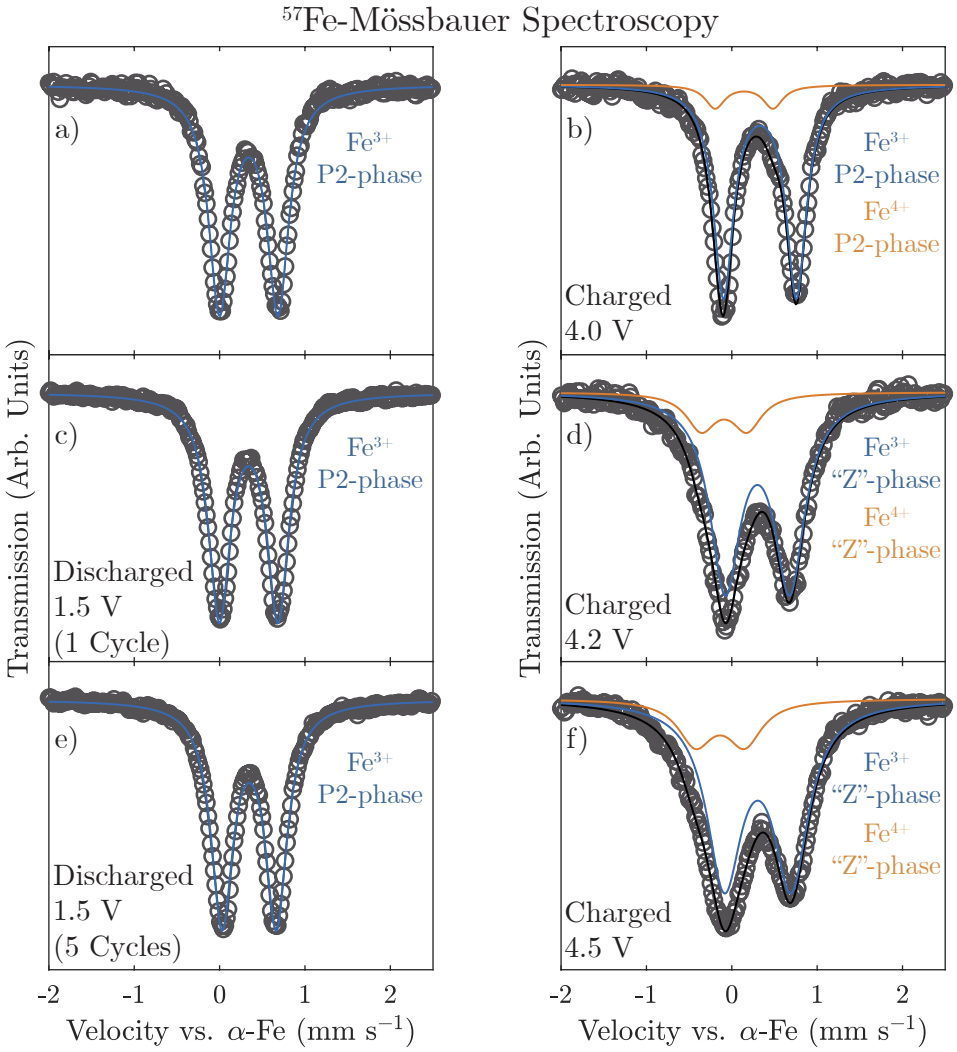

Figure 3.11: ^{57}Fe-Mössbauer Spectroscopy was conducted on a) pristine $Na_{2/3}[Ni_{1/6}Mn_{1/2}Fe_{1/3}]O_2$ and several *ex situ* samples charged to b) 4.0 V, d) 4.2 V, and f) 4.5 V as well as 1.5 V discharged samples cycled c) 1 and e) 5 times. The blue curves indicate the fitting of an Fe^{3+} doublet and the orange curves are an Fe^{4+} doublet. When necessary, a black curve is used to indicate the sum of the components. Dr. Adam Sobkowiak conducted the measurements as part of a collaboration with Uppsala University.

sample produced a doublet with hyperfine parameters, tabulated in Table 3.6, consistent with high spin (S = 5/2) Fe^{3+}. Upon charging to 4.0 V vs. Na^+/Na, an asymmetry appears in the spectra. This can be fitted with an additional doublet with a pronounced decrease in the center shift (CS) value. A decrease in the CS indicates an increase of the electron density at the nucleus. Accordingly, this doublet has previously been attributed to the presence of Fe^{4+}.[35, 36] The intensity of the

Table 3.6: ^{57}Fe-Mössbauer Spectroscopy Parameters (* = Fixed Value)

	CS (mm s^{-1})	**QS (mm s^{-1})**	**FWHM (mm s^{-1})**	**Relative Intensity**
Pristine	0.34(1)	0.68(1)	0.25(1)	100 % (Fe^{3+})
Charged 4.0 V	0.33(1)	0.85(1)	0.24(1)	90 % (Fe^{3+})
	0.14(1)	0.68(1)	0.24*	10 % (Fe^{4+})
Charged 4.2 V	0.30(1)	0.75(1)	0.31(1)	84 % (Fe^{3+})
	-0.09(1)	0.54(1)	0.31*	16 % (Fe^{4+})
Charged 4.5 V	0.30(1)	0.78(1)	0.35(1)	80 % (Fe^{3+})
	-0.14(1)	0.58(1)	0.35*	20 % (Fe^{4+})
Discharged 1.5 V, 1 cycle	0.34(1)	0.69(1)	0.25(1)	100 % (Fe^{3+})
Discharged 1.5 V, 5 cycles	0.35(1)	0.64(1)	0.25(1)	100 % (Fe^{3+})

Fe^{4+} signal increases further for samples stopped at 4.2 V and 4.5 V, up to a total spectral weight of 20%. If it is assumed that the charge passed by the battery on charging is equivalent to the amount of Na^+ extracted and that Ni is fully oxidized to the 4+ state, then the expected reaction would be as follows:

$$Na^{+}_{2/3}[Ni^{2+}_{1/6}Mn^{4+}_{1/2}Fe^{3+}_{1/3}]O^{2-}_{2} \rightarrow Na^{+}_{0.1}[Ni^{4+}_{1/6}Mn^{4+}_{1/2}Fe^{3.7+}_{1/3}]O^{2-}_{2} \quad (3.1)$$

In that case, the Fe^{4+} signal would be expected to have a contribution of 70%. This is a disparity that has been previously observed with a number of Fe containing $NaMO_2$ materials to varying degrees.[8, 36] While the possibility of partial charge compensation by $O^{2-/n-}$ (n<2) cannot be ruled out completely, a more likely cause is reduction of the cathode by reaction with the electrolyte. Fe seems to catalyze this reaction as has been clearly demonstrated by Lee et al. for charged $NaFeO_2$.[37]

The existence of tetrahedrally coordinated Fe can also be probed with ^{57}Fe-MS. The signal for such a species exhibits a very large quadrupolar splitting (QS) value as was shown by Talaie et al.[8] The addition of a doublet with large QS to the data presented here, however, did not improve the fit quality to the spectra. Therefore, it was determined that there is no significant migration of Fe in this compound. On discharge to 1.5 V, the spectra returns to a single Fe^{3+} doublet and even after 5 cycles, there are no additional signals indicating good electrochemical reversibility of the compound as a cathode.

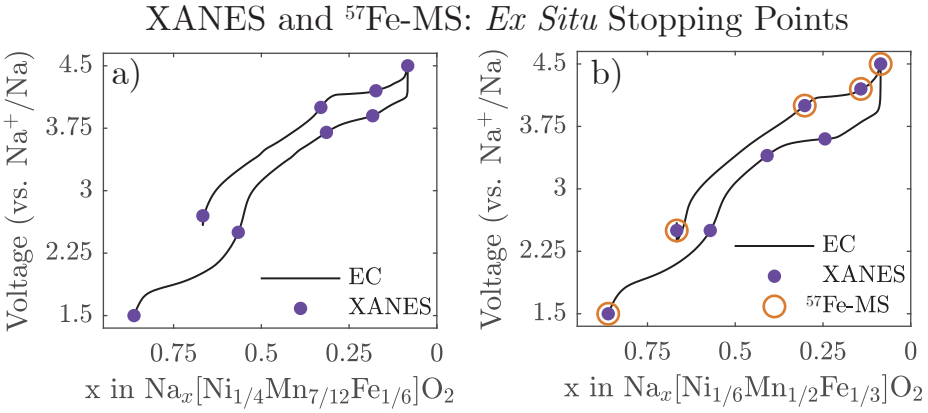

Figure 3.12: The stopping points of each of the *ex situ* samples used for XANES and ^{57}Fe-MS measurements, showing $Na_{2/3}[Ni_{1/4}Mn_{7/12}Fe_{1/6}]O_2$ in a) and $Na_{2/3}[Ni_{1/6}Mn_{1/2}Fe_{1/3}]O_2$ in b).

Despite the seemingly good chemical reversibility of $Na_{2/3}[Ni_{1/4}Mn_{7/12}Fe_{1/6}]O_2$ and $Na_{2/3}[Ni_{1/6}Mn_{1/2}Fe_{1/3}]O_2$, both compounds still show unsatisfactory cycle retention (<75 % after 50 cycles). The plateau in the electrochemical load curve above 4.0 V on charge has been seen in a number of compounds and indicates dramatic structural changes which are deleterious to capacity retention.[8, 38–40] In Chapter 4, this high voltage structural evolution will be examined in detail to better understand the mechanism of these structural transitions.

Another more general concern with P2 compounds is their Na deficiency. In Section 3.4.2, efforts were made to increase the Na content in the as-synthesized compound but this led to the formation of the O3 structure. A different route to overcoming this Na deficiency will now be discussed, which is a pre-treatment with the reducing agent: Na-naphthalide.

3.4.4 Overcoming Na Deficiency in P2 compounds

P2-type Na cathodes can only be synthesized in a Na deficient state. This can be thought of as the compound existing at approximately a 33% state of charge (at $x = 0.67$ in Na_xMO_2). In a simple "half-cell" laboratory test, metallic Na is used as an anode. The metallic Na anode can supply extra Na to the cathode if the battery is discharged to voltages below the starting point, utilizing that extra 33%

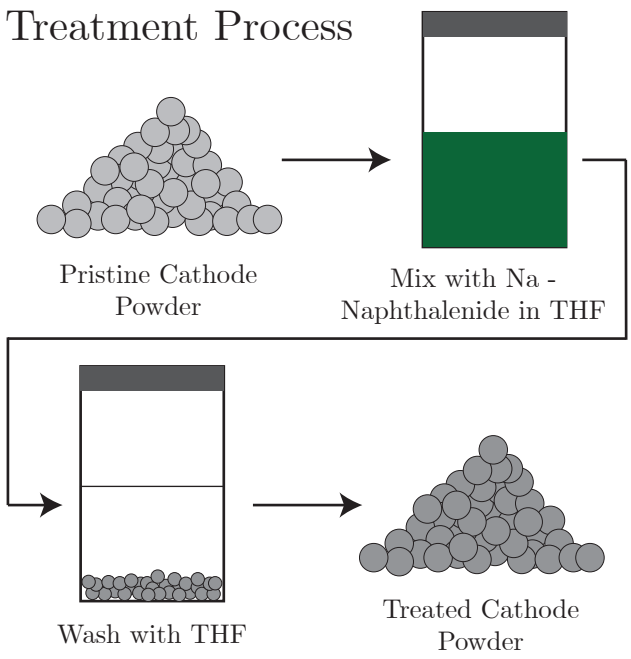

Figure 3.13: A schematic of the Na naphthalide treatment process is shown. The P2-type cathode powder is mixed with a Na naphthalide solution. The solution reduces the material, inserting Na-ions into the vacant sites in the Na layer. The powder is then washed with THF solution to remove excess solution before being dried under vacuum.

capacity. This is why the compounds presented so far can have such high discharge capacities. In a "full cell", however, hard carbon materials are most often used in place of Na metal to improve safety and reversibility. These hard carbon materials do not contain any Na and therefore cannot supply extra Na to the system to balance out the deficiency of the P2 cathode the way Na metal can.

Various efforts have been made to compensate the lack of Na in P2 compounds such as adding of a sacrificial salt (e.g. NaN_3),[41] ball milling the cathode directly with Na metal,[42] and adding excess Na_2CO_3 precursor during synthesis.[16] Here, an alternative method is reported by means of pre-treatment of the cathode material with a Na naphthalide solution.

Before the wide adoption of cathode materials that are prepared in the discharged state (e.g. $LiCoO_2$), solutions of Na and Li naphthalide were used to screen cathode materials for their intercalation chemistry.[43, 44] The reducing agent is easily prepared by adding metallic Na (or other alkali metals) to a solution of

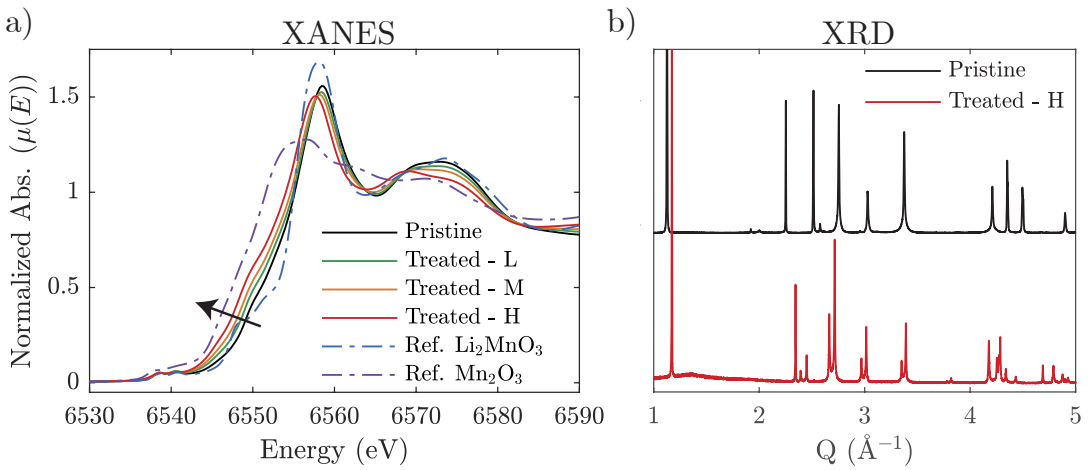

Figure 3.14: $Na_{2/3}[Ni_{1/3}Mn_{2/3}]O_2$ was treated with Na naphthalide and the success of this treatment process was investigated with a) Mn K-edge XANES to look at oxidation state changes and b) XRD to identify the structural changes. The concentration of the treatment solutions are identified as either low (L: 1/6 mol Na), medium (M: 1/3 mol Na) or high (H: 2/3 mol Na). The XANES data was measured at DLS B-18 and the XRD data was collected via the APS-11BM mail-in program.

naphthalene in tetrahydrofuran (THF) in equal molar ratios. The Na metal reduces the naphthalene to the reactive naphthalide anion as follows:

$$\mathrm{Na\ (s) + C_{10}H_8\ (sol) \rightarrow Na^+\ (sol) + [C_{10}H_8]^-\ (sol)} \tag{3.2}$$

The Na naphthalide solution is a dark green color and has almost the same reducing potential as Na metal itself (-2.71 V vs. SHE).[43]

Once the solution is prepared, it can then be directly added to a vial containing the P2 cathode powder as illustrated in Figure 3.13. The naphthalide anion reduces the material while intercalating Na^+ to keep charge neutrality. Once the reaction is complete, the treated cathode powder is washed with THF to get rid of any excess reagents and then dried under vacuum. $Na_{2/3}[Ni_{1/3}Mn_{2/3}]O_2$ was used as a model compound to test the feasibility of this treatment with the reaction expected to occur as follows:

$$\begin{aligned}\mathrm{Na^+_{2/3}[Ni^{2+}_{1/3}Mn^{4+}_{2/3}]O^{2-}_2 + Na^+[C_{10}H_8]^-\ (sol) \rightarrow} \\ \mathrm{Na^+[Ni^{2+}_{1/3}Mn^{3.5+}_{2/3}]O^{2-}_2 + C_{10}H_8\ (sol)}\end{aligned} \tag{3.3}$$

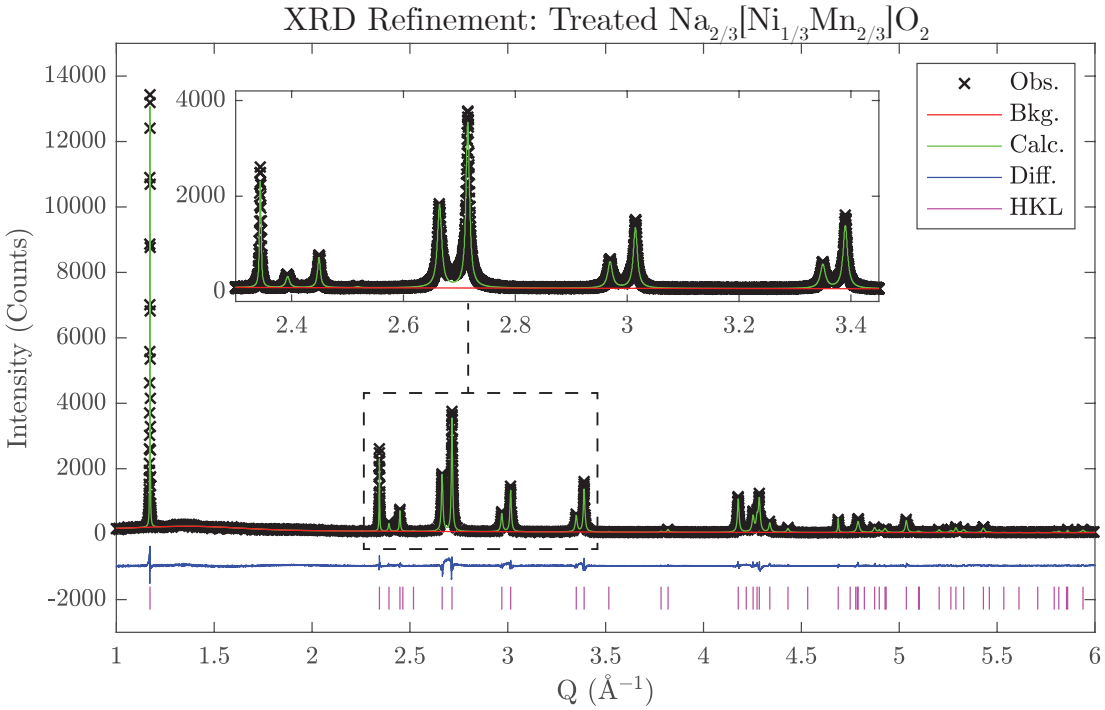

Figure 3.15: XRD data for the Na-naphthalide treated $Na_{2/3}[Ni_{1/3}Mn_{2/3}]O_2$ compound is shown with the corresponding fitting from the Rietveld refinement. Refined parameters are listed in Table 3.7. The inset clearly shows the orthorhombic distortion (peak splitting) caused by the presence of Jahn-Teller active Mn^{3+}.

XANES was conducted on the Mn K-edge to confirm the Mn oxidation state changed from 4+ to 3.5+ as predicted in Equation 3.3 (Figure 3.14a). Three concentrations of the Na naphthalide in 10 mL of THF were prepared: Low (L): 1/6 mol equivalents of $Na^+[C_{10}H_8]^-$, Medium (M): 1/3 mol equivalents, and High (H) 2/3 mol equivalents. The solutions therefore contained enough Na to fill 50%, 100%, and 200% (excess) of the available sites, respectively. The Mn K-edge progressively shifts in the negative direction with increasing concentration, indicating the reduction of Mn. In theory, the medium concentration solution should contain enough $Na^+[C_{10}H_8]^-$ to fully reduce the Mn in the compound to 3.5+, however, it seems the high concentration solution (excess) was necessary, as evidenced by the XANES edge for this sample presenting halfway (qualitatively) between the Mn_2O_3 (Mn^{3+}) reference and the untreated compound (Mn^{4+}).

The presence of a significant quantity of Jahn-Teller active Mn^{3+} in P2 compounds has previously been shown to cause an orthorhombic distortion to the ideal hexagonal

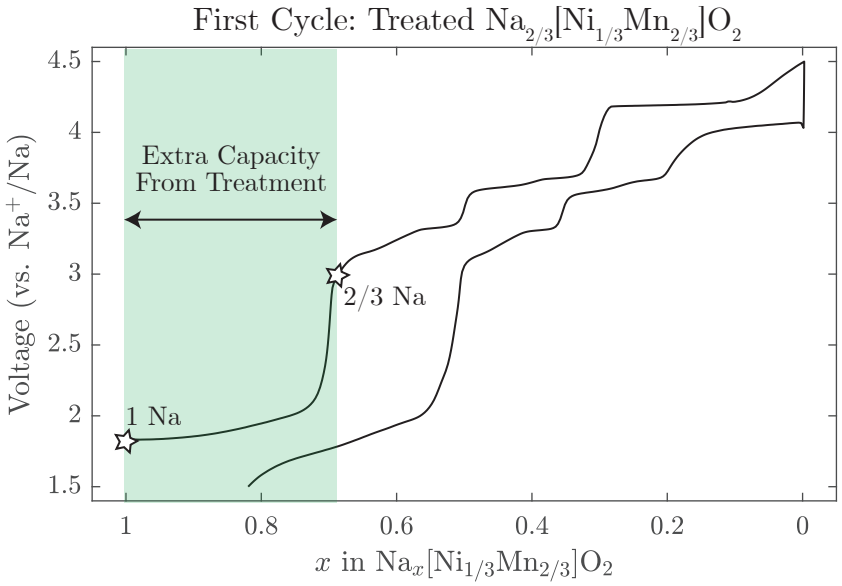

Figure 3.16: The first charge/discharge cycle for the Na naphthalide treated $Na_{2/3}[Ni_{1/3}Mn_{2/3}]O_2$ is shown. Extra capacity is clearly seen at the beginning of the first charge and is highlighted in green.

structure, termed P'2.[45] This distortion is clearly seen in the XRD when compared to the untreated sample in Figure 3.14b. The crystallographic parameters were refined by a Rietveld refinement shown in Figure 3.15 and Table 3.7. The results confirm that the structure has transitioned to the distorted P'2 structure (space group: *Cmcm*). Moreover, the total Na content refines to 0.97 in $Na_x[Ni_{1/3}Mn_{2/3}]_2$ which further verifies the the success of the treatment process. The refinement showed that all Na-ions exclusively occupy the edge sharing trigonal prismatic site (and not the face sharing site).

Finally, the treated material was galvanostatically cycled in a half cell with the

Table 3.7: Rietveld refinement results for $Na_{2/3}[Ni_{1/3}Mn_{2/3}]O_2$ treated with Na naphthalide, from data collected at APS-11BM.

S.G. *Cmcm*, *a*: 2.94044(2) Å, *b*: 5.25120(4) Å, *c*: 10.72137(7) Å, Rwp: 12.78%, Rexp: 9.76%					
Atom	**x**	**y**	**z**	**SOF**	**Uiso (Å²)**
Na (4c)	0	0.6767(2)	1/4	0.971(3)	0.0030(4)
Ni (4a)	0	0	0	1/3	0.0032(1)
Mn (4a)	0	0	0	2/3	0.0032(1)
O (8f)	0	0.6623(3)	0.9027(1)	1	0.0101(3)

electrochemical load curve shown in Figure 3.16. On assembly, the open circuit voltage read 1.77 V vs. Na^+/Na; significantly lower than the typical 2.6 V for compounds synthesized in oxygen containing atmospheres. When the cell was charged, the initial $\Delta x = 1/3$ Na was extracted along a lower voltage plateau at approximately 1.9 V (highlighted in green). This is the same voltage seen when Na is inserted into the $Na_{2/3}[Ni_{1/3}Mn_{2/3}]O_2$ compound beyond the starting composition during discharge, as was shown previously in Figure 3.4.

In summary, it has been proven that the pre-treatment of P2 compounds (using $Na_{2/3}[Ni_{1/3}Mn_{2/3}]O_2$ as a model compound) by Na naphthalide solution successfully compensates the Na deficiency of the as-synthesized compound. The feasibility of implementing this solution into a commercial electrode roll to roll process should be explored. A major challenge to this will be the high reactivity of the Na naphthalide solution. Despite this obstacle, such a process would almost certainly be more easily implemented than a ball milling step (with metallic Na) and would not have the first cycle gassing issues associated with sacrificial salts/precursors.

3.5 Conclusion

As was previously established, an ideal battery cathode should have a high capacity, high voltage, high rate, good safety, satisfactory cycling retention, and be composed of sustainable elements. As a class of compounds, P2-type Na cathodes show great promise to meet these stringent requirements. In this chapter, $Na_{2/3}[Ni_{1/3}Mn_{2/3}]O_2$ was first studied in detail as a model P2 compound due to its very favorable specific energy. Due to size/charge difference of Ni and Mn and their 1:2 ratio in the compound, the stable honeycomb ordered superstructure forms. Additionally, Na-ions were also evidenced to order, even at temperatures as high as 300 °C, demonstrating the strong thermodynamic driving force for this phenomenon to occur. Moreover, the first experimental evidence of dynamic Na ordering upon charge, corresponding to $Na_{1/2}[Ni_{1/3}Mn_{2/3}]O_2$, was shown with synchrotron *operando* XRD. The addition of low-cost Fe in the compound was probed, and shown to relieve the ordering completely. $Na_{2/3}[Ni_{1/6}Mn_{1/2}Fe_{1/3}]O_2$ was demonstrated to

utilize all three TM redox couples in charge compensating Na, giving a relatively high specific energy and improved cycling retention compared with $Na_{2/3}[Ni_{1/3}Mn_{2/3}]O_2$. Finally, the significant problem of Na deficiency in as-synthesized P2 compounds was addressed by demonstrating the effectiveness of a new pre-treatment method involving a Na naphthalide solution.

3.6 References

(1) Mo, Y.; Ong, S. P.; Ceder, G. *Chemistry of Materials* **2014**, *26*, 5208–5214.

(2) Lu, Z.; Donaberger, R. a.; Dahn, J. R. *Chemistry of Materials* **2000**, *12*, 3583–3590.

(3) Lee, D. H.; Xu, J.; Meng, Y. S. *Physical chemistry chemical physics : PCCP* **2013**, *15*, 3304–12.

(4) Gutierrez, A.; Dose, W. M.; Borkiewicz, O.; Guo, F.; Avdeev, M.; Kim, S.; Fister, T. T.; Ren, Y.; Bareño, J.; Johnson, C. S. *Journal of Physical Chemistry C* **2018**, *122*, 23251–23260.

(5) Zhao, W.; Kirie, H.; Tanaka, A.; Unno, M.; Yamamoto, S.; Noguchi, H. *Materials Letters* **2014**, *135*, 131–134.

(6) Li, Z.; Gao, R.; Zhang, J.; Zhang, X.; Hu, Z.; Liu, X. *Journal of Materials Chemistry A* **2016**, *4*, 3453–3461.

(7) Yabuuchi, N.; Kajiyama, M.; Iwatate, J.; Nishikawa, H.; Hitomi, S.; Okuyama, R.; Usui, R.; Yamada, Y.; Komaba, S. *Nature Materials* **2012**, *11*, 512–517.

(8) Talaie, E.; Duffort, V.; Smith, H. L.; Fultz, B.; Nazar, L. F. *Energy & Environmental Science* **2015**, *8*, 2512–2523.

(9) Toby, B. H.; Von Dreele, R. B. *Journal of Applied Crystallography* **2013**, *46*, 544–549.

(10) Ravel, B.; Newville, M. In *Journal of Synchrotron Radiation*, 2005; Vol. 12, pp 537–541.

(11) Lagarec, K.; Rancourt, D. *Nuclear Instruments and Methods in Physics Research Section B: Beam Interactions with Materials and Atoms* **1997**, *129*, 266–280.

(12) Borkiewicz, O. J.; Shyam, B.; Wiaderek, K. M.; Kurtz, C.; Chupas, P. J.; Chapman, K. W. *Journal of Applied Crystallography* **2012**, *45*, 1261–1269.

(13) Henke, B. L.; Gullikson, E.; Davis, J. *Atomic Data and Nuclear Data Tables* **1993**.

(14) Sears, V. F. *Neutron News* **1992**, *3*, 26–37.

(15) Paulsen, J. M.; Donaberger, R. A.; Dahn, J. R. *Chemistry of Materials* **2000**, *12*, 2257–2267.

(16) Sathiya, M.; Thomas, J.; Batuk, D.; Pimenta, V.; Gopalan, R.; Tarascon, J.-M. *Chemistry of Materials* **2017**, *29*, 5948–5956.

(17) Berthelot, R.; Carlier, D.; Delmas, C. *Nature Materials* **2011**, *10*, 74–80.

(18) Guignard, M.; Didier, C.; Darriet, J.; Bordet, P.; Elkaïm, E.; Delmas, C. *Nature materials* **2013**, *12*, 74–80.

(19) Huang, Q.; Foo, M. L.; Lynn, J. W.; Zandbergen, H. W.; Lawes, G.; Wang, Y.; Toby, B. H.; Ramirez, A. P.; Ong, N. P.; Cava, R. J. *Journal of Physics: Condensed Matter* **2004**, *16*, 5803–5814.

(20) Lu, Z.; Dahn, J. R. *Journal of The Electrochemical Society* **2001**, *148*, A1225–A1229.

(21) Ado, K.; Tabuchi, M.; Kobayashi, H.; Kageyama, H.; Nakamura, O.; Inaba, Y.; Kanno, R.; Takagi, M.; Takeda, Y. *J. Electrochem. Soc.* **1997**, *144*, L177.

(22) Kubota, K.; Yabuuchi, N.; Yoshida, H.; Dahbi, M.; Komaba, S. *MRS Bulletin* **2014**, *39*, 416–422.

(23) Nanba, Y.; Iwao, T.; de Boisse, B. M.; Zhao, W.; Hosono, E.; Asakura, D.; Niwa, H.; Kiuchi, H.; Miyawaki, J.; Harada, Y.; Okubo, M.; Yamada, A. *Chemistry of Materials* **2016**, *28*, 1058–1065.

(24) Wikipedia Vegard's law., 2017.

(25) Lei, Y.; Li, X.; Liu, L.; Ceder, G. *Chemistry of Materials* **2014**, *26*, 5288–5296.

(26) Radin, M. D.; Van der Ven, A. *Chemistry of Materials* **2016**, *28*, 7898–7904.

(27) Kim, D.; Kang, S.-H.; Slater, M.; Rood, S.; Vaughey, J. T.; Karan, N.; Balasubramanian, M.; Johnson, C. S. *Advanced Energy Materials* **2011**, *1*, 333–336.

(28) Xu, J.; Lee, D. H.; Clément, R. J.; Yu, X.; Leskes, M.; Pell, A. J.; Pintacuda, G.; Yang, X.-Q.; Grey, C. P.; Meng, Y. S. *Chemistry of Materials* **2014**, *26*, 1260–1269.

(29) Yabuuchi, N.; Hara, R.; Kajiyama, M.; Kubota, K.; Ishigaki, T.; Hoshikawa, A.; Komaba, S. *Advanced Energy Materials* **2014**, *4*, 1301453.

(30) Katcho, N. A.; Carrasco, J.; Saurel, D.; Gonzalo, E.; Han, M.; Aguesse, F.; Rojo, T. *Advanced Energy Materials* **2016**, 1601477.

(31) Delmas, C.; Fouassier, C.; Hagenmuller, P. *Physica B+C* **1980**, *99*, 81–85.

(32) Tapia-Ruiz, N.; Dose, W. M.; Sharma, N.; Chen, H.; Heath, J.; Somerville, J. W.; Maitra, U.; Islam, M. S.; Bruce, P. G. *Energy & Environmental Science* **2018**, *11*, 1470–1479.

(33) Clément, R. J.; Bruce, P. G.; Grey, C. P. *Journal of The Electrochemical Society* **2015**, *162*, A2589–A2604.

(34) Robertson, A. D.; Bruce, P. G. *Chemistry of Materials* **2003**, *15*, 1984–1992.

(35) Takeda, Y.; Nakahara, K.; Nishijima, M.; Imanishi, N.; Yamamoto, O.; Takano, M.; Kanno, R. *Materials Research Bulletin* **1994**, *29*, 659–666.

(36) Zhao, J.; Zhao, L.; Dimov, N.; Okada, S.; Nishida, T. *Journal of the Electrochemical Society* **2013**, *160*, A3077–A3081.

(37) Lee, E.; Brown, D. E.; Alp, E. E.; Ren, Y.; Lu, J.; Woo, J.-J.; Johnson, C. S. *Chemistry of Materials* **2015**, *27*, 6755–6764.

(38) Mortemard de Boisse, B.; Carlier, D.; Guignard, M.; Bourgeois, L.; Delmas, C. *Inorganic chemistry* **2014**, *53*, 11197–205.

(39) Wang, P. F.; You, Y.; Yin, Y. X.; Wang, Y. S.; Wan, L. J.; Gu, L.; Guo, Y. G. *Angewandte Chemie - International Edition* **2016**, *55*, 7445–7449.

(40) You, Y.; Xin, S.; Asl, H. Y.; Li, W.; Wang, P.-F.; Guo, Y.-G.; Manthiram, A. *Chem* **2018**, *4*, 2124–2139.

(41) Martinez De Ilarduya, J.; Otaegui, L.; López del Amo, J. M.; Armand, M.; Singh, G. *Journal of Power Sources* **2017**, *337*, 197–203.

(42) Zhang, B.; Dugas, R.; Rousse, G.; Rozier, P.; Abakumov, A. M.; Tarascon, J.-M. *Nature Communications* **2016**, *7*, 10308.

(43) Silbernagel, B. G.; Whittingham, M. S. *Materials Research Bulletin* **1976**, *11*, 29–36.

(44) Murphy, D. W.; Christian, P. A. *Science* **1979**, *205*, 651–656.

(45) Kumakura, S.; Tahara, Y.; Sato, S.; Kubota, K.; Komaba, S. *Chemistry of Materials* **2017**, *29*, 8958–8962.

4

Investigating the High Voltage Structural Evolution of P2-Type Cathodes

Contents

4.1 Abstract

Layered oxide cathodes often undergo structural transitions when charged to high voltages (> 4 V vs. Na^+/Na). Among P2-type $NaMO_2$ materials, some compounds such as $Na_{2/3}[Ni_{1/3}Mn_{2/3}]O_2$ undergo a simple (yet detrimental) transition to a fully de-sodiated O2 structure. Others progress through a more complicated structural pathway which has been difficult to probe in the past due to a considerable amount

of interlayer disorder. This uncertainty has led some authors to designate this type of high voltage structure as the "Z"-phase. In this chapter, *operando* and *ex situ* synchrotron XRD of $Na_{2/3}[Ni_{1/3-y/2}Mn_{2/3-y/2}Fe_y]O_2$ (y = 0, 1/6, 1/3) and $Na_{2/3}[Mn_{1/2}Fe_{1/2}]O_2$ are presented and analyzed. This data is further evaluated by comparison to simulated XRD patterns of structures containing varying percentages of (O2-type) stacking faults in order to discern the true structural identity of the "Z"-phase. It is shown that the "Z"-phase is not actually one unique phase but rather an *evolving intergrowth* of P2 and O2. Na extraction is compensated by an increasing fraction of vacant O2-type layers at the expense of the sodiated P2-type layers. As the OP intergrowth proceeds through key ratios of O2 to P2-type layers, semi-ordered layer stacking arrangements are evidenced. For example, when the O2:P2 ratio is 1:1, the O2 and P2-type layers tend to alternate, analogous to the OP4 structure. Understanding the nature of the "Z"-phase is important for greater utilization of $NaMO_2$ capacities and this chapter aims to contribute fundamental insight towards achieving this goal.

4.2 Introduction

Layered transition metal oxide cathodes, such as $LiCoO_2$, are currently being pushed to higher voltages each year by battery manufacturers in the pursuit of increased energy densities. This corresponds to a greater amount of Li-ions extracted on charge. In the 1990s, researchers discovered that after a critical amount of Li-ions are removed from $LiCoO_2$, structural changes occur which result in a sudden decrease of the interlayer spacing.[1] A similar phenomenon has been observed across a wide range of $LiMO_2$ and $NaMO_2$ compounds including $LiNiO_2$, $Li[Ni_{0.8}Co_{0.15}Al_{0.05}]O_2$ (NCA), $Li[Ni_{0.8}Mn_{0.1}Co_{0.1}]O_2$ (NMC811), $Na_{2/3}[Ni_{1/3}Mn_{2/3}]O_2$, and $Na_{2/3}[Mn_{1/2}Fe_{1/2}]O_2$.[2–6]

For $LiCoO_2$, Chen et al. and Van der Ven et al. showed experimentally and computationally that the decreased interlayer spacing can be explained by the staging of Li-ions which induce O1-type stacking faults into the O3 structure.[7,

8] The new phase that is formed is a hybrid of the lithiated O3 and de-lithiated O1, termed H1-3, with Li-ions occupying every other available layer.

In recent years, there has been significant debate as to the exact nature of the high voltage structural evolution in P2-type *Na-ion* cathode materials. While some compounds such as $Na_{2/3}[Ni_{1/3}Mn_{2/3}]O_2$ undergo a more straightforward biphasic transition from a partially sodiated P2 structure to a fully de-sodiated O2 structure, via layer gliding,[5, 9] other compounds evolve more complexly. One such compound is $Na_{2/3}[Mn_{1/2}Fe_{1/2}]O_2$.

When $Na_{2/3}[Mn_{1/2}Fe_{1/2}]O_2$ was first reported by Yabuuchi et al., it was suggested based on synchrotron XRD that the P2-structure transformed to a hybrid structure on charging to 4.3 V vs. Na^+/Na, analogous to the H1-3 structure of $LiCoO_2$. This new hybrid structure was reportedly composed of partially sodiated P2-type layers alternately stacked with vacant O2-type layers and labeled as the OP4 structure.[6]

Later work by Mortemard de Boisse et al. on the same compound, however, adopted a more conservative viewpoint. By using *operando* XRD, the authors demonstrated that most of the Bragg reflections broadened to an indiscernible extent on charge. They therefore decided to label the high voltage phase of $Na_{2/3}[Mn_{1/2}Fe_{1/2}]O_2$ as the "Z"-phase, highlighting its ambiguous nature.[10]

Building from this idea, Talaie et al. claimed that the high voltage "Z"-phase of $Na_{2/3}[Mn_{1/2}Fe_{1/2}]O_2$ was distinctly different from the OP4 described by Yabuuchi et al.[11] The authors used a combination of *operando* XRD and pair distribution function (PDF) analysis to argue that the high voltage phase is in fact an O2-phase with Fe (and other TMs) migrating to tetrahedral sites in the Na layer. The authors made a key observation that the *operando* XRD showed a *progressive* decrease of the interlayer space on charge and suggested this was caused by a corresponding progressive increase in TM migration to tetrahedral sites.[11] It is this continuous contraction of the interlayer spacing during the final stages of charge which will be designated in this thesis as the characteristic signature of the "Z"-phase.

The high voltage "Z"-phase has since been observed in a range of charged P2 compounds containing Ni, Mn, Fe, Cu, Mg, and Zn. [12–15] Recently, Kubota et al.

examined $Na_{2/3}[Ni_{1/4}Mn_{2/3}Cu_{1/12}]O_2$ with *ex situ* synchrotron XRD and *operando* XRD and proposed a slight modification to the OP4-phase (originally theorized for $Na_{2/3}[Mn_{1/2}Fe_{1/2}]O_2$).[16] Instead of the high voltage phase having perfectly ordered alternating P2 and O2-type layers, they suggested that the P2 and O2-type layers were randomly interspersed i.e. an intergrowth of the P2 and O2 phases.

In this chapter, the high voltage "Z"-phase will be discussed in the context of the compounds identified and examined in Chapter 3: $Na_{2/3}[Ni_{1/3-y/2}Mn_{2/3-y/2}Fe_y]O_2$ where y = 0, 1/6, and 1/3. At the outset, the biphasic P2 to O2 transition of $Na_{2/3}[Ni_{1/3}Mn_{2/3}]O_2$ will be reexamined as this constitutes one of the most simple high voltage phase transitions. It will then be shown that substituting Fe into this compound changes the phase transition mechanism from P2↔O2 to P2↔"Z". Subsequently, through the use of the XRD stacking fault simulation software FAULTS, a new model for the "Z"-phase will be proposed. Importantly, this model provides an alternative explanation for the continuous decrease of the interlayer spacing on charge which does not involve TM migration to tetrahedral sites in the Na layer. It will be argued that at any one composition snapshot, the "Z"-phase is indeed an intergrowth of P2 and O2 but one which maintains some degree of order (not random). The "Z"-phase, however, constantly evolves during charge/discharge by altering (increasing/decreasing) its ratio of O2 to P2-type layers, and therefore should not be viewed as a single phase in the traditional sense. The chapter will culminate with a new analysis of the high voltage "Z"-phase of $Na_{2/3}[Mn_{1/2}Fe_{1/2}]O_2$ utilizing this evolving intergrowth model.

4.3 Experimental

The synthesis procedure of $Na_{2/3}[Ni_{1/3}Mn_{2/3}]O_2$, $Na_{2/3}[Ni_{1/4}Mn_{7/12}Fe_{1/6}]O_2$, and $Na_{2/3}[Ni_{1/6}Mn_{1/2}Fe_{1/3}]O_2$ was described in Chapter 3. $Na_{2/3}[Mn_{1/2}Fe_{1/2}]O_2$ was synthesized via a similar solid state method in which Na_2CO_3 (5 % excess) was ball milled with stoichiometric amounts of Fe_2O_3 and Mn_2O_3 for 1 hour at 400 rpm. The powder was then pressed into a pellet and heated to 900 °C in a box furnace in air for 10 hours.

Operando XRD measurements of $Na_{2/3}[Ni_{1/3}Mn_{2/3}]O_2$, $Na_{2/3}[Ni_{1/4}Mn_{7/12}Fe_{1/6}]O_2$, and $Na_{2/3}[Ni_{1/6}Mn_{1/2}Fe_{1/3}]O_2$ were conducted in Dr. Claire Villevieille's laboratory at the Paul Scherrer Institut (PSI) on a Cu kα source PANalytical Empyrean diffractometer in Bragg-Brentano (reflection) geometry using the custom built cell previously reported.[17] Self-standing electrodes were used in the cell to avoid severe attenuation of the signal from the current collector. These electrodes were prepared by mixing 75 % active material, 10 % carbon black, and 15 % PVDF (Kynar Flex) in a suspension of acetone and ethanol. The mixture was cast with a doctor blade onto glass. Once the solvent evaporated, the laminate was peeled off the glass and electrodes were punched. The assembled *operando* cell was charged and discharged at a rate of 5 mA g^{-1} with an upper voltage cutoff of 4.5 V vs. Na^+/Na. The preparation of the self-standing electrodes as well as the *operando* XRD measurements were carried out by Dr. Juliette Billaud.

Synchrotron XRD of the $Na_{2/3}[Mn_{1/2}Fe_{1/2}]O_2$ powder was measured at the Advanced Photon Source (APS) 11-ID-B in Debeye-Scherrer (transmission) geometry with an X-ray wavelength of $\lambda = 0.2113$ Å (58.7 keV). A 2D area detector was used at a distance of 95 cm and the data was subsequently reduced using the software GSAS-II.[18] *Operando* synchrotron XRD of $Na_{2/3}[Mn_{1/2}Fe_{1/2}]O_2$ was also carried out at this location using the same parameters and the facility's custom built AMPIX cell.[19] For this measurement, electrodes were prepared by the method described in Chapter 3 but cast directly onto the separator rather than onto a current collector. The cell was charged and discharged at a rate of 10 mA g^{-1} with an upper voltage cutoff of 4.5 V vs. Na^+/Na. All XRD refinements shown in this chapter were carried out with GSAS-II.

The background for the laboratory *operando* XRD experiments stayed consistent throughout the charge/discharge cycle of the cell. Therefore, the background of the first pattern was refined with GSAS-II and then subtracted from all patterns to obtain color maps of the data using MATLAB. The data sets were also corrected for sample displacement. By contrast, the synchrotron *operando* XRD dataset of $Na_{2/3}[Mn_{1/2}Fe_{1/2}]O_2$ did not show a constant background (probably due to motor

movement). As such, each background was individually fit by interpolating a cubic spline through selected background points using MATLAB. With this method, subtle broad diffraction features are too easily incorporated into the background so the analysis focuses on the clear, discernible reflections and color maps are not included.

The computer program FAULTS[20] (an extension of the DIFFaX[21]) was used to simulate stacking faulted structures originating from the gliding of layers within the P2 structure. The specific structural parameters of the models used are discussed when appropriate in the results section.

4.4 Results and Discussion

4.4.1 $Na_{2/3}[Ni_{1/3}Mn_{2/3}]O_2$: P2 to O2 Transition

Operando XRD

Operando XRD was conducted on $Na_{2/3}[Ni_{1/3}Mn_{2/3}]O_2$ over the first charge/discharge cycle between 2.5 and 4.5 V vs. Na^+/Na with the results shown in Figure 4.1 (lattice parameters in Figure 4.1e). On initial extraction of Na from the compound, the interlayer spacing (d) steadily increases due to a decrease of shielding between adjacent repulsive oxygen layers. At the same time, the compound's intralayer TM-TM distance steadily decreases due to the shortening of the TM-O bonds as oxidation occurs.[15] This is consistent with virtually all layered oxide cathode materials. As discussed in detail in the last chapter, the step in the voltage curve at approximately 3.55 V corresponds to Na ordering when $x \approx 1/2$ for $Na_x[Ni_{1/3}Mn_{2/3}]O_2$. Two of the extra peaks which emerge from this ordering are just visible in the color map shown in Figure 4.1a and are highlighted with circles for clarity.

After charging to approximately 3.7 V (55 mAh g^{-1}), the interlayer spacing of the compound stops increasing at $d \approx 5.69$ Å. Despite the fact that the P2 diffraction peaks are retained at this point of charge, Lu et al. previously demonstrated the presence of a small percentage of O2-type stacking faults in the structure.[5] As there is no significant change of the P2 lattice parameters for approximately 20 mAh g^{-1} and no appearance of a second phase, the extraction of Na during this

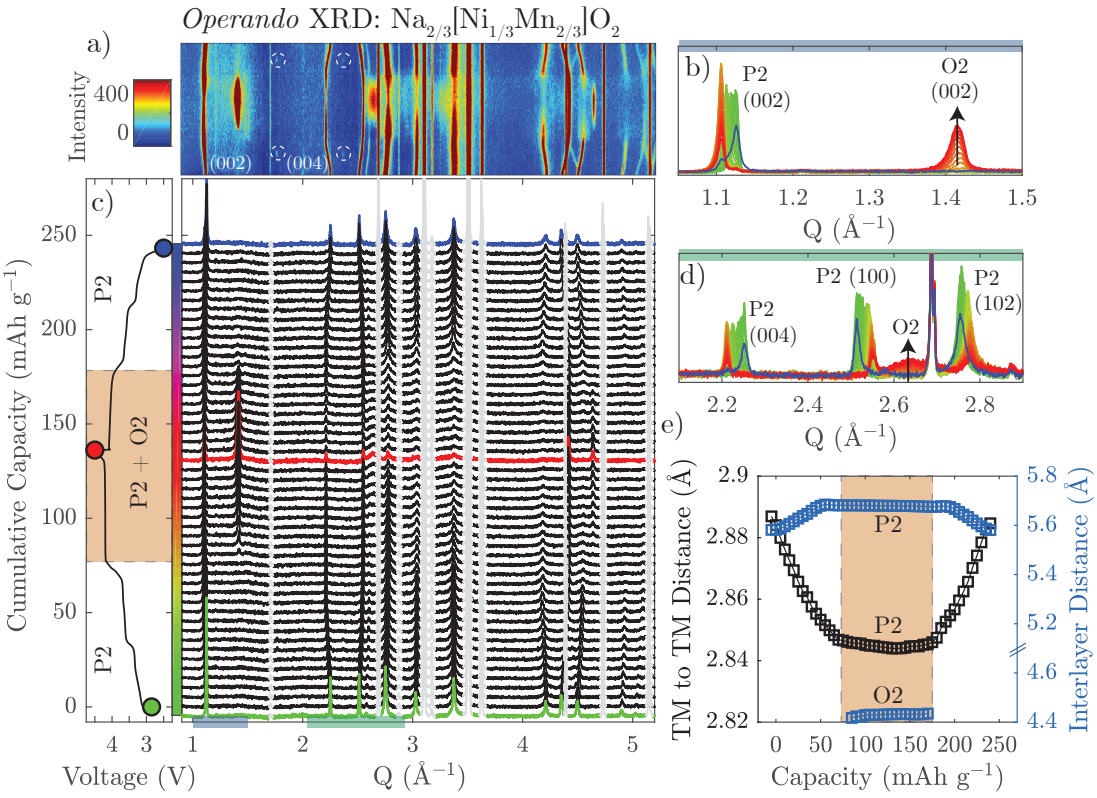

Figure 4.1: The first charge/discharge cycle of $Na_{2/3}[Ni_{1/3}Mn_{2/3}]O_2$ (2.5 - 4.5 V vs. Na^+/Na, $i = 5$ mA g^{-1}) was monitored with *operando* XRD. All data shown here is background subtracted and corrected for sample displacement. An intensity color map of the diffraction data is shown in a) and the same data is plotted in a stacked fashion next to the voltage curve in c). In b) and d), key regions of the pattern are highlighted during charge and are color coded by capacity (color bar is shown next to the voltage curve). Finally, the interlayer distance and TM to TM distance were extracted from the data at each point of charge/discharge and plotted in e).

period likely occurs through a process known as staging, where Na is completely extracted from some layers provoking a layer glide from P2 to O2-type stacking.

On further charging of the compound, there is a sudden uptick in the voltage to approximately 4.2 V where a long plateau, indicative of a biphasic transformation, can be seen. This is highlighted in orange in Figure 4.1a and e. At this point, a clear second phase is visible consistent with the growth of the O2 phase. The most intense (002) peak of the O2 phase can be seen growing at $Q = 1.41$ Å^{-1}. This corresponds to an interlayer spacing of $d \approx 4.44$ Å which is over 20 % decreased from that of the charged P2 phase. An additional broad peak centered at $Q = 2.64$ Å^{-1} can also be seen in Figure 4.1d. It will be shown in the next section

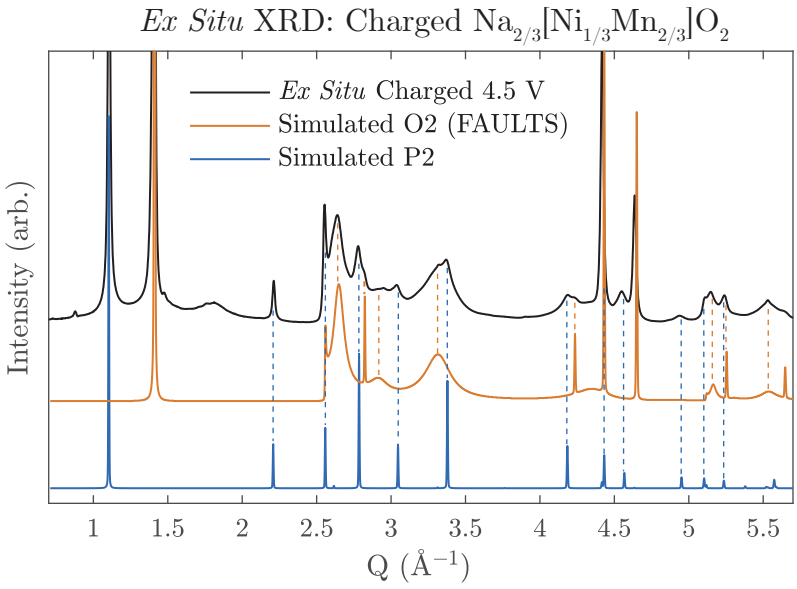

Figure 4.2: *Ex situ* synchrotron XRD was conducted on a sample of $Na_{2/3}[Ni_{1/3}Mn_{2/3}]O_2$ charged to 4.5 V vs. Na^+/Na. The P2 (0 % stacking faults) and O2 (100 % stacking faults) were simulated for comparison with the program, FAULTS. The synchrotron XRD was measured by Dr. Leighanne Gallington at APS 11-ID-B.

that the intensity in this region can be used to differentiate the O2 structure from the OP4 structure. Upon reaching the 4.5 V cutoff, the P2 reflections are still seen. This indicates the P2 to O2 transition is a kinetically slow process, as the current rate of 5 mA g^{-1} used is very low.

On discharge, the peaks corresponding to the O2 phase disappear completely while the P2 reflections return. The P2 (002) peak then appears to split slightly on discharge but this could be due to stack pressure differences within the *operando* cell. Despite this, the lattice parameters of the P2 phase (Figure 4.1e) revert to their pristine values at the end of discharge (2.5 V). The capacity fading seen in this compound stems largely from the volume change associated with the P2-O2 transition.[22]

Ex Situ Synchrotron XRD

To better understand the high voltage O2 structure, synchrotron XRD was conducted on a sample recovered from a cell charged to 4.5 V shown in black in Figure 4.2. Reflections associated with the P2 phase are still present in the diffraction pattern

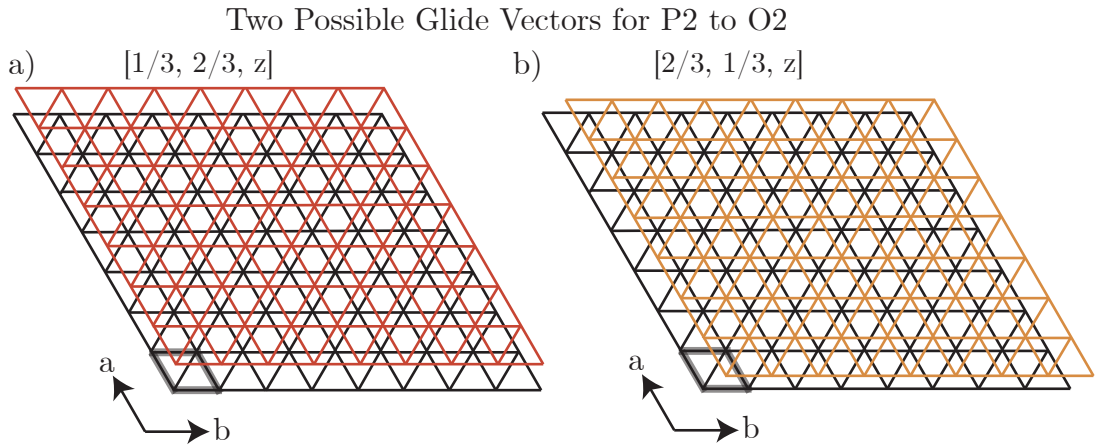

Figure 4.3: A schematic of the two possible glide vectors to transform the P2 structure to O2 are illustrated in a) and b). The vertices of the triangular grid represent the TM positions and the unit cell is bolded in the bottom left of each of the grids. In P2 configuration, the black and red/orange grids would align. Transformation to the close-packed O2 structure therefore requires a shift of the layer along one the glide vectors shown.

as they were in the *operando* XRD; however, the majority phase in the diffraction pattern is clearly O2. The stacking faults program, FAULTS (an extension of DIFFAX) was used to simulate the XRD pattern of the O2 phase (shown in orange). The peaks of this simulated pattern are broadened due to the two different glide vectors TMO_2 slabs can traverse to transform from P2 to O2 stacking. This is illustrated in Figure 4.3 which shows the difference in shifting the adjacent TMO_2 layers along the [1/3, 2/3, z] direction (red) compared with the [2/3, 1/3, z] direction (orange). The simulated pattern was generated assuming an equal probability of these two glide vectors and matches extremely well with the experimental data. In particular, it can be seen that the broad peak at $Q = 2.64$ Å^{-1}, also seen in the *operando* data, is reproduced well in the simulation.

Overall, the data shown here corroborates previous reports on the structural evolution of $Na_{2/3}[Ni_{1/3}Mn_{2/3}]O_2$.[5, 9, 15, 23, 24] In the last chapter, it was found that substitution of Mn and Ni for Fe improved the capacity retention of the cathode. In the next section, it will be shown that the improved capacity retention can be correlated to a different high voltage structural process where the P2 to O2 phase transition is avoided in favor of a transformation to the poorly understood "Z"-phase.

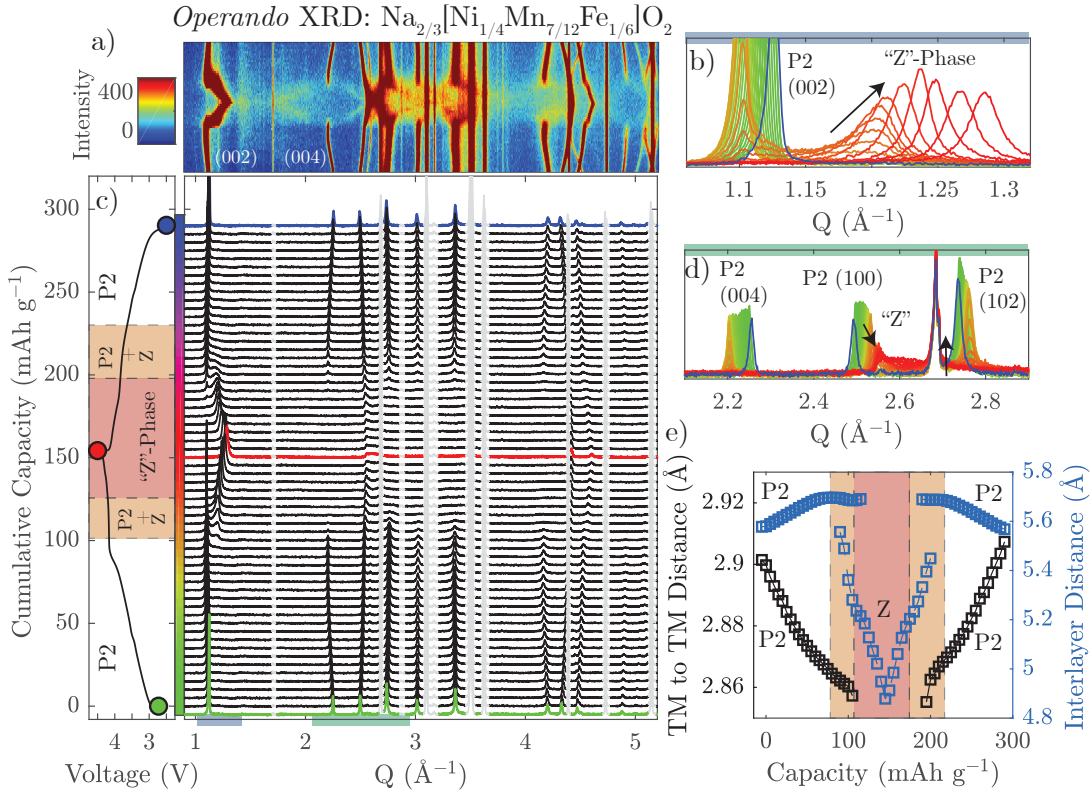

Figure 4.4: The first charge/discharge cycle of $Na_{2/3}[Ni_{1/4}Mn_{7/12}Fe_{1/6}]O_2$ (2.5 - 4.5 V vs. Na^+/Na, $i = 5$ mA g^{-1}) was monitored with *operando* XRD. All data shown here is background subtracted and corrected for sample displacement. An intensity color map of the diffraction data is shown in a) and the same data is plotted in a stacked fashion next to the voltage curve in c). In b) and d), key regions of the pattern are highlighted during charge and are color coded by capacity (color bar is shown next to the voltage curve). Finally, the interlayer distance and TM to TM distance were extracted from the data at each point of charge/discharge and plotted in e).

4.4.2 $Na_{2/3}[Ni_{1/3-y/2}Mn_{2/3-y/2}Fe_y]O_2$ (y = 1/6, 1/3): P2 to "Z"-Phase

Operando XRD

$Na_{2/3}[Ni_{1/4}Mn_{7/12}Fe_{1/6}]O_2$ and $Na_{2/3}[Ni_{1/6}Mn_{1/2}Fe_{1/3}]O_2$ were investigated with *operando* XRD to compare the high voltage structural processes to $Na_{2/3}[Ni_{1/3}Mn_{2/3}]O_2$. The results for $Na_{2/3}[Ni_{1/4}Mn_{7/12}Fe_{1/6}]O_2$ are shown in Figure 4.4 and the results for $Na_{2/3}[Ni_{1/6}Mn_{1/2}Fe_{1/3}]O_2$ in Figure 4.5.

On initial charging, the lattice of both compounds (Figures 4.4e and 4.5e) follow the expected trend of decreasing intralayer TM-TM distance and increasing interlayer distance, as was found for $Na_{2/3}[Ni_{1/3}Mn_{2/3}]O_2$. This evolution progresses

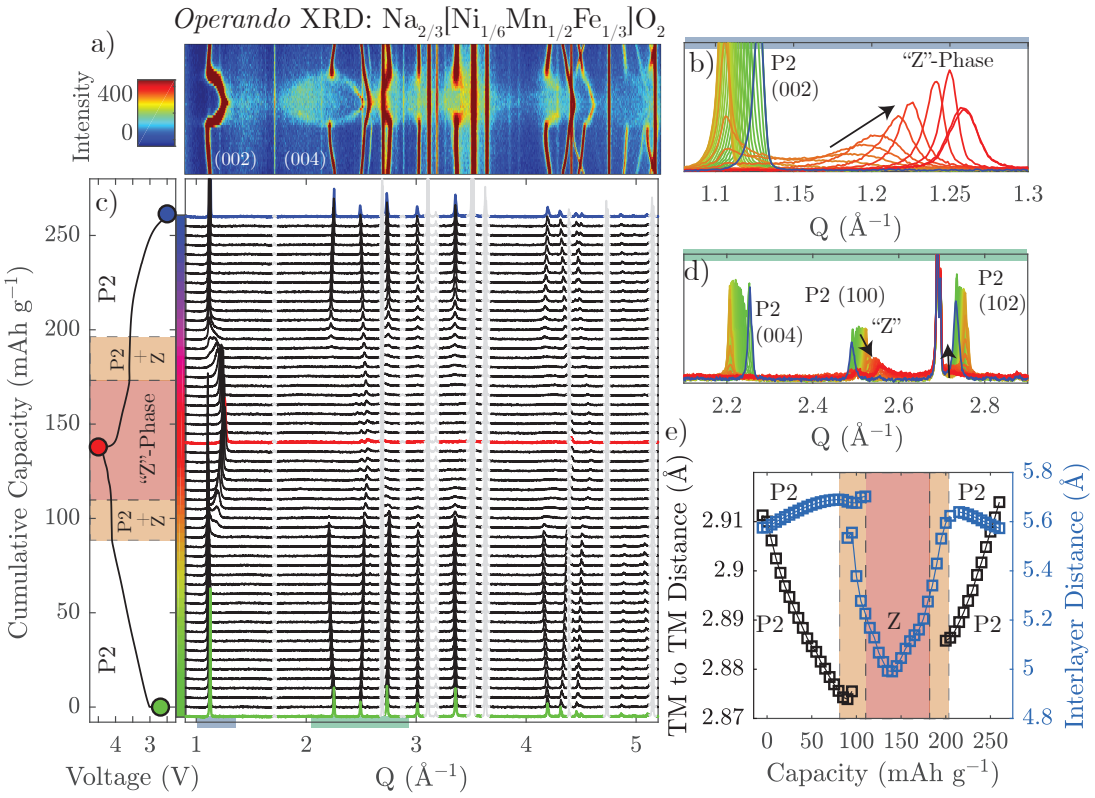

Figure 4.5: The first charge/discharge cycle of $Na_{2/3}[Ni_{1/6}Mn_{1/2}Fe_{1/3}]O_2$ (2.5 - 4.5 V vs. Na^+/Na, $i = 5$ mA g^{-1}) was monitored with *operando* XRD. All data shown here is background subtracted and corrected for sample displacement. An intensity color map of the diffraction data is shown in a) and the same data is plotted in a stacked fashion next to the voltage curve in c). In b) and d), key regions of the pattern are highlighted during charge and are color coded by capacity (color bar is shown next to the voltage curve). Finally, the interlayer distance and TM to TM distance were extracted from the data at each point of charge/discharge and plotted in e).

steadily until reaching a high voltage plateau at approximately 4.1 V, marked by an orange shaded region in Figures 4.4c, 4.4e, 4.5c, and 4.5e. This is in contrast to $Na_{2/3}[Ni_{1/3}Mn_{2/3}]O_2$ which demonstrated O2-type stacking faults as early as 3.7 V. Immediately before the 4.1 V plateau, both compounds display a large interlayer spacing of $d \approx 5.69$ Å with approximately 1/3 mol Na per formula unit remaining in the structure, similar to $Na_{2/3}[Ni_{1/3}Mn_{2/3}]O_2$.

Charging beyond 4.1 V instigates a two phase domain for both compounds, with the P2 reflections decreasing in intensity and the growth of a new peak to the right of the P2 (002) peak at $Q \approx 1.2$ Å^{-1} (Figures 4.4b and 4.5b). Assuming this reflection belongs to a $(00l)$ index of a new phase, the Q value corresponds to an

interlayer spacing of $d \approx 5.24$ Å which is significantly larger than that of the O2 phase seen for $Na_{2/3}[Ni_{1/3}Mn_{2/3}]O_2$ ($d \approx 4.44$ Å). At the end of the plateau, the P2 reflections are gone and the most intense $(00l)$ peak of the new phase begins to shift dramatically to higher Q, shaded in red in Figures 4.4c, 4.4e, 4.5c, and 4.5e. This rapid decrease of the interlayer spacing is consistent with the formation of the "Z"-phase, as discussed in the introduction of this chapter.

In both compounds, the $(00l)$ peak of the "Z"-phase seems to initially sharpen, while increasing its maximum intensity, and then broaden again near the top of charge (Figures 4.4b and 4.5b). This behavior represents an important new clue into the structural identity of the"Z"-phase, which to the best of my knowledge, has not been reported previously. Meanwhile, the P2 (102) peak of the P2 phase broadens considerably and sharply decreases in Q (Figures 4.4d and 4.5d). A final observation of note is a clear splitting of the P2 (004) peak, seen in the color maps (Figures 4.4a and 4.5a), to higher and lower Q. It will be explained in the next section how this splitting also gives significant insight into the nature of the "Z"-phase.

At the end of charge (4.5 V cutoff), the "Z"-phase of $Na_{2/3}[Ni_{1/4}Mn_{7/12}Fe_{1/6}]O_2$ attained a minimum interlayer spacing of $d \approx 4.88$ Å while $Na_{2/3}[Ni_{1/6}Mn_{1/2}Fe_{1/3}]O_2$ attained $d \approx 4.99$ Å. Both of these values represent a significant increase from the $d \approx 4.44$ Å seen for the O2 phase of $Na_{2/3}[Ni_{1/3}Mn_{2/3}]O_2$ and, consequently, a less severe overall volume contraction.

On discharge, the reflections associated with the "Z"-phase disappear completely for both $Na_{2/3}[Ni_{1/4}Mn_{7/12}Fe_{1/6}]O_2$ and $Na_{2/3}[Ni_{1/6}Mn_{1/2}Fe_{1/3}]O_2$ and the P2 structure is restored. This demonstrates that the high voltage phase transformation is largely reversible, at least for the first cycle.

While many factors can contribute to the capacity fading of an electrode on cycling, there has been a high correlation between volume change and capacity retention shown for many anode and cathode materials.[3, 25–29] Therefore, the suppression of the P2-O2 phase transition and its associated volume change by Fe substitution is likely the predominant reason for the improved capacity retention on cycling seen in Chapter 3.

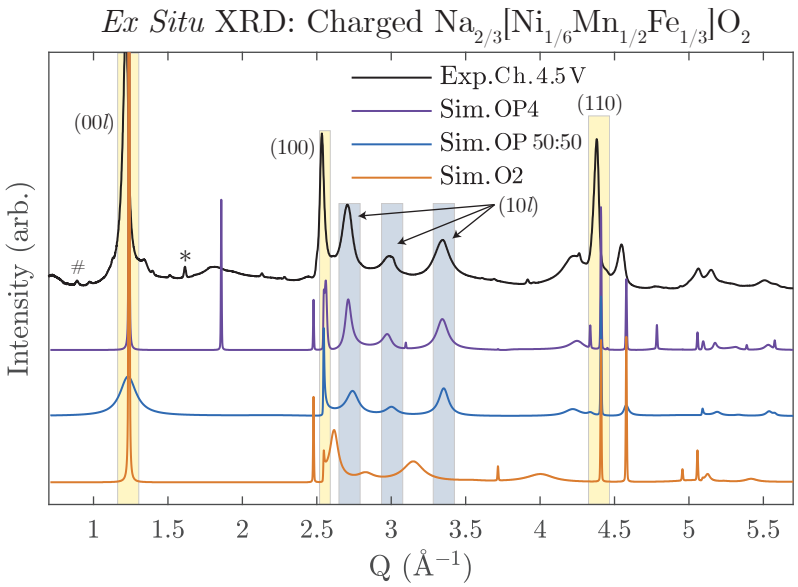

Figure 4.6: *Ex situ* synchrotron XRD conducted on a sample of $Na_{2/3}[Ni_{1/6}Mn_{1/2}Fe_{1/3}]O_2$ charged to 4.5 V vs. Na^+/Na, is shown at the top in black. Extra peaks identified with an asterisk (*) stem from the wax used to seal the capillary and the octothorpe (#) symbol indicates a small amount of hydrated P2 phase.[30] Several patterns were simulated with FAULTS for comparison. The ordered OP4 (purple) and disordered OP 50:50 (blue) intergrowths were simulated assuming different interlayer spacing of the P2 and O2 layers, matching that of $Na_{2/3}[Ni_{1/3}Mn_{2/3}]O_2$ ($d_{O2} = 4.44$ Å, $d_{P2} = 5.69$ Å). The O2 pattern (orange) was simulated assuming the average interlayer spacing ($d = 5.07$ Å). Certain peaks are highlighted with yellow or blue shading for reference in text. The synchrotron XRD was measured by Dr. Leighanne Gallington at APS 11-ID-B (Chicago, IL).

Ex Situ Synchrotron XRD

Further analysis of the "Z"-phase was carried out through *ex situ* synchrotron XRD of $Na_{2/3}[Ni_{1/6}Mn_{1/2}Fe_{1/3}]O_2$ after charge to 4.5 V (Figure 4.6). The experimentally obtained diffraction pattern at the top (black) was compared to a simulated pattern of the OP4 structure (purple), a simulated pattern of a random OP intergrowth with 50% P2 and 50% O2-type layers labeled OP 50:50 (blue), and a simulated pattern of the O2 structure (orange) with the interlayer distance set equal to the average interlayer distance of OP4.

The three most intense peaks in the experimental diffraction pattern, highlighted in yellow ((00l) peak at $Q \approx 1.24$ Å^{-1}, (100) peak at $Q \approx 2.55$ Å^{-1}, and (110) peak at $Q \approx 4.41$ Å^{-1}), are all well represented by each of the three simulated patterns.

There are, however, key differences elsewhere in the data. The experimental pattern shows three broadened ($10l$) peaks highlighted in blue. While both the OP4 and OP 50:50 simulations show similar broadened peaks in these regions, the O2 simulated pattern does not. This importantly eliminates the possibility that the "Z"-phase contains purely O2 stacking, as was claimed previously,[11, 14] and instead strongly supports the "Z"-phase being an intergrowth of P2 and O2-type layers with a ratio close to 1:1 (i.e. the ordered OP4 or disordered OP 50:50).

Although the OP4 and OP 50:50 simulations are quite similar, the OP4 pattern has several sharp peaks which are not evident in the experimental data or the OP 50:50 simulation. This indicates that the "Z"-phase of the 4.5 V charged $Na_{2/3}[Ni_{1/6}Mn_{1/2}Fe_{1/3}]O_2$ sample does not have perfectly alternating O2 and P2 layers. On the other hand, the OP 50:50 simulation, which contains completely random O2 and P2 layers, has a very broad first ($00l$) peak which does not perfectly match the experimental data either. A more thorough analysis of the possible OP intergrowth structures was therefore necessary to better understand the true identity of the "Z"-phase. The results of this analysis are shown in the following section.

4.4.3 A New "Z"-Phase Model: An Evolving Intergrowth

The computer program FAULTS was used to simulate the XRD patterns for OP intergrowth models with varying ratios of O2 to P2-type layers as well as (dis)order in their arrangement. In the previous two sections, the P2 structure of each of the studied compounds was shown to have a rather large interlayer spacing of approximately 5.69 Å immediately before the high voltage phase transformation. On the other hand, the O2 structure of $Na_{2/3}[Ni_{1/3}Mn_{2/3}]O_2$ at the end of charge had a very small interlayer spacing of just 4.44 Å. It therefore seems extremely unlikely that the O2 and P2-type layers in the "Z"-phase intergrowth have the same interlayer spacing. All modeled intergrowth structures in this section were therefore assumed to contain O2-type layers with an interlayer spacing equal to that of the O2 structure ($d_{O2} = 4.44$ Å) and P2-type layers with an interlayer spacing equal to

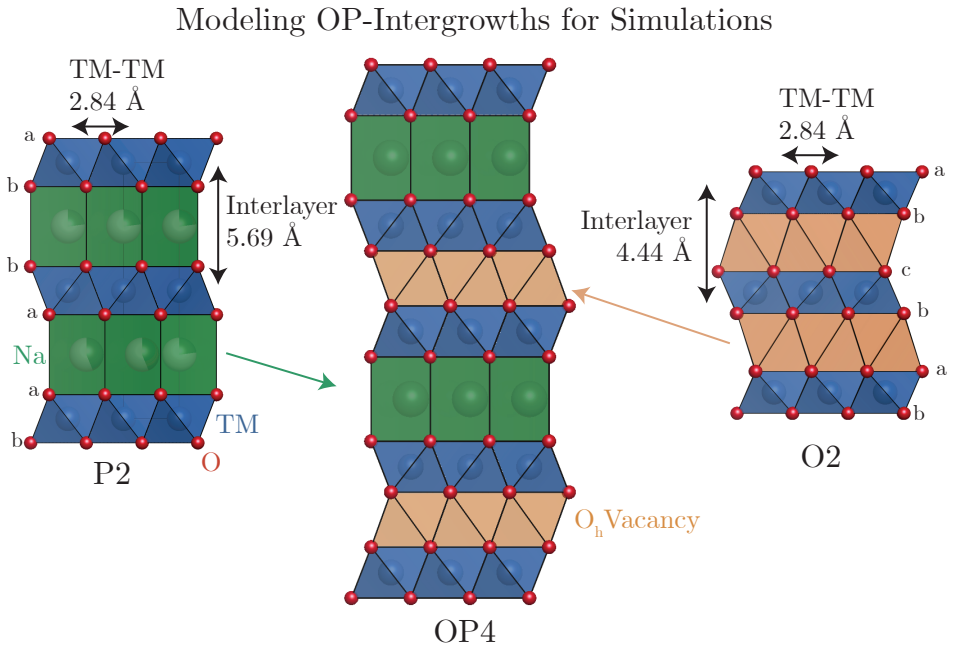

Figure 4.7: The graphic provides an illustration of the unit cell parameters used in the FAULTS XRD simulations. All intergrowth structures were modeled with P2-type layers having an interlayer spacing of 5.69 Å, approximately equal to that of the P2 structure immediately before the high voltage phase transition in $Na_{2/3}[Ni_{1/4}Mn_{7/12}Fe_{1/6}]O_2$ and $Na_{2/3}[Ni_{1/6}Mn_{1/2}Fe_{1/3}]O_2$. The O2-type layers are modeled to match the O2 phase of charged $Na_{2/3}[Ni_{1/3}Mn_{2/3}]O_2$ which has an interlayer spacing of approximately 4.44 Å. The TM to TM a parameter is kept constant at 2.84 Å for all models. An OP4 structure is shown in the middle as an example of one of the many possible OP intergrowths models.

Table 4.1: Layer Definitions for OP Intergrowth FAULTS XRD simulations.

Layer No.	**Contains Na?**	**Untransitioned Stacking**	**Transition Vector to Layer**		
			$\mathbf{t_x}$	$\mathbf{t_y}$	$\mathbf{t_z}$
1	Yes	*ab*	0	0	1
2	Yes	*ba*	0	0	1
3	No	*ab*	1/3	2/3	0.78
4	No	*ba*	1/3	2/3	0.78
5	No	*ab*	2/3	1/3	0.78
6	No	*ba*	2/3	1/3	0.78

the charged P2 structure ($d_{P2} = 5.69$ Å) as illustrated in Figure 4.7. The TM-TM distance (unit cell a parameter) was kept at a constant value of 2.84 Å.

Two series of XRD simulations were carried out with the results shown in Figure 4.8. This was accomplished by defining 6 structural layers (composed of one TMO_2 layer and one Na layer) along with corresponding transition vectors in the FAULTS

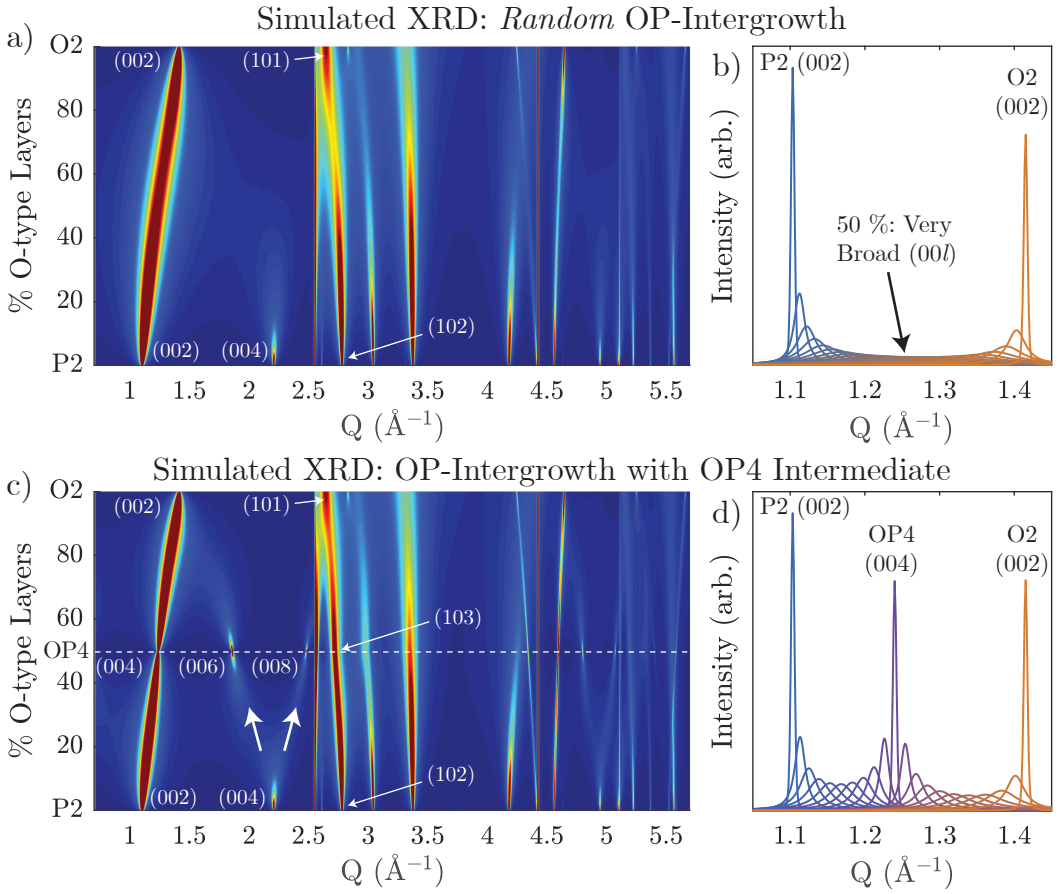

Figure 4.8: The figure shows simulated XRD data for two series of OP intergrowths with varying percentage of O2-type layers (vs. P2-type layers). The first series (a and b) is modeled based on the assumption that O2 and P2 layers are interspersed completely randomly in the structure. The second series (c and d) is modeled with an ordered intermediate OP4 structure when the O2:P2 ratio is 1:1.

input file. The layer definitions used are shown in Table 4.1. Layers 1 and 2 had transition vectors that would make them P2-type layers, whereas layers 3–6 had transition vectors that would make them O2-type layers. A transition of 1 unit in the z direction was set equal to the P2-type interlayer spacing of 5.69 Å whereas a transition of 1 unit in the x or y directions was set equal to the TM-TM distance (a parameter) of 2.84 Å. Continuous series of XRD simulations were created by varying the transition probabilities between these 6 layers.

Simulating a Series of *Random* OP Intergrowths

The first series, shown in Figure 4.8a and 4.8b, simulates the evolution of the OP intergrowth diffraction pattern while varying the percentage of O2-type layers *randomly* interspersed within the structure. This was done by the following transition probability matrix:

$$\boldsymbol{\alpha} = \begin{bmatrix} \alpha_{11} & \alpha_{12} & \dots & \alpha_{16} \\ \alpha_{21} & \alpha_{22} & \dots & \alpha_{26} \\ \vdots & \vdots & \ddots & \vdots \\ \alpha_{61} & \alpha_{62} & \dots & \alpha_{66} \end{bmatrix} = \begin{bmatrix} 0 & 1-x & 0 & x/2 & 0 & x/2 \\ 1-x & 0 & x/2 & 0 & x/2 & 0 \\ 0 & 1-x & 0 & x/2 & 0 & x/2 \\ 1-x & 0 & x/2 & 0 & x/2 & 0 \\ 0 & 1-x & 0 & x/2 & 0 & x/2 \\ 1-x & 0 & x/2 & 0 & x/2 & 0 \end{bmatrix}$$

where α_{ij} is the transition probability from layer i to layer j and x is varied from 0 (ordered P2) to 1 (ordered O2). This transition probability matrix ($\boldsymbol{\alpha}$) also assures that layers with *ab* oxygen stacking are followed only by layers with *ba* stacking (and vice versa) because the parent compound from which the "Z"-phase intergrowth evolves is the P2 structure with *ab ba* stacking. The existence probability of each layer (g_i) relates to x and the total O2-type layer percentage is derived as:

$$\%\ \text{O2-type layers} = (g_3 + g_4 + g_5 + g_6) \times 100\%$$

In Figure 4.8a and b, it is evident that the P2 (002) peak shifts to higher values of Q with increasing percentages of O2-type layers, indicating a decrease in the average interlayer spacing. This is expected from the simulation as the O2-type layers were modeled with a significantly smaller interlayer spacing than the P2-type layers. However, this also matches the characteristic contraction of the *average* interlayer spacing seen for the "Z"-phase experimentally with *operando* XRD. Until now, the only explanation for this phenomenon in the literature, to my knowledge, is a progressive transition metal migration proposed by Nazar and coworkers.[11, 14] Therefore, this simulation importantly identifies an alternative mechanism by which the signature of progressive interlayer space contraction can be produced.

Simulating a Series of OP Intergrowths to Include *Intermediate OP4*

Through examination of the *ex situ* XRD in the previous section, it was found that the end of charge (4.5 V) "Z"-phase of $Na_{2/3}[Ni_{1/6}Mn_{1/2}Fe_{1/3}]O_2$ is an OP intergrowth with approximately 50 % O2-type layers. In the simulation, however, the first $(00l)$ peak of the disordered OP intergrowth (Figure 4.8b) with 50 % O2-type layers is extremely broad and weak, not matching the experimental data. A new series of simulations was therefore conducted, assuming an ordered OP4 intergrowth as an intermediate between the P2 and O2 end members, shown in Figures 4.8c and d. The transition probability matrix for this series is as follows:

$$\boldsymbol{\alpha} = \begin{cases} \begin{bmatrix} 0 & 1-2x & 0 & x & 0 & x \\ 1-2x & 0 & x & 0 & x & 0 \\ 0 & 1 & 0 & 0 & 0 & 0 \\ 1 & 0 & 0 & 0 & 0 & 0 \\ 0 & 1 & 0 & 0 & 0 & 0 \\ 1 & 0 & 0 & 0 & 0 & 0 \end{bmatrix} & \text{for } 0 \leq x < 1/2 \\ \begin{bmatrix} 0 & 0 & 0 & 1/2 & 0 & 1/2 \\ 0 & 0 & 1/2 & 0 & 1/2 & 0 \\ 0 & 2-2x & 0 & x-1/2 & 0 & x-1/2 \\ 2-2x & 0 & x-1/2 & 0 & x-1/2 & 0 \\ 0 & 2-2x & 0 & x-1/2 & 0 & x-1/2 \\ 2-2x & 0 & x-1/2 & 0 & x-1/2 & 0 \end{bmatrix} & \text{for } 1/2 \leq x \leq 1 \end{cases}$$

where x is again varied between 0 (ordered P2) and 1 (ordered O2) but with the ordered OP4 ($x = 1/2$) as an intermediate.

This series of OP intergrowths produces very similar diffraction patterns to the random intergrowth series but with two key differences. The first is the P2 (004) peak now splits when the O2-type layers are increased to approximately 50 % into the OP4 (006) and (008) peaks. This matches extremely well with the splitting seen in the experimental data for both $Na_{2/3}[Ni_{1/4}Mn_{7/12}Fe_{1/6}]O_2$ and $Na_{2/3}[Ni_{1/6}Mn_{1/2}Fe_{1/3}]O_2$. The second difference is the most intense $(00l)$ peak (Figure 4.8d) now sharpens at 50 % O2-type layers rather than broadening. This also matches well with the

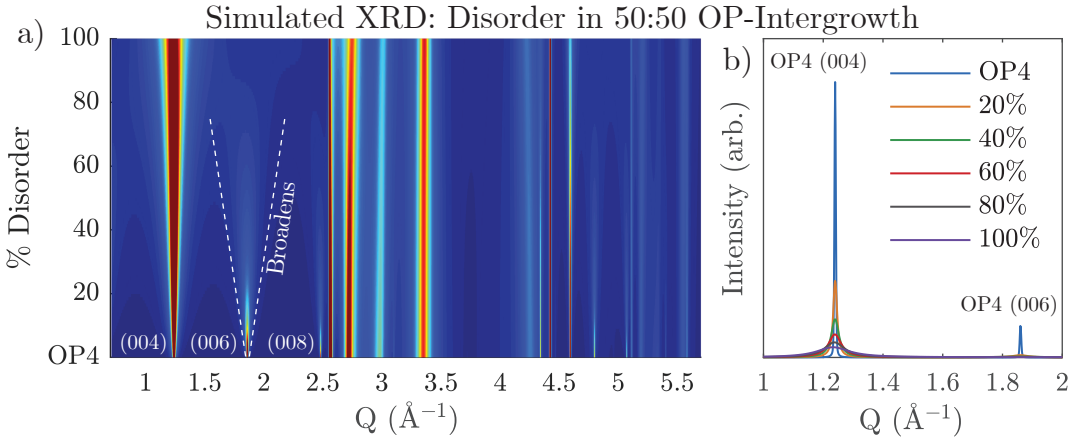

Figure 4.9: The figure shows simulated XRD data for a series of OP intergrowths with varying degrees of disorder in the alternation of P2 and O2-type layers with the ratio of O2:P2 type layers kept constant at 1:1. This series moves from the perfectly ordered OP4 structure XRD simulation to a 100% disordered OP 50:50 structure XRD simulation.

experimental *operando* XRD data discussed previously, suggesting the ordered OP4 intermediate may be preferred to a disordered OP 50:50 phase.

Simulating *Disorder* in the OP4 Structure

However, the *ex situ* XRD data of the $Na_{2/3}[Ni_{1/6}Mn_{1/2}Fe_{1/3}]O_2$ 4.5 V sample does not match a perfectly ordered OP4 structure (Figure 4.6), as was shown in the last section. Therefore, a final series of intergrowths were simulated moving from a perfectly ordered OP4 structure to a 100 % disordered (OP 50:50) intergrowth, shown in Figures 4.9a and 4.9b. The transition probability matrix for this is:

$$\boldsymbol{\alpha} = \begin{bmatrix} 0 & x/2 & 0 & 1/2 - x/4 & 0 & 1/2 - x/4 \\ x/2 & 0 & 1/2 - x/4 & 0 & 1/2 - x/4 & 0 \\ 0 & 1 - x/2 & 0 & x/4 & 0 & x/4 \\ 1 - x/2 & 0 & x/4 & 0 & x/4 & 0 \\ 0 & 1 - x/2 & 0 & x/4 & 0 & x/4 \\ 1 - x/2 & 0 & x/4 & 0 & x/4 & 0 \end{bmatrix}$$

where x constitutes the amount of disorder in the intergrowth and is varied between 0 (perfectly ordered OP4) and 1 (completely disordered OP 50:50 intergrowth).

Figures 4.9a and 4.9b both reveal that the introduction of only a small amount of disorder ($\approx 30\%$), can broaden the lower intensity peaks of the OP4 structure with high l-dependence (such as the (006) peak) to the point where they are difficult

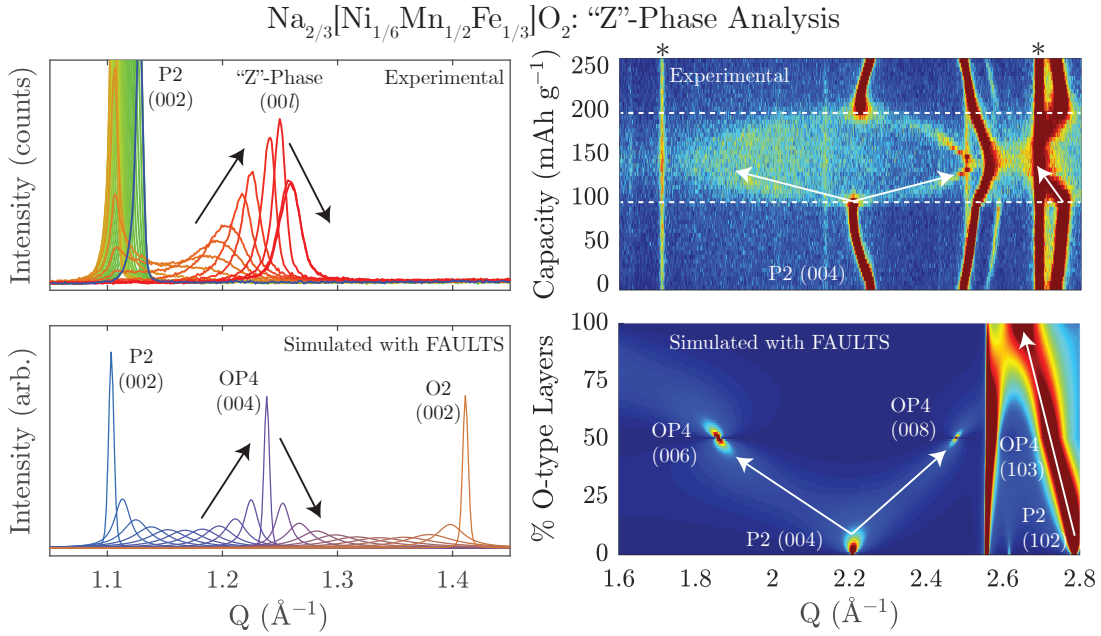

Figure 4.10: The high voltage evolution of $Na_{2/3}[Ni_{1/6}Mn_{1/2}Fe_{1/3}]O_2$ (top) is compared directly with the simulated OP intergrowth series with OP4 as an intermediate (bottom). The plots on the left focus on the most intense $(00l)$ peak while the color maps on the right focus on the more subtle changes to higher Q values. The asterisks (*) in the color map mark reflections that do not belong to the active material (i.e. stemming from carbon black and Be).

to distinguish above the background. The presence of such disorder, as well as any deviation from the ideal 50:50 ratio of OP4, could account for the discrepancies seen between the experimental and simulated XRD patterns.

Analysis of the $Na_{2/3}[Ni_{1/6}Mn_{1/2}Fe_{1/3}]O_2$ "Z"-Phase

The simulated OP intergrowth series (with OP4 as an intermediate) is compared directly with the experimental *operando* XRD data for $Na_{2/3}[Ni_{1/6}Mn_{1/2}Fe_{1/3}]O_2$ in Figure 4.10. The most intense $(00l)$ peak of the experimental data is seen to sharpen at nearly the exact same value of Q as the simulated OP4 ($d \approx$ 5.07Å). This evolution proves that the O2 and P2-type layers within this intergrowth are not randomly interspersed (as in simulations of Figures 4.8) but have a tendency to alternate when possible. Moreover, the changing position and breadth of the $(00l)$ peak implies the intergrowth steadily evolves by varying the percentage of O2-type layers as Na is extracted. The color maps corroborate this hypothesis; the

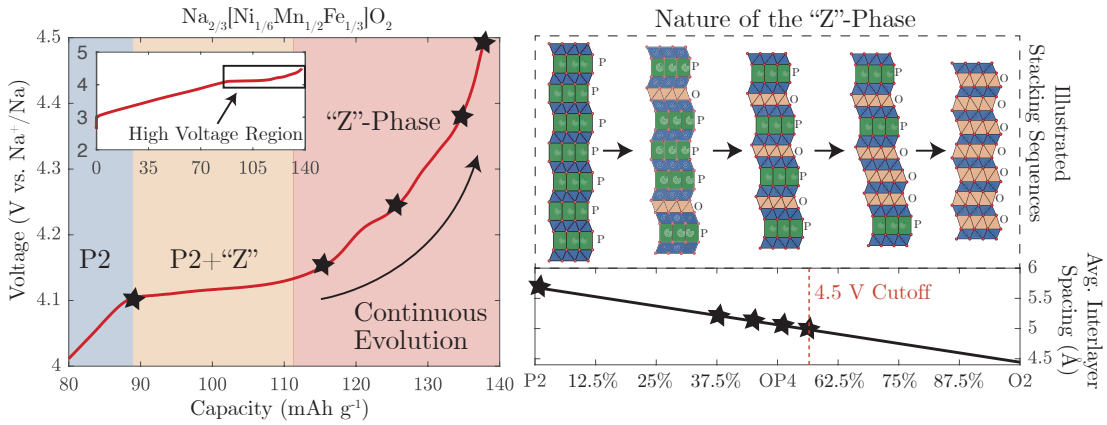

Figure 4.11: This figure summarizes the evolving OP intergrowth model for the "Z"-phase. On charging $Na_{2/3}[Ni_{1/6}Mn_{1/2}Fe_{1/3}]O_2$ to 4.1 V, Na is extracted from P2-type layers which transform to O2-type layers, decreasing the average interlayer spacing. The top left insert highlights the high voltage region of the load curve for which this graphic pertains.

experimental P2 (004) peak mirrors the simulated patterns by splitting to lower and higher values of Q while the P2 (102) peak shifts steadily to lower values of Q.

The dynamic variation in the O2:P2 type layer ratio within the "Z"-phase intergrowth suggests a staging mechanism, where Na is removed from P2-type layers which subsequently glide to form O2-type layers. The proportion of vacant O2-type layers steadily increases on charge to compensate the removal of Na. A schematic illustrating this explanation is displayed in Figure 4.11. For $Na_{2/3}[Ni_{1/6}Mn_{1/2}Fe_{1/3}]O_2$, the P2 structure initially undergoes a conventional biphasic transition on charge to an OP intergrowth containing approximately 38 % O2-type layers (based on the position of the most intense $(00l)$ peak). Further Na extraction follows through the staging mechanism described where the ratio of O2 to P2-type layers progressively increases. When the voltage reaches the 4.5 V cutoff, the OP intergrowth contains approximately 56 % O2-type layers.

It has been established that this proposed *evolving OP intergrowth model* for the "Z"-phase matches the experimental results of $Na_{2/3}[Ni_{1/6}Mn_{1/2}Fe_{1/3}]O_2$ and $Na_{2/3}[Ni_{1/4}Mn_{7/12}Fe_{1/6}]O_2$ extremely well. In the next section, it will be demonstrated that this model can be extended (and adapted) to encompass other $NaMO_2$ materials including $Na_{2/3}[Mn_{1/2}Fe_{1/2}]O_2$.

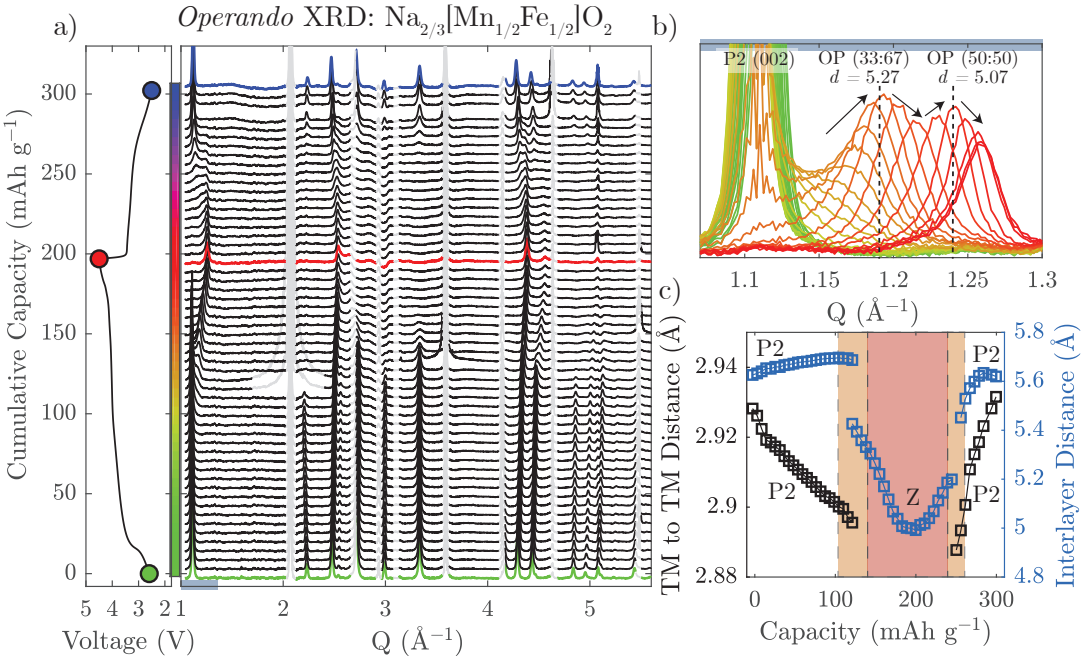

Figure 4.12: The first charge/discharge cycle of $Na_{2/3}[Mn_{1/2}Fe_{1/2}]O_2$ (2.5 - 4.5 V vs. Na^+/Na, $i = 10$ mA g^{-1}) was monitored with synchrotron *operando* XRD. All data shown here is background subtracted using a method described in the experimental section. In b) the most intense $(00l)$ peak is followed throughout charging and are color coded by capacity (color bar is shown next to the voltage curve). The interlayer distance and TM to TM distance were extracted from the data at each point of charge/discharge and plotted in c). This data was collected in the AMPIX cell at the APS 11-ID-B (Chicago, IL).

4.4.4 $Na_{2/3}[Mn_{1/2}Fe_{1/2}]O_2$: "Z"-Phase Analysis

Operando XRD

Probably the most studied of the $NaMO_2$ cathode materials, $Na_{2/3}[Mn_{1/2}Fe_{1/2}]O_2$, has been well documented to undergo a structural transformation when charged above 4 V vs. Na^+/Na.[11] Synchrotron *operando* XRD was conducted on this material to analyze the structural transformation in the context of the new evolving OP intergrowth model presented in the last section. The results are shown in Figure 4.12 with the cell background subtracted. On charging beyond the P2 solid solution region (> 4 V), most of the peaks broaden and a new reflection appears at a higher Q than the P2 (002) peak, characteristic of the "Z"-phase. In contrast to $Na_{2/3}[Ni_{1/6}Mn_{1/2}Fe_{1/3}]O_2$, however, the initial "Z"-phase that is formed has a slightly higher average interlayer spacing of $d \approx 5.35$ Å (compared with $d \approx 5.26$

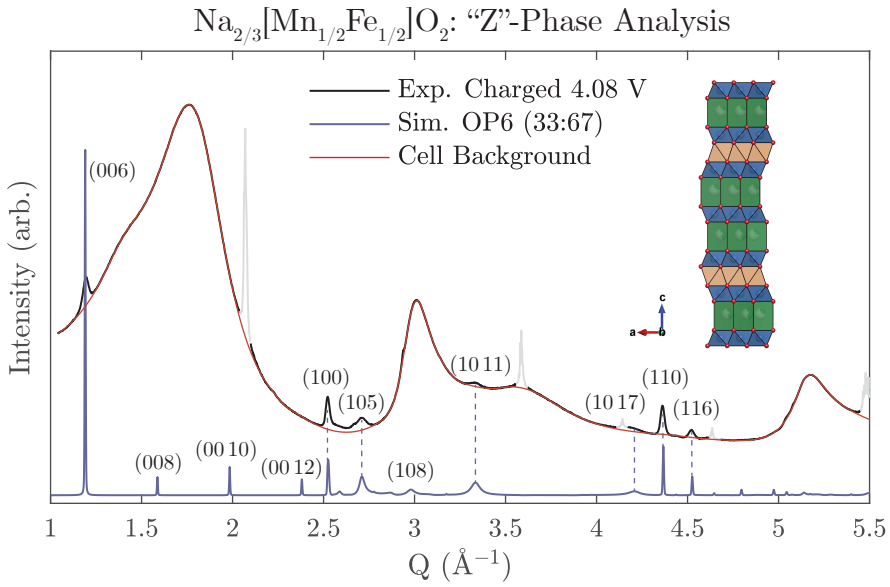

Figure 4.13: The synchrotron XRD pattern (black) shown was part of the *operando* experiment displayed in Figure 4.12, at 4.08 V during charging. The background (stemming largely from the glassy carbon windows of the cell) is shown in red and the peaks from the Na metal counter electrode are shown in grey. The ordered OP6 intergrowth (33% O2-type layers), shown in blue, was simulated with FAULTS with a parameter of 2.877 Å and interlayer spacings of $d_{O2} = 4.44$ Å, $d_{P2} = 5.69$ Å. The data was collected at APS 11-ID-B (Chicago, IL).

Å). Assuming the same O2 and P2 interlayer spacings as $Na_{2/3}[Ni_{1/6}Mn_{1/2}Fe_{1/3}]O_2$, this distance corresponds to an O2-type layer percentage of approximately 26% (12% less than that of $Na_{2/3}[Ni_{1/6}Mn_{1/2}Fe_{1/3}]O_2$ after the biphasic region).

When the compound is further charged to 4.08 V, the (00l) peak sharpens at $Q \approx 1.19$ Å^{-1} ($d \approx 5.27$ Å). The interlayer d-spacing at this point, however, does not correspond to the expected 50 % O2-type layers of the OP4 structure but rather contains 33%; a 2:1 ratio of P2 to O2-type layers. The diffraction pattern at 4.08 V was therefore compared to a simulated OP6 structure (6 TMO_2 layers per unit cell) with 33 % O2-type layers shown in full in Figure 4.13. All distinguishable peaks in the experimental pattern can be appropriately indexed by this large OP6 unit cell. Lower intensity peaks with a high l-dependence do not appear probably due a small amount of disorder in the alternation of P2 and O2-type layers, as was the case with the OP4 of $Na_{2/3}[Ni_{1/6}Mn_{1/2}Fe_{1/3}]O_2$.

With continued charging of $Na_{2/3}[Mn_{1/2}Fe_{1/2}]O_2$, the (00$l$) peak progresses

steadily to higher Q with an initial slight decrease in sharpness as the O2 to P2 ratio moves away from the ideal 1:2 of OP6 (Figure 4.12). Once Q progresses beyond ≈ 1.24 Å^{-1} ($d \approx 5.07$ Å), the peak becomes noticeably broader and its maximum intensity again drops. These changes are likely a consequence of evolving through an ordered OP 50:50 intermediate similar to $Na_{2/3}[Ni_{1/6}Mn_{1/2}Fe_{1/3}]O_2$. At the end of charge (4.5 V), the average interlayer spacing reaches $d \approx 4.99$ Å or an O2-type layer percentage of approximately 56%.

The significance of these results is the fact that the "Z"-phase can evolve through multiple ordered OP intergrowths with different O2:P2 ratios during charging. While $Na_{2/3}[Ni_{1/6}Mn_{1/2}Fe_{1/3}]O_2$ undergoes an initial biphasic transition directly to an OP intergrowth with 38% O2-type layers, $Na_{2/3}[Mn_{1/2}Fe_{1/2}]O_2$ transitions to one with only 26%. This allows the structure to evolve through the ordered OP6 at 33% stacking faults on further charging. Further work is needed to better understand the characteristics which determine the structure at the end of the biphasic transition. Through optimization, it may even be possible to completely stifle the biphasic transition in favor of a structure that steadily morphs from P2 to O2 without phase boundaries.

4.5 Conclusion

Extending the upper voltage cutoff of cathode materials is favorable in terms of energy density as more ions can be extracted which, in turn, leads to more capacity being delivered at high voltages. However, the majority of P2-type $NaMO_2$ compounds undergo a structural transition when most of the Na has been extracted that is detrimental to capacity retention on cycling. Some compounds, such as $Na_{2/3}[Ni_{1/3}Mn_{2/3}]O_2$, undergo a rather severe biphasic transition directly to a fully de-sodiated O2 phase. Others, such as $Na_{2/3}[Ni_{1/6}Mn_{1/2}Fe_{1/3}]O_2$ and $Na_{2/3}[Mn_{1/2}Fe_{1/2}]O_2$ go through a more complicated structural transformation designated as the "Z"-phase.

The evidence presented in this chapter has helped unravel the mystery of the "Z"-phase through a series of XRD experiments and stacking faults simulations.

It has been shown that the "Z"-phase is not actually one single phase but rather an evolving intergrowth of P2 and O2-type (Na)MO_2 layers. When a critical amount of Na ($x \approx 1/3$ in Na_xMO_2) remains in the structure during charge, the staging of Na-ions becomes favorable. At this time, Na is completely extracted from some of the P2-type layers which causes them to glide and create a close packed octahedral coordination of the Na vacancy sites (O2-type). The option of two unique glide vectors that transform the P2-type layers to O2-type inherently causes much of the long range order in the structure to be lost and XRD reflections, in turn, are severely broadened. Until now, this behavior has made the "Z"-phase incredibly difficult to characterize.

As Na is extracted from the OP intergrowth, the percentage of vacant O2-type layers increases at the expense of the sodiated P2-type layers. It is evident that the P2 and O2-type layers tend to arrange into *non*-random stacking sequences at key O2 to P2 ratios, such as the OP6 at 1:2 (33:67) and the OP4 at 1:1 (50:50). It is quite possible that other layer stacking arrangements (eg. OP6 (67:33)) could be included within the intergrowth's evolution if the reaction were allowed to proceed further, however, the stability of the carbonate-based electrolyte imposes an upper limit to the reaction at this time.

It is still unclear why some compounds undergo a biphasic reaction directly to O2 while others evolve through an intergrowth path. The compounds transitioning to the OP intergrowth favorably undergo less overall volume change because less Na is removed before reaching the upper voltage cutoff. This leads to improved capacity retention but worsened first cycle capacities. From an application perspective, however, cathodes transitioning to an OP intergrowth should be preferred over a biphasic P2 to O2 transition as utilizing such compounds would allow volume change to be controlled by the voltage rather than capacity. Moreover, the P2 to O2 transition should result in significant internal stress of the structure at the O2-P2 phase boundary due to lattice mismatch, which could lead to particle fracture. On the other hand, the OP intergrowth does not possess such a clear boundary during evolution and thus may impede the build up of such stresses.

Although improved with compounds evolving via the "Z"-phase, severe volume changes still pose a significant obstacle to utilizing higher voltages. As such, engineering solutions such as binder optimization could provide a route to better utilize the cathode capacity at high voltages. Tuning the chemistry of the cathodes may also alleviate some of the volume change complications. For example, introducing mobile species (such as Li^+) in the TM layer which can migrate to the Na layer on charge, may serve to "pillar" the O2-type interlayer space against severe contraction and further optimize cathodes.

Discerning the identity of the high voltage "Z"-phase represents an important advancement in the understanding of $NaMO_2$ cathode materials. The evidence presented can provide a platform for their further development and improvement.

4.6 References

(1) Amatucci, G. G.; Tarascon, J. M.; Klein, L. C. *Journal of The Electrochemical Society* **1996**, *143*, 1114–1123.

(2) Li, H.; Zhang, N.; Li, J.; Dahn, J. R. *Journal of The Electrochemical Society* **2018**, *165*, A2985–A2993.

(3) Kondrakov, A. O.; Schmidt, A.; Xu, J.; Geßwein, H.; Mönig, R.; Hartmann, P.; Sommer, H.; Brezesinski, T.; Janek, J. *Journal of Physical Chemistry C* **2017**, *121*, 3286–3294.

(4) Grenier, A.; Liu, H.; Wiaderek, K. M.; Lebens-Higgins, Z. W.; Borkiewicz, O. J.; Piper, L. F. J.; Chupas, P. J.; Chapman, K. W. *Chemistry of Materials* **2017**, *29*, 7345–7352.

(5) Lu, Z.; Dahn, J. R. *Journal of The Electrochemical Society* **2001**, *148*, A1225–A1229.

(6) Yabuuchi, N.; Kajiyama, M.; Iwatate, J.; Nishikawa, H.; Hitomi, S.; Okuyama, R.; Usui, R.; Yamada, Y.; Komaba, S. *Nature Materials* **2012**, *11*, 512–517.

(7) Chen, Z.; Lu, Z.; Dahn, J. R. *Journal of The Electrochemical Society* **2002**, *149*, A1604–A1609.

(8) Van der Ven, A.; Aydinol, M. K.; Ceder, G. *Journal of The Electrochemical Society* **1998**, *145*, 2149–2155.

(9) Lee, D. H.; Xu, J.; Meng, Y. S. *Physical chemistry chemical physics : PCCP* **2013**, *15*, 3304–12.

(10) Mortemard de Boisse, B.; Carlier, D.; Guignard, M.; Bourgeois, L.; Delmas, C. *Inorganic chemistry* **2014**, *53*, 11197–205.

(11) Talaie, E.; Duffort, V.; Smith, H. L.; Fultz, B.; Nazar, L. F. *Energy & Environmental Science* **2015**, *8*, 2512–2523.

(12) Singh, G.; Tapia-Ruiz, N.; Lopez del Amo, J. M.; Maitra, U.; Somerville, J. W.; Armstrong, A. R.; Martinez de Ilarduya, J.; Rojo, T.; Bruce, P. G. *Chemistry of Materials* **2016**, *28*, 5087–5094.

(13) Wu, X.; Xu, G.-L.; Zhong, G.; Gong, Z.; McDonald, M. J.; Zheng, S.; Fu, R.; Chen, Z.; Amine, K.; Yang, Y. *ACS Applied Materials & Interfaces* **2016**, acsami.6b06701.

(14) Talaie, E.; Kim, S. Y.; Chen, N.; Nazar, L. F. *Chemistry of Materials* **2017**, *29*, 6684–6697.

(15) Kubota, K.; Kumakura, S.; Yoda, Y.; Kuroki, K.; Komaba, S. *Advanced Energy Materials* **2018**, *8*, 1703415.

(16) Kubota, K.; Yoda, Y.; Komaba, S. *Journal of The Electrochemical Society* **2017**, *164*, A2368–A2373.

(17) Bleith, P.; Kaiser, H.; Novák, P.; Villevieille, C. *Electrochimica Acta* **2015**, *176*, 18–21.

(18) Toby, B. H.; Von Dreele, R. B. *Journal of Applied Crystallography* **2013**, *46*, 544–549.

(19) Borkiewicz, O. J.; Shyam, B.; Wiaderek, K. M.; Kurtz, C.; Chupas, P. J.; Chapman, K. W. *Journal of Applied Crystallography* **2012**, *45*, 1261–1269.

(20) Casas-Cabanas, M.; Reynaud, M.; Rikarte, J.; Horbach, P.; Rodríguez-Carvajal, J. *Journal of Applied Crystallography* **2016**, *49*, 2259–2269.

(21) Treacy, M. M. J.; Deem, M. W.; Newsam, J. M. **2005**, 1–71.

(22) Yoda, Y.; Kubota, K.; Isozumi, H.; Horiba, T.; Komaba, S. *ACS Applied Materials and Interfaces* **2018**, *10*, 10986–10997.

(23) Lu, Z.; Dahn, J. R. *Journal of The Electrochemical Society* **2001**, *148*, A710–A715.

(24) Tapia-Ruiz, N.; Dose, W. M.; Sharma, N.; Chen, H.; Heath, J.; Somerville, J. W.; Maitra, U.; Islam, M. S.; Bruce, P. G. *Energy & Environmental Science* **2018**, *11*, 1470–1479.

(25) Liu, X. H.; Zhong, L.; Huang, S.; Mao, S. X.; Zhu, T.; Huang, J. Y. *ACS Nano* **2012**, *6*, 1522–1531.

(26) Liu, Y.; Fang, X.; Zhang, A.; Shen, C.; Liu, Q.; Enaya, H. A.; Zhou, C. *Nano Energy* **2016**, *27*, 27–34.

(27) Radin, M. D.; Alvarado, J.; Meng, Y. S.; Van Der Ven, A. *Nano Letters* **2017**, *17*, 7789–7795.

(28) Radin, M. D.; Hy, S.; Sina, M.; Fang, C.; Liu, H.; Vinckeviciute, J.; Zhang, M.; Whittingham, M. S.; Meng, Y. S.; Van der Ven, A. *Advanced Energy Materials* **2017**, *7*, 1602888.

(29) Wang, K.; Yan, P.; Sui, M. *Nano Energy* **2018**, *54*, 148–155.

(30) Lu, Z.; Dahn, J. R. *Chem. Mater.* **2001**, *13*, 1252–1257.

5

Oxygen Redox Chemistry in Na and Li Transition Metal Oxide Cathodes

Contents

5.1 Abstract

It has been recently discovered that oxygen can reversibly store charge in layered sodium and lithium transition metal oxides to achieve *extra* capacity beyond the theoretical limit of transition metal redox. This provides an avenue for a true step change in the energy density of batteries. Many questions remain, however, regarding the governing mechanisms of the O-redox reaction. In this chapter, a model

"Li-rich" cathode material, $Li[Li_{1/5}Ni_{1/5}Mn_{3/5}]O_2$, is first investigated and shown to display long term reversible O-redox but with severe voltage hysteresis on the first cycle. Subsequently, $Na_{2/3}[Mg_{0.28}Mn_{0.72}]O_2$ is examined and also demonstrates O-redox, but is activated in the presence of Mg instead of Li in the transition metal layer. This compound also shows significant first cycle voltage hysteresis despite no evidence of irreversible O_2 gas loss. In order to remedy the first cycle voltage hysteresis, the effect of various transition metal substituents (Mg, Co, Fe, Ni and Zn) is explored with varying degrees of success. Finally, the study of two Li-substituted compounds, $Na_{3y}[Li_yMn_{1-y}]O_2$ ($y = 1/5, 1/4$), revealed that the first cycle hysteresis of an O-redox reaction can be controlled by a particular superstructure ordering arrangement within the transition metal layer of the compound.

5.2 Introduction

Today's lithium layered oxide cathode materials (e.g. $LiCoO_2$, NMC811) have a theoretical capacity of approximately 275 mAh g^{-1}, which corresponds to the extraction/insertion of 1 mol of Li-ions per mol TM. In practice, only about 2/3 of this capacity can be effectively utilized due to phase changes not unlike that which were discussed in Chapter 4.

Traditional understanding of intercalation cathode materials is that Li-ion (or Na-ion) extraction and insertion is charge compensated by the oxidation and reduction of TMs, for example:

$$LiCo^{3+}O_2 \rightarrow Li_{1-x}Co^{(3+x)+}O_2 + xLi^+ + xe^- \text{ (oxidation)} \tag{5.1}$$

This convention has so far set a fundamental limit on the capacities of today's cathode materials even if the structural changes at low Li contents were somehow overcome. In some compounds such as Li_2MnO_3, however, Li-ions can be extracted beyond the theoretical limit for the TM redox couples. The theoretical capacity of this compound based on TM redox is 0 mAh g^{-1}, but based on Li-content, it is 459 mAh g^{-1}; 68% more than $LiCoO_2$.

There were initially several different hypotheses for what allowed this to occur. One suggestion was that Mn^{4+} in the compound may be oxidized to Mn^{5+}.[1, 2]. However, this theory has not been well corroborated and most researchers maintain the belief that Mn^{4+} is the highest valence state achievable in an oxygen coordinated octahedral environment.[3] Later, Robertson et al. surmised that the Li-ion extraction in Li_2MnO_3 was compensated by Li^+-H^+ exchange with H^+ produced by the breakdown of the electrolyte at high voltages.[4] However, it was later agreed by most that Li_2MnO_3 seems to predominantly compensate Li extraction with irreversible oxygen gas loss (O-loss) from the structure,[5, 6] possibly via the path:

$$Li_2MnO_3 \rightarrow MnO_2 + 2Li^+ + 1/2O_2\ (g) \tag{5.2}$$

Using density function theory (DFT), the Ceder group showed that O^{2-} can be oxidized on charge when in very specific environments: Li^+-O^{2-}-Li^+ configurations at an angle close to 180°.[7] In this arrangement, the O 2p orbital is essentially non-bonding (i.e. is not stabilized by a TM) and its electrons are therefore accessible within the stability limit of the electrolyte. This theory does not account for what happens to the oxygen species (O^{n-}, n<2) after oxidation though.

Over the last decade, understanding of "Li-rich" (Li:TM ratio > 1) cathode materials has grown substantially. With *in situ* XANES and online electrochemical mass spectrometry (OEMS) measurements, it has been shown unequivocally that Mn^{4+} is not oxidized to higher valence states and electrolyte breakdown has only a negligible contribution to the charge capacity.[8, 9] What is still uncertain however, is the nature of oxygen after it has been oxidized. Is its irreversible loss from the structural lattice inevitable or can oxygen redox (O-redox) be stabilized in the solid state?

A compound that has brought us a little closer to answering this question is $Li[Li_{0.2}Ni_{0.13}Co_{0.13}Mn_{0.54}]O_2$. Luo et al. showed that the charging process can be divided into three stages: 1) normal TM oxidation (i.e. $Ni^{2+/4+}$ and $Co^{3+/4+}$), 2) further Li extraction compensated by the formation of localized electron holes on oxygen, and finally 3) O-loss from the structure.[10] It is the second stage

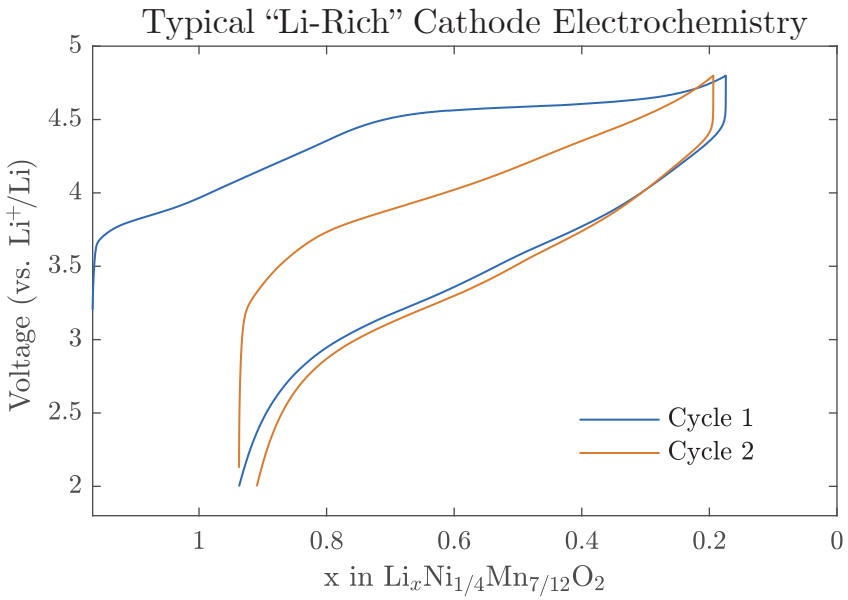

Figure 5.1: The first and second cycle voltage curves are shown for $Li[Li_{1/6}Ni_{1/4}Mn_{7/12}]O_2$ galvanostatically charged/discharged at a current rate of 30 mA g^{-1} between 2.0 and 4.8 V vs. Li^+/Li.

which is of primary interest because the O-oxidation occurs largely in the solid state and is therefore more likely to be reversible than if O^{2-} is fully oxidized to gas and is evolved from the structure. The same authors later showed that $Li[Li_{1/5}Ni_{1/5}Mn_{3/5}]O_2$ undergoes largely the same three step process on charge but has the cost/safety advantage of being Co-free.[11]

A typical electrochemical load curve of a Li-rich cathode is shown in Figure 5.1. Li-rich cathodes undergo what has been called a first cycle "activation".[12–14] With this terminology, however, it is sometimes overlooked that "activation" describes what is an irreversible process; that is, the reaction pathway taken on charge is different from the one taken on discharge. This leads to a large first cycle hysteresis, or energy inefficiency, with nearly a 1 V difference in the average charge and discharge voltages and a coulombic efficiency typically less than 80%. After the first cycle, the shape of the load curve is altered substantially as is shown in Figure 5.1 (orange). Although the energy efficiency does improve after the first cycle, the average discharge voltage of approximately 3.5 V vs. Li^+/Li is still lower than most of the current cathodes in commercial use (e.g. $LiCoO_2$: 4.0 V vs. Li^+/Li)[15, 16].

If an approach can be found to utilize the O-redox couple in a completely reversible way in Li-rich cathodes (i.e. capacity > 250 mAh g^{-1} *and* voltage > 4.3 V), this could lead to a true step change in energy storage technology.

Recently, it has been established that O can also participate in the charge compensation of layered $NaMO_2$ compounds. Because of the larger size of Na-ions compared to Li-ions, "Na-rich" compounds (Na:M ratio > 1) can so far only be synthesized with larger 4d or 5d elements, such as Ru and Ir.[17, 18]

Having an excess of Na-ions (or Li-ions in the case of Li-rich) is necessary to achieve higher capacities. However, *non* alkali metal-rich compounds also exist which could still aid our fundamental understanding of O-redox behavior. One such *non* Na-rich cathode is P2-$Na_{2/3}[Mg_{0.28}Mn_{0.72}]O_2$, which shows anomalous capacity on charge that cannot be ascribed to the $Mn^{3+/4+}$ redox couple.[19] Another important series of compounds is $Na_x[Li_yMn_{1-y}]O_2$ ($0.5 \leq x \leq 1$ and $y \geq 3x$).[20] Specifically, at the composition $Na_{3/5}[Li_{1/5}Mn_{4/5}]O_2$, the discharge voltage curve largely mimics the charge voltage curve giving real hope of completely reversible solid state O-redox.[21–23]

Many questions still exist regarding the fundamental mechanisms governing O-redox behavior. These questions can be effectively categorized into three topics:

1. Which structural or electronic properties of layered TM oxides facilitate the activation of the O-redox couple?

2. Once O is oxidized, what influences the balance between reversible O-redox (solid state) and irreversible O-loss (gas)?

3. What are the causes for the intrinsic hysteresis usually associated with O-redox and how can this be avoided?

It is the goal of this chapter to answer these questions by studying several different $NaMO_2$ and $LiMO_2$ cathodes. First, the cationic and anionic processes are differentiated in a model Li-rich cathode: $Li[Li_{1/5}Ni_{1/5}Mn_{3/5}]O_2$. It is found that solid state O-redox is not merely a first cycle phenomenon but persists on cycling,

despite the different reaction pathways on charge and discharge. Subsequently, $Na_{2/3}[Mg_{0.28}Mn_{0.72}]O_2$ is examined in order to better understand the requirements for O oxidation. This compound also surprisingly shows no O-loss despite a significant quantity of charge stored on oxygen. Finally, two different pathways are examined for reducing the first cycle hysteresis. The first avenue explored is the effect of different substituents (Mg, Co, Fe, Ni and Zn) on the electrochemical behavior. While this route is somewhat successful, a study of two Li-substituted compounds, $Na_{3y}[Li_yMn_{1-y}]O_2$ ($y = 1/5,\ 1/4$), reveals that the crystal structure, in particular the ordering within the TM layer, may play the most significant role in determining the hysteresis of an O-redox reaction.

5.3 Experimental

All Li-rich compounds were synthesized via a resorcinol formaldehyde gel (RF-gel) method. Stoichiometric amounts of $LiCH_3COO\bullet 2H_2O$, $Ni(CH_3COO)_2\bullet 4H_2O$, and $Mn(CH_3COO)_2\bullet 4H_2O$ precursors were dissolved in 50 mL of distilled water. A separate solution was also prepared containing equal parts resorcinol and formaldehyde. The two solutions were combined along with a 5% excess of Li in the form of Li_2CO_3 to control pH and then heated at 80 °C until the solution became a gel. The gel was subsequently heated at 100 °C for 12 hrs, then 500 °C for 15 hrs, followed by a final step at 850 °C for 15 hrs. This procedure is described in more detail in the Methods (Section 2.1) and in a paper by Luo et al.[24] All $NaMO_2$ compounds were synthesized by mixing Na_2CO_3 and the relevant metal oxides (Mn_2O_3 or MnO_2, NiO, ZnO, Co_3O_4, Fe_2O_3, and/or MgO), and heating to temperatures between 800 °C and 900 °C either in a box furnace in air or a tube furnace under flowing oxygen gas.

Electrode pellets were prepared by mixing the active materials with carbon Super P and PTFE in a mortar and pestle. Once the dry mixture was homogeneous, it was rolled to decrease its thickness to $\approx 100\ \mu$m and increase its structural stability. The electrode pellets were assembled into coin cells using Na or Li metal as a counter electrode, glass fiber separators, and 1M $NaPF_6$ in PC or 1M $LiPF_6$ in EC:DMC as electrolytes. These cells were charged and discharged at a constant specific current

of 10 mA g^{-1} (unless otherwise stated) using a MACCOR battery testing system. To obtain *ex situ* samples, coin cells were opened and that cathodes removed, washed with DMC, and dried under vacuum. The online electrochemical mass spectrometry (OEMS) experimental set-up utilized a Thermo Fischer quadrupole mass spectrometer with a Pfeiffer Vacuum turbomolecular pump and Bronkhorst mass-flow controllers. The electrode material was charged and discharged in a specifically designed OEMS cell with gas inlet and outlet ports and Ar gas flowing through the cell at a rate of 0.8 mL min^{-1}.

Laboratory XRD was performed on a Rigaku Smart Lab instrument with a Cu kα source in parallel beam geometry. Synchrotron XRD was collected at the Advanced Photon Source (APS) in Chicago, IL on 11-ID-B with an area detector at a distance of 95 cm from the sample using an X-ray wavelength of $\lambda = 0.2113$ Å. *Operando* synchrotron XRD data was collected using the AMPIX cell described by Borkiewicz et al.[25]. Data reduction as well as Rietveld and Pawley refinements were done using the software GSAS-II.[26] As was the case for other chapters, all diffraction data is plotted in terms of Q (i.e. $2\pi/d$) for better comparability between data sets of different radiation wavelength (λ). *Ex situ* total scattering data was also collected at APS 11-ID-B with an X-ray wavelength of $\lambda = 0.2113$ Å but the detector distance was set to 18 cm in order to obtain a larger range of Q. Data reduction was handled with the software GSAS-II and the pair distribution function was calculated using the software PDFGetX3.[27]

X-ray absorption spectroscopy (XAS) of the Mn K-edge was measured in transmission mode at Diamond Light Source B-18 and data was normalized with the Athena software package.[28] Soft XAS on the O K-edge of $Na_{2/3}[Mg_{0.28}Mn_{0.72}]O_2$ was measured on beamline 8.0.1 of the Advanced Light Source (ALS) in Berkeley, CA in total fluorescence yield (TFY) mode. Soft XAS on the O K-edge and Ni L-edges of $Li[Li_{1/5}Ni_{1/5}Mn_{3/5}]O_2$ and the O K-edge, Mn L-edges, and Co L-edges of $Na_{2/3}[Mg_{1/4}Mn_{7/12}Co_{1/6}]O_2$ were measured on beamline BL27SU of the Spring 8 synchrotron (Sayo, Japan) in partial fluorescence yield (PFY) using the appropriate emission line. Resonant inelastic X-ray scattering (RIXS) maps of

the O K-edge for $Li[Li_{1/5}Ni_{1/5}Mn_{3/5}]O_2$ and $Na_{2/3}[Mg_{0.28}Mn_{0.72}]O_2$ were measured at beamline 8.0.1 of the ALS in Berkeley, CA USA.[29] Single excitation energy RIXS spectra for $Na_{2/3}[Mg_{1/4}Mn_{7/12}Co_{1/6}]O_2$ were measured at beamline BL27SU of the Spring 8 synchrotron (Sayo, Japan).

Computational modeling of the compounds was done with density functional theory (DFT) as implemented in the Quantum ESPRESSO package. [30] The generalized gradient approximation (GGA) of the exchange and correlation functional, devised by Perdew, Burke and Ernzerhof, was employed.[31] The core valence interaction was described using norm-conserving pseudopotentials and ultrasoft pseudopotentials for $Na_{2/3}[Mg_{1/3}Mn_{2/3}]O_2$ and $Li[Li_{1/6}Ni_{1/4}Mn_{7/12}]O_2$ respectively.[32] The electron wave functions were modeled with a basis set of plane-waves within an optimized energy cutoff and Monkhorst–Pack k-point grid of 100 Ry and a $3 \times 3 \times 3$ for $Na_{2/3}[Mg_{1/3}Mn_{2/3}]O_2$ and 80 Ry and 2 x 2 x 4 for $Li[Li_{1/6}Ni_{1/4}Mn_{7/12}]O_2$ to adequately sample the Brillouin zone. A Hubbard-U correction term was included in the calculations to more correctly model the Mn (U = 4.0 eV) and Ni (U = 6.0 eV) 3d states. The simplified rotational-invariant formulation of U by Cococcioni and de Gironcoli was used for this purpose.[33] Supercells, composed of several units cells were used to model the compound of interest. These supercells were relaxed until all forces on the atoms decreased to less than 0.08 eV $Å^{-1}$ and the total stress of the cell was below 0.5 kbar. All crystal structures throughout the chapter are visualized using the software VESTA.[34]

5.4 Results and Discussion

5.4.1 $Li[Li_{1/5}Ni_{1/5}Mn_{3/5}]O_2$: A Model Li-rich Cathode

$Li[Li_{1/5}Ni_{1/5}Mn_{3/5}]O_2$ was synthesized via the RF-gel method described in the experimental and section 2.1.2 of the Methods. This compound can be thought of as a solid solution midway between $Li[Ni_{1/2}Mn_{1/2}]O_2$ and Li_2MnO_3 or a nano-composite of the two end members. Synchrotron XRD was conducted on the material and is shown in Figure 5.2. There are superstructure peaks fitting the monoclinic *C2/m* space group which stem from the honeycomb ordering of Li and Mn. The

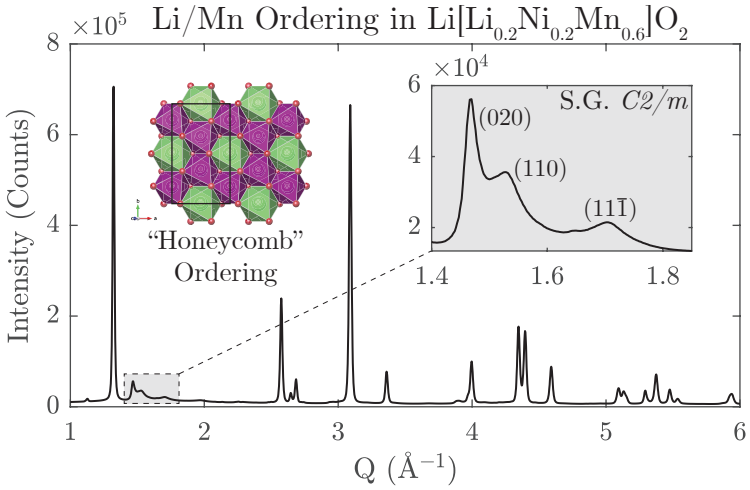

Figure 5.2: The synchrotron XRD is shown for $Li[Li_{1/5}Ni_{1/5}Mn_{3/5}]O_2$. Peaks in the region of 1.4 to 1.85 $Å^{-1}$, shown in the inset, stem from the long range ordering of Li and Mn.

in-plane ordering of the metals is the same as was discussed in Chapter 3 for $Na_{2/3}[Ni_{1/3}Mn_{2/3}]O_2$. In well crystallized Li_2MnO_3, these superstructure peaks are sharp, however in $Li[Li_{1/5}Ni_{1/5}Mn_{3/5}]O_2$, the peaks are broadened due to stacking faults.[35–37] It is difficult to model the broadened superstructure peaks properly in a Rietveld refinement so this region was excluded from the refinement and the more simple $R\bar{3}m$ space group, typical of the O3 structure, was used. The fitting of the refinement is shown in Figure 5.3 with the refined structural parameters displayed in Table 5.1. There was very little anti-site exchange evidenced between Li and Ni ($< 2\%$) demonstrating reasonable success of the synthesis procedure.

Operando XRD

The structural changes in this compound were monitored by *operando* XRD (Figure 5.4). The patterns are background subtracted and stacked from bottom to top corresponding to the electrochemical load curve. Key points in the load curve are colored corresponding to the capacity-based color bar (green: pristine, yellow: end of theoretical capacity from $Ni^{2+/4+}$, red: end of first charge, and blue: end of first discharge. The O3 phase persists throughout the first charge/discharge cycle with no second phase visible at the end of charge.

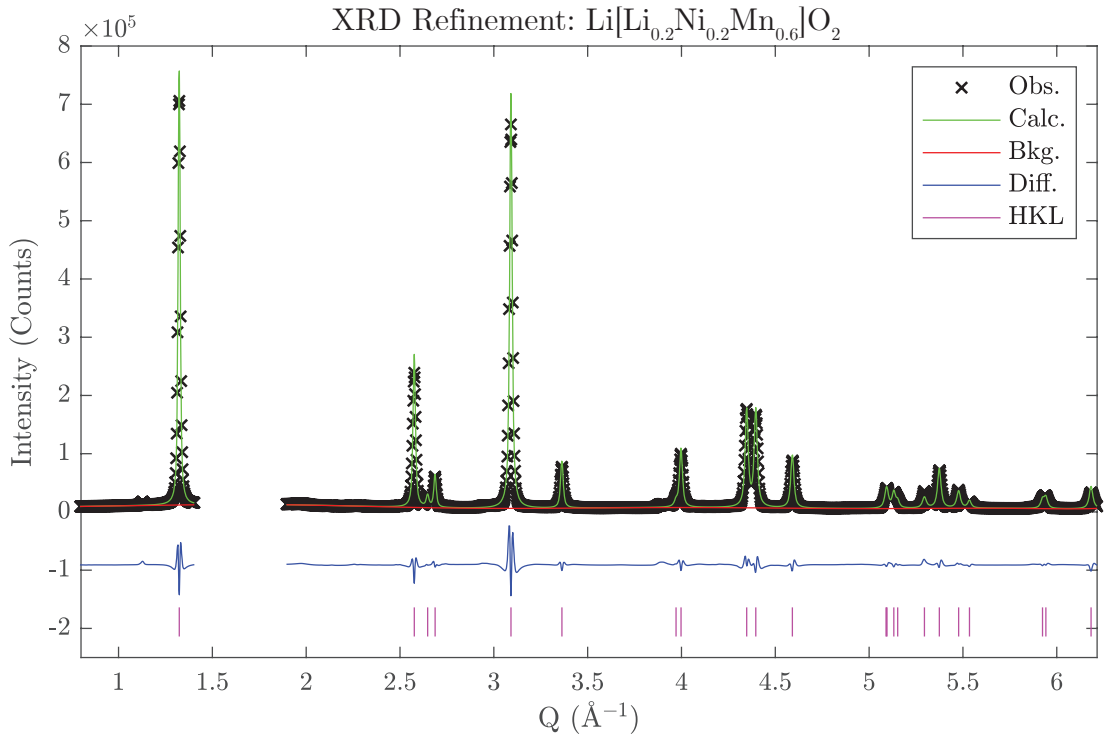

Figure 5.3: XRD data is shown with the corresponding fitting from the Rietveld refinement. The region of $Q = 1.4$–1.85 Å was excluded from the refinement as this region contains broadened superstructure peaks. Refined structural parameters are listed in Table 5.1. This data set was collected at APS 11-ID-B.

One of the most noticeable changes is in the monoclinic superstructure peaks, highlighted in Figure 5.4b. After reaching the end of the $Ni^{2+/4+}$ redox couple (yellow line), the intensity of the superstructure peaks decrease dramatically and continuously until the end of charge (red line). The intensity is not recovered on discharge (blue line). Additionally, the asymmetric evolution of the interlayer

Table 5.1: Results from the Rietveld refinement of pristine $Li[Li_{1/5}Ni_{1/5}Mn_{3/5}]O_2$. The fit is shown in Figure 5.3

S.G. $R\bar{3}m$, a: 2.8586(2) Å, c: 14.2401(8) Å, Rwp: 10.94%, Rexp: 0.66%					
Atom	**x**	**y**	**z**	**SOF**	**Uiso (Å²)**
Li (3a)	0	0	0	0.988(2)	0.01
Ni (3a)	0	0	0	0.012(2)	0.01
Li (3b)	0	0	1/2	0.212(2)	0.0016(5)
Ni (3b)	0	0	1/2	0.188(2)	0.0016(5)
Mn (3b)	0	0	1/2	0.6	0.0016(5)
O (6c)	0	0	0.2418(2)	1	0.007(1)

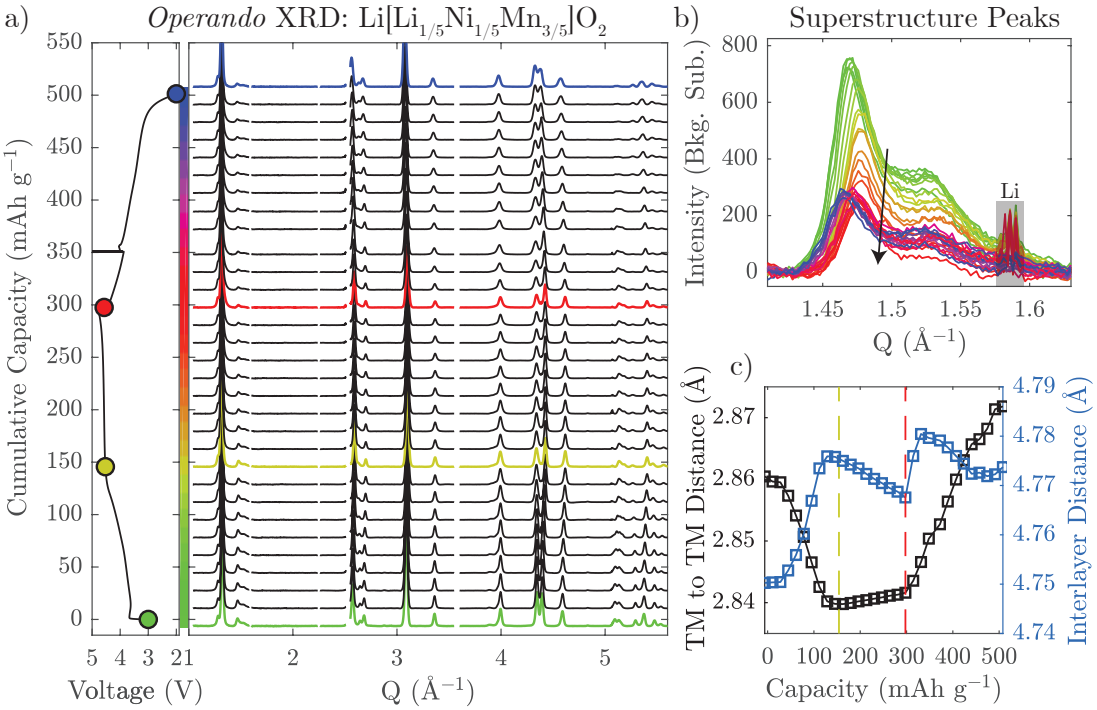

Figure 5.4: *Operando* XRD data for $Li[Li_{1/5}Ni_{1/5}Mn_{3/5}]O_2$ is plotted (background subtracted) in a) along with the electrochemical load curve. Key points in the load curve are colored according to the capacity color bar: green - pristine, yellow - end of theoretical TM redox, red - end of charge, and blue - end of discharge. The superstructure peak evolution is shown in b) and is seen to decrease on charge. The refined cell parameters are shown in c). This data was collected in the AMPIX cell at the APS 11-ID-B (Chicago, IL).

distance (Figure 5.4c) corroborates the occurrence of structural reorganization. These phenomena strongly suggest the breakdown of intralayer (in-plane) honeycomb ordering as O is oxidized. From this, it seems likely that the structural reorganization is intimately linked with, if not the cause of, the first cycle electrochemical hysteresis.

One explanation for the structural reorganization could be the O-loss that $Li[Li_{1/5}Ni_{1/5}Mn_{3/5}]O_2$ experiences near the top of charge.[38] It has also been suggested that TM migration to the Li layer may play a role in the charge compensation mechanism.[39] Each of these processes could wield considerable influence on the electrochemical reversibility. In an attempt to isolate and decipher the multitude of factors influencing the structural evolution of this compound, soft XAS was carried out at the O K-edge and Ni L-edge.

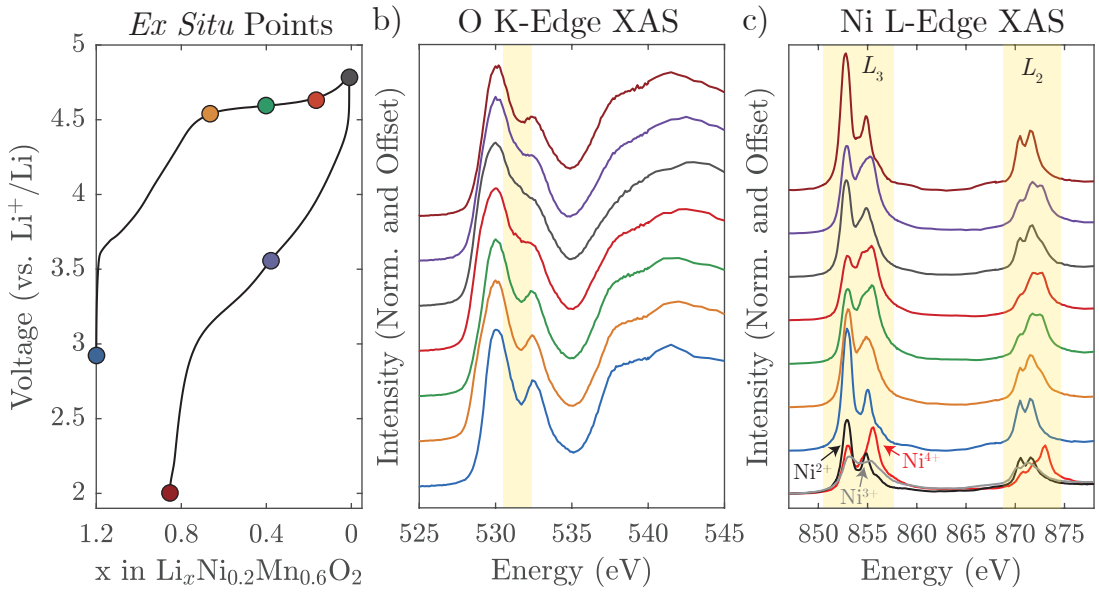

Figure 5.5: Normalized *ex situ* soft XAS data for $Li[Li_{1/5}Ni_{1/5}Mn_{3/5}]O_2$ is presented for each of the points marked in a). The O K-edge is shown in b) and the Ni L_3 and L_2-edges are shown in c). The highlighted yellow regions show the main changes to each edge, both indicating a change in oxidation state of the element. The reference Ni L-edge spectra (bottom of c) for Ni^{2+}, Ni^{3+} and Ni^{4+} are from $LiNi_{1/2}Mn_{3/2}O_4$, $LiNiO_2$, and electrochemically prepared $Ni_{1/2}Mn_{3/2}O_4$, respectively. These samples were prepared by Dr. Niccolo Guerrini and measured at Spring 8 (Sayo, Japan) beamline BL27SU.

Ex Situ Soft XAS and RIXS Mapping

Cells were stopped at various points on the load curve during both charge and discharge (Figure 5.5a), disassembled, and the *ex situ* cathode samples removed, washed with DMC, and then dried for this soft XAS measurement. In the pristine compound, the electronic states just above the Fermi energy correspond to empty Mn and Ni 3d orbitals mixing with O 2p. The O K-edge pre-edge region (Figure 5.5b) corresponds to the O 2p character of those states, while the Ni L-edge (Figure 5.5c) probes the Ni 3d character.[40] The L-edge of Ni is complicated by splitting of the Ni 2p core state to give the L_3 and L_2 absorption features.

Clear changes can be seen on the O K pre-edge across the electrochemical plateau in the section highlighted in yellow. This is consistent with an increase in the hole states on O and/or a change in the covalency of the TM-O bond[40] and therefore demonstrates the participation of O in charge compensation. There are also significant changes in the Ni L-edge spectra but surprisingly, many of

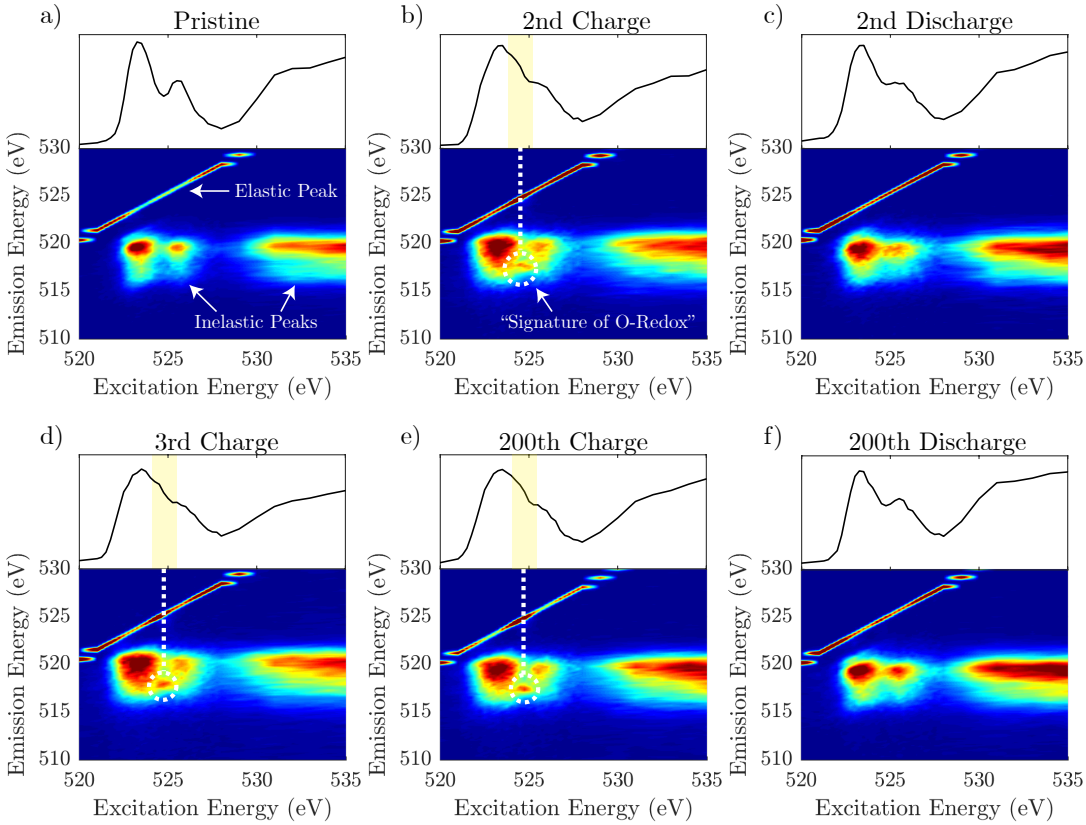

Figure 5.6: RIXS maps for pristine $Li[Li_{1/5}Ni_{1/5}Mn_{3/5}]O_2$ and *ex situ* samples are shown for various cycle numbers ending on either charge (4.8 V) or discharge (2.0 V). The *ex situ* samples were prepared by Dr. Niccolo Guerrini. The measurement was conducted at the ALS 8.0.1 (Berkeley, CA) on a low angle spectrometer which caused the elastic peak to appear more intense.

these changes occur after the end of the theoretical $Ni^{2+/4+}$ region of the load curve (orange line). By comparing the spectra to the measured standards, shown at the bottom, it appears that Ni never fully achieves the 4+ oxidation state, despite the fact that the capacity at which the plateau commences, matches exactly with the theoretical value (0.4 e^-). This begs the question of what the exact role of Ni is in the charge compensation mechanism and to what extent it has an effect on the O-redox behavior.

To understand the electronic changes to O in more detail, resonant inelastic X-ray scattering (RIXS) maps were measured on *ex situ* samples after each of the first few charge/discharge cycles as well as the 200th charge and discharge, shown in Figure 5.6. The map of the pristine uncycled cathode, shown in Figure 5.6a

has two key parts: 1) the elastic peak which varies its emission energy directly with excitation energy and 2) the inelastic peak which varies its intensity but maintains a more constant emission energy. The integrated intensity of the map as a function of excitation energy reproduces the O K-edge absorption spectra, which is shown above each map.

After charging to 4.8 V vs. Li^+/Li, a new inelastic feature appears in the RIXS at slightly lower emission energies, highlighted by a white dashed circle. Recently, it has been claimed that this feature is a signature of oxidized O. [39, 41] Notably, this signature still appears at the end of the 200th charge (Figure 5.6e) and disappears on discharge (Figure 5.6f). This demonstrates the persistence of O participation on cycling, despite the hysteresis evidenced in the electrochemical load curve.

The above spectroscopic methods clearly evidence the participation of O on the first cycle and its continued reversibility on cycling. However, it remains unclear what the cause of the first cycle hysteresis is and why Ni does not appear to be oxidized fully from 2+ to 4+. Density functional theory (DFT) calculations were therefore invoked to better understand this discrepancy.

DFT Calculations

DFT calculations were carried out on the similar composition $Li[Li_{1/6}Ni_{1/4}Mn_{7/12}]O_2$ as this reduced the number of atoms needed in the supercell to 48 (12 formula units) and was therefore less computationally expensive. This compound was also experimentally synthesized, by the RF-Gel method described previously, in order to compare the cell parameters and voltage evolution as a function of Li content with those determined through first principles.

Three compositions, $Li_xNi_{1/4}Mn_{7/12}O_2$ (x = 7/6, 11/12, 2/3), were inspected in detail where the Ni oxidation state should nominally be 2+, 3+, and 4+ respectively. $x = 0$ was also probed by DFT but this composition could not be obtained experimentally so the results should be taken with caution.

When Li is partially removed from this compound, there exists a large number of possible Li-vacancy configurations. Considering available octahedral sites, the

total number of configurations for $x = 11/12$ and $2/3$ is 364 and 3003, respectively. These configurations were initially ranked by electrostatic energy (assuming the nominal oxidation states) using the Python Materials Genomics package,[42] and the 12 lowest energy configurations were used as input for the DFT calculation.

Surprisingly, when a considerably higher ranked (# 1500 by electrostatic energy) configuration for $x = 2/3$ was used as input for DFT to check for robustness of the method, the relaxed structure resulted in a lower total energy (more stable) than the previously 12 that were sampled. Upon inspection of the structure, it was evident that Li had spontaneously migrated into tetrahedral sites above the Li sites in the TM layer. If Li layer tetrahedral sites are also considered among the possible Li-vacancy configurations, the total number of configurations grow to 31,824 and 43,758 for $x = 11/12$ and $2/3$, respectively. Even considering this, however, the lowest electrostatic energy configuration still did not have Li occupying tetrahedral sites. Although this is by no means a deep dive into the methodology of predicting Li-vacancy configurations (as this was not the goal of the study), these findings clearly demonstrate that blindly assuming a strong correlation between the electrostatic energy of the inputted structural model with the total energy of the DFT relaxed structural model is not advisable.

In the end, 12 configurations were sampled for $x = 11/12$ and 23 for $x = 2/3$. The formation energy for each configuration, with respect to the two end phases (at x = 0 and 7/6), is plotted in Figure 5.7a with lines connecting the lowest

Table 5.2: $Li[Li_{1/6}Ni_{1/4}Mn_{7/12}]O_2$ cell parameter comparison between experimentally observed (top) and those calculated by DFT (bottom).

	a (Å)	**b** (Å)	**c** (Å)	α (°)	β (°)	γ (°)
x = 7/6	9.928	8.598	5.043	90.000	109.614	90.000
	10.115	8.758	5.096	90.000	109.401	90.000
x = 11/12	9.890	8.565	5.055	90.000	109.1469	90.000
	9.992	8.709	5.136	89.834	108.953	89.9071
x = 2/3	9.883	8.559	5.059	90.000	109.501	90.000
	9.925	8.690	5.248	90.008	111.256	89.999
x = 0	N/A	N/A	N/A	N/A	N/A	N/A
	9.929	8.648	4.880	90.000	109.186	90.000

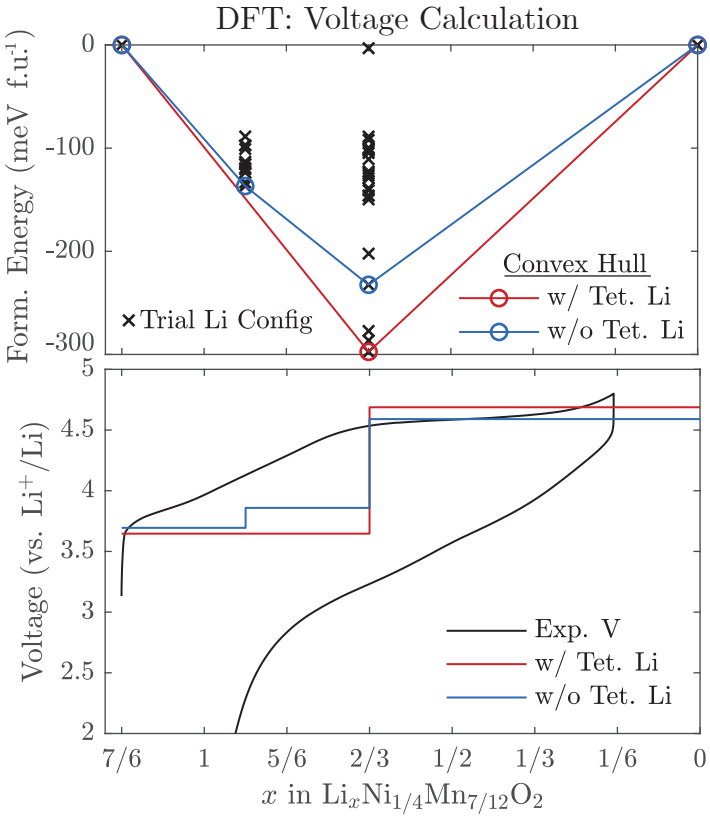

Figure 5.7: The formation energy of the various Li-vacancy configurations for $Li_xNi_{1/4}Mn_{7/12}O_2$ ($x = 2/3$, $11/12$) are plotted with respect to the fully lithiated and fully de-lithiated end members ($x = 0$, $7/6$). The convex hull line, marking the lowest energy path, is drawn in red. The corresponding calculated voltage profile is presented below and compared with the experimental voltage profile. Since Li occupancy of tetrahedral sites in Li-rich compounds is somewhat controversial, the convex hull and voltage profile not including these configurations is also shown in blue.

energy configurations in the convex hull (configurations illustrated in Figure 5.8). If entropic effects are ignored, the equilibrium voltage of the (de-)intercalation reaction can be approximated through the change of total energies calculated by DFT using the following equation[43]:

$$\overline{V}(x_1, x_2) \approx -\frac{E(\mathrm{Li}_{x_1}\mathrm{MO}_2) - E(\mathrm{Li}_{x_2}\mathrm{MO}_2) - (x_1 - x_2)E(\mathrm{Li})}{(x_1 - x_2)F} \tag{5.3}$$

where $x_1 > x_2$, $\overline{V}$ is the average voltage, $E(\mathrm{Li})$ is the DFT calculated total energy of Li metal reference, and F is the Faraday constant.

Figure 5.7b shows the calculated voltages, considering the lowest total energy structures, plotted alongside the experimental voltage curve. The red line includes

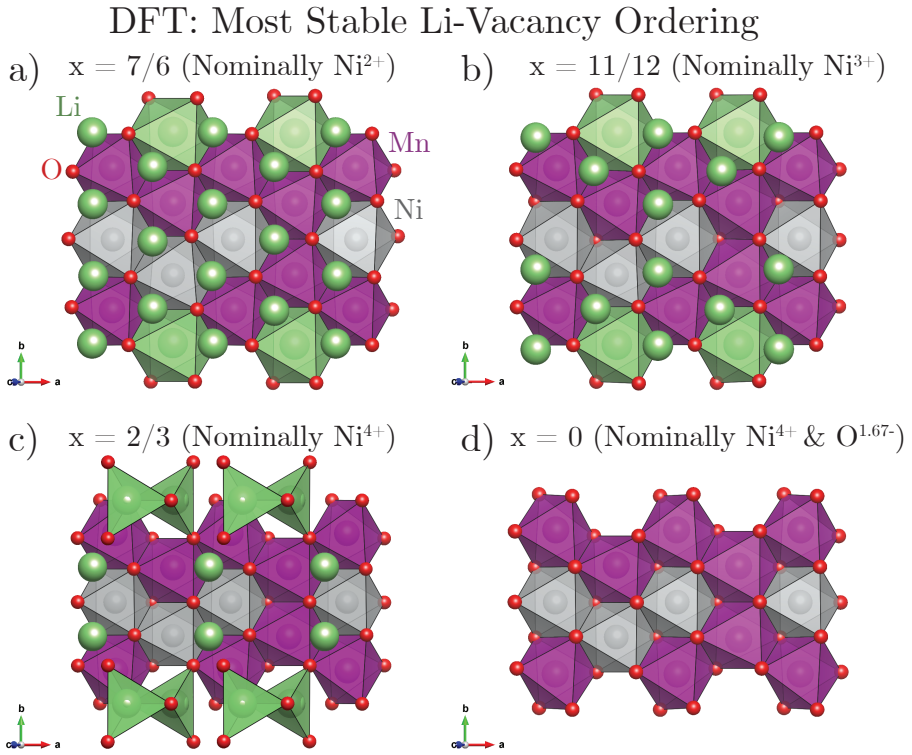

Figure 5.8: The most stable Li-vacancy configurations calculated by DFT are shown for $Li_xNi_{1/4}Mn_{7/12}O_2$ at a) $x = 7/6$ (fully lithiated), b) $x = 11/12$, c) $x = 2/3$, and d) $x = 0$ (fully de-lithiated). The polyhedra are drawn for Li occupying octahedral sites in the TM layer as well as tetrahedral sites in the Li layer but not for octahedral sites in the Li layer.

configurations in which Li relaxed to occupy tetrahedral sites and the blue line only considers configurations where Li occupies octahedral sites. A more thorough sampling of the compositions and possible configurations would probably lead to a better reproduction of the experimental voltage curve. For the goal of determining the role of Ni in the compound however, the reasonable agreement seen between the experimental and calculated voltages is sufficient validation of the computational model. Moreover, the differences between the calculated lattice parameters at each composition and the values determined experimentally from *ex situ* XRD (Table 5.2) are within an acceptable margin of error (<5%).

The TM-O bond distance usually correlates well with the TM valence state.[44] These distances are plotted for each of the 3 Ni (grey) and 7 Mn (purple) to the 6 coordinating O in the relaxed supercell. A dashed line of the same color marks the average bond distance. As Li is removed from the structure, the average Ni-O bond

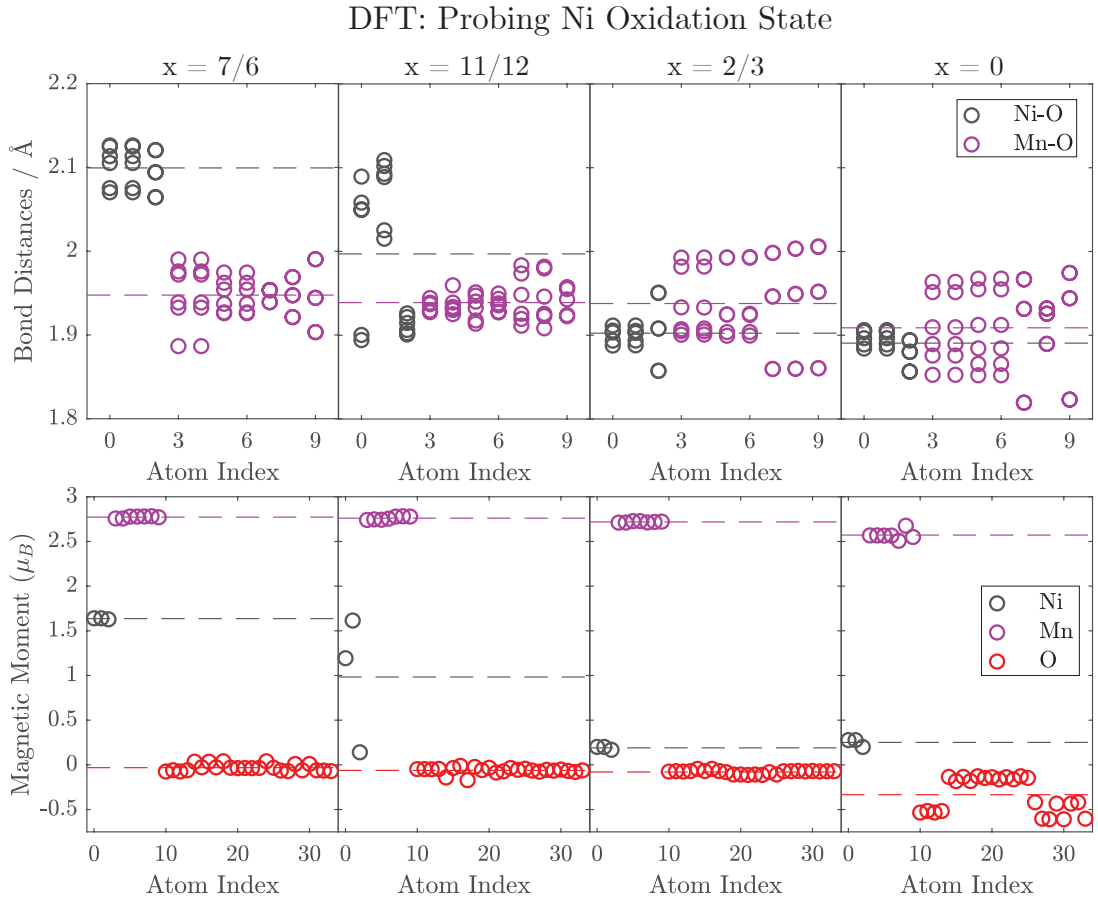

Figure 5.9: The bond distances and magnetic moments extracted from the output of the DFT calculation for the lowest energy configuration at each of the relevant compositions for $Li_xNi_{1/4}Mn_{7/12}O_2$ (x = 7/6, 11/12, 2/3, 0). The dashed lines indicate the average value of the points per bond/atom type.

distance decreases from 2.1 Å for $x = 7/6$ to 2.0 Å for $x = 11/12$ and 1.9 Å for $x = 2/3$. There is virtually no further change of the Ni-O bond distance upon full de-lithiation to x = 0. This matches well with the expected oxidation of Ni from 2+ to 4+. The Mn-O bond distance on the other hand maintains a fairly constant average value of approximately 1.95 Å although some distortion is evident.

The magnetic moments of the compound corroborate these conclusions. In the pristine material ($x = 7/6$), the average magnetic moment on the Ni atoms is 1.6 μ_B, which is relatively close to the nominal value of 2 μ_B for Ni^{2+} (e_g $\uparrow\uparrow$). At $x = 11/12$, the average value drops to 1.0 μ_B (nominally Ni^{3+}: 1.0 μ_B, e_g $\uparrow$) and at $x = 2/3$, the average magnetic moment drops to approximately 0.2 μ_B (nominally Ni^{4+}: 0.0 μ_B, t_2g $\uparrow\downarrow\uparrow\downarrow\uparrow\downarrow$). Removing the rest of the Li from the structure, again,

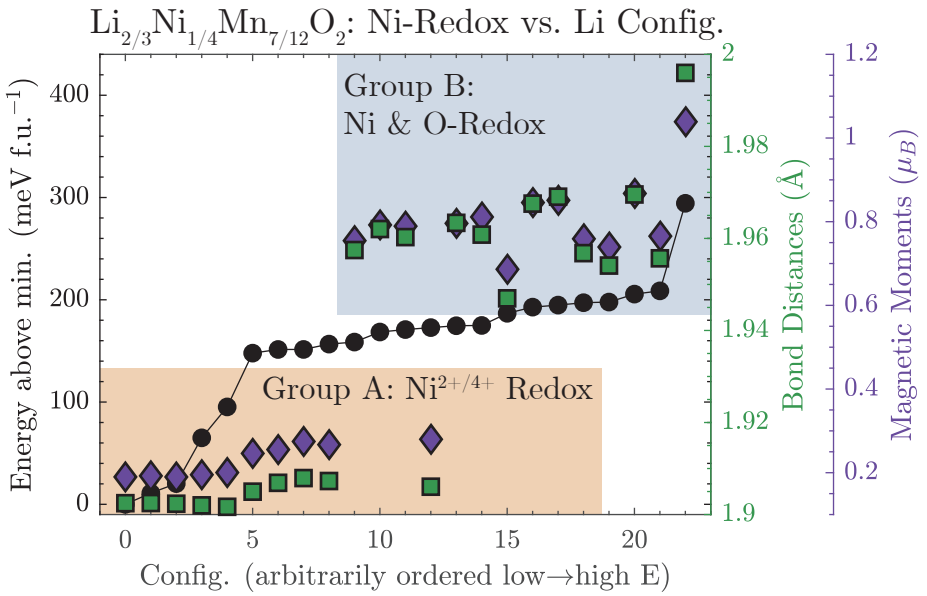

Figure 5.10: For each of the 23 Li-vacancy configurations probed, three properties are plotted on separate axes. These are the average total energy above the minimum (black circle), the average Ni-O bond distance (green square), and the average Ni magnetic moment (purple diamond). Based on the average Ni-O bond distances and magnetic moments (and not the total energies), the configurations cluster into two main groups (A and B) which are differentiated by their Ni oxidation state.

does not produce any significant change for Ni. The Mn average magnetic moment stays fairly constant at approximately 2.8 μ_B, similar to the nominal value of 3.0 μ_B for Mn^{4+} (t_2g ↑↑↑). Considering the magnetic moments and bond distances of Ni in the compound, it appears Ni should be oxidized from 2+ to 4+ as expected. Why then is Ni not evidenced experimentally to fully oxidize?

Returning to the ranking of Li-vacancy configurations for the $x = 2/3$ composition, a closer examination of magnetic moments and Ni-O bond distances revealed a high sensitivity of Ni and O oxidation states to the Li configuration. This is shown in Figure 5.10 where an arbitrary configuration number is assigned to each model on the x-axis and the total energy (black), bond distances (green), and magnetic moments (purple) for each configuration are plotted on the respective y-axes. Overall, the configurations could be classified into one of two groups where A) Ni appears to be fully oxidized to 4+ (bond distances < 1.95 Å, magnetic moment < 0.25 μ_B), or B) O is oxidized along with Ni, lowering the average oxidation state of Ni.

Generally, group A configurations were found to be more stable when compared with group B. However, this does not necessarily preclude the possibility of having some regions of the cathode where group B type configurations are prevalent. Moreover, DFT can only relax the atomic positions if doing so decreases the total energy of the system; it has no way to traverse even a small activation barrier should it arise on the path towards a global energy minimum. Therefore, having an accurate structural model to input for the calculation is imperative. Looking back at the *operando* XRD experiment, it was seen that the honeycomb ordering in the TM layer is largely lost when charged into the plateau region of the electrochemical load curve. Since this DFT study focused on the $x = 2/3$ composition, just before the plateau region, the possibility of TM layer disorder was not examined. However, due to the longer time scales of relaxation associated with an *ex situ* soft XAS Ni L-edge measurement, it may be possible that TM rearrangement occurred, lowering the energy of the system while redistributing negative charge from O to Ni.

Conclusions

To summarize, $Li[Li_{1/5}Ni_{1/5}Mn_{3/5}]O_2$, a model Li-rich cathode, was probed for its electrochemical and structural properties. Through *operando* XRD, it was shown that the long range honeycomb superstructure ordering between Li and Mn disappeared on the first charge and was not regained on discharge. This structural change may be partially (or fully) to blame for the first cycle electrochemical hysteresis. From soft XAS measurements, it was determined that Ni and O were both oxidized on the first charge but Ni to a lesser extent than expected (i.e. $<$ 4+). Despite the irreversible loss of the superstructure on the first charge, RIXS measurements showed that O continues to reversibly participate in the charge compensation of Li on extended cycling. The DFT results provided new insight regarding the dependency of the Ni and O redox processes on the Li-vacancy configuration. The possibility of dynamic relaxation of the crystal and electronic structures of the material during experiment will be the topic of future work.

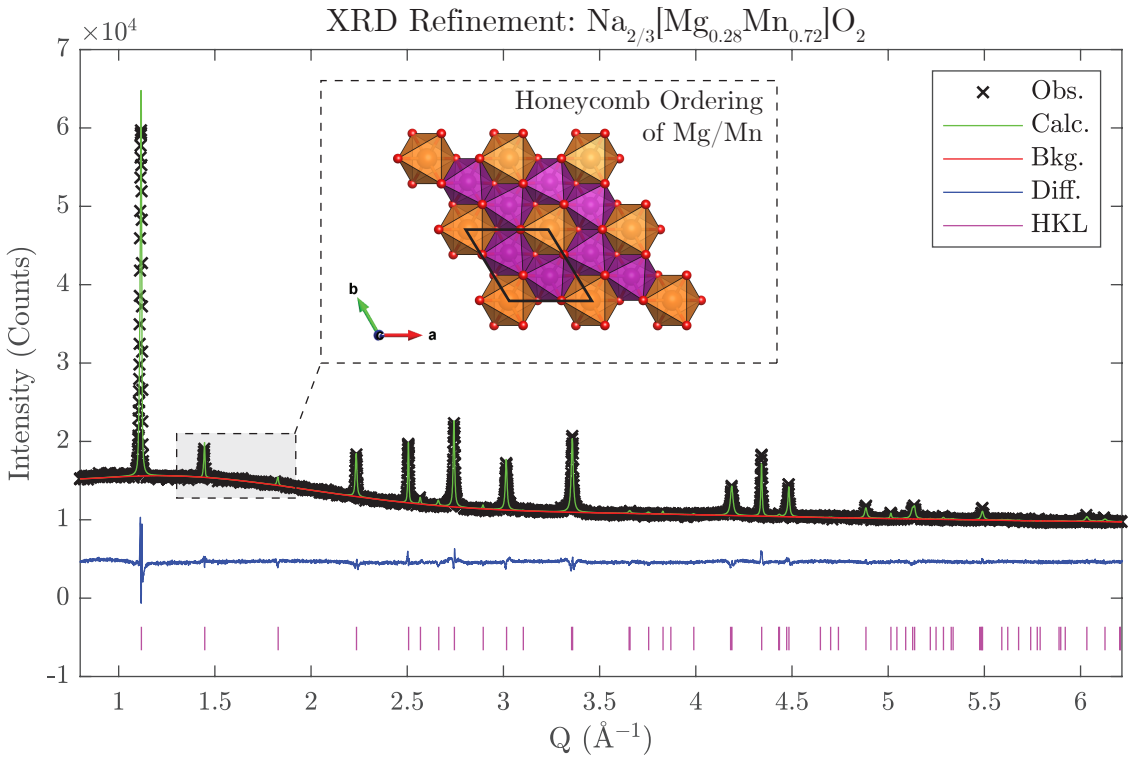

Figure 5.11: XRD data is shown with the corresponding Rietveld refinement fitting for $Na_{2/3}[Mg_{0.28}Mn_{0.72}]O_2$ collected on the Cu source Rigaku lab instrument. The inset shows the Mg/Mn honeycomb ordering which gives the superstructure peaks seen in the Q = 1.4–1.9 Å^{-1} range. Refined parameters are shown in Table 5.3

5.4.2 $Na_{2/3}[Mg_{0.28}Mn_{0.72}]O_2$: Oxygen Redox Without Excess Alkali Ions or O_2 Gas Loss

The limitations of Li_2MnO_3-based Li-rich cathodes in terms of hysteresis, voltage decay, and O-loss has inspired work on more exotic compounds such as those based on the (de-)intercalation of Na instead of Li. Seo et al. reported the importance of the ionic Li - O interaction for activating O-redox in "Li-rich" cathodes, and it was later shown by Rozier et al. that the Na - O interaction in $Na_2Ru_{1-y}Sn_yO_3$ (y = 1/4, 1/2, 3/4) also sufficed for this purpose.[45, 46]. This begged the question whether a *non* alkali metal ion could still be sufficiently ionic to activate O. At that time, $Na_{2/3}[Mg_{0.28}Mn_{0.72}]O_2$ had recently been reported to have anomalously high capacity.[19] It was therefore decided to examine this compound to clarify whether the Mg - O interaction could invoke O-participation and explain the higher than expected capacity.

Table 5.3: Rietveld refinement results for $Na_{2/3}[Mg_{0.28}Mn_{0.72}]O_2$. The corresponding fitting is plotted in Figure 5.11.

S.G. *P6₃/mcm*, *a*: 5.0123(1), *c*: 11.2389(4), Rwp: 1.69%, Rexp: 0.92%					
Atom	**x**	**y**	**z**	**SOF**	**Uiso (Å²)**
Na (6g)	0.301	0	1/4	0.382(3)	0.075(3)
Na(4c)	1/3	2/3	1/4	0.427(4)	0.075(3)
Mg (2b)	0	0	0	0.84	0.0112(5)
Mn (2b)	0	0	0	0.16	0.0112(5)
Mn (2d)	1/3	2/3	0	1	0.0112(5)
O (12k)	0.3418(7)	0.3418(7)	0.0772(2)	1	0.019(1)

Pristine Structure and First Cycle Voltage Curve

Assuming the nominal composition, $Na_{2/3}[Mg_{0.28}Mn_{0.72}]O_2$ has the oxidation states of $Na_{2/3}{}^{+}[Mg_{0.28}{}^{2+}Mn_{0.11}{}^{3+}Mn_{0.61}{}^{4+}]O_2{}^{2-}$. Given the complications that can sometimes arise (TM and O vacancies, multiple phases, etc. [47–49]) in synthesizing mixed Mn oxidation states, it was initially attempted to synthesize $Na_{2/3}[Mg_{1/3}Mn_{2/3}]O_2$ but this resulted in MgO impurities. It was therefore decided to retain the composition reported by Yabuuchi et al. as this could be synthesized as a pure phase.

Powder XRD is shown in Figure 5.11 with the fitting of the data by Rietveld refinement (refined values in Table 5.3). This compound crystallizes into the P2 structure but shows superstructure peaks related to the honeycomb type ordering of Mg and Mn in the TM layer.[20, 50] A larger unit cell with space group $P6_3/mcm$ was used to account for these extra reflections in the refinement. Within a single TM layer, the honeycomb arrangement of Mg and Mn is the same as Li_2MnO_3 and $Na_{2/3}[Ni_{1/3}Mn_{2/3}]O_2$, but the stacking of these layers differs slightly.[20]

The electrochemical load curve for the material is shown in Figure 5.12. The first section of the charge curve with rapidly rising voltage matches well with the oxidation of the small amount of Mn^{3+} in the compound (highlighted blue). The cathode material then displays a long plateau region (highlighted orange) reminiscent of the voltage profile of $Li[Li_{1/6}Ni_{1/4}Mn_{7/12}]O_2$ (Figure 5.1). Overall, approximately 0.5 mol of Na is extracted beyond what is theoretically possible through compensation by the $Mn^{3+/4+}$ redox couple alone.

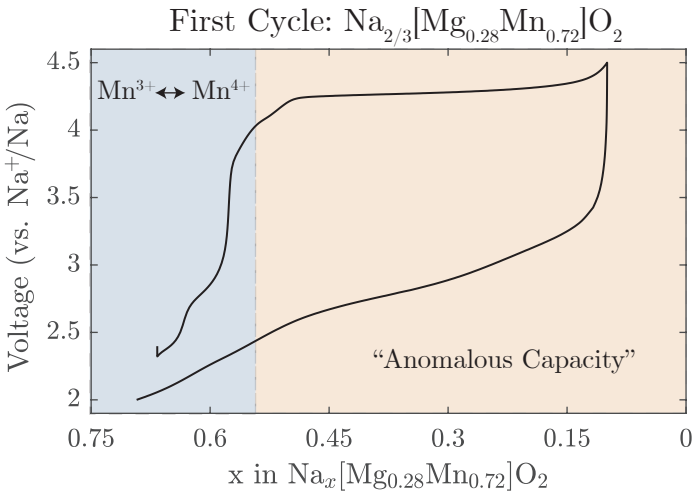

Figure 5.12: The first electrochemical cycle of $Na_{2/3}[Mg_{0.28}Mn_{0.72}]O_2$ is shown cycled at 10 mA g^{-1} between 2.0 and 4.5 V vs. Na^+/Na.

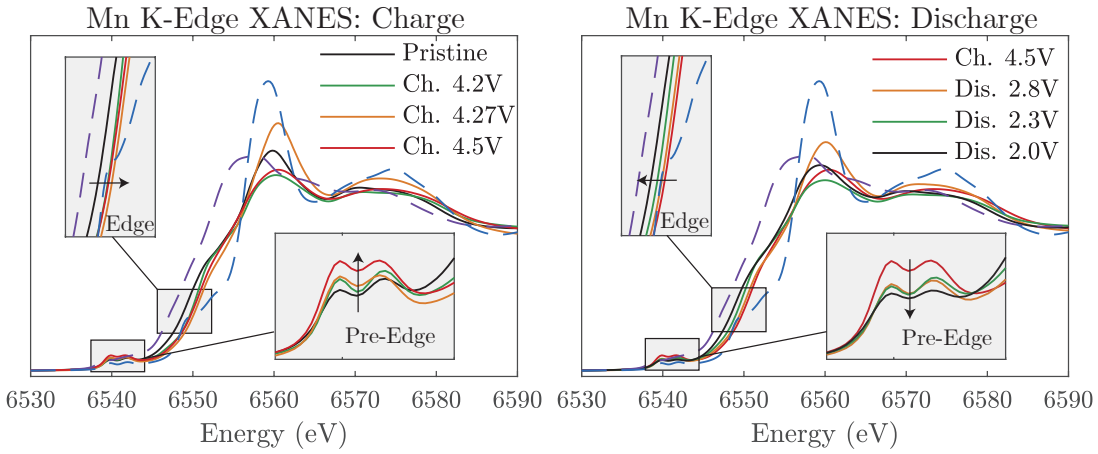

Figure 5.13: Mn K-Edge XANES was conducted on *ex situ* samples of $Na_{2/3}[Mg_{0.28}Mn_{0.72}]O_2$ stopped at the labeled voltages on charge (left plot) or discharge (right plot). The dashed lines are reference spectra for Mn^{4+} in Li_2MnO_3 (blue) and Mn^{3+} in Mn_2O_3 (purple). The main edge and pre-edge are both expanded in the insets to see the subtle changes. The *ex situ* samples were prepared, in part, by Dr. Urmimala Maitra and were measured at DLS B18.

Mn K-Edge XANES

To rule out the possibility of further oxidation of Mn beyond 4+, Mn K-edge XANES was employed. The results, shown in Figure 5.13, are plotted alongside reference samples $Mn_2{}^{3+}O_3$ (purple dashed) and $Li_2Mn^{4+}O_3$ (blue dashed). *Ex situ* analysis of the material was conducted by charging (and discharging) the material

to different voltages and collecting the electrode for measurement. Stopping points during the charging of the cell are shown in the left plot while the samples stopped during discharge are shown on the right. First, looking at the energy of the main edge (which is expanded in the inset), it is evident that there is a slight shift to higher energies between the pristine sample and the sample charged to 4.2 V. This matches well with the expectation that the small amount of Mn^{3+} in the compound is oxidized to Mn^{4+} during the initial stage of charge. Subsequently, no further shifts are seen in the edge indicating that Mn is not further oxidized. The pre-edge and white line of the near edge structure, however, do show significant changes consistent with changes in the local environment of Mn. In particular, the increase in the pre-edge intensity is believed to stem from a greater mixing of the Mn 4p and 3d electronic states due to decreasing centrosymmetry (i.e. increasing distortion) of the octahedral sites in which it resides.[51, 52] Because the main edge does not shift, however, this distortion likely arises from structural changes and not from changes to the Mn valence state. On discharge, the Mn K-edge progressively shifts back to approximately the same energy as the pristine sample and the pre-edge intensity is also reduced. From this data set, it is concluded that $Mn^{4+/3+}$ redox plays a minor role in the charge compensation of the compound, both on charge and discharge, and there is no indication that Mn is oxidized beyond 4+.

DFT Calculations

The absence of Mn^{5+} in the XANES measurements provides indirect evidence of the participation of O on charge. For more direct insight, however, DFT calculations were again performed. For simplicity, the structural model used for the calculation

Table 5.4: Comparison of $Na_{2/3}[Mg_{1/3}Mn_{2/3}]O_2$ DFT cell parameters with experimental values of $Na_{2/3}[Mg_{0.28}Mn_{0.72}]O_2$.

	a (Å)	**b** (Å)	**c** (Å)	α (°)	β (°)	γ (°)
Experimental $\mathbf{Na_{2/3}[Mg_{0.28}Mn_{0.72}]O_2}$	10.025	10.025	11.239	90.000	90.000	120.000
DFT $\mathbf{Na_{2/3}[Mg_{1/3}Mn_{2/3}]O_2}$	10.238	10.238	11.271	90.000	90.000	120.015

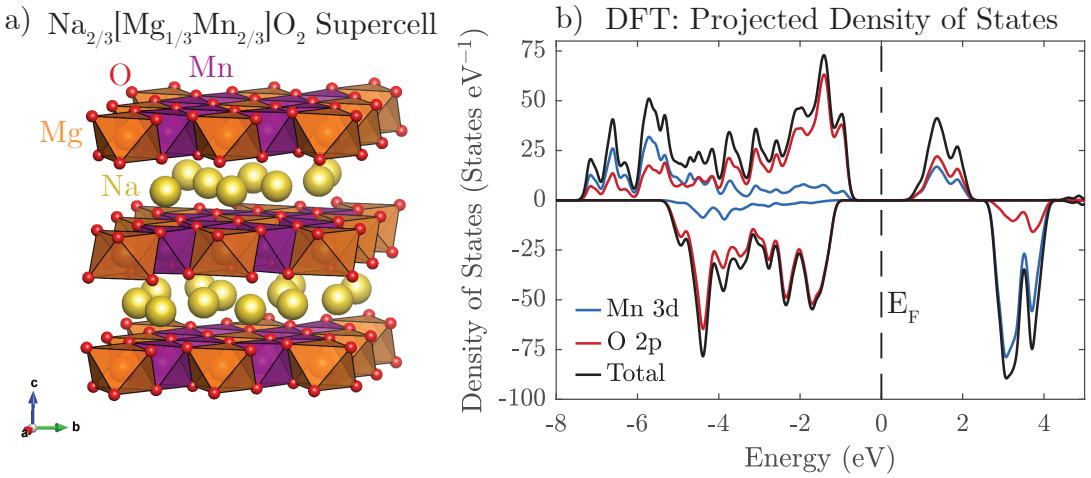

Figure 5.14: The relaxed structural model of $Na_{2/3}[Mg_{1/3}Mn_{2/3}]O_2$ from the DFT calculations is shown in a) and the calculated projected density of states (PDOS) is shown in b). The Fermi energy (E_F) is indicated by the dashed black line. From the PDOS, it is clear that the states just below the Fermi energy are dominated by O 2p character.

was based on $Na_{2/3}[Mg_{1/3}Mn_{2/3}]O_2$, with all Mn nominally in the 4+ valence state. A 2 x 2 x 1 supercell of the hexagonal unit cell was created (Figure 5.14a) and Na-ions were placed in the low energy "large zig zag" configuration.[53, 54] The cell parameters and atomic positions were relaxed and very good agreement (< 3 % difference) was seen between the experimental and calculated values despite the slightly different compositions (Table 5.4).

Once the supercell was relaxed, the projected density of states was calculated to determine the relative energies and mixing between the Mn 3d states and O 2p states above and below the Fermi energy. These results are plotted in Figure 5.14b with the 0 eV arbitrarily set to the middle of the band gap. It is immediately clear that the states just below the Fermi energy are dominated by O 2p character. It is these states which electrons will be first removed from when the cathode material is charged. While the Mn 3d states are quite dispersed in the valence band, the majority of the weight can be found more than 5 eV below the Fermi energy which would be inaccessible (i.e. Mn^{5+} is very unlikely). The DFT results combined with the XANES measurements strongly indicate that O is oxidized in $Na_{2/3}[Mg_{0.28}Mn_{0.72}]O_2$. However, as was discussed previously, this activation can occur in the form of direct oxidation to O_2 gas (O-loss) or solid state O-redox (with or without hysteresis).

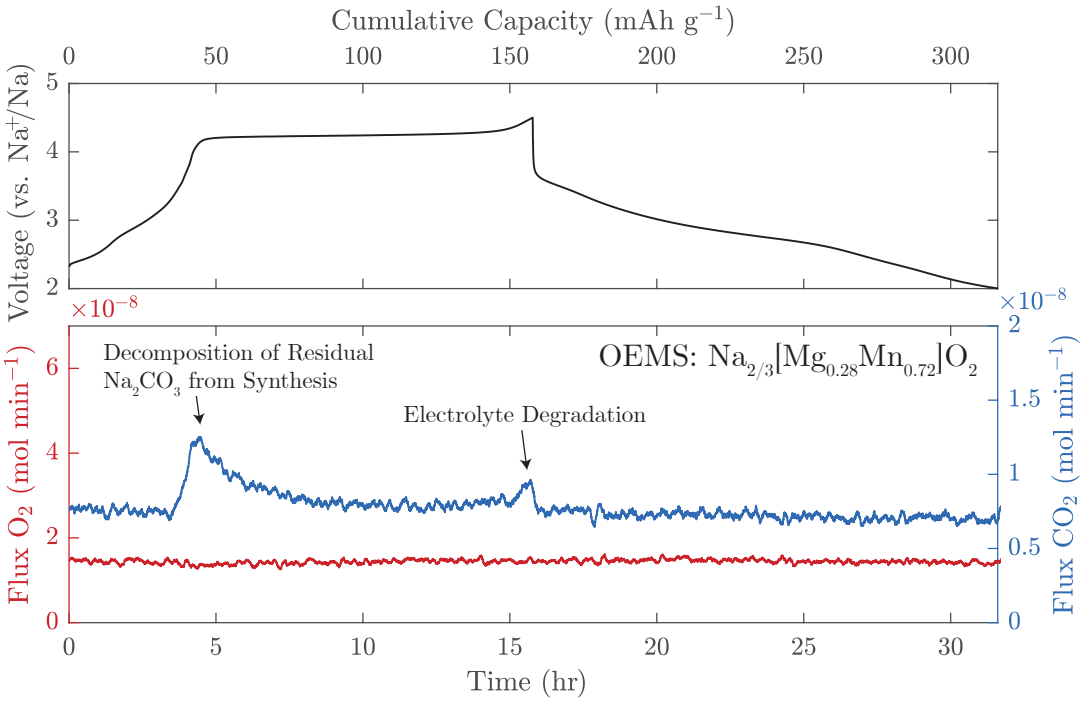

Figure 5.15: OEMS was conducted on the first cycle of $Na_{2/3}[Mg_{0.28}Mn_{0.72}]O_2$. There is no evidence of any direct O-loss in the form of O_2. A small amount of CO_2 is seen at the beginning and end of the plateau region. This was attributed to the decomposition of residual Na_2CO_3 from the surface of the active material and electrolyte degradation respectively.[55] This OEMS experiment was completed by Mr. Robert House.

Online electrochemical mass spectrometry (OEMS) was therefore used to monitor the gas evolution from the cathode material over the first cycle.

Online Electrochemical Mass Spectrometry

The OEMS results are presented in Figure 5.15 with the electrochemical load curve shown on the top axis and the gas evolution shown on the bottom. Both O_2 and CO_2 were monitored as the cell was charged and discharged. Unlike many "Li-rich" materials, $Na_{2/3}[Mg_{0.28}Mn_{0.72}]O_2$ showed absolutely no direct O_2 gas loss. A small amount of CO_2 gas was observed which was resolved to originate from residual Na_2CO_3 from synthesis and degradation of the carbonate based electrolyte. This was determined through an ^{18}O isotope labeling experiment not presented here.[55] As recently as 2016, O-loss was believed by many to be inevitable in systems based on 3d TMs.[56] The lack of irreversible O-loss from $Na_{2/3}[Mg_{0.28}Mn_{0.72}]O_2$ on charge

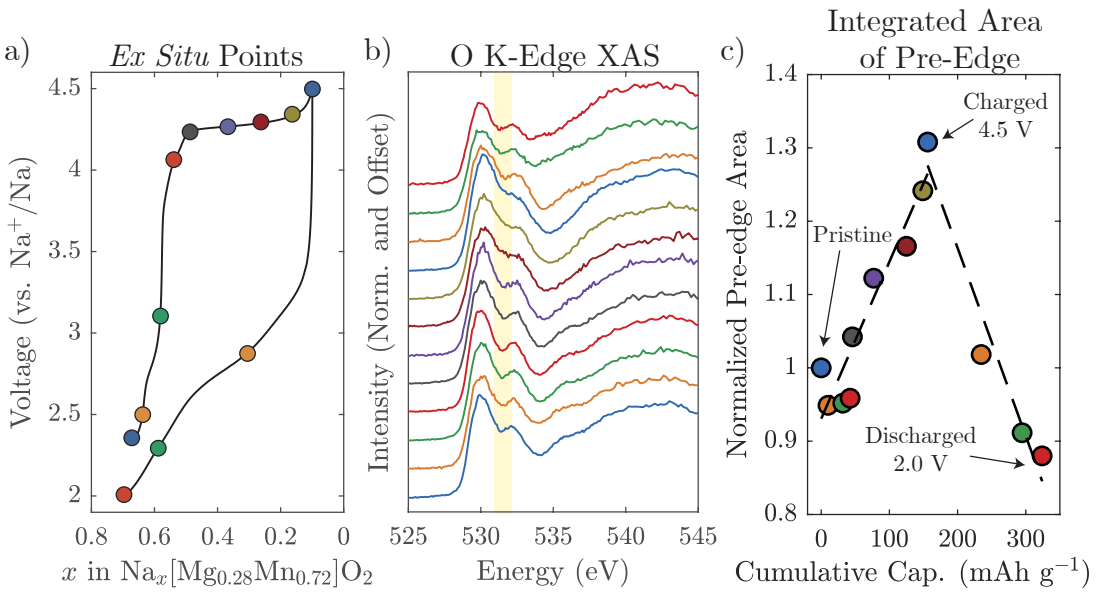

Figure 5.16: The O K-edge XAS spectra were measured in total fluorescence yield (TFY) mode for several *ex situ* samples of $Na_{2/3}[Mg_{0.28}Mn_{0.72}]O_2$ with voltage stopping points shown in a). The spectra, presented in b), show a growth of intensity in the middle of the pre-edge region, highlighted in yellow. This increased intensity is quantified in c) and shows a clear trend as a function of the state of charge. These *ex situ* samples were prepared, in part, by Dr. Urmimala Maitra. Measurements were conducted at the ALS 8.0.1 (Berkeley, CA).

suggests this compound operates instead through reversible solid state O-redox. To prove this, soft XAS and RIXS of the O K-edge were conducted in order to identify the correct mechanism for the O-redox process.

O K-Edge Soft XAS and RIXS Mapping

O K-edge soft XAS was conducted on *ex situ* samples of $Na_{2/3}[Mg_{0.28}Mn_{0.72}]O_2$ stopped at 12 points along the first cycle. These stopping points are marked in Figure 5.16a. As was the case with $Li[Li_{1/5}Ni_{1/5}Mn_{3/5}]O_2$, a general broadening of the O K-edge is seen (Figure 5.16b) with intensity increasing on charge in the middle of the two peaks in the pre-edge (highlighted yellow). On discharge, the opposite occurs with the pre-edge peaks becoming more defined once again.

The O K-edge pre-edge region reveals the O 2p character of the states just above the Fermi energy. The spectrum is sometimes difficult to interpret, however, as a strong mixing of the O 2p and TM 3d states generally exists in this region. Given

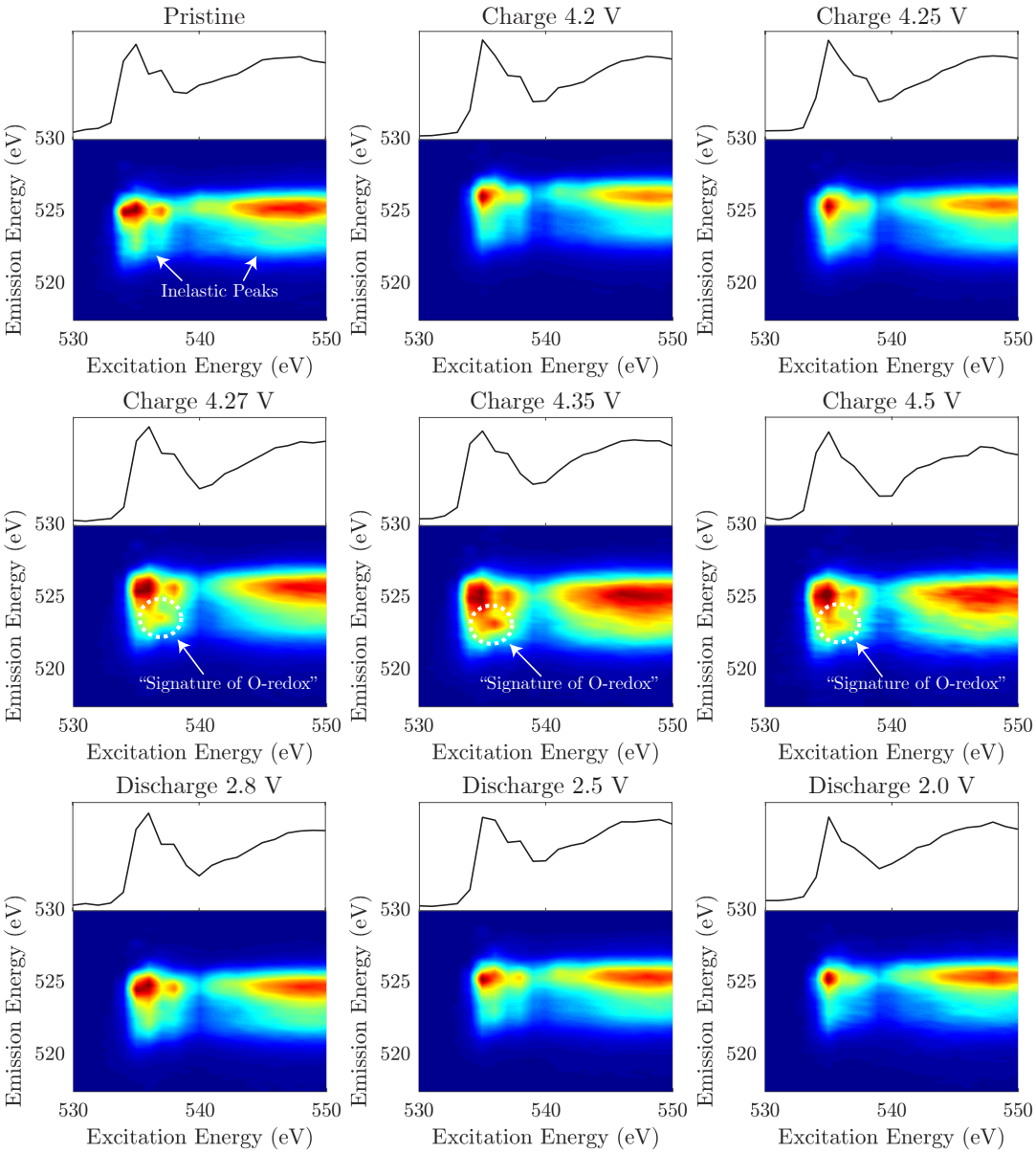

Figure 5.17: RIXS maps of the O K-edge are shown for various stopping points in the first cycle of $Na_{2/3}[Mg_{0.28}Mn_{0.72}]O_2$. An extra emission feature emerges upon charging beyond 4.25 V, indicating solid state O oxidation. These *ex situ* samples were prepared, in part, by Dr. Urmimala Maitra. Measurements were conducted at the ALS 8.0.1 (Berkeley, CA).

that the DFT results for the pristine compound showed significant O 2p character at the top of the valence band, it is highly likely that it is these states (primarily of O 2p character) which are seen in the soft XAS after electrons and Na are removed from the compound on charging. To further understand the nature of these new O 2p dominant hole states, RIXS maps of the O K-edge were once again utilized.

RIXS maps were measured for a collection of *ex situ* samples stopped at different voltages on the first charge/discharge cycle and are shown in Figure 5.17. The pristine sample shows an inelastic emission at approximately 525 eV which varies its intensity with excitation energy. The integrated intensities (with respect to the excitation energy) reproduce the absorption spectra for the O K-edge shown above each map. On the samples charged to 4.2 V and 4.25 V (beginning of the voltage plateau), no significant changes are seen in the maps from the pristine. This is consistent with the majority of the charge compensation for this region coming from the oxidation of Mn, as seen in the XANES (Figure 5.13). For samples stopped at higher voltages further along the plateau, however, a new feature is observed at lower emission energies. This is the same feature seen earlier for charged samples of $Li[Li_{1/5}Ni_{1/5}Mn_{3/5}]O_2$ and described in the literature as the "signature" of O-redox.[39, 41] It is also consistent with O hole states being relatively localized in character (i.e. having a narrow energy band).[38] On discharged samples, the O-redox "signature" is not seen even for the sample stopped at 2.8 V (approximately 0.25 mol Na re-intercalated). This is somewhat surprising given the length of the voltage plateau on charge nominally corresponds to the removal of approximately 0.5 mol Na via O oxidation. One possible explanation may be the instability of the O-redox couple in contact with the electrolyte.[57] A similar phenomenon was concluded to explain the behavior of Fe^{4+} in $NaFeO_2$.[58] This explanation also fits well with the small amount of electrolyte oxidation seen in the OEMS results. Further work is needed to fully understand this behavior.

Discussion of O-Loss Mechanism

Overall, the O K-edge XAS and RIXS maps of $Na_{2/3}[Mg_{0.28}Mn_{0.72}]O_2$ clearly demonstrate reversible solid state O-redox. Importantly, this is the first time O-redox has been documented for a compound that does not possess an excess of alkali metal ions (i.e. alkali metal ions in the TM layer). These results agree well with DFT in proving that O can be oxidized even in the presence of higher valence Mg^{2+} (as compared to than Li^+ or Na^+).

A question that remains unanswered, however, is how $Na_{2/3}[Mg_{0.28}Mn_{0.72}]O_2$ avoids O-loss while other O-redox compounds, including $Li[Li_{1/5}Ni_{1/5}Mn_{3/5}]O_2$, do not. Based on the reported findings, a new mechanism for O-loss in 3d TM layered oxide systems was recently proposed.[55] In Li-rich compounds such as $Li[Li_{1/5}Ni_{1/5}Mn_{3/5}]O_2$, Li is removed from both the TM and Li layers of the compound.[59] When this compound approaches the upper voltage cutoff of 4.8 V, the structure is highly depleted of Li ($x < 0.2$ in $Li_xNi_{1/5}Mn_{3/5}O_2$). In this highly de-lithiated state, many O are coordinated by 2 or fewer cations. Their valence electrons will therefore be pushed higher in energy (i.e. become more unstable), and this creates the driving force for O-loss from the structure. It is indeed seen for $Li_xNi_{1/5}Mn_{3/5}O_2$ that the capacity on charge beyond $x = 0.2$ is dominated by O-loss.[11] $Na_{2/3}[Mg_{0.28}Mn_{0.72}]O_2$, on the other hand, never achieves this highly depleted state on charging since Mg^{2+} is retained in the structure on charge. This presence therefore prevents O de-stabilization and loss.

Conclusion

In this section, $Na_{2/3}[Mg_{0.28}Mn_{0.72}]O_2$ was shown to compensate Na^+ removal by the activation of the O-redox couple without any O-loss. An important corollary to these results is that O-loss can now be decoupled from voltage hysteresis. Dramatic first cycle hysteresis is seen in the great majority of compounds exhibiting O-redox, but this is the first compound that does not show O-loss coinciding with the hysteresis. Voltage hysteresis in the cathode (or anode) is directly related to the energy efficiency of the system. As such, the average voltage on discharge should ideally be as close to the average charge voltage as possible. In the next two sections, the underlying mechanisms of the voltage hysteresis are discussed and two different avenues of improvement are pursued.

5.4.3 TM Substitution to Improve First Cycle Hysteresis

After validating O-redox activity in $Na_{2/3}[Mg_{0.28}Mn_{0.72}]O_2$, it was investigated whether the first cycle voltage hysteresis of the O-redox couple could be effectively

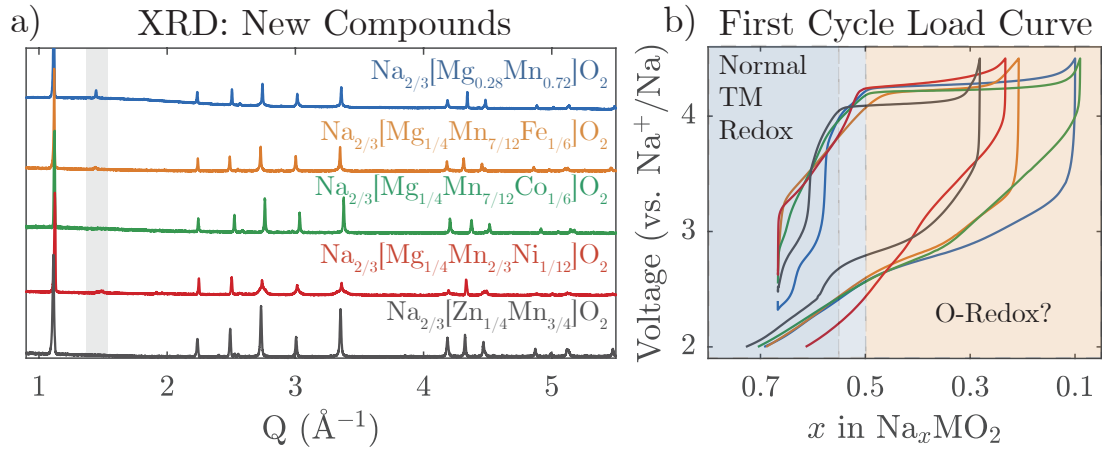

Figure 5.18: Four new compounds were synthesized and their XRD patterns and first cycle electrochemical load curves are shown compared with the previously discussed $Na_{2/3}[Mg_{0.28}Mn_{0.72}]O_2$. The XRD shows all compounds form the P2 structure and some of the compounds show the honeycomb superstructure peak (shaded grey). The first cycle load curves show that all compounds display a plateau beyond their theoretical TM redox capacity ($Na_{2/3}[Mg_{0.28}Mn_{0.72}]O_2$: first dashed grey line, all others: second dashed grey line). These compounds were synthesized and characterized, in part, by Dr. Urmimala Maitra and Dr. Nuria Tapia-Ruiz.

reduced through TM substitution. A small exploratory study was conducted on several P2-$Na_{2/3}MO_2$ compounds where M = $[Mg_{1/4}Mn_{7/12}Fe_{1/6}]$, $[Mg_{1/4}Mn_{7/12}Co_{1/6}]$, $[Mg_{1/4}Mn_{2/3}Ni_{1/12}]$, and $[Zn_{1/4}Mn_{3/4}]$. The XRD and electrochemical results for these compounds are presented in Figures 5.18a and b respectively.

XRD and First Cycle Voltage Curves

From the XRD results, it is clear that all the newly synthesized compounds crystallize into the P2 structure as expected with a Na composition of 2/3. The location of the most intense reflection of the honeycomb-type superstructure ordering is highlighted in grey. A small peak can be seen in this region for M = $[Mg_{0.28}Mn_{0.72}]$, $[Mg_{1/4}Mn_{7/12}Fe_{1/6}]$, and $[Mg_{1/4}Mn_{2/3}Ni_{1/12}]$ but not for M = $[Mg_{1/4}Mn_{7/12}Co_{1/6}]$ and $[Zn_{1/4}Mn_{3/4}]$. The lack of honeycomb ordering is particularly surprising for the Zn containing compound given that Zn should possess the same charge (2+) and approximately the same ionic radius as Mg. An abnormal amount of *hkl*-dependent broadening is seen for the M = $[Mg_{1/4}Mn_{2/3}Ni_{1/6}]$ composition. This may indicate a small amount of phase separation.

Each of these compounds were then tested in a half cell to examine their electrochemical performance. The first charge/discharge cycle for each compound is shown in Figure 5.18b with statistics documented in Table 5.5. All of the compounds, with the exception of $Na_{2/3}[Mg_{0.28}Mn_{0.72}]O_2$ (0.11 mol Na), have a theoretical TM-redox capacity on first charge of 1/6 mol Na, which is shaded in blue. Na extraction beyond this point likely stems from O oxidation and is shaded orange for clarity.

$Na_{2/3}[Zn_{1/4}Mn_{3/4}]O_2$ outperforms the other compounds in terms of energy efficiency. Looking at the voltage curve, the reason for this stems from the O-redox voltage plateau on first charge being approximately 150 mV lower in voltage than the Mg containing compounds. In a very recent report by Bai et al. on $Na_{2/3}[Zn_{2/9}Mn_{7/9}]O_2$, it was shown through DFT calculations that some mixing of the Zn 3d and O 2p states occurs.[60] It is plausible that this mixing could give rise to the lower voltage plateau seen here by slightly lowering the total energy of the de-sodiated structure with O hole states. The amount of Na that is able to be extracted from this compound, however, is less than all others and its average discharge voltage shows no improvement over $Na_{2/3}[Mg_{0.28}Mn_{0.72}]O_2$.

$Na_{2/3}[Mg_{1/4}Mn_{7/12}Fe_{1/6}]O_2$ and $Na_{2/3}[Mg_{1/4}Mn_{2/3}Ni_{1/12}]O_2$ both do not show any significant improvement over $Na_{2/3}[Mg_{0.28}Mn_{0.72}]O_2$ in the performance metrics outlined in Table 5.5. $Na_{2/3}[Mg_{1/4}Mn_{7/12}Co_{1/6}]O_2$ on the other hand delivers better capacity on discharge and does so with a slightly improved energy efficiency of 75% (compared to 71%). For that reason, this compound represented an intriguing possibility for better controlling O-redox by TM substitution and warranted further study.

Table 5.5: First cycle statistics for new O-redox compounds (extra capacity from insertion of Na beyond the pristine composition, 2/3, was not counted)

Compound: M in $Na_{2/3}MO_2$	**Energy Efficiency**	**Ch., Dis. Avg. Voltage**	**Ch., Dis. Capacity**
$Mg_{0.28}Mn_{0.72}$	71 %	4.00 V, 2.73 V	0.57, 0.59 mol Na
$Mg_{1/4}Mn_{7/12}Fe_{1/6}$	70 %	4.02 V, 2.69 V	0.46, 0.48 mol Na
$Mg_{1/4}Mn_{7/12}Co_{1/6}$	75 %	4.07 V, 2.86 V	0.58, 0.61 mol Na
$Mg_{1/4}Mn_{2/3}Ni_{1/12}$	63 %	4.06 V, 2.90 V	0.43, 0.38 mol Na
$Zn_{1/4}Mn_{3/4}$	81 %	3.89 V, 2.73 V	0.39, 0.45 mol Na

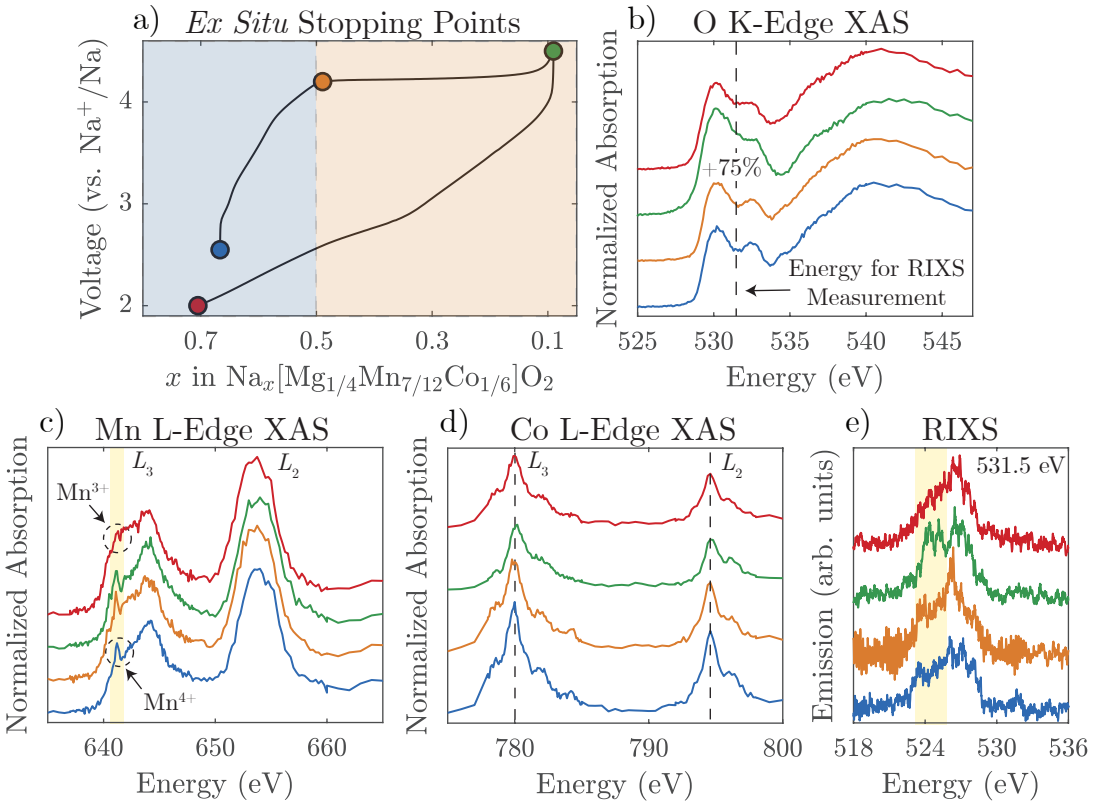

Figure 5.19: *Ex situ* soft XAS and RIXS were conducted on the pristine electrode, samples charged to 4.2 V and 4.5 V, and a sample discharged to 2.0 V, shown in a). The figure shows normalized stacked absorption spectra for the b) O K-edge, c) Mn L-edges, and d) Co L-edges. The RIXS spectra for the excitation energy of 531.5 eV is shown in d). The *ex situ* samples were prepared by Dr. Nuria Tapia-Ruiz. The measurement was conducted at Spring 8 (Sayo, Japan), Beamline BL27SU.

Soft XAS and RIXS

Ex situ soft XAS and RIXS were conducted on the pristine compound, samples stopped at 4.2 V and 4.5 V on charge, and a sample stopped at 2.0 V on discharge (illustrated in Figure 5.19a). The O K-edge XAS (Figure 5.19b) shows the most change between the samples on charge. From the sample stopped at 4.2 V to the sample stopped at 4.5 V, the area under the pre-edge grew by approximately 75%. While some of the increased area is located in the middle of the pre-edge, as is seen for $Na_{2/3}[Mg_{0.28}Mn_{0.72}]O_2$ and $Li[Li_{1/5}Ni_{1/5}Mn_{3/5}]O_2$, the intensity over the whole pre-edge region seems to also increase. One must keep in mind during the analysis of soft XAS that the technique is inherently sensitive to the near surface region of the particles due to the relatively low penetration of low energy

X-rays.[61] Accordingly, if a thick O containing surface layer, such as Na_2CO_3, were to build up on the compound, this may significantly suppress the signal stemming from the mixed TM 3d - O 2p states in the pre-edge region. This perhaps contributes to the increase in integrated intensity seen here, as this surface layer is removed upon charging to high voltages.

The Mn L-edges (Figure 5.19c) show minimal change on charge but a slight difference in the structure of the L_3 edge in the discharged sample, which is consistent with reduction of Mn from 4+ to 3+.[62] The Co L-edges (Figure 5.19d) show no noticeable changes in their structure or position between the samples. Co oxidation would usually manifest itself in a shift of the most intense peak of the L_3 edge to higher energies, although this can be quite subtle such is the case for de-lithiated $LiCoO_2$.[63, 64] The lack of Co oxidation beyond 3+ on charge is reminiscent of the Ni oxidation state conundrum discussed previously for $Li[Li_{1/5}Ni_{1/5}Mn_{3/5}]O_2$. It is possible there is a similar link between the Co and O oxidation states here, although a more in-depth characterization would be required before conclusions could be made.

Finally, RIXS spectra were measured at a single excitation energy (due to beam time constraints) of 531.5 eV, shown in Figure 5.19e. An increased intensity at lower emission energies is seen for the sample charged to 4.5 V. This is consistent with the O-redox signature seen in the RIXS maps for $Na_{2/3}[Mg_{0.28}Mn_{0.72}]O_2$ and $Li[Li_{1/5}Ni_{1/5}Mn_{3/5}]O_2$, demonstrating that solid state O-redox does indeed occur for this compound.

Conclusion

In summary, some improvement to the first cycle energy efficiency, compared with $Na_{2/3}[Mg_{0.28}Mn_{0.72}]O_2$, was made through TM substitution. This was particularly evident in the samples which included Zn or Co, both of which coincidentally did not show honeycomb-related superstructure peaks in XRD. Nonetheless, the soft X-ray spectroscopy measurements on $Na_{2/3}[Mg_{1/4}Mn_{7/12}Co_{1/6}]O_2$ did not reveal any noticeable mechanistic differences compared with $Na_{2/3}[Mg_{0.28}Mn_{0.72}]O_2$. Moreover, the inclusion of Co is not desirable from a cost perspective and therefore the

improvement seen for this compound is probably too modest to have any wider-reaching implications. The lower charge voltage of $Na_{2/3}[Zn_{1/4}Mn_{3/4}]O_2$ compared with the Mg containing compounds could be fundamentally interesting and a more rigorous study of this compound should be the topic of future work.

5.4.4 $Na_{3y}[Li_yMn_{1-y}]O_2$ ($y = 1/5$, $1/4$): Superstructure-Controlled First Cycle Hysteresis

Another potential avenue for decreasing hysteresis is to try to make the O-redox couple and corresponding structural evolution more reversible in nature. Currently, most O-redox compounds show a voltage plateau on charge during O-oxidation followed by a sloped voltage curve on discharge, indicating two different processes (seen in Figure 5.1). In 2016, Du et al. reported a new P3-type compound, $Na_{3/5}[Li_{1/5}Mn_{4/5}]O_2$, which remarkably showed a plateau on both charge and discharge, above 4 V vs. Na^+/Na.[21] Later Rong et al. reinvestigated this same material and postulated that the reversibility of the O-redox reaction stemmed from the avoidance of O-loss by maintaining the P3-type structure on charging.[65] This conclusion, however, does not explain the fact that no O-loss is seen when charging $Na_{2/3}[Mg_{0.28}Mn_{0.72}]O_2$, yet hysteresis still occurs. In this section, it will be argued that the voltage hysteresis of most O-redox compounds stems from an intrinsic instability of honeycomb-ordered TM layer on charging. This will be shown by the comparison of two P2-type compounds, with only slightly different compositions ($Na_{3/5}[Li_{1/5}Mn_{4/5}]O_2$ and $Na_{3/4}[Li_{1/4}Mn_{3/4}]O_2$), which surprisingly exhibit very different first cycle voltage curves (low and high hysteresis). The favorable electrochemistry of P2-$Na_{3/5}[Li_{1/5}Mn_{4/5}]O_2$ originates from an increased stability of TM-layer during charging by a new ordering scheme which is designated here as "ribbon" ordering.

Structure of the Pristine Materials

P2-$Na_{3/5}[Li_{1/5}Mn_{4/5}]O_2$ and P2-$Na_{3/4}[Li_{1/4}Mn_{3/4}]O_2$ were both synthesized via solid state methods. $Na_{3/5}[Li_{1/5}Mn_{4/5}]O_2$ was synthesized as a P2-type compound, rather than P3, by changing to a higher synthesis temperature than previous reports.[21]

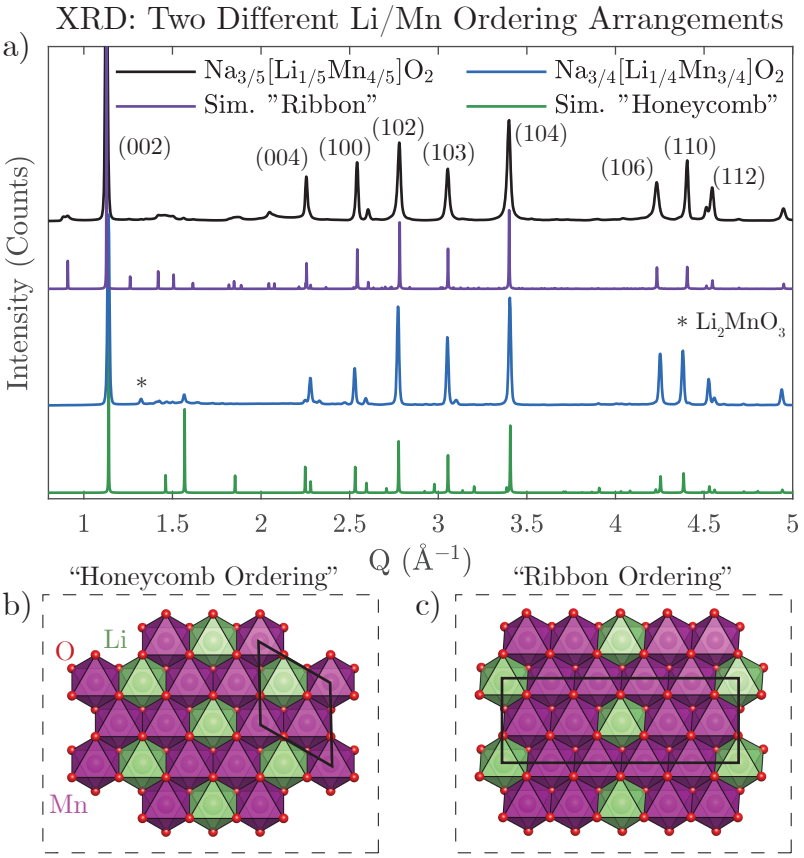

Figure 5.20: Synchrotron XRD patterns are shown for $Na_{3/5}[Li_{1/5}Mn_{4/5}]O_2$ (black) and $Na_{3/4}[Li_{1/4}Mn_{3/4}]O_2$ (blue) along with simulated patterns for the "ribbon" (purple) and "honeycomb" (green) superstructures in a). The *hkl* values of the peak are assigned from the small hexagonal P2 unit cell with $P6_3/mmc$ symmetry. The ideal TM layer ordering arrangements giving rise to these superstructure peaks are illustrated in b) and c) for $Na_{3/4}[Li_{1/4}Mn_{3/4}]O_2$ (honeycomb ordering) and $Na_{3/5}[Li_{1/5}Mn_{4/5}]O_2$ (ribbon ordering), respectively, with the unit cell overlaid as a black rectangle. This data was collected at the APS 11-ID-B (Chicago, IL) and the compounds were synthesized by Dr. Urmimala Maitra.

The powder synchrotron XRD patterns for each compound are shown in Figure 5.20a with the main peaks indexed using the more recognizable small hexagonal unit cell which has the $P6_3/mmc$ space group.

$Na_{3/4}[Li_{1/4}Mn_{3/4}]O_2$ shows a single superstructure peak consistent with honeycomb ordering of Li and Mn, which was also reported for the composition, $Na_{5/6}[Li_{1/4}Mn_{3/4}]O_2$, by Yabuuchi et al.[20] Although the Mn:Li ratio of 3:1 is not the perfect stoichiometry to achieve honeycomb ordering (Mn:Li, 2:1), it seems to be sufficiently close in this case. This is not surprising given the high propensity for Mn^{4+} and Li^+ cations to

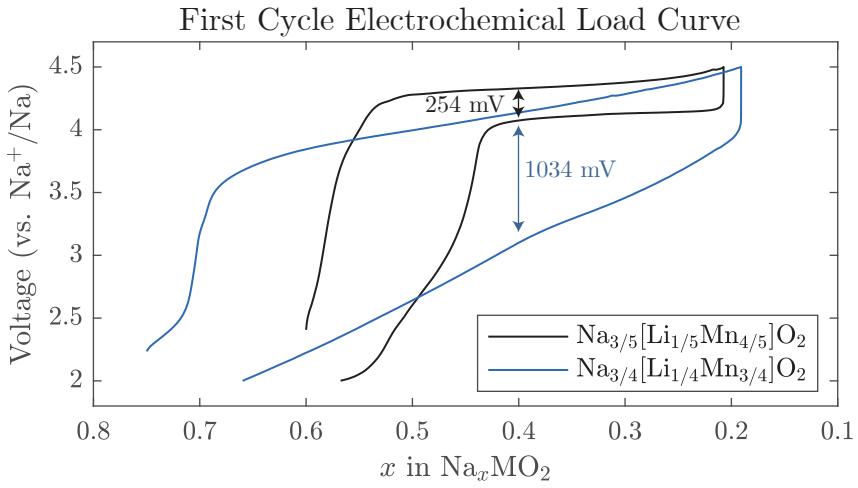

Figure 5.21: The first cycle electrochemical voltage curves are shown for $Na_{3/5}[Li_{1/5}Mn_{4/5}]O_2$ (black) and $Na_{3/4}[Li_{1/4}Mn_{3/4}]O_2$ (blue). The voltage difference between charge and discharge at $x = 0.4$ (arbitrarily picked) is also included.

order to reduce electrostatic repulsion.[66] A small amount of Li_2MnO_3 impurity phase is also evidenced in the XRD. $Na_{3/5}[Li_{1/5}Mn_{4/5}]O_2$ on the other hand shows several superstructure peaks which could be indexed to a 5 x $\sqrt{3}$ monoclinic supercell (space group: $P2_1/c$) of the original small hexagonal P2 unit cell. This ordering scheme is labeled hereon as "ribbon" ordering.

An illustration of the ideal TM layer ordering for both compounds are shown in Figures 5.20b and c. In both cases, the local environment of Li is very similar, each with 6 surrounding Mn. The local environment of Mn, however, differs in the two cases. In the honeycomb ordering, there is a single Mn environment in which it is surrounded by 3 other Mn and 3 Li. In the ribbon ordering, there are two Mn environments with one group being surrounded by 4 other Mn and 2 Li, and the second group surrounded by 5 other Mn and 1 Li. This rather minor difference in the two ordering schemes has profound implications for the electrochemistry.

Electrochemistry

The first cycle voltage curves of both compounds are overlaid with one another in Figure 5.21. $Na_{3/5}[Li_{1/5}Mn_{4/5}]O_2$ shows a reversible plateau at approximately 4.2 V vs. Na^+/Na while $Na_{3/4}[Li_{1/4}Mn_{3/4}]O_2$ demonstrates a more sloped voltage profile on charge and discharge. This leads to a first cycle energy efficiency of 79%

for $Na_{3/5}[Li_{1/5}Mn_{4/5}]O_2$ and only 63% for $Na_{3/4}[Li_{1/4}Mn_{3/4}]O_2$ (but higher charge and discharge capacities in the latter case). More importantly, the reemergence of the voltage plateau on discharge demonstrates the possibility of O^{n-} reduction at high voltages (> 4 V). To better understand the electrochemical reversibility of $Na_{3/5}[Li_{1/5}Mn_{4/5}]O_2$, and lack thereof in $Na_{3/4}[Li_{1/4}Mn_{3/4}]O_2$, *operando* XRD was conducted on both compounds with special attention paid to the superstructure peaks.

Operando XRD

The structural evolution of $Na_{3/4}[Li_{1/4}Mn_{3/4}]O_2$ was monitored through *operando* XRD over the first charge and discharge and is shown in Figure 5.22. The patterns of the highlighted regions are colored based on the capacity. On charging, the P2 (002) peak (Figure 5.22b) shows a shift of the reflection to lower Q before rapidly decreasing in height and broadening asymmetrically towards higher Q. A similar effect has been seen in other compounds and was convincingly ascribed to the creation of O2-type stacking faults with Li migrating from its sites in TM layer to vacant octahedral sites in Na layer as suggested by ^{6}Li magic angle spinning-nuclear magnetic resonance (MAS-NMR).[22, 67]

Contrary to what occurs in the Li-rich case, the peaks highlighted in Figure 5.22c show continuous shifts during charge and discharge ruling out the possibility of a two phase mechanism. This is consistent with the sloped nature of the voltage curve on charge. Moreover, the progression of the intralayer TM-TM distance (Figure 5.22e) also testifies to this as it consistently decreases on charge and increases on discharge.

The evolution of the most intense superstructure peak, (1/3 1/3 1), stemming from the honeycomb ordering of Li and Mn is shown in Figure 5.22d. Like the superstructure peaks of $Li[Li_{1/5}Ni_{1/5}Mn_{3/5}]O_2$, this peak shows an irreversible decrease in intensity on charge and does not regain any intensity on discharge. During charging, one might attribute this decrease in intensity to O2-type stacking faults as many of the non-superstructure peaks (eg. (106)) also decrease in intensity. On subsequent discharge, if the TMO_2 layers do not glide back along the same glide

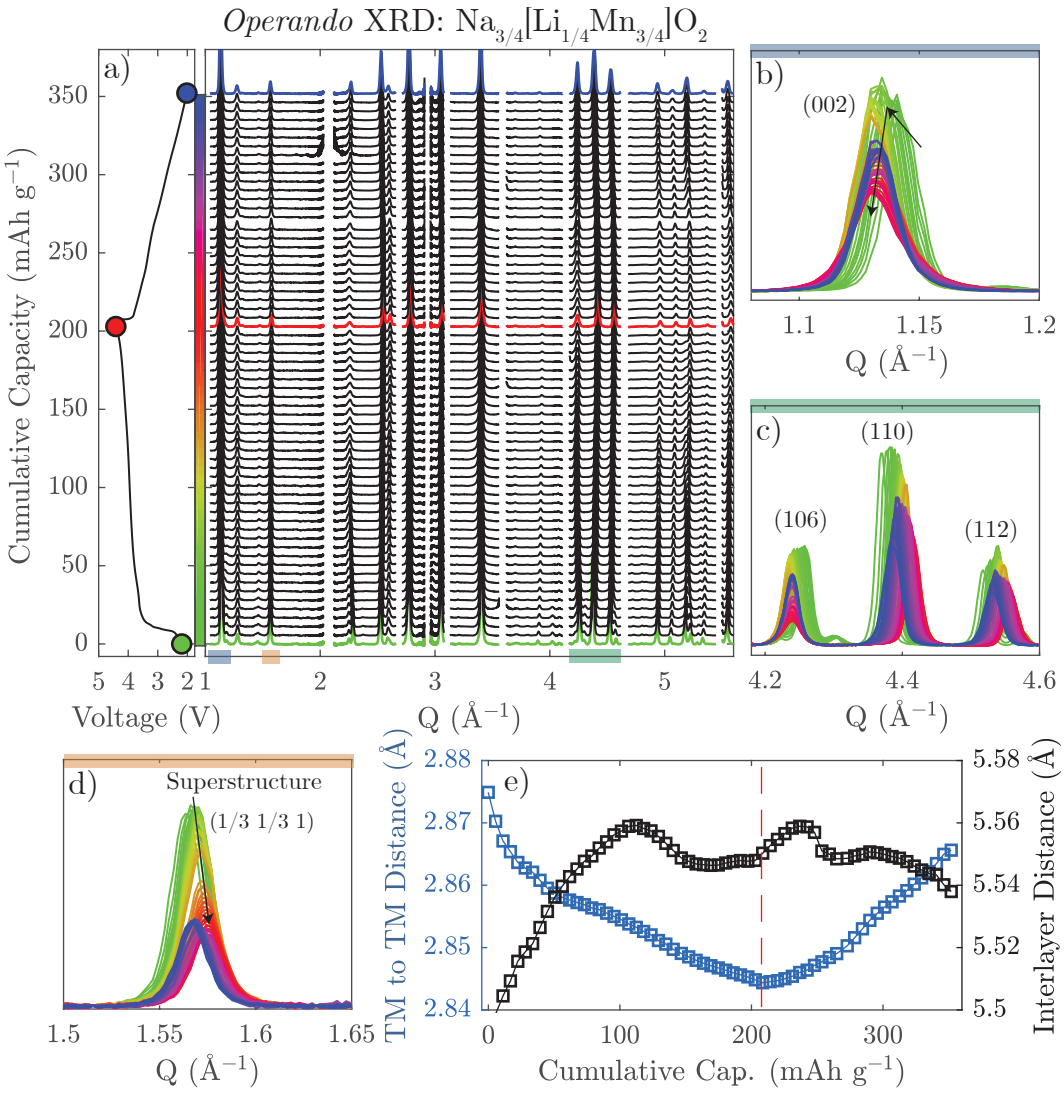

Figure 5.22: *Operando* XRD data from $Na_{3/4}[Li_{1/4}Mn_{3/4}]O_2$ is plotted (background subtracted) in a) along with the electrochemical load curve. Key points in the load curve are colored according to the capacity color bar: green - pristine, red - end of charge, and blue - end of discharge. The (002) peak evolution is shown b), higher angle peaks shown in c), the honeycomb superstructure peak in d) and the refined intralayer TM-TM and interlayer distances are plotted in e). This data was collected in the AMPIX cell at the APS 11-ID-B (Chicago, IL).

vector that they traversed on charge, the *interlayer* superstructure ordering would be permanently lost. Alternatively, the break down of the *intralayer* superstructure (i.e. in-plane ordering) would also cause the same effect. Since the breakdown of intralayer order ensued upon charging $Li[Li_{1/5}Ni_{1/5}Mn_{3/5}]O_2$, it seems likely the same process may occur for $Na_{3/4}[Li_{1/4}Mn_{3/4}]O_2$ as well.

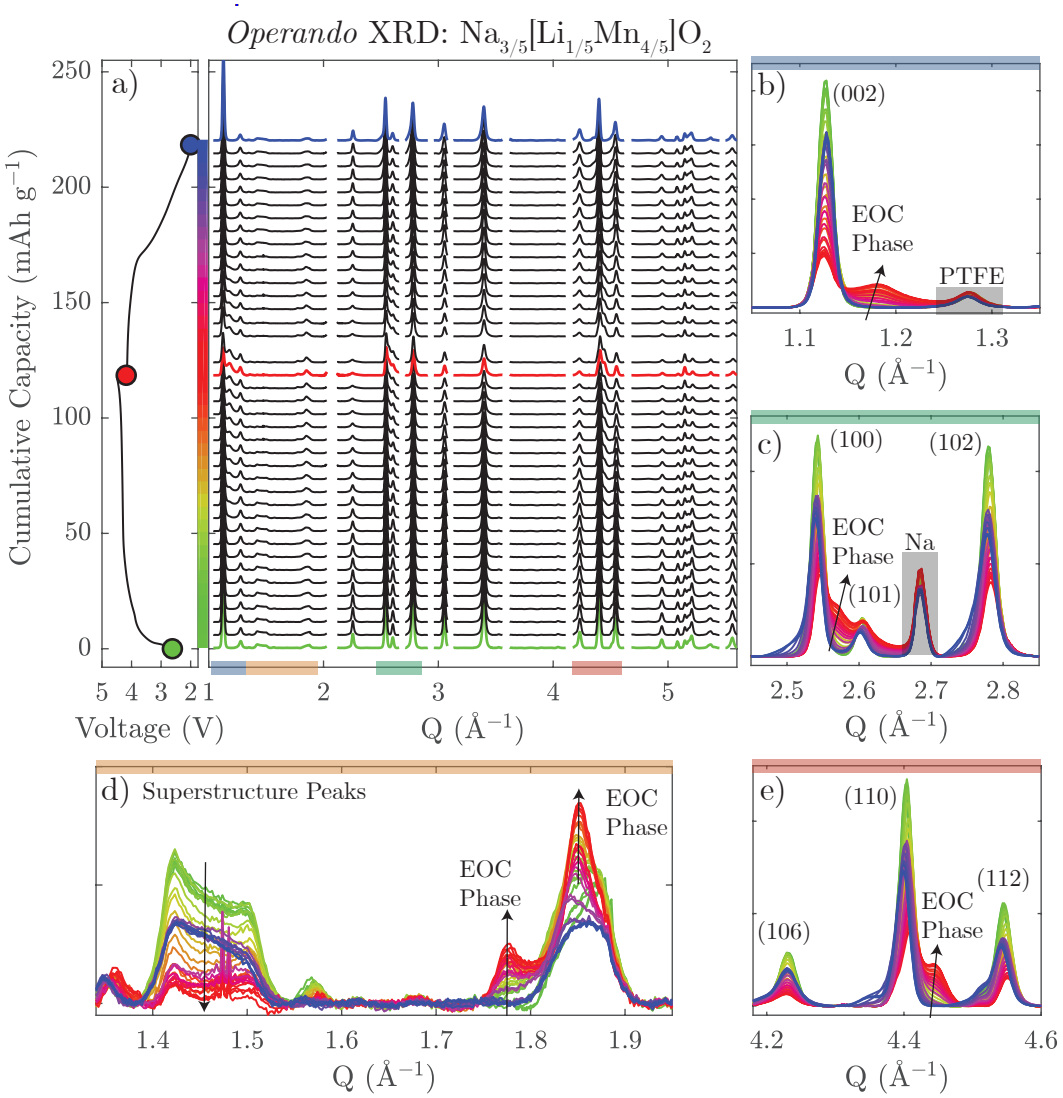

Figure 5.23: *Operando* XRD data from $Na_{3/5}[Li_{1/5}Mn_{4/5}]O_2$ is plotted (background subtracted) in a) along with the electrochemical load curve. Key points in the load curve are colored according to the capacity color bar: green - pristine, red - end of charge, and blue - end of discharge. The (002) peak evolution is shown b), higher angle peaks shown in c) and e), and the superstructure peaks from "ribbon" ordering are shown in d). This data was collected in the AMPIX cell at the APS 11-ID-B (Chicago, IL).

Operando synchrotron XRD was also performed on the low hysteresis compound $Na_{3/5}[Li_{1/5}Mn_{4/5}]O_2$ (Figure 5.23). Looking first at the P2 (002) peak (highlighted in Figure 5.23b), on charging a new peak appears to higher Q of the (002) peak, indicative of a new phase forming with smaller interlayer spacing. This will be labeled as the "end of charge" (EOC) phase for simplicity. Like $Na_{3/4}[Li_{1/4}Mn_{3/4}]O_2$, it is very likely that the emergence of the EOC phase coincides with the gliding of

some (if not all) P2-type Na layers to O2-type stacking as well as the migration of mobile Li into the Na layer. In Figures 5.23c and e, the (100) and (110) peaks also show appearance of new peaks (as shoulders) from the EOC phase, also at higher Q values. It is difficult to interpret the exact indexing of the EOC phase, given the small number of reflections available. However, as the EOC phase manifests itself as higher Q shoulders on the P2 peaks, this should indicate that the EOC phase has a smaller in-plane and interlayer spacing than the original P2 phase. The peaks shown with a- and c-axis dependence, such as the (102) and (106), broaden without any clear secondary phase. This is again consistent with the EOC phase containing O2-type stacking faults which can occur along two possible glide vectors.[68]

The Q range of 1.35 to 1.95 Å^{-1}, shown in Figure 5.23d, contains many of the superstructure peaks stemming from the ribbon ordering of Li and Mn. The set of two peaks centered at $Q \approx 1.45$ Å^{-1} decrease in intensity on charge. Interestingly, on discharge these peaks regain some of their intensity again. This is in clear contrast to what occurs in the honeycomb ordering superstructure peaks of $Li[Li_{1/5}Ni_{1/5}Mn_{3/5}]O_2$ and $Na_{3/4}[Li_{1/4}Mn_{3/4}]O_2$ which do not regain intensity. Additionally, the reflections around 1.8 Å^{-1} actually show an increased intensity on charge, demonstrating that the TM layer likely remains well ordered even in the EOC phase. A final observation of note is that none of diffraction peaks regain the same sharpness as the pristine material during discharge. This shows that despite the improved structural reversibility associated with the ribbon superstructure, there is still some irreversibility. This is not surprising given that the discharge voltage plateau is shorter in length than the voltage plateau on charge.

Pair Distribution Function Analysis

Since many of the XRD reflections of $Na_{3/4}[Li_{1/4}Mn_{3/4}]O_2$ and $Na_{3/5}[Li_{1/5}Mn_{4/5}]O_2$ broaden on charge due to the breakdown of long range structure (i.e. stacking faults), *ex situ* total X-ray scattering was also measured to better understand the changes of the local structure of the compound on charge. The pair distribution function (PDF), $G(r)$, was derived from the total scattering data for each of the *ex*

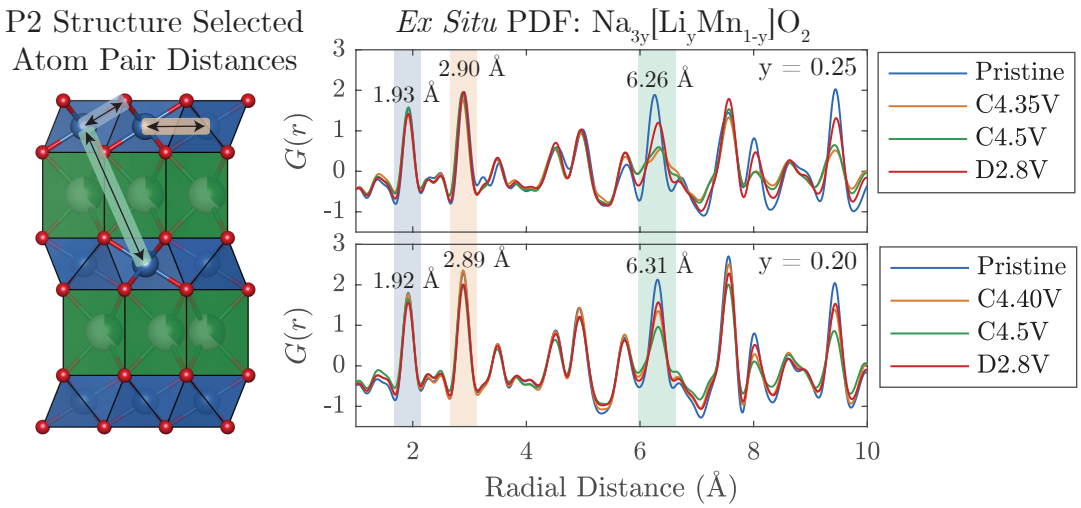

Figure 5.24: *Ex situ* PDF profiles of high hysteresis $Na_{3/4}[Li_{1/4}Mn_{3/4}]O_2$ and low hysteresis $Na_{3/5}[Li_{1/5}Mn_{4/5}]O_2$ are presented. Key peaks in the data are highlighted and are dominated by the contribution of the following pairs: nearest neighbor Mn-O (blue), in-plane Mn-Mn (orange), and interlayer Mn-Mn (green). These are also presented on the illustrated structure on the left. The *ex situ* samples were prepared by Dr. Urmimala Maitra. The total scattering measurement was conducted at the APS 11-ID-B (Chicago, IL).

situ samples and is presented in Figure 5.24. Each peak in the PDF represents one or more atom-atom pairs at a particular distance (r) apart within the structure. The peak intensity is dependent on the number of atom pairs at that distance as well as the scattering power of the two atoms involved.[69] As Mn has a much larger X-ray scattering factor than Li, O, or Na, its contribution dominates the PDF. Three of the most significant peaks in the PDF are highlighted in blue, orange, and green and layered over the structure to the left of the figure for ease of understanding. These peaks primarily correspond to the nearest neighbor Mn-O, in-plane Mn-Mn, and interlayer Mn-Mn pairs, respectively. The interlayer Mn-Mn pair (green) shows a significant broadening in both samples charged to 4.5 V. This is consistent with the O2-type stacking faults proposed from the *operando* XRD results. On the other hand, the peaks from the intralayer Mn-O (blue) and Mn-Mn (orange) remain largely unchanged in intensity.

As discussed above, previous ^{6}Li MAS-NMR work carried out on $NaMO_2$ compounds has suggested that Li, which occupies TM sites in the pristine structure,

can reversibly migrate between the TM layer and the Na layer during charge and discharge.[22, 67] It has also been proposed that TMs can reversibly migrate to the Li-layer in Li-rich compounds.[14, 39] In the O2 structure, TM sites share a face with an octahedral site in the Na layer above (below) and a tetrahedral site in the Na layer below (above). Mn is known to be stable in both of these coordination environments (albeit at lower oxidation states) and therefore interlayer migration could indeed be a possibility.[70] However, one may expect the significant quantity of migrated Li^+ to effectively "pillar" the Na layer such that sites would be too large for Mn to occupy.

From the PDF data shown above, the migration of Mn to tetrahedral sites in Na layer can be ruled out as this would generate a new Mn-Mn pair distance of approximately 3.3 Å, as is shown by Talaie et al., which is not seen here.[71] The possibility of Mn migration to octahedral sites within the Na layer would also produce a similar Mn-Mn pair distance, therefore, this also is not evidenced to any appreciable extent. However, it would be challenging to observe in-plane movement of the Mn cations, which could occur to allow for clustering of the octahedral vacancies left by the migrated Li species.

Taking in all of the above presented data, a possible new model to explain the hysteresis in O-redox compounds will now be discussed by comparing $Na_{3/5}[Li_{1/5}Mn_{4/5}]O_2$ (low-hysteresis) and $Na_{3/4}[Li_{1/4}Mn_{3/4}]O_2$ (high-hysteresis).

Discussion

$Na_{3/4}[Li_{1/4}Mn_{3/4}]O_2$ contains honeycomb ordering of the Mn and Li within the TM layer in its pristine state. All Mn is nominally 4+ in this compound and therefore all capacity extracted on charge is expected to come from the oxidation of O. Upon charging to 4.5 V, *operando* XRD showed that the honeycomb ordering was irreversibly lost and the average voltage on discharge was lower by approximately 1 V. From a charge repulsion perspective, the observed loss of honeycomb ordering is not sensible. Even with Li leaving the TM layer, the honeycomb ordering should be the most stable configuration to mitigate repulsion between adjacent

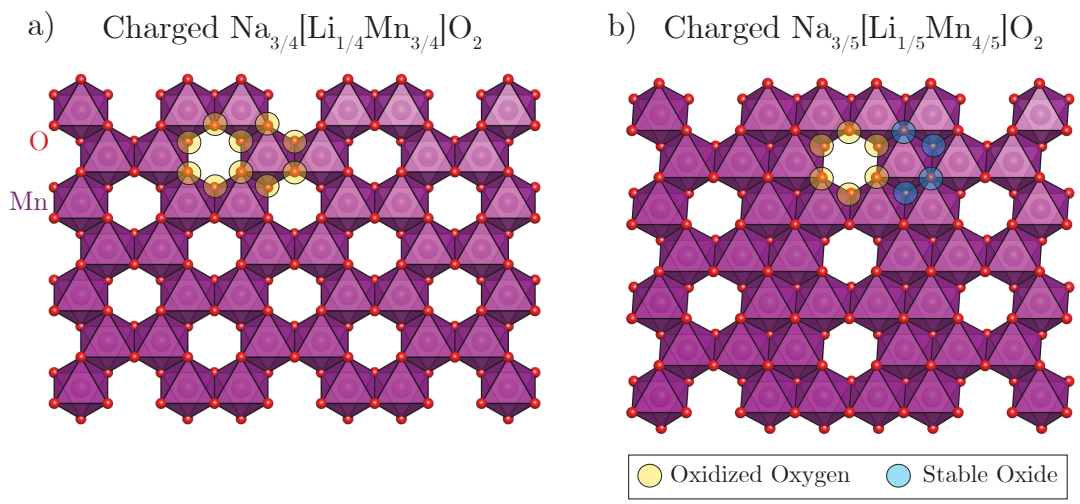

Figure 5.25: Models for a possible charged TM layer for a) $Na_{3/4}[Li_{1/4}Mn_{3/4}]O_2$ and b) $Na_{3/5}[Li_{1/5}Mn_{4/5}]O_2$ are presented. O coordinating the TM vacancy (left by Li) is labeled as oxidized (yellow) and those that are not are labeled as "stable oxide" (blue). It is clear that in the ribbon ordering of $Na_{3/5}[Li_{1/5}Mn_{4/5}]O_2$, a smaller percentage of O can be oxidized, making the structure more robust against cation rearrangement

Mn^{4+}. The rearrangement of the Mn ions must then be driven by something else (e.g. O oxidation).

Looking at a top-down view of the honeycomb ordered TM layer in the charged structure when Li has moved to the Na layer (Figure 5.25a), it is clear that all the O are in the same local environment, coordinated in the plane by two Mn and one vacancy. When a significant amount of charge is taken from O during charging, two things occur to raise the energy of the system and drive the movement of Mn: 1) the destabilization of Mn which are all now exclusively coordinated by oxidized O and 2) a degeneracy of the now partially filled O electronic states. These two phenomena can simultaneously be corrected with the movement of Mn to a vacant octahedral site, either in the plane or out of the plane. In doing so, the migrated Mn creates new O environments which are coordinated by only one Mn and two vacancies in the plane and are therefore higher in energy. The degenerate oxidized O states are then able to disproportionate, breaking the degeneracy and stabilizing the structure.

On discharge, Na is reinserted between the TMO_2 slabs, prompting the layers to glide back to P2-type stacking and Li to return to the TM layer. The Mn and Li

are no longer uniformly ordered to mitigate coulombic repulsion, however, and the overall energy of the structure is then comparably higher on discharge than it was at the same composition on charge. In the electrochemical load curve, this would be reflected as a lower voltage on discharge, as is seen experimentally.

The ribbon ordering of the Li and Mn helps to prevent this voltage drop. $Na_{3/5}[Li_{1/5}Mn_{4/5}]O_2$ also theoretically compensates the removal of Na on charge exclusively by the oxidation of O. However, unlike $Na_{3/4}[Li_{1/4}Mn_{3/4}]O_2$, the ordered superstructure is retained after 1 charge/discharge cycle. Looking now at the top down view of the ribbon ordered TM layer (Figure 5.25b) in the charged structure (when Li has moved to the Na layer), there are already two different environments of O. 40% of the O is coordinated by 3 Mn and cannot be oxidized, creating a backbone of structural integrity. The other 60% of O are coordinated by two Mn and one vacancy. The electronic states of these O will be at a higher energy and will therefore be the states which electrons are removed from. There are also two different environments for the Mn. One of these sites will be coordinated by 4 oxidized O while the other will only be coordinated by 2 oxidized O. Neither is as unstable as the Mn environment of the honeycomb structure (6 surrounding oxidized O). Thus, the barrier for Mn migration in the charged ribbon structure should be much higher than the honeycomb structure.

When Na is reinserted into $Na_{3/5}[Li_{1/5}Mn_{4/5}]O_2$ on discharge, the layers glide to reform the P2 structure and Li can return to the correct TM sites. In this case, the structure will be the same on discharge as it was on charge (at any composition) and the electrochemical load curve would exhibit minimal hysteresis, as is seen experimentally. Currently, a large computational effort is underway to verify this model and will be presented in an upcoming publication.

5.5 Conclusion

In this chapter, the governing mechanisms of O-redox were explored. This can be summarized into 3 main questions:

1. What structural/electronic properties facilitate O-oxidation?

It was demonstrated through soft X-ray spectroscopic techniques that O can be successfully oxidized in the presence of Li (as previously reported) and also in the presence of Mg (newly reported). From these observations, it seems that the model proposed by Seo et al., in which O oxidation can occur if O is coordinated in the TM layer by alkali metal-ions, can be extended to alkaline earth metal-ions as well. This is presumably due to the highly ionic nature of the Mg^{2+} - O^{2-} interaction.

2. How can solid state O-redox be favored over gaseous O-loss during charge?

Also from studying $Na_{2/3}[Mg_{0.28}Mn_{0.72}]O_2$, it was found that O-loss can be successfully avoided when O remains coordinated to at least 3 cations on average during charge. In $Li[Li_{1/5}Ni_{1/5}Mn_{3/5}]O_2$, the largest contributor to the first charge capacity is solid state O-oxidation which is reversible in nature and stays active even on the 200th cycle. However, the compound also experiences O-loss which primarily occurs when more than 1 mol Li per formula unit has been extracted.[11] This occurs when the average coordination number of O becomes less than three. In $Na_{2/3}[Mg_{0.28}Mn_{0.72}]O_2$, there is no O-loss as the average coordination number of O is always at least three because Mg is retained in the compound during charging.

3. Why is there almost always a significant hysteresis of the voltage curve on the first cycle when invoking "reversible" solid state O-redox?

This is probably the most complicated question to answer but also has the most reward for finding a solution. Currently, most Li-rich O-redox compounds possess honeycomb-type ordering of Li and Mn and all of these experience a large energy inefficiency on the first cycle. While it was previously believed that O-loss and hysteresis were somehow linked, that has been shown not to be the case here when examining $Na_{2/3}[Mg_{0.28}Mn_{0.72}]O_2$. Changing the chemical makeup of the TM layer (i.e. substituting Mn^{3+} by Co^{3+}) can help to boost the discharge voltage and raise the energy efficiency, but this doesn't help to fix the irreversible breakdown of the

honeycomb ordering which is the underlying cause for the hysteresis. Instead, it was found that P2-type $Na_{3/5}[Li_{1/5}Mn_{4/5}]O_2$ with the "ribbon" superstructure boasts a reversible plateau above 4 V due to added stability against cation rearrangement. This is one of the first compounds to utilize the O-redox couple in a truly reversible way. Extrapolating these results, one very exciting prospect is the possibility of synthesizing a Na-rich or Li-rich compound with the ribbon ordering superstructure. In doing this, it could be possible to create a low-cost cathode material capable of delivering both high capacities and high voltage, and thus a step change in the battery energy density.

In my opinion, the prognosis of O-redox cathode materials is very positive. The massive amount of research undertaken over the past few years to understand the fundamental mechanisms of this class of materials has now provided a platform for finally making a breakthrough.

5.6 References

(1) Kalyani, P.; Chitra, S.; Mohan, T.; Gopukumar, S. *Journal of Power Sources* **1999**, *80*, 103–106.

(2) Freire, M.; Kosova, N. V.; Jordy, C.; Chateigner, D.; Lebedev, O. I.; Maignan, A.; Pralong, V. *Nature Materials* **2016**, *15*, 173–177.

(3) Ammundsen, B.; Paulsen, J. *Advanced Materials* **2001**, *13*, 943–956.

(4) Robertson, A. D.; Bruce, P. G. *Chemistry of Materials* **2003**, *15*, 1984–1992.

(5) Francis Amalraj, S.; Markovsky, B.; Sharon, D.; Talianker, M.; Zinigrad, E.; Persky, R.; Haik, O.; Grinblat, J.; Lampert, J.; Schulz-Dobrick, M.; Garsuch, A.; Burlaka, L.; Aurbach, D. *Electrochimica Acta* **2012**, *78*, 32–39.

(6) Chen, H.; Islam, M. S. *Chemistry of Materials* **2016**, *28*, 6656–6663.

(7) Seo, D.-h.; Lee, J.; Urban, A.; Malik, R.; Kang, S.; Ceder, G. *Nature Chemistry* **2016**, *8*, 692–697.

(8) Croy, J. R.; Park, J. S.; Dogan, F.; Johnson, C. S.; Key, B.; Balasubramanian, M. *Chemistry of Materials* **2014**, *26*, 7091–7098.

(9) Renfrew, S. E.; McCloskey, B. D. *Journal of the American Chemical Society* **2017**, *139*, 17853–17860.

(10) Luo, K.; Roberts, M. R.; Hao, R.; Guerrini, N.; Pickup, D. M.; Liu, Y.-S.; Edström, K.; Guo, J.; Chadwick, A. V.; Duda, L. C.; Bruce, P. G. *Nature Chemistry* **2016**, *8*, 684–691.

(11) Luo, K.; Roberts, M. R.; Guerrini, N.; Tapia-Ruiz, N.; Hao, R.; Massel, F.; Pickup, D. M.; Ramos, S.; Liu, Y. S.; Guo, J.; Chadwick, A. V.; Duda, L. C.; Bruce, P. G. *Journal of the American Chemical Society* **2016**, *138*, 11211–11218.

(12) Croy, J. R.; Gallagher, K. G.; Balasubramanian, M.; Chen, Z.; Ren, Y.; Kim, D.; Kang, S. H.; Dees, D. W.; Thackeray, M. M. *Journal of Physical Chemistry C* **2013**, *117*, 6525–6536.

(13) Croy, J. R.; Balasubramanian, M.; Gallagher, K. G.; Burrell, A. K. *Accounts of Chemical Research* **2015**, *48*, 2813–2821.

(14) Kleiner, K.; Strehle, B.; Baker, A. R.; Day, S. J.; Tang, C. C.; Buchberger, I.; Chesneau, F. F.; Gasteiger, H. A.; Piana, M. *Chemistry of Materials* **2018**, *30*, 3656–3667.

(15) Lu, Z.; MacNeil, D. D.; Dahn, J. R. *Electrochemical and Solid-State Letters* **2001**, *4*, A191–A194.

(16) Chen, Z.; Dahn, J. *Electrochimica Acta* **2004**, *49*, 1079–1090.

(17) Mortemard de Boisse, B.; Liu, G.; Ma, J.; Nishimura, S.-i.; Chung, S.-C.; Kiuchi, H.; Harada, Y.; Kikkawa, J.; Kobayashi, Y.; Okubo, M.; Yamada, A. *Nature Communications* **2016**, *7*, 11397.

(18) Perez, A. J.; Batuk, D.; Saubanère, M.; Rousse, G.; Foix, D.; McCalla, E.; Berg, E. J.; Dugas, R.; H. W. van den Bos, K.; Doublet, M.-L.; Gonbeau, D.; Abakumov, A. M.; Van Tendeloo, G.; Tarascon, J.-M. *Chemistry of Materials* **2016**, *28*, 8278–8288.

(19) Yabuuchi, N.; Hara, R.; Kubota, K.; Paulsen, J.; Kumakura, S.; Komaba, S. *J. Mater. Chem. A* **2014**, *2*, 16851–16855.

(20) Yabuuchi, N.; Hara, R.; Kajiyama, M.; Kubota, K.; Ishigaki, T.; Hoshikawa, A.; Komaba, S. *Advanced Energy Materials* **2014**, *4*, 1301453.

(21) Du, K.; Zhu, J.; Hu, G.; Gao, H.; Li, Y.; Goodenough, J. B. *Energy and Environmental Science* **2016**, *9*, 2575–2577.

(22) De la Llave, E.; Talaie, E.; Levi, E.; Nayak, P. K.; Dixit, M.; Rao, P. T.; Hartmann, P.; Chesneau, F.; Major, D. T.; Greenstein, M.; Aurbach, D.; Nazar, L. F. *Chemistry of Materials* **2016**, *28*, 9064–9076.

(23) Risthaus, T.; Zhou, D.; Cao, X.; He, X.; Qiu, B.; Wang, J.; Zhang, L.; Liu, Z.; Paillard, E.; Schumacher, G.; Winter, M.; Li, J. *Journal of Power Sources* **2018**, *395*, 16–24.

(24) Luo, K.; Roberts, M. R.; Hao, R.; Guerrini, N.; Liberti, E.; Allen, C. S.; Kirkland, A. I.; Bruce, P. G. *Nano Letters* **2016**, *16*, 7503–7508.

(25) Borkiewicz, O. J.; Shyam, B.; Wiaderek, K. M.; Kurtz, C.; Chupas, P. J.; Chapman, K. W. *Journal of Applied Crystallography* **2012**, *45*, 1261–1269.

(26) Toby, B. H.; Von Dreele, R. B. *Journal of Applied Crystallography* **2013**, *46*, 544–549.

(27) Juhás, P.; Davis, T.; Farrow, C. L.; Billinge, S. J. *Journal of Applied Crystallography* **2013**, *46*, 560–566.

(28) Ravel, B.; Newville, M. In *Journal of Synchrotron Radiation*, 2005; Vol. 12, pp 537–541.

(29) Qiao, R.; Li, Q.; Zhuo, Z.; Sallis, S.; Fuchs, O.; Blum, M.; Weinhardt, L.; Heske, C.; Pepper, J.; Jones, M.; Brown, A.; Spucces, A.; Chow, K.; Smith, B.; Glans, P.-A.; Chen, Y.; Yan, S.; Pan, F.; Piper, L. F. J.; Denlinger, J.; Guo, J.; Hussain, Z.; Chuang, Y.-D.; Yang, W. *Review of Scientific Instruments* **2017**, *88*, 033106.

(30) Giannozzi, P.; Baroni, S.; Bonini, N.; Calandra, M.; Car, R.; Cavazzoni, C.; Ceresoli, D.; Chiarotti, G. L.; Cococcioni, M.; Dabo, I.; Dal Corso, A.; de Gironcoli, S.; Fabris, S.; Fratesi, G.; Gebauer, R.; Gerstmann, U.; Gougoussis, C.; Kokalj, A.; Lazzeri, M.; Martin-Samos, L.; Marzari, N.; Mauri, F.; Mazzarello, R.; Paolini, S.; Pasquarello, A.; Paulatto, L.; Sbraccia, C.; Scandolo, S.; Sclauzero, G.; Seitsonen, A. P.; Smogunov, A.; Umari, P.; Wentzcovitch, R. M. *Journal of Physics: Condensed Matter* **2009**, *21*, 395502.

(31) Perdew, J. P.; Burke, K.; Ernzerhof, M. *Physical Review Letters* **1996**, *77*, 3865–3868.

(32) Schlipf, M.; Gygi, F. *Computer Physics Communications* **2015**, *196*, 36–44.

(33) Cococcioni, M.; de Gironcoli, S. *Physical Review B* **2005**, *71*, 035105.

(34) Momma, K.; Izumi, F. *Journal of Applied Crystallography* **2011**, *44*, 1272–1276.

(35) Bréger, J.; Jiang, M.; Dupré, N.; Meng, Y. S.; Shao-Horn, Y.; Ceder, G.; Grey, C. P. *Journal of Solid State Chemistry* **2005**, *178*, 2575–2585.

(36) Boulineau, A.; Croguennec, L.; Delmas, C.; Weill, F. *Chemistry of Materials* **2009**, *21*, 4216–4222.

(37) Boulineau, A.; Croguennec, L.; Delmas, C.; Weill, F. *Solid State Ionics* **2010**, *180*, 1652–1659.

(38) Luo, K.; Roberts, M. R.; Guerrini, N.; Tapia-Ruiz, N.; Hao, R.; Massel, F.; Pickup, D. M.; Ramos, S.; Liu, Y. S.; Guo, J.; Chadwick, A. V.; Duda, L. C.; Bruce, P. G. *Journal of the American Chemical Society* **2016**, *138*, 11211–11218.

(39) Gent, W. E.; Lim, K.; Liang, Y.; Li, Q.; Barnes, T.; Ahn, S.-J.; Stone, K. H.; McIntire, M.; Hong, J.; Song, J. H.; Li, Y.; Mehta, A.; Ermon, S.; Tyliszczak, T.; Kilcoyne, D.; Vine, D.; Park, J.-H.; Doo, S.-K.; Toney, M. F.; Yang, W.; Prendergast, D.; Chueh, W. C. *Nature Communications* **2017**, *8*, 2091.

(40) De Groot, F. M. F.; Grioni, M.; Fuggle, J. C.; Ghijsen, J.; Sawatzky, G. A.; Petersen, H. *Physical Review B* **1989**, *40*, 5715–5723.

(41) Xu, J.; Sun, M.; Qiao, R.; Renfrew, S. E.; Ma, L.; Wu, T.; Hwang, S.; Nordlund, D.; Su, D.; Amine, K.; Lu, J.; McCloskey, B. D.; Yang, W.; Tong, W. *Nature Communications* **2018**, *9*, 947.

(42) Ong, S. P.; Richards, W. D.; Jain, A.; Hautier, G.; Kocher, M.; Cholia, S.; Gunter, D.; Chevrier, V. L.; Persson, K. A.; Ceder, G. *Computational Materials Science* **2013**, *68*, 314–319.

(43) Urban, A.; Seo, D.-H.; Ceder, G. *npj Computational Materials* **2016**, *2*, 16002.

(44) Lin, F.; Liu, Y.; Yu, X.; Cheng, L.; Singer, A.; Shpyrko, O. G.; Xin, H. L.; Tamura, N.; Tian, C.; Weng, T. C.; Yang, X. Q.; Meng, Y. S.; Nordlund, D.; Yang, W.; Doeff, M. M. *Chemical Reviews* **2017**, *117*, 13123–13186.

(45) Seo, D.-H.; Lee, J.; Urban, A.; Malik, R.; Kang, S.; Ceder, G. *Nature Chemistry* **2016**, *8*, 692–697.

(46) Rozier, P.; Sathiya, M.; Paulraj, A.-R.; Foix, D.; Desaunay, T.; Taberna, P.-L.; Simon, P.; Tarascon, J.-M. *Electrochemistry Communications* **2015**, *53*, 29–32.

(47) Parant, J.-P.; Olazcuaga, R.; Devalette, M.; Fouassier, C.; Hagenmuller, P. *Journal of Solid State Chemistry* **1971**, *3*, 1–11.

(48) Stoyanova, R.; Carlier, D.; Sendova-Vassileva, M.; Yoncheva, M.; Zhecheva, E.; Nihtianova, D.; Delmas, C. *Journal of Solid State Chemistry* **2010**, *183*, 1372–1379.

(49) Billaud, J.; Singh, G.; Armstrong, A. R.; Gonzalo, E.; Roddatis, V.; Armand, M.; Rojo, T.; Bruce, P. G. *Energy Environ. Sci.* **2014**, *7*, 1387–1391.

(50) Paulsen, J. M.; Donaberger, R. A.; Dahn, J. R. *Chemistry of Materials* **2000**, *12*, 2257–2267.

(51) Croy, J. R.; Park, J. S.; Dogan, F.; Johnson, C. S.; Key, B.; Balasubramanian, M. *Chemistry of Materials* **2014**, *26*, 7091–7098.

(52) Croy, J. R.; Iddir, H.; Gallagher, K.; Johnson, C. S.; Benedek, R.; Balasubramanian, M. *Physical Chemistry Chemical Physics* **2015**, *17*, 24382–24391.

(53) Lee, D. H.; Xu, J.; Meng, Y. S. *Physical chemistry chemical physics : PCCP* **2013**, *15*, 3304–12.

(54) Katcho, N. A.; Carrasco, J.; Saurel, D.; Gonzalo, E.; Han, M.; Aguesse, F.; Rojo, T. *Advanced Energy Materials* **2016**, 1601477.

(55) Maitra, U.; House, R. A.; Somerville, J. W.; Tapia-Ruiz, N.; Lozano, J. G.; Guerrini, N.; Hao, R.; Luo, K.; Jin, L.; Pérez-Osorio, M. A.; Massel, F.; Pickup, D. M.; Ramos, S.; Lu, X.; McNally, D. E.; Chadwick, A. V.; Giustino, F.; Schmitt, T.; Duda, L. C.; Roberts, M. R.; Bruce, P. G. *Nature Chemistry* **2018**, *10*, 288–295.

(56) Xie, Y.; Saubanère, M.; Doublet, M.-L. *Energy & Environmental Science* **2017**, *10*, 266–274.

(57) Xu, W.; Xu, K.; Viswanathan, V. V.; Towne, S. A.; Hardy, J. S.; Xiao, J.; Nie, Z.; Hu, D.; Wang, D.; Zhang, J. G. *Journal of Power Sources* **2011**, *196*, 9631–9639.

(58) Lee, E.; Brown, D. E.; Alp, E. E.; Ren, Y.; Lu, J.; Woo, J.-J.; Johnson, C. S. *Chemistry of Materials* **2015**, *27*, 6755–6764.

(59) Li, X.; Tang, M.; Feng, X.; Hung, I.; Rose, A.; Chien, P. H.; Gan, Z.; Hu, Y. Y. *Chemistry of Materials* **2017**, *29*, 8282–8291.

(60) Bai, X.; Sathiya, M.; Mendoza-Sánchez, B.; Iadecola, A.; Vergnet, J.; Dedryvère, R.; Saubanère, M.; Abakumov, A. M.; Rozier, P.; Tarascon, J.-M. *Advanced Energy Materials* **2018**, *2*, 1802379.

(61) Li, Q.; Qiao, R.; Wray, L. A.; Chen, J.; Zhuo, Z.; Chen, Y.; Yan, S.; Pan, F.; Hussain, Z.; Yang, W. *Journal of Physics D: Applied Physics* **2016**, *49*, 413003.

(62) Cheng, J.-H.; Pan, C.-J.; Lee, J.-F.; Chen, J.-M.; Guignard, M.; Delmas, C.; Carlier, D.; Hwang, B.-J. *Chemistry of Materials* **2014**, *26*, 1219–1225.

(63) Yoon, W.-S.; Kim, K.-B.; Kim, M.-G.; Lee, M.-K.; Shin, H.-J.; Lee, J.-M.; Lee, J.-S.; Yo, C.-H. *The Journal of Physical Chemistry B* **2002**, *106*, 2526–2532.

(64) Uchimoto, Y.; Sawada, H.; Yao, T. *Journal of Power Sources* **2001**, *97-98*, 326–327.

(65) Rong, X.; Liu, J.; Hu, E.; Liu, Y.; Wang, Y.; Wu, J.; Yu, X.; Page, K.; Hu, Y. S.; Yang, W.; Li, H.; Yang, X. Q.; Chen, L.; Huang, X. *Joule* **2018**, *2*, 125–140.

(66) Bréger, J.; Meng, Y. S.; Hinuma, Y.; Kumar, S.; Kang, K.; Shao-Horn, Y.; Ceder, G.; Grey, C. P. *Chemistry of Materials* **2006**, *18*, 4768–4781.

(67) Xu, J.; Lee, D. H.; Clément, R. J.; Yu, X.; Leskes, M.; Pell, A. J.; Pintacuda, G.; Yang, X.-Q.; Grey, C. P.; Meng, Y. S. *Chemistry of Materials* **2014**, *26*, 1260–1269.

(68) Lu, Z.; Dahn, J. R. *Journal of The Electrochemical Society* **2001**, *148*, A1225–A1229.

(69) Chapman, K. W. *MRS Bulletin* **2016**, *41*, 231–238.

(70) Christiansen, T. L.; Bojesen, E. D.; Sondergaard, M.; Birgisson, S.; Becker, J.; Iversen, B. B. *CrystEngComm* **2016**, *18*, 1996–2004.

(71) Talaie, E.; Duffort, V.; Smith, H. L.; Fultz, B.; Nazar, L. F. *Energy & Environmental Science* **2015**, *8*, 2512–2523.

6
Conclusion and Future Work

Contents

6.1 Conclusion

The world has a strong need for higher performing, lower cost batteries to sustain technological innovation in portable electronics, reduce the price of electric vehicles, and facilitate the further integration of renewable energy sources. The Na-ion battery has the potential to play a critical role in achieving these goals due to its utilization of abundant elements (e.g. Na, Fe, Mn, O) but only if the chemistry is better optimized. This thesis has focused on strengthening the knowledge-base of Na-ion layered oxide cathodes as their moderate voltages and theoretically high capacities make them suitable cathode candidates. A short summary of the results and key conclusions is communicated here.

In Chapter 3, P2-$Na_{2/3}[Ni_{1/3}Mn_{2/3}]O_2$ was first investigated due to its high voltage. It was found that this compound was limited by a variety of factors including poor cyclability and a strong driving force for its Na-ions to order. However, its

Na-deficiency in the as-synthesized compound could be overcome using a new pre-treatment procedure with Na-naphthalide. Partial Fe substitution was explored because Fe is extremely abundant and redox active in Na-ion compounds. Two new compositions were identified ($Na_{2/3}[Ni_{1/4}Mn_{7/12}Fe_{1/6}]O_2$ and $Na_{2/3}[Ni_{1/6}Mn_{1/2}Fe_{1/3}]O_2$) that displayed a suppression of Na-ion ordering and improved cyclability relative to $Na_{2/3}[Ni_{1/3}Mn_{2/3}]O_2$.

In Chapter 4, the underlying mechanism of the improved cyclability was investigated and determined to be a change in the structural evolution at high voltages (low Na contents) which produced less volume contraction. This distinct high voltage structural evolution of $Na_{2/3}[Ni_{1/4}Mn_{7/12}Fe_{1/6}]O_2$ and $Na_{2/3}[Ni_{1/6}Mn_{1/2}Fe_{1/3}]O_2$, known as the "Z"-phase, was resolved as an evolving, semi-ordered P2-O2 intergrowth that changes its ratio of P2 to O2-type layers as a function of state of charge.

In Chapter 5, the possibility of oxygen redox (in addition to conventional TM redox) in layered oxide cathodes was examined. It was found that the Mg-O interaction was sufficiently ionic to activate the oxygen redox couple in $Na_{2/3}[Mg_{0.28}Mn_{0.72}]O_2$, which occurred without O-loss from the compound. Moreover, all oxygen redox compounds possessing "honeycomb"-type ordering in the TM layer were found to exhibit a large first cycle hysteresis. In contrast, $Na_{3/5}[Li_{1/5}Mn_{4/5}]O_2$, possessing "ribbon"-type TM ordering, displayed a much more reversible first cycle behavior. It was speculated this improved performance may be due to stifled intra and interlayer TM migration.

All of these results chapters sought to communicate new fundamental insights into Na-ion layered oxide cathodes in order to improve their performance. Importantly, all inquiries were carried out without straying from the Na-ion battery philosophy of utilizing abundant (and thus sustainable) elements. Although it is still unclear whether the Na-ion chemistry will ever displace Li-ion for certain applications, it is apparent that a low-cost and high performing cathode material will need to be developed to achieve this. The analyses conducted in this thesis of compounds that

charge compensate the (de-)intercalation of Na-ions through the $Fe^{3+/4+}$ and $O^{2-/n-}$ ($n < 2$) redox couples support this goal and generate optimism for achieving it.

6.2 Suggested Future Work

There are several promising prospects for future research on Na-ion cathodes that derive from the work presented in this thesis:

- Na-naphthalide pre-treatment was shown to successfully overcome Na-deficiency in P2-type compounds. Further investigation is needed, however, to determine the long term cycling stability of the treated compounds and whether naphthalide causes any changes to the surface chemistry. Moreover, a solution possessing such reducing power may come with processing challenges. Thus, it would be shrewd to research how this pre-treatment step could be integrated into manufacturing lines.

- It was speculated in Chapter 3 that Fe is reduced in $Na_{2/3}[Ni_{1/6}Mn_{1/2}Fe_{1/3}]O_2$ through a reaction with the electrolyte. To test this theory, the surface chemistry of all Fe-containing $NaMO_2$ compounds in the charged state must be better characterized. In addition, developing surface coating strategies may also be beneficial as, to the best of my knowledge, this has not yet been applied to Fe-containing $NaMO_2$ compounds.

- While $Na_{2/3}[Ni_{1/3}Mn_{2/3}]O_2$ displayed relatively low hysteresis in the high voltage region, $Na_{2/3}[Ni_{1/6}Mn_{1/2}Fe_{1/3}]O_2$ showed a noticeably larger hysteresis in this same region. A physical explanation for this phenomenon has so far yet to materialize. The future investigation of this behavior is of fundamental importance to the utilization of Fe in $NaMO_2$ compounds.

- A new model for the P2→"Z"-phase structural evolution was outlined in Chapter 4. No such model currently exists, however, for O3-type compounds. While a P2-type layer can only transition to O2 stacking, an O3-type layer can glide to form either P3 or O1 stacking. The interplay of multiple

stacking sequences at high voltages may have an effect on a compound's reversibility, thus the structural evolution of O3-type compounds warrants further investigation.

- The interlayer contraction and associated volume change of layered oxide cathode materials remains an unresolved challenge. This obstacle may be addressed through the development of specialized binders or by substitution of mobile species such as Li^+ into the TM layer. Another possible avenue to combat this issue could be the addition of Ca^{2+} into the Na layer during synthesis. Like Li^+, this ion may serve to "pillar" the layers against severe contraction.

- The findings on oxygen redox relayed in this thesis open up an exciting opportunity to develop materials that exhibit superstructure-controlled behavior. Implementing the TM layer ribbon ordering into compounds with excess Na^+ or Li^+ could elicit the first oxygen redox compounds capable of delivering high capacities at a high voltage. Due to the success of the ribbon ordering, it would also be prudent to investigate other TM layer orderings (with less Li) to further optimize the reversibility.

Despite the remaining obstacles, the Na-ion battery research field is rapidly progressing and shows no sign of slowing its growth in the near future. This momentum provides hope that one day soon, Na-ion batteries could well be an efficient, economical, and effective option for satisfying the world's increasing need for energy storage.

Appendices

$\mathbf{Na}_x[\mathbf{Ni}_{(x-y)/2}\mathbf{Mn}_{1-(x+y)/2}\mathbf{Fe}_y]\mathbf{O}_2$ Ternary Diagram XRD

Description of Refinement Methodology

The P2 and O3 structural models were fit to the following XRD patterns in order to obtain the ternary composition diagrams of Figure A.1. The variables of interest extracted from the data were the weight fraction as well as the lattice parameters of each phase. In depth structural characterization of each compound was not the aim of this study, and as such, only relatively short XRD collection times were used. Efforts were therefore made to reduce the complexity of the refinement procedure so as to extract only the critical information. A Pawley refinement of the data was conducted first to achieve the best possible profile parameters. Subsequently, profile variables were fixed to the ideal values and a Rietveld refinement was carried out (in order to get weight fractions). Site occupancies (SOF) and atom positions (x, y, and z) were fixed to reasonable values in the Rietveld refinement. The isotropic atomic displacement factors (Uiso) were refined only for the TM site of the structure (P2: site 2a, O3: site 3b) as the scattering power of the TM is high compared to Na and O. A spherical harmonics model was used as necessary to correct for preferred orientation (caused by the flat plate sample holder).

Refinement Results

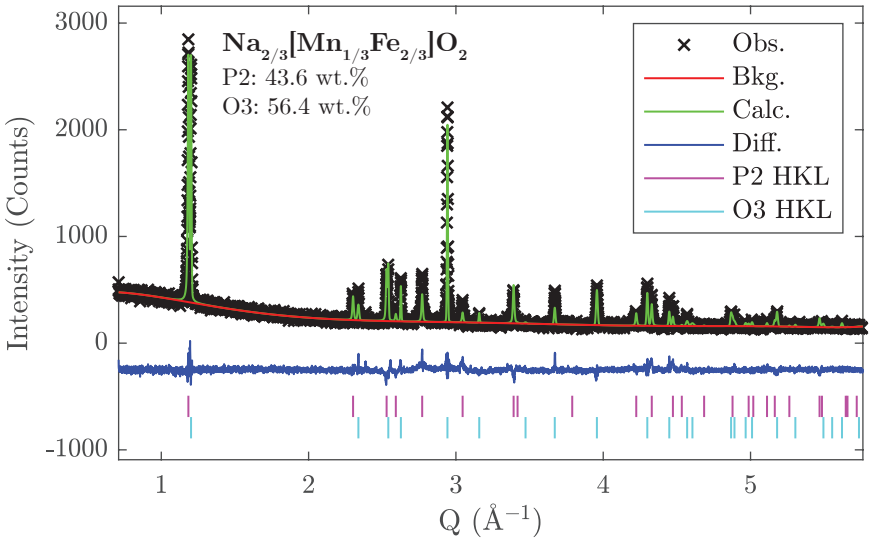

Figure A.1: XRD data for $Na_{2/3}[Mn_{1/3}Fe_{2/3}]O_2$ (composition 1) is shown with the corresponding fitting from the Rietveld refinement. Refined parameters are listed in Table A.1.

Table A.1: Rietveld Refinement results for $Na_{2/3}[Mn_{1/3}Fe_{2/3}]O_2$ (composition 1) for the ternary composition diagram (Figure 3.7).

P2: S.G. *P6$_3$/mmc*, *a*: 2.9372(1) Å, *c*: 11.2117(7) Å, Wt. %: 43.6(9), Rwp: 8.97%, Rexp: 6.41%					
Atom	**x**	**y**	**z**	**SOF**	**Uiso (Å^2)**
Na (2b)	0	0	1/4	1/6	0.01
Na (2d)	2/3	1/3	1/4	1/2	0.01
Mn (2a)	0	0	0	1/3	0.008(2)
Fe (2a)	0	0	0	2/3	0.008(2)
O (4f)	2/3	1/3	-0.094	1	0.01
O3: S.G. *R$\bar{3}$m*, *a*: 2.9584(1) Å, *c*: 16.5494(8) Å Wt. %: 56.4(7)					
Atom	**x**	**y**	**z**	**SOF**	**Uiso (Å^2)**
Na (3a)	0	0	0	2/3	0.01
Mn (3b)	0	0	1/2	1/3	0.005(1)
Fe (3b)	0	0	1/2	2/3	0.005(1)
O (6c)	0	0	0.24	1	0.01

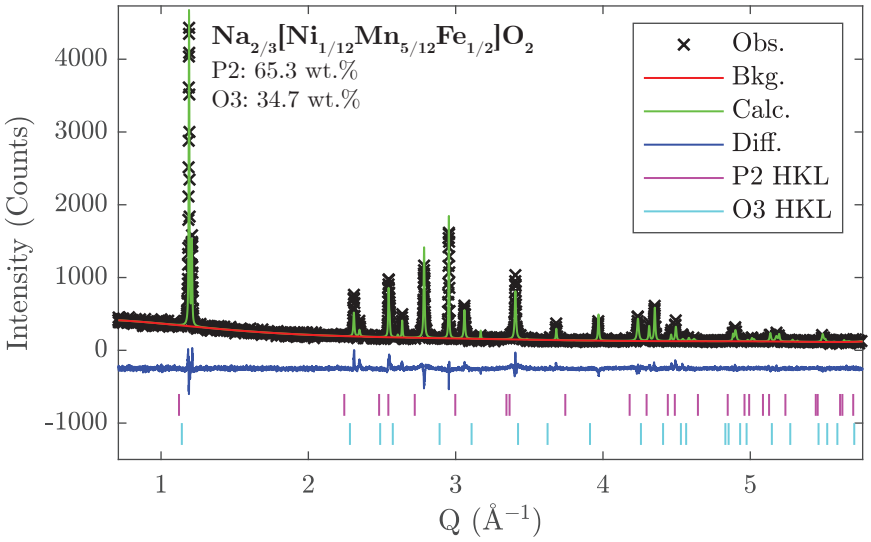

Figure A.2: XRD data for $Na_{2/3}[Ni_{1/12}Mn_{5/12}Fe_{1/2}]O_2$ (composition 2) is shown with the corresponding fitting from the Rietveld refinement. Refined parameters are listed in Table A.2.

Table A.2: Rietveld Refinement results for $Na_{2/3}[Ni_{1/12}Mn_{5/12}Fe_{1/2}]O_2$ (composition 2) for the ternary composition diagram (Figure 3.7).

P2: S.G. *P6₃/mmc*, *a*: 2.9251(1) Å, *c*: 11.2007(5) Å, Wt. %: 65.3(7), Rwp: 9.06%, Rexp: 6.88%					
Atom	**x**	**y**	**z**	**SOF**	**Uiso (Å²)**
Na (2b)	0	0	1/4	1/6	0.01
Na (2d)	2/3	1/3	1/4	1/2	0.01
Ni (2a)	0	0	0	1/12	0.0001(9)
Mn (2a)	0	0	0	5/12	0.0001(9)
Fe (2a)	0	0	0	1/2	0.0001(9)
O (4f)	2/3	1/3	-0.094	1	0.01
O3: S.G. *R$\bar{3}$m*, *a*: 2.9515(1) Å, *c*: 16.5180(7) Å Wt. %: 34.7(5)					
Atom	**x**	**y**	**z**	**SOF**	**Uiso (Å²)**
Na (3a)	0	0	0	2/3	0.01
Ni (3b)	0	0	1/2	1/12	0.002(2)
Mn (3b)	0	0	1/2	5/12	0.002(2)
Fe (3b)	0	0	1/2	1/2	0.002(2)
O (6c)	0	0	0.24	1	0.01

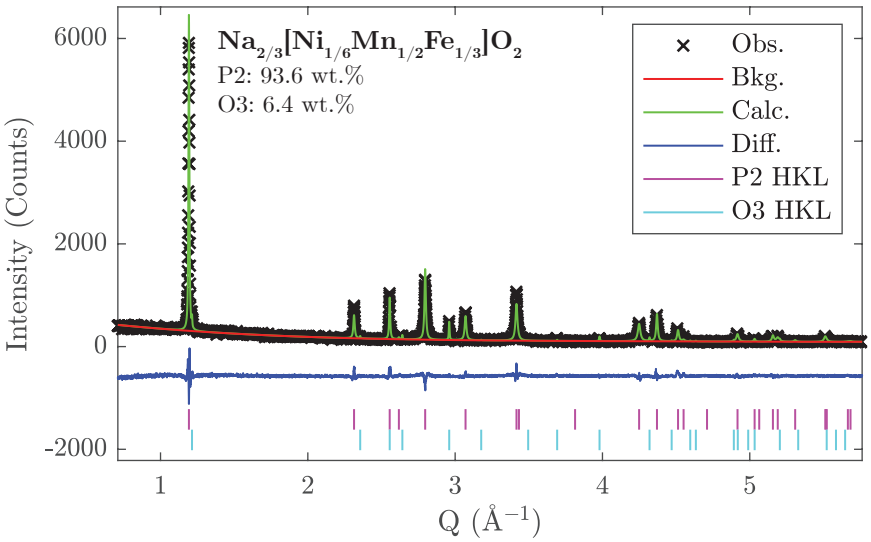

Figure A.3: XRD data for $Na_{2/3}[Ni_{1/6}Mn_{1/2}Fe_{1/3}]O_2$ (composition 3) is shown with the corresponding fitting from the Rietveld refinement. Refined parameters are listed in Table A.3.

Table A.3: Rietveld refinement results for $Na_{2/3}[Ni_{1/6}Mn_{1/2}Fe_{1/3}]O_2$ (composition 3) for the ternary composition diagram (Figure 3.7).

P2: S.G. *P6₃/mmc*, *a*: 2.9130(1) Å, *c*: 11.1805(6) Å, Wt. %: 93.59(9), Rwp: 9.67%, Rexp: 7.21%					
Atom	**x**	**y**	**z**	**SOF**	**Uiso (Å²)**
Na (2b)	0	0	1/4	1/6	0.01
Na (2d)	2/3	1/3	1/4	1/2	0.01
Ni (2a)	0	0	0	1/6	0.0037(7)
Mn (2a)	0	0	0	1/2	0.0037(7)
Fe (2a)	0	0	0	1/3	0.0037(7)
O (4f)	2/3	1/3	-0.094	1	0.01
O3: S.G. *R$\bar{3}$m*, *a*: 2.9476(3) Å, *c*: 16.464(2) Å Wt. %: 6.4(1)					
Atom	**x**	**y**	**z**	**SOF**	**Uiso (Å²)**
Na (3a)	0	0	1/4	2/3	0.01
Ni (3b)	0	0	0	1/6	0.005(1)
Mn (3b)	0	0	0	1/2	0.005(1)
Fe (3b)	0	0	0	1/3	0.005(1)
O (6c)	0	0	0.24	1	0.01

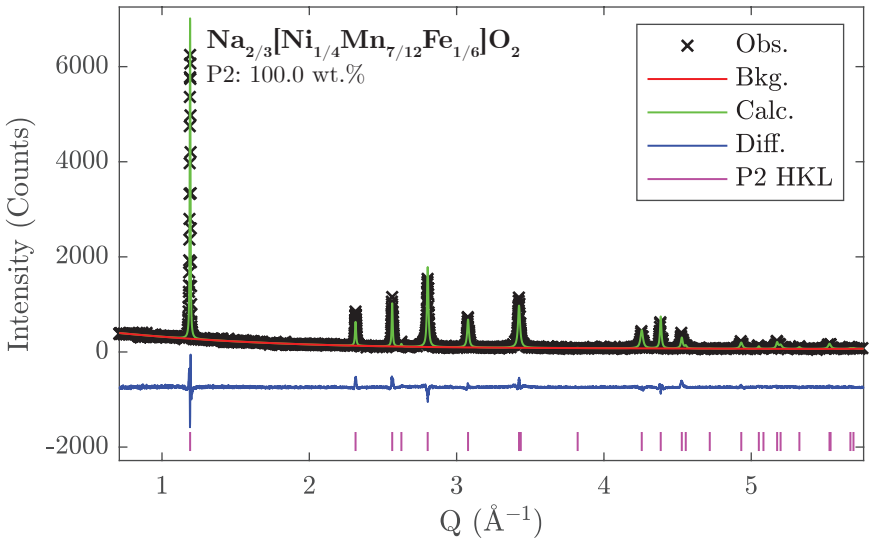

Figure A.4: XRD data for $Na_{2/3}[Ni_{1/4}Mn_{7/12}Fe_{1/6}]O_2$ (composition 4) is shown with the corresponding fitting from the Rietveld refinement. Refined parameters are listed in Table A.4.

Table A.4: Rietveld refinement results for $Na_{2/3}[Ni_{1/4}Mn_{7/12}Fe_{1/6}]O_2$ (composition 4) for the ternary composition diagram (Figure 3.7).

P2: S.G. *P6₃/mmc*, *a*: 2.9002(1) Å, *c*: 11.1604(5) Å, Rwp: 10.66%, Rexp: 7.79%					
Atom	**x**	**y**	**z**	**SOF**	**Uiso (Å²)**
Na (2b)	0	0	1/4	1/6	0.01
Na (2d)	2/3	1/3	1/4	1/2	0.01
Ni (2a)	0	0	0	1/4	0.0018(6)
Mn (2a)	0	0	0	7/12	0.0018(6)
Fe (2a)	0	0	0	1/6	0.0018(6)
O (4f)	2/3	1/3	-0.094	1	0.01

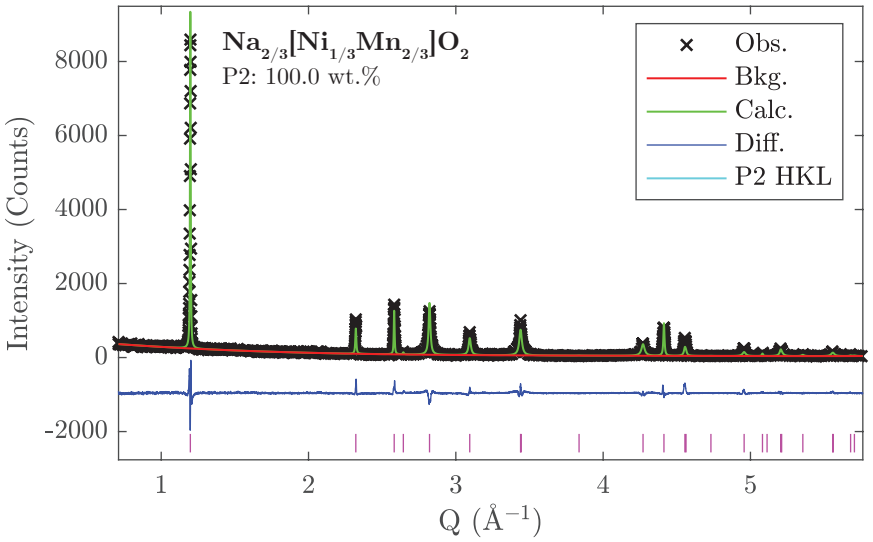

Figure A.5: XRD data for $Na_{2/3}[Ni_{1/3}Mn_{2/3}]O_2$ (composition 5) is shown with the corresponding fitting from the Rietveld refinement. Refined parameters are listed in Table A.5.

Table A.5: Rietveld refinement results for $Na_{2/3}[Ni_{1/3}Mn_{2/3}]O_2$ (composition 5) for the ternary composition diagram (Figure 3.7).

P2: S.G. *P6$_3$/mmc*, *a*: 2.8857(1) Å, *c*: 11.1568(6) Å, Rwp: 14.97%, Rexp: 8.42%					
Atom	**x**	**y**	**z**	**SOF**	**Uiso (Å^2)**
Na (2b)	0	0	1/4	1/6	0.01
Na (2d)	2/3	1/3	1/4	1/2	0.01
Ni (2a)	0	0	0	1/3	0.0006(7)
Mn (2a)	0	0	0	2/3	0.0006(7)
O (4f)	2/3	1/3	-0.094	1	0.01

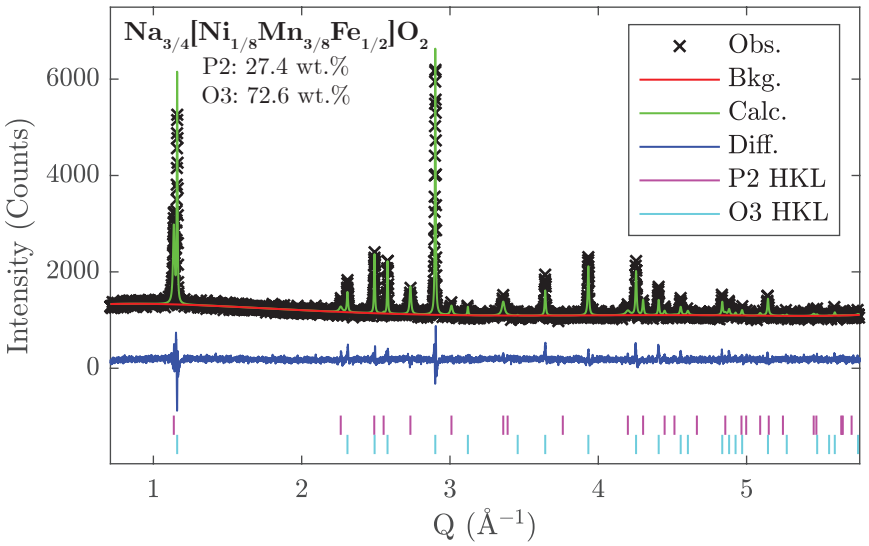

Figure A.6: XRD data for $Na_{3/4}[Ni_{1/8}Mn_{3/8}Fe_{1/2}]O_2$ (composition 6) is shown with the corresponding fitting from the Rietveld refinement. Refined parameters are listed in Table A.6.

Table A.6: Rietveld refinement results for $Na_{3/4}[Ni_{1/8}Mn_{3/8}Fe_{1/2}]O_2$ (composition 6) for the ternary composition diagram (Figure 3.7).

P2: S.G. *P6₃/mmc*, *a*: 2.9254(4) Å, *c*: 11.1453(9) Å, Wt. %: 27.4(8), Rwp: 3.78%, Rexp: 2.88%					
Atom	**x**	**y**	**z**	**SOF**	**Uiso (Å²)**
Na (2b)	0	0	1/4	1/4	0.01
Na (2d)	2/3	1/3	1/4	1/2	0.01
Ni (2a)	0	0	0	1/8	0.027(4)
Mn (2a)	0	0	0	3/8	0.027(4)
Fe (2a)	0	0	0	1/2	0.027(4)
O (4f)	2/3	1/3	-0.094	1	0.01
O3: S.G. *R$\bar{3}$m*, *a*: 2.95781(6) Å, *c*: 16.3912(4) Å Wt. %: 72.6(29)					
Atom	**x**	**y**	**z**	**SOF**	**Uiso (Å²)**
Na (3a)	0	0	1/4	3/4	0.01
Ni (3b)	0	0	0	1/8	0.001(2)
Mn (3b)	0	0	0	3/8	0.001(2)
Fe (3b)	0	0	0	1/2	0.001(2)
O (6c)	0	0	0.24	1	0.01

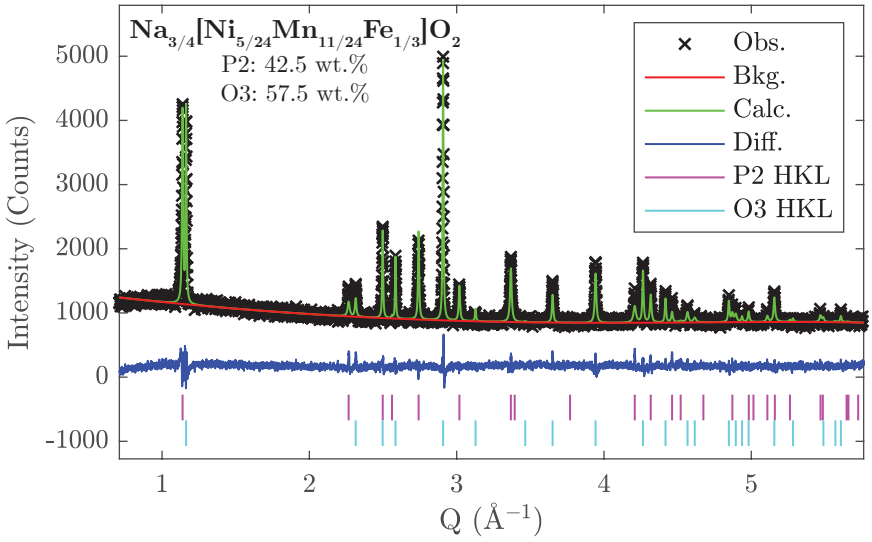

Figure A.7: XRD data for $Na_{3/4}[Ni_{5/24}Mn_{11/24}Fe_{1/3}]O_2$ (composition 7) is shown with the corresponding fitting from the Rietveld refinement. Refined parameters are listed in Table A.7.

Table A.7: Rietveld refinement results for $Na_{3/4}[Ni_{5/24}Mn_{11/24}Fe_{1/3}]O_2$ (composition 7) for the ternary composition diagram (Figure 3.7).

P2: S.G. *P6$_3$/mmc*, *a*: 2.9150(2) Å, *c*: 11.1341(6) Å, Wt. %: 42.5(4), Rwp: 4.18%, Rexp: 3.19%					
Atom	**x**	**y**	**z**	**SOF**	**Uiso (Å²)**
Na (2b)	0	0	1/4	1/4	0.01
Na (2d)	2/3	1/3	1/4	1/2	0.01
Ni (2a)	0	0	0	5/24	0.017(1)
Mn (2a)	0	0	0	11/24	0.017(1)
Fe (2a)	0	0	0	1/3	0.017(1)
O (4f)	2/3	1/3	-0.094	1	0.01
O3: S.G. *R$\bar{3}$m*, *a*: 2.9511(1) Å, *c*: 16.3539(7) Å Wt. %: 57.5(39)					
Atom	**x**	**y**	**z**	**SOF**	**Uiso (Å²)**
Na (3a)	0	0	1/4	3/4	0.01
Ni (3b)	0	0	0	5/24	0.0001(30)
Mn (3b)	0	0	0	11/24	0.0001(30)
Fe (3b)	0	0	0	1/3	0.0001(30)
O (6c)	0	0	0.24	1	0.01

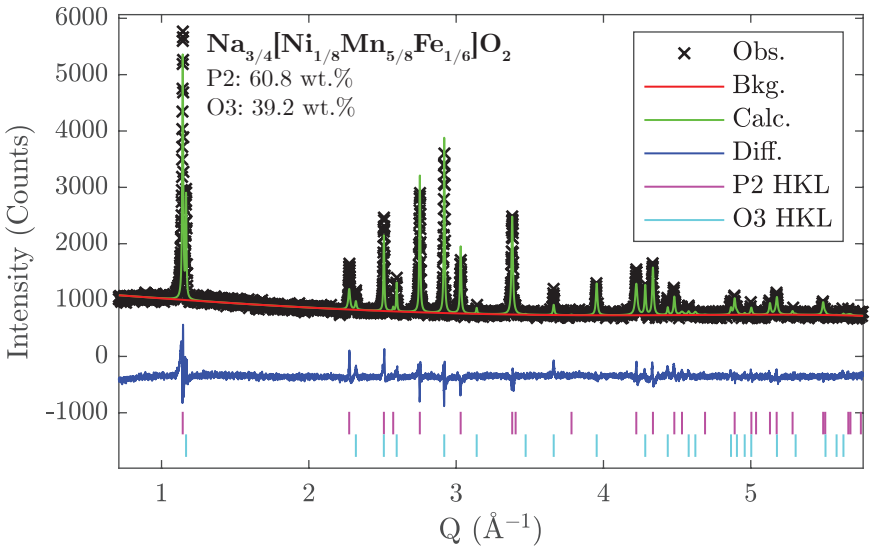

Figure A.8: XRD data for $Na_{3/4}[Ni_{7/24}Mn_{13/24}Fe_{1/6}]O_2$ (composition 8) is shown with the corresponding fitting from the Rietveld refinement. Refined parameters are listed in Table A.8.

Table A.8: Rietveld refinement results for $Na_{3/4}[Ni_{7/24}Mn_{13/24}Fe_{1/6}]O_2$ (composition 8) for the ternary composition diagram (Figure 3.7).

P2: S.G. *P6₃/mmc*, *a*: 2.90345(9) Å, *c*: 11.1069(3) Å, Wt. %: 60.8(22), Rwp: 5.06%, Rexp: 3.39%					
Atom	**x**	**y**	**z**	**SOF**	**Uiso (Å²)**
Na (2b)	0	0	1/4	1/4	0.01
Na (2d)	2/3	1/3	1/4	1/2	0.01
Ni (2a)	0	0	0	7/24	0.009(2)
Mn (2a)	0	0	0	13/24	0.009(2)
Fe (2a)	0	0	0	1/6	0.009(2)
O (4f)	2/3	1/3	-0.094	1	0.01
O3: S.G. *R$\bar{3}$m*, *a*: 2.9390(1) Å, *c*: 16.3319(7) Å Wt. %: 39.2(43)					
Atom	**x**	**y**	**z**	**SOF**	**Uiso (Å²)**
Na (3a)	0	0	1/4	3/4	0.01
Ni (3b)	0	0	0	7/24	0.004(5)
Mn (3b)	0	0	0	13/24	0.004(5)
Fe (3b)	0	0	0	1/6	0.004(5)
O (6c)	0	0	0.24	1	0.01

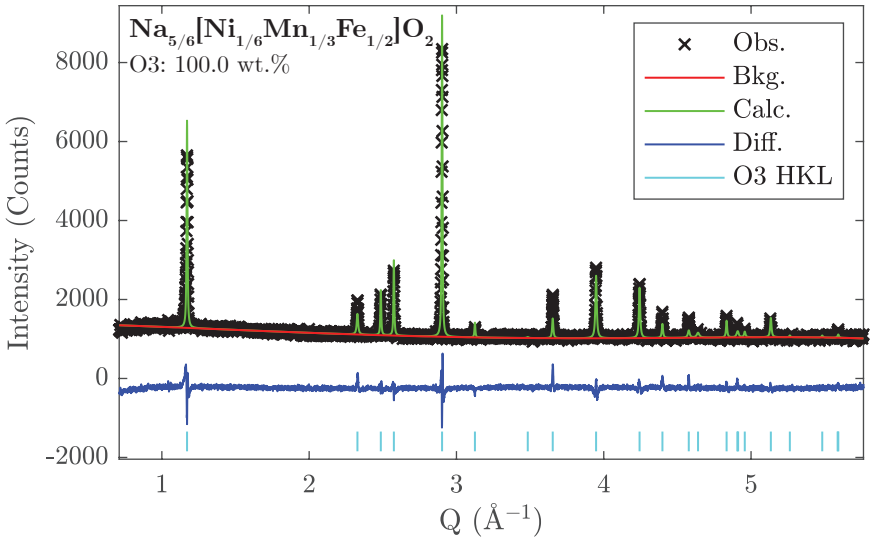

Figure A.9: XRD data for $Na_{5/6}[Ni_{1/6}Mn_{1/2}Fe_{1/3}]O_2$ (composition 9) is shown with the corresponding fitting from the Rietveld refinement. Refined parameters are listed in Table A.9.

Table A.9: Rietveld refinement results for $Na_{5/6}[Ni_{1/6}Mn_{1/2}Fe_{1/3}]O_2$ (composition 9) for the ternary composition diagram (Figure 3.7).

O3: S.G. $R\bar{3}m$, a: 2.96742(6) Å, c: 16.2756(3) Å Rwp: 4.33%, Rexp: 2.95%					
Atom	**x**	**y**	**z**	**SOF**	**Uiso (Å²)**
Na (3a)	0	0	1/4	5/6	0.01
Ni (3b)	0	0	0	1/6	0.008(4)
Mn (3b)	0	0	0	1/3	0.008(4)
Fe (3b)	0	0	0	1/2	0.008(4)
O (6c)	0	0	0.24	1	0.01

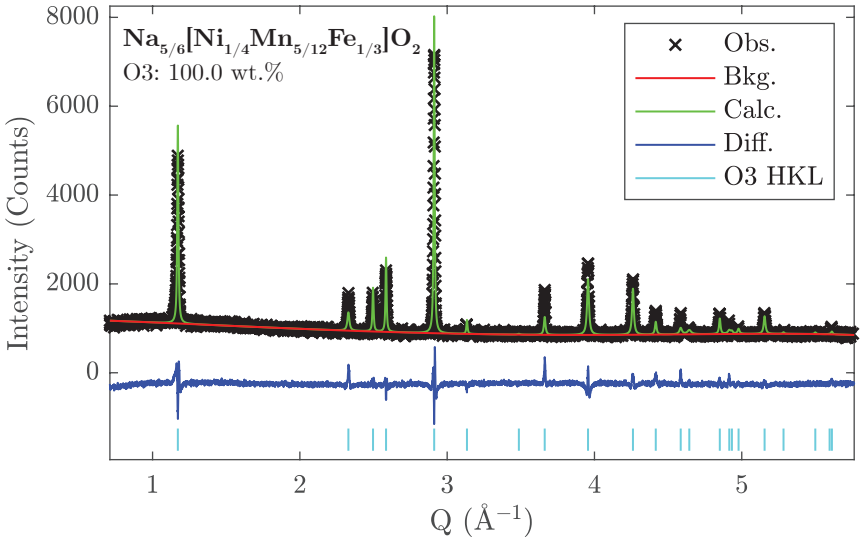

Figure A.10: XRD data for $Na_{5/6}[Ni_{1/4}Mn_{5/12}Fe_{1/3}]O_2$ (composition 10) is shown with the corresponding fitting from the Rietveld refinement. Refined parameters are listed in Table A.10.

Table A.10: Rietveld refinement results for $Na_{5/6}[Ni_{1/4}Mn_{5/12}Fe_{1/3}]O_2$ (composition 10) for the ternary composition diagram (Figure 3.7).

O3: S.G. $R\bar{3}m$, a: 2.95452(8) Å, c: 16.2613(4) Å Rwp: 4.89%, Rexp: 3.18%					
Atom	**x**	**y**	**z**	**SOF**	**Uiso (Å²)**
Na (3a)	0	0	1/4	5/6	0.01
Ni (3b)	0	0	0	1/4	0.006(3)
Mn (3b)	0	0	0	5/12	0.006(3)
Fe (3b)	0	0	0	1/3	0.006(3)
O (6c)	0	0	0.24	1	0.01

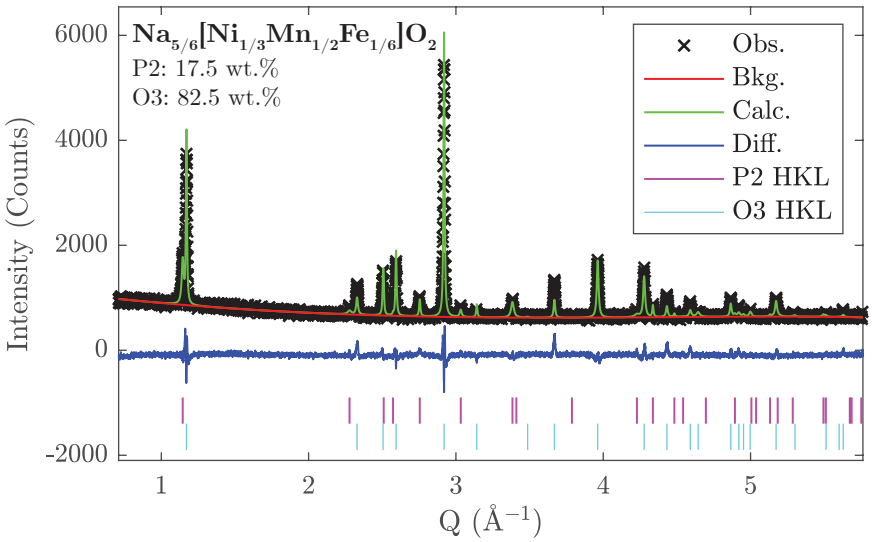

Figure A.11: XRD data for $Na_{3/4}[Ni_{1/3}Mn_{1/2}Fe_{1/6}]O_2$ (composition 11) is shown with the corresponding fitting from the Rietveld refinement. Refined parameters are listed in Table A.11.

Table A.11: Rietveld refinement results for $Na_{3/4}[Ni_{1/3}Mn_{1/2}Fe_{1/6}]O_2$ (composition 11) for the ternary composition diagram (Figure 3.7).

P2: S.G. *P6$_3$/mmc*, *a*: 2.9024(3) Å, *c*: 11.082(1) Å, Wt. %: 17.5(3), Rwp: 4.88%, Rexp: 3.67%					
Atom	**x**	**y**	**z**	**SOF**	**Uiso (Å^2)**
Na (2b)	0	0	1/4	1/3	0.01
Na (2d)	2/3	1/3	1/4	1/2	0.01
Ni (2a)	0	0	0	1/3	0.045(3)
Mn (2a)	0	0	0	1/2	0.045(3)
Fe (2a)	0	0	0	1/6	0.045(3)
O (4f)	2/3	1/3	-0.094	1	0.01
O3: S.G. *R$\bar{3}$m*, *a*: 2.94248(8) Å, *c*: 16.2568(4) Å Wt. %: 82.5(49)					
Atom	**x**	**y**	**z**	**SOF**	**Uiso (Å^2)**
Na (3a)	0	0	1/4	5/6	0.01
Ni (3b)	0	0	0	1/3	0.006(3)
Mn (3b)	0	0	0	1/2	0.006(3)
Fe (3b)	0	0	0	1/6	0.006(3)
O (6c)	0	0	0.24	1	0.01

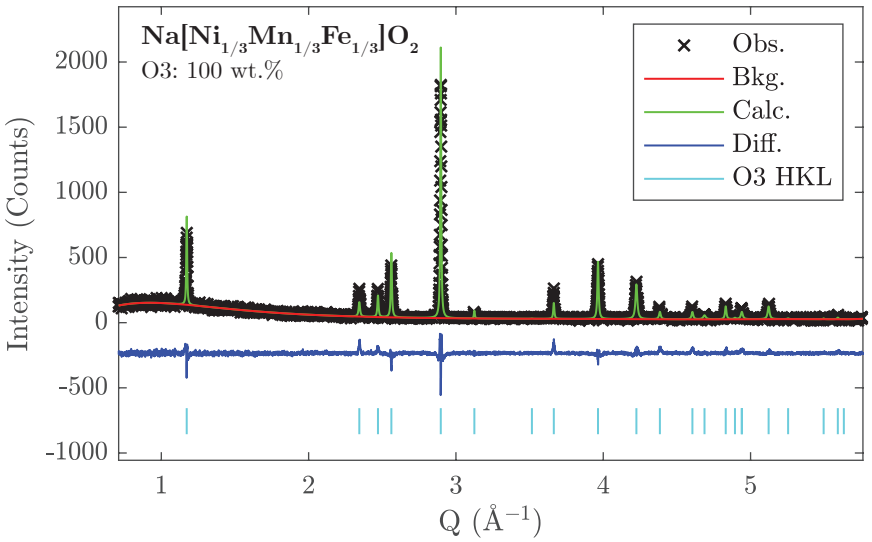

Figure A.12: XRD data for $Na[Ni_{1/3}Mn_{1/3}Fe_{1/3}]O_2$ (composition 12) is shown with the corresponding fitting from the Rietveld refinement. Refined parameters are listed in Table A.12.

Table A.12: Rietveld refinement results for $Na[Ni_{1/3}Mn_{1/3}Fe_{1/3}]O_3$ (composition 12) for the ternary composition diagram (Figure 3.7).

O3: S.G. $R\bar{3}m$, a: 2.9722(1) Å, c: 16.0739(6) Å Rwp: 13.54%, Rexp: 12.36%					
Atom	**x**	**y**	**z**	**SOF**	**Uiso (Å²)**
Na (3a)	0	0	1/4	1	0.01
Ni (3b)	0	0	0	1/3	0.001(2)
Mn (3b)	0	0	0	1/3	0.001(2)
Fe (3b)	0	0	0	1/3	0.001(2)
O (6c)	0	0	0.24	1	0.01

$\mathbf{Na_{2/3}[Ni_{1/3-y/2}Mn_{2/3-y/2}Fe_y]O_2}$ ($y = 1/6, 1/3$) Synchrotron XRD Refinements

Description of Refinement Methodology

The P2 ($P6_3/mmc$) structural model was fit to the synchrotron XRD patterns of $Na_{2/3}[Ni_{1/4}Mn_{7/12}Fe_{1/6}]O_2$ and $Na_{2/3}[Ni_{1/6}Mn_{1/2}Fe_{1/3}]O_2$. A Pawley refinement of the data was conducted first to achieve the best possible profile parameters. Subsequently, profile variables were fixed to the ideal values and a Rietveld refinement was carried out. The Na site occupancy of the two sites was constrained to sum to 2/3 (matching the nominal composition). The isotropic displacement factors for the Na were constrained to be equivalent. The isotropic displacement factors of the TMs were constrained to be equivalent as they occupy the same site.

Refinement Results

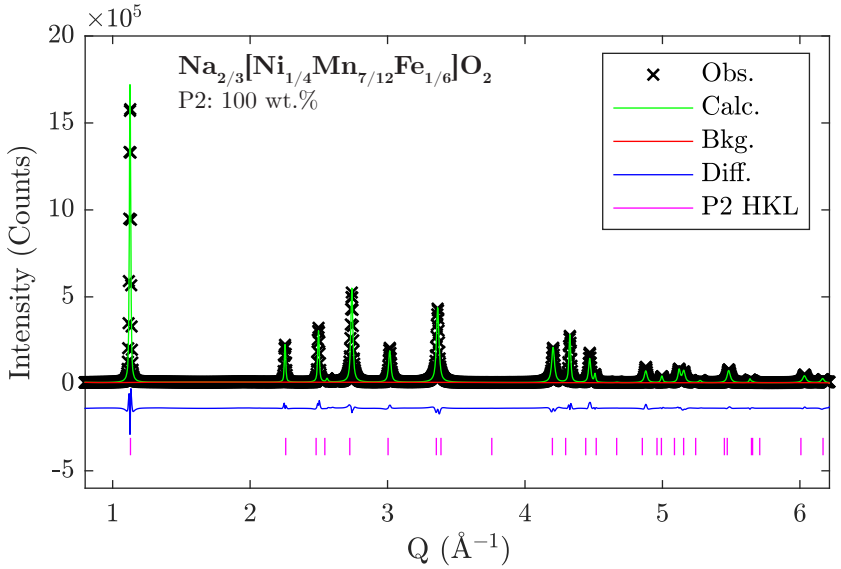

Figure A.13: Synchrotron XRD data for $Na_{2/3}[Ni_{1/4}Mn_{7/12}Fe_{1/6}]O_2$ is shown with the corresponding fitting from the Rietveld refinement. Refined parameters are listed in Table A.13.

Table A.13: Rietveld refinement results for $Na_{2/3}[Ni_{1/4}Mn_{7/12}Fe_{1/6}]O_2$ (Figure A.13).

P2: S.G. *P6₃/mmc*, *a*: 2.9045(1) Å, *c*: 11.1467(5) Å, Rwp: 11.41%, Rexp: 0.61%					
Atom	**x**	**y**	**z**	**SOF**	**Uiso (Å²)**
Na (2b)	0	0	1/4	0.227(4)	0.035(2)
Na (2d)	2/3	1/3	1/4	0.440(4)	0.035(2)
Ni (2a)	0	0	0	1/4	0.0041(4)
Mn (2a)	0	0	0	7/12	0.0041(4)
Fe (2a)	0	0	0	1/6	0.0041(4)
O (4f)	2/3	1/3	-0.0910(3)	1	0.011(1)

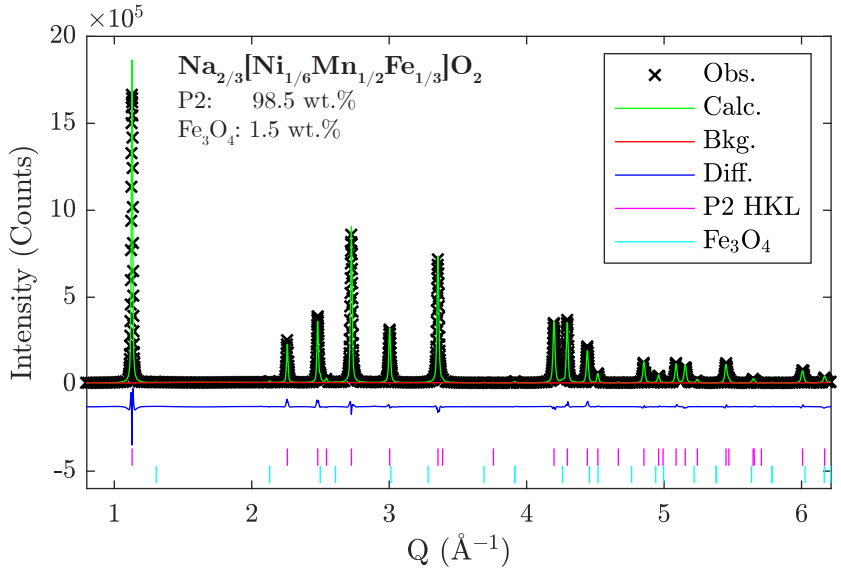

Figure A.14: Synchrotron XRD data for $Na_{2/3}[Ni_{1/6}Mn_{1/2}Fe_{1/3}]O_2$ is shown with the corresponding fitting from the Rietveld refinement. Refined parameters are listed in Table A.14.

Table A.14: Rietveld refinement results for $Na_{2/3}[Ni_{1/6}Mn_{1/2}Fe_{1/3}]O_2$ (Figure A.14).

P2: S.G. *P6₃/mmc*, *a*: 2.92527(4) Å, *c*: 11.1251(1) Å, Wt. %: 98.5(3), Rwp: 8.71%, Rexp: 0.58%					
Atom	**x**	**y**	**z**	**SOF**	**Uiso (Å²)**
Na (2b)	0	0	1/4	0.196(2)	0.024(1)
Na (2d)	2/3	1/3	1/4	0.471(2)	0.024(1)
Ni (2a)	0	0	0	1/6	0.0048(2)
Mn (2a)	0	0	0	1/2	0.0048(2)
Fe (2a)	0	0	0	1/3	0.0048(2)
O (4f)	2/3	1/3	-0.0940(1)	1	0.0150(5)
Fe_3O_3: S.G. *Fd$\bar{3}$m*, *a*: 8.342(1) Å Wt. %: 1.49(5)					
Atom	**x**	**y**	**z**	**SOF**	**Uiso (Å²)**
Fe (8a)	1/8	1/8	1/8	1	0.01
Fe (16d)	1/2	1/2	1/2	1	0.01
O (32e)	1/4	1/4	1/4	1	0.01

List of Figures